University of Stuttgart
Germany

UHASSELT

The Phase Field Approach for Reactive Fluid–Solid Interfaces: Modeling and Homogenization

Lars von Wolff

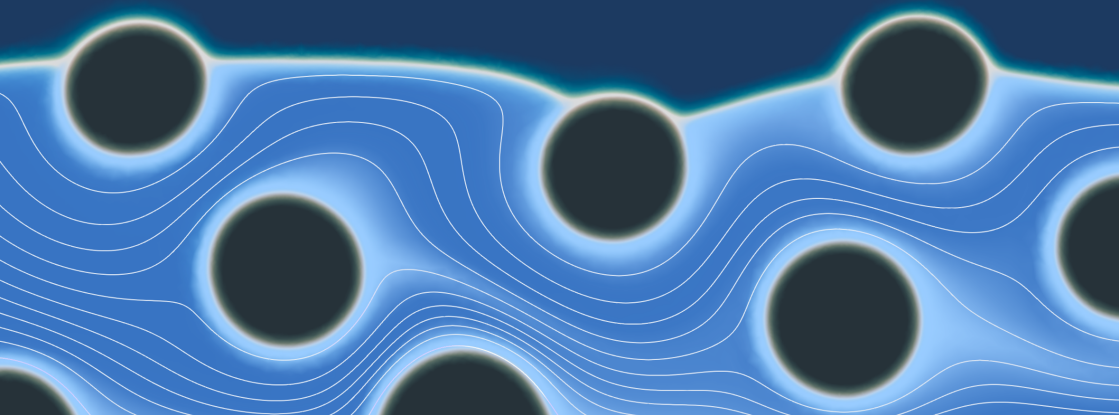

The Phase Field Approach for Reactive Fluid–Solid Interfaces: Modeling and Homogenization

Von der Fakultät Mathematik und Physik und dem
Stuttgarter Zentrum für Simulationswissenschaft (SC SimTech)
der Universität Stuttgart zur Erlangung der Würde eines
Doktors der Naturwissenschaften (Dr. rer. nat.)
genehmigte Abhandlung

und von der Universität Hasselt zur Erlangung der Würde eines
Doctor of Sciences: Mathematics
genehmigte Abhandlung

vorgelegt von

Lars Philipp Adam Freiherr von Wolff

aus Tübingen

Hauptberichter:	Prof. Dr. Christian Rohde	Universität Stuttgart
Mitberichter:	Prof. Dr. Iuliu Sorin Pop	Universität Hasselt
	Prof. Dr. Harald Garcke	Universität Regensburg
	Prof. Dr. Grégoire Allaire	École Polytechnique

Tag der mündlichen Prüfung: 22. September 2022

Institut für Angewandte Analysis und Numerische Simulation,
Universität Stuttgart

2023

Depot number: D/2022/2451/86

University of Stuttgart
Germany

Acknowledgements

This work was supported by the Deutsche Forschungsgemeinschaft (DFG, German Research Foundation) – Project Number 327154368 – SFB 1313; the Research Foundation Flanders (FWO) – Project G0G1316N; and the Hasselt University – Project BOF19BL12.

Contents

Abstract vii

Related Publications ix

1 Introduction 3
- 1.1 Reactive Multi-Phase Flow in Porous Media 3
  - 1.1.1 Example for Microstructural Evolution: EICP in Porous Media 4
- 1.2 Phase Field Models for Multi-Phase Flow 6
- 1.3 Matched Asymptotic Expansions and the Sharp Interface Limit 12
  - 1.3.1 Sharp Interface Limit for the Allen–Cahn Equation 16
- 1.4 Upscaling in Porous Media 18

I Phase Field Models for Reactive Fluid–Solid Interfaces 23

2 The Allen–Cahn–Navier–Stokes Model 25
- 2.1 The Reactive Transport Problem For Single-Phase Flow 26
  - 2.1.1 The Sharp Interface Formulation 26
  - 2.1.2 The Phase Field Formulation 29
  - 2.1.3 The Regularized Phase Field Formulation . . 33

2.2 The Sharp Interface Limit 34
2.2.1 Outer Expansions 35
2.2.2 Inner Expansions 35
2.3 Numerical Investigation of the Phase Field Model . . 39
2.3.1 Dissolution of a Calcite Crystal 39
2.3.2 Effect of Flow Field Strength on Dissolution . 41

3 The Cahn–Hilliard–Navier–Stokes Model 45
3.1 The Reactive Transport Problem for Multi-Phase Flow 46
3.1.1 The Sharp Interface Formulation 46
3.1.2 The $2f1s$-Phase Field Model 55
3.1.3 The δ-$2f1s$-Phase Field Model 64
3.1.4 Conservation of Total Mass, Ions and Volume Fraction 65
3.1.5 Thermodynamical Consistency 66
3.1.6 Algebraic Consistency 72
3.2 The Sharp Interface Limit 76
3.2.1 Outer Expansions 77
3.2.2 Inner Expansions, Leading Order 79
3.2.3 Inner Expansions, First Order 85
3.2.4 Triple Point Expansions 89
3.3 Discretization and Implementation 90
3.4 Numerical Investigation of the Phase Field Model . . 95
3.4.1 Nucleus in Channel Flow 95
3.4.2 Variable Slip Length 95

4 The Cahn–Hilliard–Navier–Stokes Model as a Diffuse-Domain Model 99
4.1 Multi-phase Flow in a Diffuse Domain 101
4.1.1 The Sharp Interface Formulation 101
4.1.2 The DD-$2f1s$-Phase Field Model 105
4.1.3 Thermodynamical Consistency 109
4.2 The Sharp Interface Limit 112
4.2.1 Outer Expansions 113
4.2.2 Inner Expansions, Leading Order 114
4.2.3 Inner Expansions, First Order 116

4.2.4 Triple Point Expansions 116
4.3 Numerical Investigation 123

II Upscaling of Reactive Flow 127

5 Upscaling the Allen–Cahn Model Using Periodic Homogenization 129
5.1 Upscaling 129
5.1.1 The Scale Separation 131
5.1.2 Non-Dimensional Model Equations 133
5.1.3 The Formal Asymptotic Expansions 137
5.1.4 The Upscaled Allen–Cahn–Navier–Stokes Model 143
5.2 Numerical Investigation for the Upscaled Model . . . 144
5.2.1 Solutions to Cell Problems 145

6 Upscaling the Allen–Cahn Model in a Thin Strip 151
6.1 Upscaling 152
6.1.1 Transversal Averaging 152
6.1.2 The Averaged Allen–Cahn–Navier–Stokes Model 156
6.2 Numerical Investigation 157
6.2.1 Comparison to the Sharp Interface Formulation 158
6.2.2 Comparison to the Original Two-Dimensional Formulation 159

7 Upscaling the Cahn–Hilliard Model in a Thin Strip 163
7.1 Non-dimensionalization 163
7.2 Upscaling in a Thin Strip 168
7.2.1 Scaling of Non-Dimensional Numbers 168
7.2.2 Asymptotic Expansions 170
7.2.3 The Upscaled δ-2f1s-Model 176
7.3 Sharp-Interface Limit of the Upscaled δ-2f1s-Model 178
7.3.1 Assumptions and Scaling of Non-Dimensional Numbers 178
7.3.2 Outer Expansions 179
7.3.3 Inner Expansions 181
7.3.4 The Upscaled Sharp-Interface Model 189

7.3.5 The Upscaled Sharp-Interface Model in a Simplified Geometry with Symmetry 191
7.3.6 Asymptotic Consistency 194
7.4 Numerical Scheme for the Upscaled δ-$2f1s$-Model . . 196
7.5 Numerical Investigation 199
7.5.1 Comparison: Formation of an N-Wave 200
7.5.2 Comparison: Precipitation 202

III Applications **207**

8 Investigation of Crystal Growth in Enzymatically Induced Calcite Precipitation 209
8.1 Micro-Fluidic Experiments 212
8.1.1 Experimental Setup and Procedure 212
8.1.2 Kinetics of Urea Hydrolysis 213
8.2 Phase Field Model for EICP 215
8.2.1 Modifications to the δ-$1f1s$ Model 215
8.2.2 Numerical Implementation 218
8.2.3 Calculation of the Inflow Conditions 220
8.3 Results and Discussion 221
8.3.1 Movement of Centroids 223
8.3.2 Growth of Crystal Aggregates 226
8.4 Conclusions 229

Conclusion 233

Bibliography 237

Abstract

The overarching topic of this dissertation is multi-phase flow in porous media. In the presence of salts and their ions, precipitation and dissolution can alter the pore-space and have a great impact on flow through porous media. Therefore, we need reliable models that can describe these effects accurately both on the pore-scale and on larger scales.

In this dissertation, we first propose several pore-scale models for multi-phase flow including reactive fluid–solid interfaces. In these models, both fluid–fluid and fluid–solid interfaces are resolved as diffuse interfaces using the phase field method. We investigate the thermodynamical consistency of the models and find their sharp interface limit using asymptotic analysis.

We proceed to upscale the pore-scale models either using homogenization in a periodic porous medium or transversal averaging in the simplified geometry of a thin strip. The results are multi-scale models consisting of averaged equations for flux and ion concentration, with parameters that have to be determined through cell problems. These cell problems encode information about the geometry of the microscale at each macroscopic point.

Lastly, we apply the developed models to investigate enzymatically induced calcite precipitation. We compare simulation results to micro-fluidic experiments and find excellent agreement, in particular for the growth direction of crystal aggregates.

Zusammenfassung

Das übergeordnete Thema dieser Dissertation ist die Mehrphasenströmung in porösen Medien. In Anwesenheit von Salzen und ihren Ionen können Präzipitation und Auflösung den Porenraum verändern und die Strömung durch poröse Medien stark beeinflussen. Daher

benötigen wir zuverlässige Modelle, die diese Effekte sowohl auf der Porenskala als auch auf größeren Skalen exakt beschreiben können.

In dieser Dissertation schlagen wir zunächst mehrere Modelle für Mehrphasenströmungen einschließlich reaktiver Flüssig–Festkörper-Grenzflächen auf der Porenskala vor. Dabei werden sowohl Flüssig–Flüssig- als auch Flüssig–Festkörper-Grenzflächen mit Hilfe der Phasenfeldmethode als diffuse Grenzschicht aufgelöst. Wir untersuchen die thermodynamische Konsistenz der Modelle und finden ihren scharfen Grenzflächen-Limes mithilfe asymptotischer Analysis.

Wir betrachten den Skalenübergang der Porenskala-Modelle zur Darcy-Skala durch Homogenisierung in einem periodischen porösen Medium oder durch transversale Mittelung in der vereinfachten Geometrie eines dünnen Streifens. Das Ergebnis sind Multiskalenmodelle, die aus gemittelten Gleichungen für Fluss und Ionenkonzentration bestehen. Die Parameter dieser Gleichungen müssen duch Zellprobleme bestimmt werden, die die Geometrie der Mikroskala an jedem makroskopischen Punkt beschreiben.

Abschließend wenden wir die entwickelten Modelle an, um enzymatisch induzierte Kalzitausfällung zu untersuchen. Wir vergleichen die Simulationsergebnisse mit mikrofluidischen Experimenten und stellen eine exzellente Übereinstimmung fest, insbesondere für die Wachstumsrichtung der Kristallaggregate.

Related Publications

Part of the thesis work has already been published and is linked below.

Bringedal, C., L. von Wolff, and I. S. Pop. *Phase field modeling of precipitation and dissolution processes in porous media: upscaling and numerical experiments*. Multiscale Modeling & Simulation 18.2 (2020). DOI: 10.1137/19M1239003.

Rohde, C. and L. von Wolff. *A ternary Cahn–Hilliard–Navier–Stokes model for two-phase flow with precipitation and dissolution*. Mathematical Models and Methods in Applied Sciences 31.01 (2021). DOI: 10.1142/S0218202521500019.

von Wolff, L. and I. S. Pop. *Upscaling of a Cahn-Hilliard Navier-Stokes model with precipitation and dissolution in a thin strip*. Journal of Fluid Mechanics 941 (2022). DOI: 10.1017/jfm.2022.308.

von Wolff, L., F. Weinhardt, H. Class, J. Hommel, and C. Rohde. *Investigation of crystal growth in enzymatically induced calcite precipitation by micro-fluidic experimental methods and comparison with mathematical modeling*. Transport in Porous Media 137.2 (2021). DOI: 10.1007/s11242-021-01560-y.

Additionally, the following is supplementary to the thesis.

von Wolff, L. *The DUNE-phasefield module (release 1.0)*. Version V1. DaRUS (2021). DOI: 10.18419/darus-1634.

The publication [Bringedal, von Wolff, et al. 2020] includes work presented in Chapter 2, Chapter 5 and Chapter 6. These chapters were written in collaboration with Carina Bringedal and Sorin Pop. The numerical experiments in Section 2.3, Section 5.2 and Section 6.2 have been performed by Carina Bringedal. The publication [Rohde and von Wolff 2021] includes work of Chapter 3, and the numerical implementation described in Section 3.3 is online available at [von Wolff 2021]. The contents of Chapter 4 are not yet published. The publication [von Wolff and Pop 2022] includes work presented in

Chapter 7. The publication [von Wolff, Weinhardt, et al. 2021] contains work presented in Chapter 8. The micro-fluidic experiments were conducted by Felix Weinhardt, and Sections 8.1.1 and 8.1.2 were written by Felix Weinhardt. Section 8.3 was written in collaboration with Felix Weinhardt.

Introduction

1 Introduction

1.1 Reactive Multi-Phase Flow in Porous Media

Multi-phase flow and reactive transport processes are commonly encountered in engineering applications, getting particularly important in the context of porous media flow. Examples comprise processes like concrete carbonation, geological CO_2–sequestration involving calcite precipitation, ion exchange in fuel cells or the spreading of biofilms in the soil's vadose zone. While modeling of multi-phase flow in porous media is challenging in itself, these applications are even more complex as the involved solid phase can change over time. The evolving porous medium skeleton in turn changes the overall flow dynamics.

To describe multi-phase flow in porous media it is necessary to understand the phase-interfaces inside the porous medium, as they control to a large extent the behavior of the fluid flow. These interfaces include fluid–solid interfaces, usually between a fluid phase and the solid porous medium skeleton, as well as fluid–fluid interfaces between the fluid phases. Some fluid–solid interfaces can be altered due to chemical reactions, and such reactive fluid–solid interfaces introduce additional non-linearities in the system.

An important property of any porous medium is the occurrence of multiple spatial scales. On the pore-scale the fluid phases and the solid porous medium skeleton can be identified clearly, occupying

certain positions in well-defined volumes. This also means that all interfaces between phases are resolved on the pore-scale. Because the overall size of the porous medium is much bigger than the pore-scale, it is usually not feasible to resolve the pore-scale. Instead, averaged quantities are considered on a larger scale, i.e., the Darcy-scale.

Processes in porous media can be modelled at different length scales. When formulated on the pore-scale, the models are capable to describe the detailed processes accurately. On the other hand, they are defined in a highly complex domain, and this makes such models difficult to use for large spatial scales. For some simple processes in homogeneous porous media there exist fundamental laws for effective quantities on the Darcy-scale, e.g. Darcy's law for single-phase flow, effective laws for diffusion governed by Fick's law and for heat transfer governed by Fourier's law. More complex processes are much more difficult to describe through effective laws, in particular processes involving evolving pore-scale interfaces, such as fluid–fluid interfaces and reactive fluid–solid interfaces. Currently, such processes are approximated on an empirical basis through constitutive relationships that are stated directly at the Darcy-scale. In this context, upscaling is a natural way to derive mathematical models that, on one hand, can be used for practical applications, and, on the other hand, do incorporate accurately the influence of evolving small-scale interfaces at the pore-scale.

1.1.1 Example for Microstructural Evolution: EICP in Porous Media

A pertinent example of multi-phase flow in porous media with an evolving micro-structure is enzymatically induced calcium carbonate precipitation (EICP). To illustrate a process where the results of this thesis can be directly applied, we give a short overview of EICP in the following.

Enzymatically induced calcium carbonate precipitation is an engineering technology that employs enzymatic activity for altering

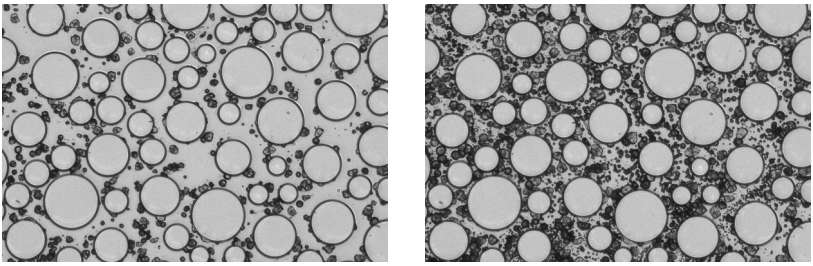

Figure 1.1: EICP in a micro-fluidic cell (images with permission from Felix Weinhardt). The solid matrix consisting of circles is impermeable for the fluid. From the left to the right image, calcium carbonate (dark gray) is precipitating over a time of 11 hours and this leads to a decrease in porosity and permeability.

geochemistry, thus resulting in precipitation of calcium carbonate. For this, ureases are used, which are widespread enzymes in soil bacteria and plants. Ureases catalyze the hydrolysis reaction of urea ($(NH_2)_2CO$), resulting at typical environmental conditions in the products bicarbonate (HCO_3^-) and ammonium (NH_4^+), i.e.,

$$\begin{aligned} CO(NH_2)_2 + 3H_2O \xrightarrow{urease} NH_4^+ + H_2NCOO^- + 2H_2O \\ \longrightarrow 2NH_4^+ + HCO_3^- + OH^-. \end{aligned}$$

The produced bicarbonate (HCO_3^-) can dissociate to yield carbonate ions (CO_3^{2-}). In the presence of calcium ions (Ca^{2+}) this results in calcium carbonate ($CaCO_3$) precipitation. Therefore, the overall reaction can be stated as

$$CO(NH_2)_2 + 2\,H_2O + Ca^{2+} \longrightarrow 2\,NH_4^+ + CaCO_3\downarrow.$$

EICP offers an engineering option to precipitate calcium carbonate in-situ, and by that to alter porous medium parameters such as porosity and permeability as well as the strength and stiffness of the medium. Hence, EICP can be used e.g. to seal high-permeable leakage pathways.

Figure 1.1 shows an experiment of EICP in a micro-fluidic cell. The calcium carbonate forms multiple nuclei in the pore space, and these nuclei continue to grow into grains through precipitation. While these grains can be transported by fluid, they usually remain affixed to the solid matrix (or in this case to the front- and backplate of the micro-fluidic cell).

1.2 Phase Field Models for Multi-Phase Flow

To describe multi-phase flow and an evolving solid phase on the pore-scale, the evolution of the interfaces between the phases has to be modeled. There are multiple approaches to model evolving interfaces of types fluid–fluid, reactive fluid–solid and non-reactive fluid–solid as encountered in our multi-phase flow scenario. From a physical point of view, the most well-grounded is the sharp interface formulation. The interfaces are represented as codimension-1 manifolds, and their movement is described by their normal velocity at each point of the interface. The normal velocity is determined from transmission conditions that connect to bulk models valid in the respective phases.

An alternative approach to model the evolving interfaces is through diffuse interface methods. Here, the interface is described as a zone of small positive width. The most common type of diffuse interface method is the phase field method. It introduces an additional order parameter ϕ as an approximation of the characteristic function, and hence ϕ attains the value 1 in one domain and 0 in the other. Because ϕ is chosen to be continuous, it has a smooth transition zone of non-zero width across the interface.

The evolution of the phase field variable ϕ is given by a phase field equation, which usually can be derived from a minimization of a free energy functional. Most commonly used are the Allen–Cahn equation [Allen and Cahn 1979] and Cahn–Hilliard equation [Cahn and Hilliard 1958]. They both arise from modeling the phase

separation of mixed systems, as encountered e.g. in the spinodal decomposition of alloys.

For a domain $\Omega \subset \mathbb{R}^N$, $N \in \{2, 3\}$, with boundary $\partial\Omega$ and outer normal $\mathbf{n}$, the Allen–Cahn equation for the phase field variable ϕ is given by

$$\partial_t \phi = \frac{M}{\varepsilon}\left(\varepsilon \nabla^2 \phi - \frac{1}{\varepsilon} W'(\phi)\right) \qquad \text{in } \Omega, \tag{1.1}$$

$$\partial_{\mathbf{n}} \phi = 0 \qquad \text{on } \partial\Omega. \tag{1.2}$$

Here the mobility M determines the time scale of the evolution. In the simplest case it is chosen to be constant, while more involved models also allow for the mobility to depend on ϕ. The phase field parameter ε determines the width of the diffuse interface zone. In Section 1.3 we show that for $\varepsilon \to 0$ a sharp interface model is recovered. The function W is a double well function, e.g. $W(\phi) = 8\phi^2(1-\phi)^2$ as shown in Figure 1.2.

Distant from the diffuse interface zone the phase field variable ϕ attains values corresponding to the minima of W. For the scope of this work we always choose the minima at 0 and 1, although other choices are also common in literature, in particular the choice -1 and 1. The Allen–Cahn equation is a L^2-gradient flow to the

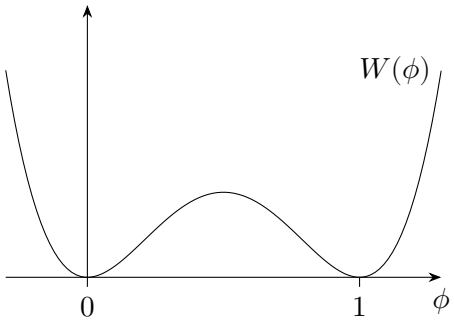

Figure 1.2: Plot of the double well potential $W(\phi) = 8\phi^2(1-\phi)^2$.

Ginzburg–Landau free energy

$$F(\phi, \nabla\phi) = \int_\Omega \left(\frac{W(\phi)}{\varepsilon} + \frac{1}{2}\varepsilon \left|\nabla\phi\right|^2 \right), \tag{1.3}$$

and therefore the free energy F is decreasing in time. The free energy functional F is composed of a bulk free energy, with a minimum for each of the pure phases, and an interfacial energy penalizing large gradients in the phase field variable ϕ.

In the same setting the Cahn–Hilliard equation is given by

$$\partial_t \phi = \nabla \cdot (M \nabla \mu) \qquad \text{in } \Omega, \tag{1.4}$$

$$\mu = \frac{W'(\phi)}{\varepsilon} - \varepsilon \nabla^2 \phi \qquad \text{in } \Omega, \tag{1.5}$$

$$\partial_{\mathbf{n}} \phi = 0 \qquad \text{on } \partial\Omega, \tag{1.6}$$

$$\partial_{\mathbf{n}} \mu = 0 \qquad \text{on } \partial\Omega. \tag{1.7}$$

Again, the mobility M determines the speed of the evolution, and is chosen to be constant in simple models. Obviously equation (1.5) describing the chemical potential μ can be inserted into equation (1.4) to obtain a fourth order differential equation for ϕ. The Cahn–Hilliard equation is a H^{-1}-gradient flow to the Ginzburg–Landau free energy (1.3). This again implies that the free energy F is decreasing in time.

While similar in structure, there are some important differences between the Allen–Cahn equation and the Cahn–Hilliard equation. For the Allen–Cahn equation it is easy to prove, using the maximum principle for elliptic equations, that for initial values of ϕ between 0 and 1 the phase field variable remains bounded by 0 and 1. When interpreting the phase field variable as a mass-fraction or volume-fraction this ensures that ϕ stays in the physical regime. In contrast, while there exist L^∞-bounds for the Cahn–Hilliard equation [Caffarelli and Muler 1995], the phase field variable ϕ is not bounded in the admissible physical regime $[0, 1]$. The Cahn–Hilliard equation is conservative with regard to ϕ. This can be easily seen by inter-

preting (1.4) as a transport equation with the appropriate boundary condition (1.7). On the other hand, the Allen–Cahn equation is generally not conservative, although conservative reformulations for two-phase flow [Jeong and Kim 2017] and multi-component systems [Mu et al. 2018] exist. However, these formulations are only globally and not locally conservative. While the Allen–Cahn equation is a second-order partial differential equation, the Cahn–Hilliard equation contains fourth-order spatial derivatives. Consequently, numerical algorithms might require smaller time steps for the Cahn–Hilliard equation. Both the Allen–Cahn equation and the Cahn–Hilliard equation form interfaces that evolve due to curvature effects. While the Allen–Cahn equation approximates mean curvature flow (see Section 1.3.1 below), the Cahn–Hilliard equation approximates the Mullins–Sekerka free boundary problem.

Next, we combine the phase field equations with other physical phenomena. Phase field models have been coupled in various applications to describe e.g. dendritic growth [Takaki 2014], tumor growth (see [Oden et al. 2010] and references therein) and fracture propagation [Egger et al. 2019]. In the following we focus on coupling the phase field equations with the incompressible Navier–Stokes equations to model multi-phase flow.

The basic model for incompressible two-phase flow, called "Model H", was presented in [Hohenberg and Halperin 1977]. It couples the Cahn–Hilliard equation with the incompressible Navier–Stokes equations and reads

$$\nabla \cdot \mathbf{v} = 0 \qquad \text{in } \Omega, \tag{1.8}$$

$$\begin{aligned} \partial_t(\rho\mathbf{v}) + \nabla \cdot (\rho\mathbf{v} \otimes \mathbf{v}) &= -\nabla p + \nabla \cdot (2\gamma \nabla \mathbf{v}) \\ &\quad + \varepsilon\sigma \nabla \cdot (\nabla\phi \otimes \nabla\phi) \qquad \text{in } \Omega, \end{aligned} \tag{1.9}$$

$$\partial_t \phi + \nabla \cdot (\phi v - \varepsilon \nabla \mu) = 0 \qquad \text{in } \Omega, \tag{1.10}$$

$$\mu = \frac{W'(\phi)}{\varepsilon} - \varepsilon \nabla^2 \phi \qquad \text{in } \Omega, \tag{1.11}$$

$$\nabla\phi \cdot \mathbf{n} = 0 \qquad \text{on } \partial\Omega, \tag{1.12}$$

$$\nabla\mu \cdot \mathbf{n} = 0 \qquad \text{on } \partial\Omega, \tag{1.13}$$

$$\mathbf{v} = 0 \qquad \text{on } \partial\Omega. \tag{1.14}$$

Here $\mathbf{v}$ is the fluid velocity, ρ is the constant fluid density, p is the pressure, γ is the constant fluid viscosity, and σ is the constant surface tension. Also, $\mathbf{n}$ is the outer normal unit vector of Ω. The density and viscosity of both fluid phases is the same. There are two terms coupling the Navier–Stokes equations (1.8), (1.9) with the Cahn–Hilliard equations (1.10), (1.11). Firstly, the phase field variable ϕ gets transported with the fluid velocity $\mathbf{v}$ in (1.10). Secondly, the term $\varepsilon\sigma\nabla\cdot(\nabla\phi\otimes\nabla\phi)$ in equation (1.9) models surface tension between the two fluid phases.

As the model is based on the Cahn–Hilliard equation, the interfaces still evolve due to curvature effects approximating the Mullins–Sekerka problem. Therefore, the mobility of the Cahn–Hilliard equation is chosen to be equal to ε, so that additional curvature effects arising from the Cahn–Hilliard evolution are small and vanish for $\varepsilon \to 0$.

Multiple models have been proposed to generalize Model H to fluids with different densities. Because the mass averaged generalizations proposed by [Lowengrub and Truskinovsky 1998] lead to a non divergence-free vector field, we base our work in Chapter 3 on the volume-averaged model in [Abels, Garcke, et al. 2012]. Here the phase field variable ϕ is interpreted as the volume fraction of the first fluid phase. With constant fluid densities ρ_1 and ρ_2 the density of the fluid mixture is given as

$$\rho_f = \phi\rho_1 + (1-\phi)\rho_2.$$

The model reads

$$\nabla\cdot\mathbf{v} = 0, \tag{1.15}$$

$$\begin{aligned}\partial_t(\rho_f\mathbf{v}) + \nabla\cdot((\rho_f\mathbf{v} + \rho_1\mathbf{J} - \rho_2\mathbf{J})\otimes\mathbf{v}) &= -\nabla p + \nabla\cdot(2\gamma(\phi)\nabla^s\mathbf{v}) \\ &\quad + \varepsilon\sigma\nabla\cdot(\nabla\phi\otimes\nabla\phi),\end{aligned} \tag{1.16}$$

$$\partial_t\phi + \nabla\cdot(\phi v + \mathbf{J}) = 0, \tag{1.17}$$

$$\mathbf{J} = -\varepsilon \nabla \mu, \tag{1.18}$$

$$\mu = \frac{W'(\phi)}{\varepsilon} - \varepsilon \Delta \phi, \tag{1.19}$$

in Ω with boundary conditions (1.12)–(1.14). Compared to Model H (1.8)–(1.11) this model introduces an additional flux term in the momentum equation (1.16). This is due to the fact, that the Cahn–Hilliard evolution can be seen as an additional flux $\mathbf{J}$ for the fluid phases and has to be included in the momentum transport to ensure thermodynamical consistency.

For a generalization to three fluid phases, [Boyer, Lapuerta, et al. 2010; Boyer and Lapuerta 2006] introduced consistency principles that lead to particular choices of the bulk free energy. Based thereon models for more than three fluid phases have been proposed in e.g. [Boyer and Minjeaud 2014; Dunbar et al. 2019]. When considering more than two phases, three interfaces can meet at a triple junction. Analysis of this triple junction [Bronsard and Reitich 1993; Dunbar et al. 2019; Garcke, Nestler, et al. 1998] shows that the free energy functional implies a contact angle condition between the three interfaces.

For phase field models describing fluid–solid interfaces, one can introduce a solid phase as a fluid with very high viscosity, as in [Anderson et al. 2000]. This is also the idea in [Zhang and Klapper 2010; Zhang and Klapper 2011], where microbially induced calcium carbonate precipitation is considered. In contrast, we follow the work of [Beckermann et al. 1999] (see also [Jeong, Goldenfeld, et al. 2001; Sun and Beckermann 2004]), who assign a zero-velocity to the solid phase and solve the flow equations only in the volume fraction occupied by fluid.

The publication [van Noorden and Eck 2011] incorporates a kinetic reaction at the phase boundary. In [Xu and Meakin 2008] a phase field model for precipitation and dissolution is proposed, in [Redeker et al. 2016] precipitation is considered for one solid and two fluid phases. Both works only consider diffusion in the fluid phase, and ignore the fluid flow.

1.3 Matched Asymptotic Expansions and the Sharp Interface Limit

The width of the diffuse transition zone is controlled by the phase field parameter ε. An essential property of a phase field formulation is that it can be seen as an approximation to a sharp-interface model (i.e., bulk equations and boundary conditions at the evolving interface). This can be justified by investigating the limit $\varepsilon \to 0$, called the sharp interface limit. The complexity of phase field models allows for a rigorous treatment of the sharp interface limit only in simple cases, such as the Allen–Cahn equation [Mottoni and Schatzman 1995], the Cahn–Hilliard equation [Alikakos et al. 1994], simple solidification [Caginalp and Chen 1998], or more recently a Stokes–Allen–Cahn system [Abels and Liu 2018]. For rigorous sharp interface limits including boundary conditions, see [Moser 2021]. For more complex models the sharp interface limit can be analyzed by using the formal technique of matched asymptotic expansions. For phase field models this has been pioneered by [Caginalp and Fife 1988], see also [Elder et al. 2001; Li et al. 2009] for some general results. In the following we present the method of matched asymptotic expansions exemplary for the Allen–Cahn equation.

We are interested in a regime of solutions where bulk phases, characterized through small gradients in the phase field parameter ϕ, are separated by interfaces that are smooth manifolds of codimension one. We distinguish between the behavior of the solution close to the interface and far away from it. For this we assume now, that away from the interface we can write solutions to the Allen–Cahn model (1.1) in terms of *outer expansions* of the unknown ϕ, i.e., we can write it in the form

$$\phi^{\text{out}}(t,\mathbf{x}) = \phi_0^{\text{out}}(t,\mathbf{x}) + \varepsilon\phi_1^{\text{out}}(t,\mathbf{x}) + \varepsilon^2\phi_2^{\text{out}}(t,\mathbf{x}) + \dots \,, \tag{1.20}$$

where ϕ_k^{out}, $k \in \mathbb{N}_0$ does not depend on ε. We will insert expansion (1.20) into (1.1) and group terms by powers of ε, using Taylor expansions of the nonlinearities. If the respective derivatives exist,

we have for a generic function $h \in C^2(\mathbb{R})$ and a generic expansion $u = u_0 + \varepsilon u_1 + ...$ the calculation

$$h(u) = h(u_0 + \varepsilon u_1 + ...) = h(u_0) + \varepsilon h'(u_0)u_1 + O(\varepsilon^2).$$

For the inner expansion, valid close to the diffuse interface, we introduce *local coordinates*. To do so, we let

$$\Gamma(t) = \{\mathbf{x} \in \Omega : \phi(t, \mathbf{x}) = 1/2\}. \tag{1.21}$$

By our assumption, Γ is a smooth $(N-1)$-dimensional manifold embedded in $\Omega \subset \mathbb{R}^N$ and depending on time t. Observe that Γ depends on t, and in particular also on ε. Let $\mathbf{s}$ be a local parameterization along $\Gamma(t)$ ($\mathbf{s}$ being a scalar in the two-dimensional case and a vector in $\mathbb{R}^2$ in the three-dimensional case), so that $\mathbf{x}(t, \mathbf{s}) \in \Gamma$. Let $\mathbf{n} \in \mathbb{R}^N$ be the normal unit vector at $\Gamma(t)$ pointing into the phase with $\phi = 0$. We denote by

$$\nu(t, \mathbf{s}) = \partial_t \mathbf{x}(t, \mathbf{s}) \cdot \mathbf{n}(t, \mathbf{s})$$

the normal velocity of the interface. With this, one can define local curvilinear coordinates $(\zeta, \mathbf{s})$ near the interface Γ through

$$\mathbf{x}(t, \mathbf{s}, \zeta) = \mathbf{x}(t, \mathbf{s}) + \zeta \mathbf{n}(t, \mathbf{s}),$$

see Figure 1.3 for an illustration. With this construction ζ is the signed distance from the point $\mathbf{x}(t, \mathbf{s}, \zeta)$ to the interface.

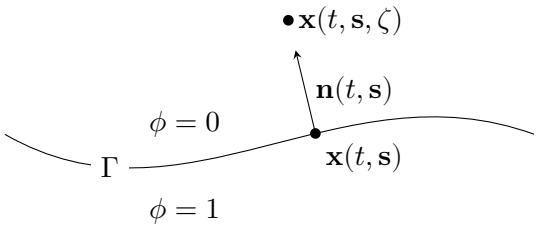

Figure 1.3: Local curvilinear coordinates for the interface $\Gamma(t)$.

It can be shown (see [Caginalp and Fife 1988], the appendix of [Abels, Garcke, et al. 2012], and Lemma 14.17 in [Gilbarg and Trudinger 2001]) that

$$|\nabla\zeta| = 1, \quad \nabla\zeta \cdot \nabla s_i = 0, \quad \partial_t \zeta = -\nu_n,$$
$$\nabla^2\zeta = \sum_{i=1}^{N-1} \frac{-\kappa_i}{1-\kappa_i\zeta} = \frac{-\kappa + 2\Pi\zeta}{1-\kappa\zeta+\Pi\zeta^2},$$

where κ_i are the principal curvatures of the interface. Further, we introduce $\kappa = \sum_{i=1}^{N-1} \kappa_i$, i.e., κ is equal to $N-1$ times the mean curvature. Also, $\Pi = \kappa_1\kappa_2$ is the Gaussian curvature of the interface for $N = 3$ and $\Pi = 0$ for $N = 2$. As Γ depends on t and ε, so do the local coordinates around the interface. We make this explicit for $\mathbf{x}(t,\mathbf{s})$ with the expansion $\mathbf{x}(t,\mathbf{s}) = \mathbf{x}_0(t,\mathbf{s}) + \varepsilon\mathbf{x}_1(t,\mathbf{s}) + \ldots$, where $\mathbf{x}_0$ is a point on the interface $\Gamma_0^{\text{out}}(t)$ defined through $\phi_0^{\text{out}} = 1/2$. Similarly we expand $\mathbf{n}(t,\mathbf{s}) = \mathbf{n}_0(t,\mathbf{s}) + \varepsilon\mathbf{n}_1(t,\mathbf{s}) + O(\varepsilon^2)$, where $\mathbf{n}_0(t,\mathbf{s})$ is the normal vector of $\Gamma_0^{\text{out}}(t)$ at $\mathbf{x}_0(t,\mathbf{s})$. We also define $\nu_0 = \partial_t\mathbf{x}_0(t,\mathbf{s}) \cdot \mathbf{n}_0(t,\mathbf{s})$.

We expect the diffuse interface width being proportional to ε. Therefore, let $z = \zeta/\varepsilon$ be a rescaled signed distance to the interface. For generic scalar and vectorial variables u and $\mathbf{U}$ we obtain the transformation rules (see [Caginalp and Fife 1988] and the Appendix of [Abels, Garcke, et al. 2012])

$$\partial_t u = -\frac{1}{\varepsilon}\nu_0\partial_z u + O(1), \tag{1.22}$$
$$\nabla u = \frac{1}{\varepsilon}\partial_z u\mathbf{n}_0 + \nabla_{\Gamma_0^{\text{out}}} u + O(\varepsilon), \tag{1.23}$$
$$\nabla \cdot \mathbf{U} = \frac{1}{\varepsilon}\partial_z \mathbf{U} \cdot \mathbf{n}_0 + \nabla_{\Gamma_0^{\text{out}}} \cdot \mathbf{U} + O(\varepsilon), \tag{1.24}$$
$$\nabla \mathbf{U} = \frac{1}{\varepsilon}\partial_z \mathbf{U} \otimes \mathbf{n}_0 + \nabla_{\Gamma_0^{\text{out}}} \mathbf{U} + O(\varepsilon), \tag{1.25}$$
$$\nabla^2 u = \frac{1}{\varepsilon^2}\partial_{zz} u - \frac{1}{\varepsilon}\kappa_0\partial_z u + O(1), \tag{1.26}$$

where κ_0 is the sum of the principal curvatures of Γ_0^{out} and $\nabla_{\Gamma_0^{\text{out}}}$ is

the surface gradient of Γ_0^{out}. As we work only with the leading order terms ν_0, $\mathbf{n}_0$, $\nabla_{\Gamma_0^{\text{out}}}$, κ_0 in the following, we drop the indices in the notation.

We assume that close to the interface we can write solutions to the Allen–Cahn model (1.1) in terms of *inner expansions* of the unknown ϕ, reading

$$\phi^{\text{in}}(t,\mathbf{s},z) = \phi_0^{\text{in}}(t,\mathbf{s},z) + \varepsilon\phi_1^{\text{in}}(t,\mathbf{s},z) + \dots \,. \tag{1.27}$$

Note that expansion (1.27) already uses the local, rescaled coordinates $\mathbf{s}$ and z.

For the outer expansion and a fixed t and $\mathbf{s}$ we denote the limit $\mathbf{x}(t,\mathbf{s},\zeta) \to \mathbf{x}(t,\mathbf{s},0)$ from positive ζ by $\mathbf{x}_+$ and from negative ζ by $\mathbf{x}_-$. We match the corresponding limit values of the outer expansion with the ones for the inner expansion, obtained when $z \to \pm\infty$. More precisely, we formally write for a generic variable u with outer expansion u^{out} and inner expansion u^{in},

$$u^{\text{out}}(t,\mathbf{x}(t,\mathbf{s},\varepsilon z)) = u^{\text{in}}(t,\mathbf{s},z).$$

Lengthy calculations [Caginalp and Fife 1988] lead to the following *matching conditions* in the limit $z \to \pm\infty$.

$$u_0^{\text{in}}(t,\mathbf{s},\pm\infty) = u_0^{\text{out}}(t,\mathbf{x}_\pm), \tag{1.28}$$

$$\partial_z u_0^{\text{in}}(t,\mathbf{s},\pm\infty) = 0, \tag{1.29}$$

$$\partial_z u_1^{\text{in}}(t,\mathbf{s},\pm\infty) = \nabla u_0^{\text{out}}(t,\mathbf{x}_\pm)\cdot\mathbf{n}. \tag{1.30}$$

In particular, combining (1.28) and (1.30) we have for a generic vector valued variable $\mathbf{U}$ with outer expansion $\mathbf{U}^{\text{out}}$ and inner expansion $\mathbf{U}^{\text{in}}$

$$\partial_z \mathbf{U}_1^{\text{in}}(t,\mathbf{s},\pm\infty)\otimes\mathbf{n} + \nabla_\Gamma \mathbf{U}_0^{\text{in}}(t,\mathbf{s},\pm\infty) = \nabla\mathbf{U}_0^{\text{out}}(t,\mathbf{x}_\pm). \tag{1.31}$$

1.3.1 Sharp Interface Limit for the Allen–Cahn Equation

We now use the method of matched asymptotic expansions to formally calculate the sharp interface limit for the Allen–Cahn equation (1.1). We first substitute the outer expansion (1.20) for ϕ into the Allen–Cahn equation (1.1). For the $O(\varepsilon^{-2})$ term, which is the leading order, one obtains

$$W'(\phi_0^{\text{out}}) = 0.$$

With the choice $W(\phi) = 8\phi^2(1-\phi)^2$, this equation has three solutions: $\phi_0^{\text{out}} = 0$, $1/2$, or 1. Using the formal argument in [van Noorden and Eck 2011], the first and the last solution are stable since $W''(0) > 0$ and $W''(1) > 0$, whereas $\phi_0^{\text{out}} = 1/2$ is unstable since $W''(1/2) < 0$. In view of this, we see that in the limit $\varepsilon \to 0$ one obtains the solutions $\phi_0^{\text{out}} = 0$ and $\phi_0^{\text{out}} = 1$, and let $\Omega_1(t)$ and $\Omega_2(t)$ be the (time dependent) sub-domains of Ω where ϕ_0^{out} is 1 and 0, respectively.

Next we consider an interface with $\Omega_1(t)$ on the side of negative z and $\Omega_2(t)$ on the side of positive z. We substitute the inner expansion (1.27) into the Allen–Cahn equation (1.1). The leading order terms are of order $O(\varepsilon^{-2})$ and satisfy

$$0 = \partial_z^2 \phi_0^{\text{in}} - W'(\phi_0^{\text{in}}). \tag{1.32}$$

Using (1.28) we obtain the boundary conditions

$$\lim_{z\to-\infty} \phi_0^{\text{in}}(t,z,\mathbf{s}) = 1 \qquad \text{and} \qquad \lim_{z\to\infty} \phi_0^{\text{in}}(t,z,\mathbf{s}) = 0.$$

Furthermore, $\phi_0^{\text{in}}(t,0,\mathbf{s}) = 0.5$ as the location of the interface is defined by $\phi = 1/2$ according to (1.21).

Multiplying (1.32) by $\partial_z \phi_0^{\text{in}}$, integrating the result in z and using the matching conditions(1.28)–(1.30) one gets

$$\frac{1}{2}(\partial_z \phi_0^{\text{in}})^2 = W(\phi_0^{\text{in}}). \tag{1.33}$$

This can be interpreted as an equipartition of the two energy terms in the Ginzburg–Landau free energy (1.3). With boundary conditions for ϕ_0^{in} at $z \to \pm\infty$, the centering condition $\phi_0^{\text{in}}(t, 0, \mathbf{s}) = 1/2$, and explicitly using $W(\phi) = 8\phi^2(1-\phi)^2$, the unique solution of (1.33) is given by

$$\phi_0^{\text{in}}(t, z, \mathbf{s}) = \phi_0^{\text{in}}(z) = \frac{1}{1+e^{4z}} = \frac{1}{2}\left(1 - \tanh\left(2z\right)\right). \tag{1.34}$$

With (1.34) the shape of ϕ across the diffuse transition zone is determined.

Next, we determine the interface velocity. When inserting the inner expansion (1.27) into the Allen–Cahn equation (1.1), the first order terms are of size $O(\varepsilon^{-1})$, and one obtains

$$(W''(\phi_0^{\text{in}}) - \partial_z^2)\phi_1^{\text{in}} = \left(\frac{\nu}{M} - \kappa\right)\partial_z \phi_0^{\text{in}}.$$

We multiply by $\partial_z \phi_0^{\text{in}}$ and calculate

$$\begin{aligned}&\int_{-\infty}^{\infty} (W''(\phi_0^{\text{in}}) - \partial_z^2)\phi_1^{\text{in}} \partial_z \phi_0^{\text{in}} dz \\ &= \int_{-\infty}^{\infty} \partial_z (W'(\phi_0^{\text{in}}) - \partial_z^2 \phi_0^{\text{in}})\phi_1^{\text{in}} dz = 0,\end{aligned}$$

where we have used partial integration with matching conditions (1.28)–(1.30), as well as (1.32). We therefore have

$$0 = \int_{-\infty}^{\infty} (W''(\phi_0^{\text{in}}) - \partial_z^2)\phi_1^{\text{in}} \partial_z \phi_0^{\text{in}} dz = \left(\frac{\nu}{M} - \kappa\right)\int_{-\infty}^{\infty} (\partial_z \phi_0^{\text{in}})^2 dz.$$

With (1.34) we have $0 \neq \int_{-\infty}^{\infty} (\partial_z \phi_0^{\text{in}})^2 dz$, and we therefore find the condition for the moving interface

$$\nu = M\kappa. \tag{1.35}$$

We find that the sharp interface limit of the Allen–Cahn equation is given by two domains Ω_1 and Ω_2 with an interface Γ between them

moving by the mean curvature flow (1.35).

When using the same techniques to derive the sharp interface limit of the Cahn–Hilliard equation (1.4)–(1.5), one finds the Mullins–Sekerka free boundary problem, i.e., in the two domains Ω_1 and Ω_2 one has to solve

$$\Delta \mu_0^{\text{out}} = 0, \tag{1.36}$$

with the interface conditions on Γ given by

$$\mu_0^{\text{out}} = C\kappa, \qquad \nu = M[\![\nabla \mu_0^{\text{out}} \cdot \mathbf{n}]\!],$$

with a constant C depending on the exact form of the double well function $W(\phi)$ (e.g. $C = 1/3$ for $W(\phi) = 8\phi(1-\phi)^2$), and $[\![\cdot]\!]$ denoting the jump of a quantity over the interface Γ.

1.4 Upscaling in Porous Media

In a porous medium, two different length scales are encountered. The first is the pore-scale, where the location of each phase is resolved. At a larger scale, the so-called Darcy-scale, averaged quantities are used to describe the behavior of the system. On the pore-scale, the detailed interaction of the phases can be modeled. But the geometric complexity of the pore-scale limits the size of pore-scale simulations, and therefore Darcy-scale models are used in most situations of practical relevance. In this context, upscaling techniques are used to derive Darcy-scale models from pore-scale models.

One set of such techniques are volume averaging techniques, see for example [Bahar et al. 2016; Quintard and Whitaker 1988; Quintard and Whitaker 1994; Quintard and Whitaker 1999; Tartakovsky et al. 2007; Whitaker 1999; Whitaker 1986], and thermodynamically constrained averaging theory (TCAT), as done in [Gray and Miller 2005; Jackson et al. 2012; Rybak et al. 2015]. We focus in this work on asymptotic expansions and homogenization techniques (see e.g. [Hornung 1996] for an introduction). Rigorous results can be

obtained via two-scale convergence [Allaire 1992] or H-convergence [Tartar 1990]. We refer to [Davit et al. 2013] for a comparison between volume averaging and homogenization techniques.

As a first step of homogenization, we identify the scale separation parameter β as the ratio of typical pore-scale length to typical Darcy-scale length. We assume that β is small, and will later consider the limit $\beta \to 0$ to derive averaged models.

The derived Darcy-scale models depend on the relation between the time scales of the different processes (diffusion, advection, and reaction) at the pore-scale, where different relations lead to different upscaled models. These relations can be expressed through dimensionless numbers like Péclet and Damköhler numbers, after the pore-scale model is brought to non-dimensional form. As we investigate the limit $\beta \to 0$ we are interested in the order of magnitude of these non-dimensional numbers with respect to the scale separation parameter β.

In this work we assume the time scales of diffusion, advection and reaction to be in balance, i.e., of order $O(\beta^0)$. The resulting Darcy-scale model reflects non-equilibrium chemical kinetics. One also might consider equilibrium kinetics, either introduced at the pore-scale or through a regime of high Damköhler number. For equilibrium kinetics at scale of pores, the pore-scale models need to be adapted, with impact on the upscaled models (see e.g. [Battiato, Tartakovsky, et al. 2009]). Homogenization techniques can still be employed in other regimes, including high Péclet and Damköhler numbers, but in particular the former needs to remain within a regime that avoids turbulent flows and allows diffusion to dominate at the scale of pores. We mention [Allaire and Hutridurga 2012; Battiato and Tartakovsky 2011; Bringedal, Berre, et al. 2016b; Choquet and Mikelić 2009; Kumar, van Noorden, et al. 2011; Mikelić, Devigne, et al. 2006; Quintard and Whitaker 1994; van Duijn, Mikelić, et al. 2008; Wood et al. 2011; Wood 2007] for the derivation of Darcy-scale models by either homogenization or volume averaging, and under dominating advection or for fast reaction kinetics. A comprehensive discussion

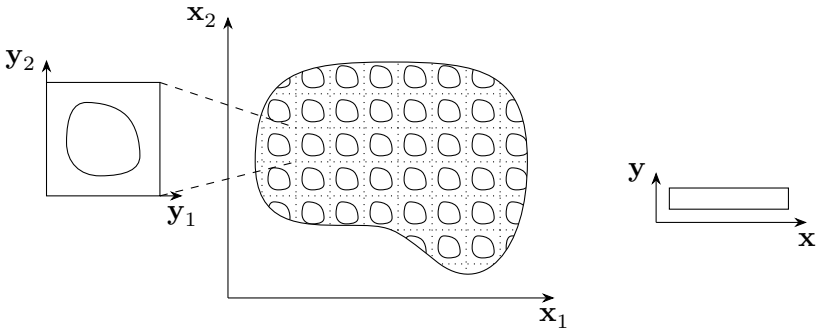

Figure 1.4: Pore-scale coordinates $\mathbf{y}$ *and Darcy-scale coordinates* $\mathbf{x}$ *for homogenization. Left: Periodic porous medium with unit cell. Right: Thin strip geometry.*

can be found in [Battiato, Tartakovsky, et al. 2009], addressing models with mixing-controlled heterogeneous reactions at different scales and under various regimes for the Péclet and Damköhler numbers.

For the homogenization, we additionally have to make assumptions on the geometry of the porous medium. We focus in this work on two cases, see Figure 1.4. In a *periodic porous medium*, the pore-scale contains a unit cell, which is periodically repeating. The typical pore-scale length is given by the size of the unit cell. We focus on this geometry in Chapter 5. In a *thin strip*, the scale separation is given by the length of the thin strip being much bigger than its width. The typical pore-scale length is given by the width of the thin strip. This simplified geometry depicts a long and thin pore. We focus on this geometry in Chapters 6 and 7.

As the next step, we assume asymptotic expansions in terms of β of the unknown variables in the pore-scale model. For a generic unknown variable u we write

$$u(t, \mathbf{x}) = u_0(t, \mathbf{x}, \mathbf{y}) + \beta u_1(t, \mathbf{x}, \mathbf{y}) + \beta^2 u_2(t, \mathbf{x}, \mathbf{y}) + \dots ,$$

where u_k, $k \in \mathbb{N}_0$ do not depend on β. We denote by $\mathbf{x}$ the Darcy-scale coordinate, and by $\mathbf{y}$ the pore-scale coordinate, see Figure 1.4. The asymptotic expansion does explicitly depend on the pore-scale coordinate, and we require $u_k(t, \mathbf{x}, \cdot)$ to be periodic in the case of a periodic porous medium. We insert these asymptotic expansions into the equations of the pore-scale model and group by powers of β. Terms u_k of the expansion not depending on $\mathbf{y}$ are now new Darcy-scale variables. We find equations for the Darcy-scale variables by averaging over $\mathbf{y}$ in the pore-scale equations. Some terms might not upscale, and still depend on the geometry of the pore-scale, and we use *cell problems* to determine the average of these terms. The resulting models are of multi-scale type, with Darcy-scale equations and (decoupled) cell problems at each macroscopic point.

In the following, we give an overview over existing literature concerning upscaling including mineral precipitation and dissolution. Models at the Darcy-scale have been considered from a theoretical point of view in [Knabner et al. 1995], where consistent reaction rates are formulated for the dissolution and precipitation processes, and traveling waves solutions are found. The existence and uniqueness of such solutions are further analyzed in [van Duijn and Knabner 1997]. At the pore-scale, the existence of weak solutions is proved in [van Duijn and Pop 2004], while uniqueness is obtained in [van Noorden, Pop, and Röger 2007]. Also, [van Duijn and Pop 2004] analyzes the occurrence of dissolution fronts in a thin strip, introducing a free boundary separating regions where mineral is present from those which are mineral-free. In [Kumar, Neuss-Radu, et al. 2016], homogenization techniques are employed to prove rigorously that the Darcy-scale model in [Knabner et al. 1995] is the upscaled counterpart of the pore-scale model in [van Duijn and Pop 2004]. We also mention the homogenization of sulfate corrosion of concrete in [Fatima et al. 2011] as a dissolution process with more complex chemistry.

In all cases mentioned above, the mineral layer is assumed to have a negligible thickness when compared even to the microscale (the pores) and therefore the presence of a mineral is accounted in form of

a concentration. A different approach is adopted in [van Noorden and Pop 2007], where the mineral layer is assumed to have a non-negligible thickness and therefore precipitation and dissolution can alter the flow domain at the microscale. The existence and uniqueness of a weak solution for this free-boundary model is proved, however, in the simplified case of a one-dimensional domain. The work [van Noorden 2009a] extends this by considering a general porous medium with periodic grains, and a level set formulation is used to account for the presence of the free boundary at the pore-scale. These models were later extended to include temperature-dependence [Bringedal, Berre, et al. 2016a], where the effective properties were considered further in [Bringedal and Kumar 2017]. A similar model is considered in [Schulz et al. 2017], but restricted to pore-scale diffusion processes in evolving domains. There a Darcy-scale model is derived, for which the existence of strong solutions is proved up to clogging. In [Schulz 2019] the model is extended towards stokes flow and weak solvability is investigated. In [Ray et al. 2019] a two-scale model is proposed, using a level set formulation at the pore-scale.

For the geometry of a thin strip (in two spatial dimensions) or tube (in three dimensions), we mention [van Noorden 2009b] for a model describing precipitation and dissolution for one fluid phase, which has been extended and upscaled in [Agosti et al. 2016; Bringedal, Berre, et al. 2015; Kumar, van Noorden, et al. 2011; Kumar, Wheeler, et al. 2013], and [Lunowa et al. 2021; Mikelić 2009; Mikelić and Paoli 2000; Picchi and Battiato 2018; Sharmin, Bringedal, et al. 2020] for unsaturated single-phase flow or two-phase flow models. We also mention [van Noorden, Pop, Ebigbo, et al. 2010] for the upscaling of biofilm growth in a thin strip.

Pore-scale phase field models are upscaled in [Baňas and Mahato 2017; Bunoiu et al. 2020; Daly and Roose 2015; Metzger and Knabner 2021; Schmuck et al. 2013; Schmuck et al. 2012; Sharmin, Bastidas, et al. 2022]. Kinetic reactions at phase field interfaces have been introduced and upscaled in [Redeker et al. 2016; van Noorden and Eck 2011].

Part I
Phase Field Models for Reactive Fluid–Solid Interfaces

2 The Allen–Cahn–Navier–Stokes Model

In this chapter we derive an Allen–Cahn model for a domain that is altered due to dissolution and precipitation. More precisely, it consists of a fluid domain and a mineral domain. Dissolved ions can form a mineral, hence they can leave the fluid domain and rather become part of the stationary mineral domain. Due to this, the space available for flow (the fluid domain) is reduced whereas the mineral domain is increasing. Oppositely, the mineral domain shrinks as minerals dissolve into ions becoming part of the fluid. In contrast to the upcoming Chapter 3 we are only interested in a single fluid phase. This allows us to upscale this model later in Chapter 5 without the additional difficulties arising from fluid–fluid interfaces.

This chapter is organized as follows. In Section 2.1 we first present a sharp interface formulation, and based on this the phase field formulation is introduced. Next, in Section 2.2 we show that the phase field formulation reduces to the sharp interface formulation when the width of the diffuse interface approaches zero. Two numerical examples showing the behavior of the phase field formulation are included in Section 2.3. In particular, we show how the flow affects the dissolution process.

2.1 The Reactive Transport Problem For Single-Phase Flow

Before introducing the phase field formulation, we formulate first the corresponding sharp interface model including a free boundary. Both models are restricted to the case where only one fluid phase is present, which, in the case of a porous medium, can be seen as a single-phase, fully saturated flow. Moreover, the density and viscosity of the fluid are assumed constant. Furthermore, we only consider a simplified electrochemical system, where the precipitate is formed at the boundaries of the flow domain (the pore walls) and is the product of the reaction between two ions diffusing into and transported by the flowing fluid. If the diffusion coefficients of the two ions are the same, whereas the system is electro-neutral, one can simplify the chemistry by only considering one equation for the solute concentration, as knowing the concentration of one solute and using the electro-neutrality of the system the other concentration is obtained straightforwardly (see [Knabner et al. 1995; van Duijn and Pop 2004; van Noorden and Pop 2007]).

The models below are given in a dimensional framework. The non-dimensionalization is discussed in Chapter 5, in Section 5.1.2.

2.1.1 The Sharp Interface Formulation

We start with the sharp interface formulation, which motivates later the phase field model. In this case, we let $\Omega \subset \mathbb{R}^N$, $N \in \{2, 3\}$ denote the entire domain (the porous medium), which is divided into two disjoint sub-domains: one occupied by the fluid, and another occupied by the mineral. The mineral layer is the result of precipitation and dissolution, and has therefore a variable thickness that is not known a-priori. Hence, the domains occupied by the fluid and by the mineral are both time-dependent. Letting $t \geq 0$ stand for the time variable, and denoting by $\Omega_f(t)$ the (time-dependent) fluid domain,

the conservation laws for the fluid, its momentum and for the solute are:

$$\nabla \cdot \mathbf{v} = 0 \qquad \text{in } \Omega_f(t), \tag{2.1a}$$

$$\rho_1 \partial_t \mathbf{v} + \rho_1 \nabla \cdot (\mathbf{v} \otimes \mathbf{v}) + \nabla p = \gamma_f \nabla^2 \mathbf{v} \qquad \text{in } \Omega_f(t), \tag{2.1b}$$

$$\partial_t c + \nabla \cdot (\mathbf{v} c) = D \nabla^2 c \qquad \text{in } \Omega_f(t). \tag{2.1c}$$

Here $\mathbf{v}$ is velocity and p is pressure in the fluid, and ρ_1 and γ_f are the constant density and viscosity of the fluid. Finally, c is solute concentration and D its diffusivity.

In the mineral domain $\Omega_m(t)$, the mineral is immobile and has a constant concentration c^*, which reduces (2.1a)–(2.1c) to

$$\mathbf{v} = 0 \text{ in } \Omega_m(t).$$

In what follows we assume that the concentration in the mineral is always larger than the one in the fluid, namely $c^* > c(x,t)$ for all $t \geq 0$ and $x \in \Omega_f(t)$.

We let $\Gamma(t)$ stand for the free boundary separating $\Omega_f(t)$ and $\Omega_m(t)$. Observe that for any time t one has

$$\Omega = \Omega_f(t) \cup \Omega_m(t) \cup \Gamma(t), \text{ and } \Omega_f(t) \cap \Omega_m(t) = \emptyset.$$

At $\Gamma(t)$, to guarantee the mass balance we adopt the Rankine–Hugoniot boundary conditions for the fluid and for the solute. We assume that the chemistry does not lead to any volume change, which means that one mineral mole takes exactly the same volume as the one occupied in the fluid by the ion moles forming the mineral (see [Bringedal, Berre, et al. 2016a; van Noorden 2009a]). With this, the conditions at the moving interface are

$$\nu_n - \alpha\kappa = -\frac{1}{c^*} r(c) \qquad \text{on } \Gamma(t), \tag{2.2a}$$

$$\mathbf{v} = 0 \qquad \text{on } \Gamma(t), \tag{2.2b}$$

$$\nu_n (c^* - c) = \mathbf{n} \cdot D \nabla c \qquad \text{on } \Gamma(t), \tag{2.2c}$$

where ν_n is the speed of the moving interface in the normal direction $\mathbf{n}$ pointing into the mineral, α is the mobility of the interface, and κ is $N-1$ times the mean curvature of the moving interface.

Observe that (2.2a) is describing the movement of the free boundary due to precipitation and dissolution. More precisely, the function r is the difference between the precipitation rate and the dissolution rate. Without being restricted to this choice, we use a simple reaction rate inspired by the mass action kinetics, namely

$$r(c) = r_p(c) - r_d = k\left(\frac{c^2}{c_{\text{eq}}^2} - 1\right), \tag{2.3}$$

where c_{eq} is the (known) equilibrium concentration for which $c^* > c_{\text{eq}}$, and k is a reaction constant of dimension $\frac{\text{mol}}{\text{m}^2\,\text{s}}$. This choice of reaction rate corresponds to a precipitation rate increasing with ion concentration and a constant dissolution rate. Note that, to avoid dissolution whenever no mineral is present, in [Knabner et al. 1995; van Duijn and Pop 2004] the dissolution rate is given as a multi-valued rate involving the Heaviside graph.

As follows from (2.2a), next to the precipitation and dissolution, the free boundary is also moving due to surface curvature. The latter effect is more common for two-phase flow, but can also occur for interfaces separating a fluid and solid phase. This assumption is natural when minimizing the surface free energy [Adamson and Gast 1967; Schlögl 1972]. In our case, α is very small.

The last two conditions at $\Gamma(t)$ are ensuring the mass balance for the fluid and for the solute. Since we assume no volume change in connection with the chemistry, the normal component of the fluid velocity is zero at the moving boundary. Combined with the no-slip condition it follows that the fluid velocity $\mathbf{v}$ is zero at the moving boundary. Finally, (2.2c) is the Rankine–Hugoniot condition for the ions. The flux on the right-hand side is due to diffusion as the convective flux is zero, following from (2.2b). Also, the mineral is immobile, so the flux in the mineral sub-domain is 0 whereas the concentration u^* is fixed.

Similar sharp interface models were previously implemented using the level set approach, see [Bringedal, Berre, et al. 2016a; Bringedal and Kumar 2017; Schulz et al. 2017; van Noorden 2009a].

2.1.2 The Phase Field Formulation

An alternative to the sharp-interface formulation given above is to consider a phase-field formulation. In this case one uses a phase field, which is an approximation of the characteristic function. The non-dimensional phase field ϕ is close to and approaches 1 in the fluid phase, and to 0 in the mineral, and has a smooth transition of (dimensional) width $O(\varepsilon) > 0$ separating the phases. In other words, $\varepsilon > 0$ is a phase field parameter related to the thickness of the diffusive transition region. It is to be expected that when passing ε to 0, one obtains in the limit the original sharp-interface model. In consequence, the phase-field approach replaces the interface between the two phases by a smooth transition region where diffusive effects are included. The advantage is that the model equations can now be defined on a stationary domain (here Ω) and not in time-evolving domains. This approach, however, requires the flow and transport equations to also be defined in the mineral phase as well. Here we extend the phase field models in [Redeker et al. 2016; van Noorden and Eck 2011] to include flow:

$$\varepsilon^2 \partial_t \phi + \alpha W'(\phi) = \alpha \varepsilon^2 \nabla^2 \phi - 4\varepsilon\phi(1-\phi)\frac{1}{c^*} r(c), \tag{2.4a}$$

$$\nabla \cdot (\phi \mathbf{v}) = 0, \tag{2.4b}$$

$$\begin{aligned} \rho_1 \partial_t(\phi \mathbf{v}) + \rho_1 \nabla \cdot (\phi \mathbf{v} \otimes \mathbf{v}) = &-\phi \nabla p + \gamma_f \phi \nabla^2(\phi \mathbf{v}) \\ &- d(\phi, \varepsilon)\mathbf{v} + \frac{1}{2}\rho_1 \mathbf{v} \partial_t \phi, \end{aligned} \tag{2.4c}$$

$$\partial_t(\phi(c - c^*)) + \nabla \cdot (\phi \mathbf{v} c) = D \nabla \cdot (\phi \nabla c). \tag{2.4d}$$

The model is explained in detail below.

2.1.2.1 Comments on the Phase Field Equation (2.4a)

The parameter $\varepsilon > 0$ appearing in the phase field equation is assumed small and is related to the width of the diffuse interface. Further, $W(\phi) = 8\phi^2(1-\phi)^2$ is the double-well potential, which ensures that the phase field mainly attains values (close to) 0 and 1 for small values of ε. Formally, this follows from the observation that, if ε is small, the term $W'(\phi)$ dominates in (2.4a), implying that ϕ approaches one of the three equilibrium values $0, 1/2, 1$. Later we show that $1/2$ is an unstable equilibrium, from which the conclusion follows.

The reaction rate $r(c)$ and diffusion parameter α are the same as in the sharp interface formulation. Note that, due to the $4\phi(1-\phi)$ factor, the reaction term is non-zero only in the diffuse transition zone between the two phases and this factor assures that ϕ stays between 0 and 1. Note that in sharp-interface models further dissolution, after all mineral is dissolved, is usually avoided by using a multi-valued dissolution rate based on a Heaviside graph (see [Knabner et al. 1995; van Duijn and Pop 2004]), which complicates the analysis and the development of numerical schemes (see [Agosti et al. 2016; Kumar, Pop, et al. 2013]). This is superfluous for the phase field formulation proposed here as in the absence of mineral only the water phase is present, implying $\phi \equiv 1$ and therefore no dissolution can take place.

2.1.2.2 Comments on the Flow Equations (2.4b) and (2.4c)

The flow equations are now also defined in the mineral phase. To ensure that flow only occurs in the fluid and not in the mineral, some modifications have been made: Firstly, the flow velocity $\mathbf{v}$ and pressure gradient ∇p have become $\phi\mathbf{v}$ and $\phi\nabla p$. This leaves the flow equations unchanged in the fluid phase when $\phi = 1$, whereas these quantities are vanishing in the mineral phase where $\phi = 0$.

Secondly, the term $d(\phi, \varepsilon)\mathbf{v}$ is added. Here, $d(\phi, \varepsilon)$ is decreasing in the first argument, surjective, twice differentiable and fulfills $d(1, \varepsilon) = 0$ and $d(0, \varepsilon) > 0$. This way, $\mathbf{v} = 0$ is the only possible solution when $\phi = 0$ (also see assumption A.4 in [Garcke, Hecht, et al. 2015]). Moreover, this term must also ensure that the velocities in the diffuse transition zone between $\phi = 0$ and $\phi = 1$ are low and therefore works as an interpolation function for velocities in this zone. In [Beckermann et al. 1999], dealing with a similar model for melting and solidification, an artificial friction term is introduced to ensure the desired behavior for $\phi\mathbf{v}$ inside the diffuse interface. Using the current notation, their friction term would correspond to $d(\phi, \varepsilon) = \frac{K(1-\phi)^2\phi}{\varepsilon^2}$ for some constant K [Beckermann et al. 1999]. However, as will be explained in Remark 2.2, a term of $O(\varepsilon^{-2})$ would hamper the phase field model to approach the sharp interface model when $\varepsilon \searrow 0$, and is therefore not adopted here.

A similar idea is adopted in [Garcke, Hecht, et al. 2015], focusing on shape optimization, where the term $d(\phi, \varepsilon) = \frac{K}{\sqrt{\varepsilon}}\frac{(1-\phi)n}{\phi+n}$ is applied. The constant $n > 0$ determines the shape of the function d. More precisely, a larger value of n leads to a function that is close to an affine one, behaving as $(1-\phi)$. In [Garcke, Hecht, et al. 2015], $n = 10$ was found to work better regarding numerical results. Inspired by [Garcke, Hecht, et al. 2015], we let here $d(\phi, \varepsilon) = \frac{K}{\varepsilon}\frac{(1-\phi)n}{\phi+n}$ with $n = 10$. In Section 5.2.1.1 we show that this gives good numerical results for the present model. However, any function d fulfilling the requirements listed previously can be adopted, the specific choice being rather based on the impact on the numerical behavior.

Finally, the term $\frac{1}{2}\rho_1\mathbf{v}\partial_t\phi$ added to (2.4c) accounts for the combined flow with accumulation of the phase field variable, to ensure conservation of kinetic energy when there is precipitation. Note that the two time derivatives can be combined and rewritten to $\rho_1\sqrt{\phi}\partial_t(\sqrt{\phi}\mathbf{v})$, a formulation used in e.g. [Boyer, Lapuerta, et al. 2010].

2.1.2.3 Comments on the Ion Transport Equation (2.4d)

Compared to [Redeker et al. 2016], the only difference appearing in the ion transport equation (2.4d) is in the presence of the convective term. Note that the time derivative can be rewritten as $\partial_t(\phi c + (1-\phi)c^*)$. This is nothing but the derivative of the phase field weighted convex combination of ion concentrations c (in the fluid phase) and the mineral concentration c^* (in the mineral phase). Recalling that in the mineral phase there is no diffusive or convective transport, (2.4d) represents the total mass balance of the species.

2.1.2.4 Decreasing Energy of the Phase Field Formulation

The energy associated with the model (2.4) is given by

$$F = \frac{1}{2}\rho_1\phi\mathbf{v}^2 + \alpha\varepsilon^{-1}W(\phi) + \frac{1}{2}\alpha\varepsilon|\nabla\phi|^2 + \phi g(c),$$

and is the sum of the kinetic energy, the free energy of the phase field, and the energy of the ions. The function $g(c)$ is defined implicitly as a solution to the equation

$$\frac{1}{c^*}r(c) = g(c) - g'(c)c + g'(c)c^*.$$

As $r(c)$ is increasing with c, $g(c)$ is convex for $c < c^*$. Differentiating the above, we get that

$$\partial_t(\phi g(c)) = g'(c)\partial_t(\phi(c-c^*)) + \frac{1}{c^*}r(c)\partial_t\phi.$$

When considering (2.4) on a bounded domain Ω with no-slip boundary conditions for $\mathbf{v}$ and zero Neumann boundary conditions for ϕ

and c at the boundary $\partial\Omega$, one gets

$$\frac{\mathrm{d}}{\mathrm{d}t}\int_\Omega F d\mathbf{x} = \int_\Omega \Big[-\gamma_f \nabla(\phi\mathbf{v}) : \nabla(\phi\mathbf{v}) - d(\phi,\varepsilon)\mathbf{v}^2 - D\phi g''(c)|\nabla c|^2 \\ - \varepsilon^{-1}(\chi - \frac{1}{c^*}r(c))(\chi - 4\phi(1-\phi)\frac{1}{c^*}r(c))\Big] d\mathbf{x},$$

where $\chi = \alpha\varepsilon\nabla^2\phi - \alpha\varepsilon^{-1}W'(\phi)$. The first three terms on the right-hand side describe energy dissipation due to viscosity, friction close to the mineral, and diffusion of ions. The fourth term might be positive and thus lead to an increasing energy. This is the case if curvature effects (see (2.2a)) counteract the ion reaction. However, for fixed ε, we get a bounded energy growth as in [Redeker et al. 2016]. Note that the increasing energy is possible due to the factor $4\phi(1-\phi)$ in the reactive term in (2.4a). Using a multi-valued Heaviside graph for the dissolution rate instead of the $4\phi(1-\phi)$-factor, as commented on in Section (2.1.2.1), would result in a model with decreasing energy, while a regularized Heaviside graph would not. To limit the values of ϕ between 0 and 1 and to ease the following analysis and numerical implementation, we choose to keep the factor $4\phi(1-\phi)$ and not use a Heaviside graph.

2.1.3 The Regularized Phase Field Formulation

The model (2.4) is formulated in the full domain Ω. In doing so, the term $d(\phi,\varepsilon)\mathbf{v}$ is included to ensure that $\mathbf{v} = 0$ in the mineral phase. Observe that the ion concentration c and the fluid pressure p are also defined in the region occupied by the mineral in the sharp interface formulation. For c, a possible extension in the mineral domain is c^*, but this may lead to difficulties related to the regularity of c in the transition from the phase field model to the sharp interface one, when $\varepsilon \to 0$. Moreover, there is no indication about how to extend p in the mineral domain. At the same time, the model in (2.4) does not provide any information about what values c and p should attain in the mineral domain. Although the structure of the phase field equation (2.4a) assures that ϕ never reaches 0 (nor

1), unless initialized so or if appearing on the boundary $\partial\Omega$, ϕ can become arbitrarily close to 0 (and 1). From a numerical point of view, this can lead to a badly conditioned discretization, as the last two equations in (2.4) are close to degenerate whenever $\phi \searrow 0$ and cannot be used to determine c and p in the mineral. To avoid this, we regularize the model by adding a small, non-dimensional $\delta > 0$ to the phase field ϕ in the mass, momentum and solute conservation equations. The regularized model becomes

$$\varepsilon^2 \partial_t \phi + \alpha W'(\phi) = \alpha\varepsilon^2 \nabla^2 \phi - 4\varepsilon\phi(1-\phi)\frac{1}{c^*} r(c), \tag{2.5a}$$

$$\nabla \cdot \big((\phi+\delta)\mathbf{v}\big) = 0, \tag{2.5b}$$

$$\begin{aligned}\rho_1 \partial_t\big((\phi+\delta)\mathbf{v}\big) + \rho_1 \nabla\cdot\big((\phi+\delta)\mathbf{v}\otimes\mathbf{v}\big) &= -(\phi+\delta)\nabla p \\ &+\gamma_f(\phi+\delta)\nabla^2\big((\phi+\delta)\mathbf{v}\big) - d(\phi,\varepsilon)\mathbf{v} + \frac{1}{2}\rho_1 \mathbf{v}\partial_t\phi,\end{aligned} \tag{2.5c}$$

$$\partial_t\big((\phi+\delta)(c-c^*)\big) + \nabla\cdot\big((\phi+\delta)\mathbf{v}c\big) = D\nabla\cdot\big((\phi+\delta)\nabla c\big). \tag{2.5d}$$

Note that this regularization is only needed to facilitate the numerical discretization. For completeness, we use it also in the analysis given below.

Remark 2.1: *The results for decreasing and limited growth of the free energy discussed in Section 2.1.2.4 are also valid for the regularized formulation. To see this, one only needs to replace ϕ by $\phi + \delta$ in the terms associated with the kinetic energy and the energy of the ions.*

2.2 The Sharp Interface Limit

As stated before, the phase field model can be seen as an approximation of the sharp interface model, defined in the entire domain and where the free boundary is replaced by a diffuse interface region. To justify this, we investigate the limit of the phase field model in (2.5) as ε, the width of the diffuse transition zone, approaches zero and show that this limit is exactly the model in Section 2.1.1 For

this we follow the ideas of [Caginalp and Fife 1988], as presented in Section 1.3.

We investigate the behavior of the solution as $\varepsilon \searrow 0$ by expanding the unknowns in terms of ε and equating terms of similar order. This is done in two different ways, close to the diffuse interface (the inner expansions) and away from it (the outer expansions), which are connected by applying matching conditions in the transition region where both expansions are valid.

Throughout this matched asymptotic analysis we take the regularization parameter as $\delta = \varepsilon / L_{\text{ref}}$ with a typical length scale L_{ref} (independent of ε). This choice is made for convenience as δ is not needed in the sharp-interface model. In subsequent sections, δ and ε can be chosen independently.

2.2.1 Outer Expansions

We employ outer expansions in powers of ε as presented in Section 1.3 for the primary variables ϕ, $\mathbf{v}$, p and c.

With the same argument presented in Section 1.3.1 we find that the leading order terms of (2.5a) are given by $W'(\phi_0^{\text{out}}) = 0$ and only allow for the two stable solutions $\phi_0^{\text{out}} = 0$ and $\phi_0^{\text{out}} = 1$.

Using the outer expansions in the flow equations (2.5b) and (2.5c) and the ion conservation (2.5d), it is straightforward to show that the original sharp interface model equations (2.1) are recovered for the points in $\Omega_0^f(t)$. Moreover, for the flow equations one also obtains $\mathbf{v}_0^{\text{out}} = 0$ in $\Omega_0^m(t)$.

2.2.2 Inner Expansions

We now apply the inner expansions and the matching conditions (as presented in Section 1.3) to the phase field model to recover the boundary conditions at the evolving interface.

2.2.2.1 Phase Field Equation

For the leading order terms of the phase field equation (2.5a) we use the same argument as presented in Section 1.3.1 and find that ϕ_0^{in} is given by

$$\phi_0^{\text{in}}(t, \mathbf{s}, z) = \phi_0^{\text{in}}(z) = \frac{1}{1 + e^{4z}} = \frac{1}{2}(1 - \tanh(2z)). \tag{2.6}$$

For the $O(\varepsilon)$ terms one obtains

$$(W''(\phi_0^{\text{in}}) - \partial_z^2)\phi_1^{\text{in}} = (\nu_{n,0} - \alpha\kappa_0)\partial_z\phi_0^{\text{in}} - 4\phi_0^{\text{in}}(1 - \phi_0^{\text{in}})\frac{1}{c^*}r(c_0^{\text{in}}).$$

As in Section 1.3.1 the left-hand side can be viewed as a Fredholm operator of index zero, depending on ϕ_0^{in} and applied to ϕ_1^{in}. Therefore, the equation has a solution if and only if the right-hand side is orthogonal to the kernel of the Fredholm operator, which contains $\partial_z\phi_0^{\text{in}}$. Since $\nu_{n,0}$, κ_0 and c_0^{in} are independent of z (the latter is shown in the following section), the solvability condition implies

$$\begin{aligned}
0 &= \int_{-\infty}^{\infty} \left((\nu_{n,0} - \alpha\kappa_0)\partial_z\phi_0^{\text{in}} - 4\phi_0^{\text{in}}(1 - \phi_0^{\text{in}})\frac{1}{c^*}r(c_0^{\text{in}}) \right) \partial_z\phi_0^{\text{in}} dz \\
&= (\nu_{n,0} - \alpha\kappa_0) \int_{-\infty}^{\infty} (\partial_z\phi_0^{\text{in}})^2 dz \\
&\quad - 4\frac{1}{c^*}r(c_0^{\text{in}}) \int_{-\infty}^{\infty} \phi_0^{\text{in}}(1 - \phi_0^{\text{in}})\partial_z\phi_0^{\text{in}} dz \\
&= (\nu_{n,0} - \alpha\kappa_0 + \frac{1}{c^*}r(c_0^{\text{in}})) \int_{-\infty}^{\infty} (\partial_z\phi_0^{\text{in}})^2 dz,
\end{aligned}$$

where we have used the relation

$$\partial_z\phi_0^{\text{in}} = -4\phi_0^{\text{in}}(1 - \phi_0^{\text{in}}) \tag{2.7}$$

following from (1.33) in Section 1.3.1. As $\int_{-\infty}^{\infty} (\partial_z\phi_0^{\text{in}})^2 dz > 0$ we

have

$$0 = (\nu_{n,0} - \alpha\kappa_0 + \frac{1}{c^*} r(c_0^{\text{in}})).$$

Applying matching conditions for c at the moving interface we obtain the condition

$$\nu_{n,0} = \alpha\kappa_0 - \frac{1}{c^*} r(c_0^{\text{out}}(t, \mathbf{y}_{1/2-})),$$

which is the first boundary condition (2.2a) at the moving interface.

2.2.2.2 Mass Conservation Equation

The dominating $O(\varepsilon^{-1})$ term arising from inserting the inner expansions into (2.5b) is

$$\partial_z(\phi_0^{\text{in}} \mathbf{v}_0^{\text{in}}) \cdot \mathbf{n}_0 = 0. \tag{2.8}$$

By integrating with respect to z and using matching conditions, we obtain

$$\mathbf{v}_0^{\text{out}}(t, \mathbf{y}_{1/2-}) \cdot \mathbf{n}_0 = 0.$$

In other words, the normal component of the velocity is zero at the moving interface. To conclude the same for the tangential component, we consider the momentum conservation equation.

2.2.2.3 Momentum Conservation Equation

The dominating $O(\varepsilon^{-2})$ term in the momentum equation (2.5c) is

$$\gamma_f \phi_0^{\text{in}} \partial_z^2(\phi_0^{\text{in}} \mathbf{v}_0^{\text{in}}) = 0.$$

Note that $\phi_0^{\text{in}} > 0$. Integrating with respect to z and using matching conditions results in

$$\mathbf{v}_0^{\text{out}}(t, \mathbf{y}_{1/2-}) = 0,$$

which is the second boundary condition (2.2b) at the moving interface.

Remark 2.2: *Note that choosing* $d(\phi,\varepsilon) = \frac{K\phi(1-\phi)^2}{\varepsilon^2}$ *as in [Beckermann et al. 1999], would lead to the dominating* $O(\varepsilon^{-2})$ *terms being*

$$\gamma_f \phi_0^{\text{in}} \partial_z^2(\phi_0^{\text{in}} \mathbf{v}_0^{\text{in}}) = K\phi_0^{\text{in}}(1-\phi_0^{\text{in}})^2 \mathbf{v}_0^{\text{in}}.$$

Although γ_f *and* K *are constants, and* ϕ_0^{in} *is known through* (2.6)*, solving this equation for* $\mathbf{v}_0^{\text{in}}$ *is not straightforward, and therefore it is unclear whether* $\mathbf{v}_0^{\text{out}}(t,\mathbf{y}_{1/2-}) = 0$ *is recovered in this case.*

2.2.2.4 Ion Conservation Equation

The dominating $O(\varepsilon^{-2})$ term obtained by inserting the inner expansions into (2.5d) is

$$\partial_z(\phi_0^{\text{in}} \partial_z c_0^{\text{in}}) = 0.$$

Integrating with respect to z and using matching conditions and the fact that $\phi_0^{\text{in}} > 0$, we obtain

$$\partial_z c_0^{\text{in}} = 0,$$

hence $c_0^{\text{in}} = c_0^{\text{in}}(t,\mathbf{s})$ as mentioned in the previous section.

Taking advantage of $\partial_z c_0^{\text{in}} = 0$ and of (2.8), the $O(\varepsilon^{-1})$ terms satisfy

$$-\nu_{n,0}(c_0^{\text{in}} - c^*)\partial_z \phi_0^{\text{in}} = D\partial_z(\phi_0^{\text{in}} \partial_z c_1^{\text{in}}).$$

Integrating with respect to z from $-\infty$ to $+\infty$ and applying matching conditions, lead to

$$\nu_{n,0}(c_0^{\text{out}}(t,\mathbf{y}_{1/2-}) - c^*) = -D\nabla c_0^{\text{out}}(t,\mathbf{y}_{1/2-}) \cdot \mathbf{n}_0,$$

which is the third boundary condition (2.2c) at the moving interface.

2.3 Numerical Investigation of the Phase Field Model

We consider two numerical examples showing the applicability and the potential of the model (2.5), by studying the dissolution of a mineral crystal located in a channel and subject to a flow field. The first example is from the benchmark study [Molins, Soulaine, et al. 2020] and we assess how the phase field model (2.5) behaves for a specific case compared to the results in the benchmark study. Secondly, we make a qualitative assessment of how the mineral dissolution process is affected by the strength of the flow field, inspired by the sharp-interface simulations in [Molins, Trebotich, et al. 2017].

2.3.1 Dissolution of a Calcite Crystal

We consider the benchmark problem II from [Molins, Soulaine, et al. 2020]. Here, calcite dissolves through the chemical reaction

$$\mathrm{CaCO_3}(s) + \mathrm{H^+}(l) \rightarrow \mathrm{Ca^{2+}}(l) + \mathrm{HCO_3^-}(l).$$

Since $\mathrm{H^+}$ is needed for calcite to dissolve, we model this as a one-way reaction where (2.5d) is replaced by

$$\partial_t((\phi+\delta)(c_{H^+}+c^*))+\nabla\cdot((\phi+\delta)\mathbf{v}c_{H^+}) = D\nabla\cdot((\phi+\delta)\nabla c_{H^+}), \quad (2.9)$$

and using the simple, linear reaction rate

$$r(c_{H^+}) = -kc_{H^+} \quad (2.10)$$

in (2.5a). This means there is no precipitation, and the dissolution rate increases with larger access to $\mathrm{H^+}$. Note the change in sign in the time derivative in (2.9) compared to (2.5d). This is since $\mathrm{H^+}$ is consumed for calcite to dissolve, and not produced. Writing the time derivative as $\partial_t(\phi c_{H^+} - (1-\phi)c^*))$ as in Section 2.1.2.3, shows that we are conserving the difference of $\mathrm{H^+}$ and the mineral, reflecting that as one calcite molecule dissolves, one $\mathrm{H^+}$ atom is consumed. We

do not model the concentrations of the solutes Ca^{2+} and HCO_3^- as they do not affect the reaction rate.

We follow the same setup as [Molins, Soulaine, et al. 2020] by considering a two-dimensional channel of length 1 mm and width 0.5 mm, where a circular calcite crystal of initial radius 0.1 mm is centered in (0.5, 0.25) mm. A uniform flow field of given velocity $\mathbf{v}_{\text{in}} = 0.0012$ m/s is applied at $x = 0$ mm. Initially and at the inlet a concentration of $c_{H^+} = 10$ mol/m^3 is applied. Top and bottom of the channel are no-slip boundaries, while fluid can leave through the outlet at $x = 1$ mm. We refer to Table 2.1 for all specified parameters to model (2.5a)–(2.5c) and (2.9). All parameters not related to the phase field are taken from [Molins, Soulaine, et al. 2020].

Table 2.1: Parameters corresponding to benchmark II in [Molins, Soulaine, et al. 2020], and phase-field parameters.

Parameter	Symb.	Value	Units
Fluid density	ρ_1	10^3	kg m^{-3}
Fluid viscosity	γ_f	10^{-3}	kg m^{-1} s^{-1}
Diffusion coefficient	D	10^{-9}	m^2 s^{-1}
Inlet velocity	$\mathbf{v}_{\text{in}}$	0.0012	m s^{-1}
Reaction rate constant in (2.10)	k	8.9×10^{-3}	mol m^{-2} s^{-1}
Inlet and inital concentration	c_{H^+}	10	mol m^{-3}
Calcite molar density	c^*	27100	mol m^{-3}
Phase field interface width	ε	2.5×10^{-5}	m
Phase field mobility	α	2.8×10^{-14}	m^2 s^{-1}
Phase field regularization	δ	10^{-6}	-
Flow dissipation; $d(\phi, \varepsilon) = \frac{10K(1-\phi)}{\varepsilon(\phi+10)}$	K	25	kg m^{-2} s^{-1}

The model equations are discretized using a finite volume method on a uniform, rectangular staggered grid of 200×200 grid cells. The phase field, pressure and solute are defined in the centers of

the control volumes, while the velocity is defined at the center of the edges. Convective fluxes are approximated by an upstream approximation and diffusive fluxes are discretized using a two-point approximation. The model is discretized in time using the backward Euler scheme with a constant time-step size $\Delta t = 1.35$ s until the end time $t = 2700$ s $= 45$ min. The resulting nonlinear systems of equations are solved using Newton iterations in each time step, with the previous time step as initial guess.

Figure 2.1 shows the shape of the calcite crystal initially, and after 15, 30 and 45 minutes. The shapes are shown by plotting the $\phi = 0.5$ isolines of the phase field. The initially circular calcite crystal dissolves unevenly due to the accessibility of H^+ varying with the flow around the crystal. Since the flow takes place from the left to the right, the dissolution is strongest at the left part of the calcite crystal, and reduces while moving to the right part of the crystal. A similar effect when considering calcite precipitation instead of dissolution is investigated and quantified in Chapter 8.

Comparing to the corresponding Figure 8 in [Molins, Soulaine, et al. 2020], we see the same qualitative change in shape. The crystal dissolves slightly faster in our approach compared to [Molins, Soulaine, et al. 2020], which could be due to the non-conservative property of the Allen–Cahn equation.

2.3.2 Effect of Flow Field Strength on Dissolution

We consider a qualitative comparison with respect to how mineral dissolves when located in a flow field of different strengths inspired by the setup in [Molins, Trebotich, et al. 2017, Sec. 3.1]. We are especially interested in the correlation between flow velocity and effective dissolution rate of the mineral, as our investigation in Chapter 8 shows analogous findings for calcite precipitation. As in the previous test, we consider a channel of length 1 mm and width 0.5 mm, with an initially circular mineral located in $(0.5, 0.25)$ mm having radius 0.1 mm. At $x = 0$ a uniform flow field of a given

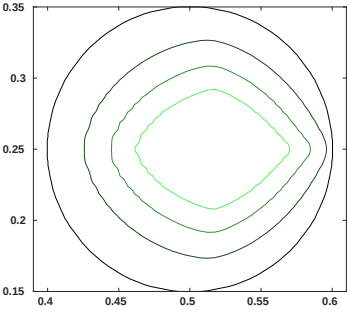

Figure 2.1: The mineral shape while dissolving (zoomed-in view of the channel where the calcite is being present initially). The evolution of the calcite boundary at t = 0, 15 min, 30 min and 45 min (from the outermost curve to the innermost one). The axis scales are in mm.

velocity is applied, the fluid can flow out at $x = 1$, while top and bottom are no-slip boundaries. We now use the original model (2.5) and reaction rate (2.3). To trigger dissolution of the mineral we apply an equilibrium concentration $c_{\text{eq}} = 0.5$ mol/m^3, and use for the solute an initial concentration of c_{eq} and a Dirichlet boundary condition at the inlet of $c_{\text{eq}}/2$. The Péclet and Damköhler numbers are defined as

$$\text{Pe} = \frac{Lq_{\text{in}}}{D}, \quad \text{Da} = \frac{k}{c_{\text{eq}} q_{\text{in}}},$$

where $D = 5 \times 10^{-9}$ is the diffusivity of the solute, $k = 1.9 \times 10^{-5}$ is the reaction constant, and L is the length of the channel. By varying q_{in} between (a) 1.2×10^{-5} m/s, (b) 1.2×10^{-4} m/s, (c) 1.2×10^{-3} m/s and (d) 0.012 m/s we consider the four Péclet and Damköhler numbers given in Table 2.2, which are the same cases as applied in [Molins, Trebotich, et al. 2017]. We use a mineral concentration of $c^* = 1$ mol/m^3. This is an artificially low value of a mineral density, but causes the mineral to change shape faster as it dissolves. For the phase field we use the same parameters as in Table 2.1.

Table 2.2: Non-dimensional numbers in the four simulations.

Simulation	(a)	(b)	(c)	(d)
Péclet number	2.4	24	240	2400
Damköhler number	3.173	0.317	0.032	0.003

The model (2.5) is discretized using the same control volume method as before using a uniform, rectangular staggered grid of 200×200 grid cells. The model is time stepped using backward Euler with a constant time-step size $\Delta t = \Delta y / q_{\text{in}}$ and the nonlinear systems of equations are solved using Newton iterations in each time step, with the previous time step as initial guess.

The four simulations are carried out until the mineral is dissolved completely. Figure 2.2 shows the isolines $\phi = 0.5$ at different time steps to indicate the shapes of the mineral as it dissolves. Although we consider a different chemical system than in [Molins, Trebotich, et al. 2017], we see how the later isolines go from being circular for low velocities to more elongated at larger velocities as in [Molins, Trebotich, et al. 2017, Figure 2]. For low velocities, the reaction rate is quite similar for the entire mineral surface, although with an increase at the front where lower solute concentrations are first met. At larger velocity, dissolution is faster on the sides as dissolved solute is more efficiently transported away triggering further dissolution. The mineral generally dissolves faster when the Péclet number increases, although the same reaction rate has been used. This is caused by the dissolving mineral creating a local increase in the solute concentration, which is transported away more quickly when the flow velocity is large. We see how the interplay between velocity and diffusion gives different shapes of the mineral as it dissolves, and also different effective reaction rates [Dentz et al. 2011]. These observations are analogous to our observations for calcite precipitation in Chapter 8.

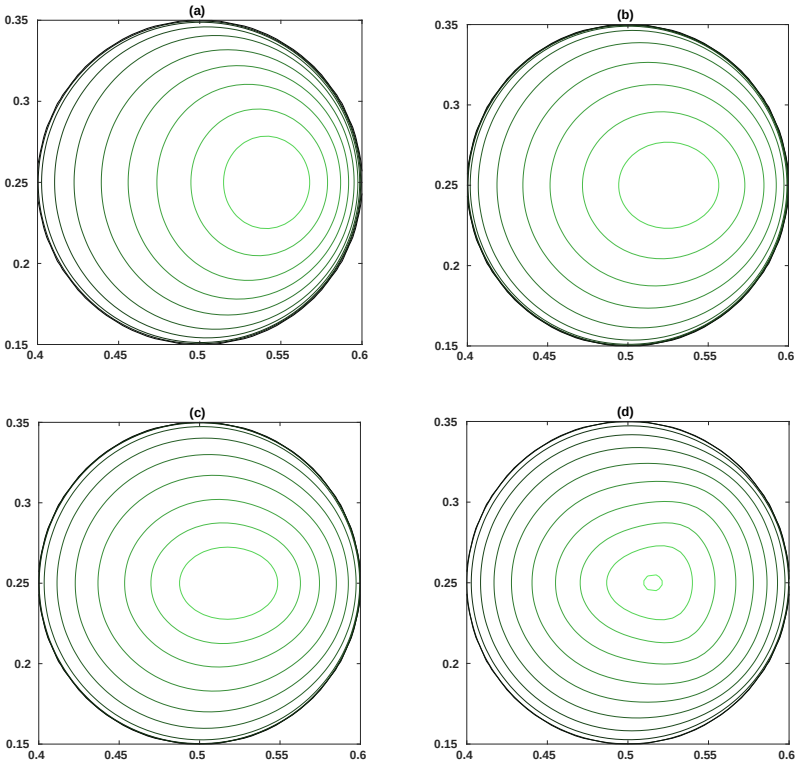

Figure 2.2: The mineral shapes while dissolving (zoomed-in view of the channel where the calcite is being present initially). Black line shows initial shape, while increasingly brighter green shows the shape at later time steps. Cases (a)-(d) correspond to the cases in Table 2.2. The last isolines are at times (a) $t = 3.4$ s, (b) $t = 1.6$ s, (c) $t = 1.1$ s, (d) $t = 0.79$ s. The axis scales are in mm.

3 The Cahn–Hilliard–Navier–Stokes Model

In this chapter we propose and analyze a mathematical model that governs the incompressible flow of two immiscible fluids that interact with each other and a third solid phase composed of a pure mineral material. This mineral is supposed to be solvable in exactly one of the fluid phases. Analogous to Chapter 2 we account for the process of precipitation enlarging the domain occupied by the solid phase, as well as dissolution transferring solid material to the fluid phase. For a pertinent example one might think of a mixture of water, oil and sodium chloride, the latter being present as solid, and resolved in water only.

Notably, our model incorporates a Navier-slip condition at the fluid–solid interfaces instead of a no-slip condition. Without the slip condition, the contact point is non-moving, and classical results [Pukhnachev and Solonnikov 1982] show that the sharp interface model would not be well posed. Existing phase field models with a Navier-slip condition (see [Qian et al. 2003; Qian et al. 2006; Xu, Di, et al. 2018]) describe the solid only as a fixed outer boundary, while our model allows for a dynamic diffuse fluid–solid interface.

The structure of this chapter is as follows. First, we explain the underlying sharp interface ansatz in Section 3.1.1 that fixes the transmission condition between the bulk phases via conservation constraints, reactive mass exchange and the interfaces' curvature influence. The phase field model itself, called $2f1s$-model, is derived

in Section 3.1.2, see equations (3.26)–(3.31). To avoid degeneration a modification with a small parameter δ is necessary, leading to the δ-$2f1s$-model in Section 3.1.3, see equations (3.45)–(3.50). By construction, solutions of the δ-$2f1s$-model obey the physical constraints of total mass, volume fraction and ion concentration conservation. Introducing a new free energy function it is proven that classical solutions of the phase field model obey the second law of thermodynamics (see Theorem 3.1.1 in Section 3.1.5). We relate the δ-$2f1s$-model for simplified scenarios to previously suggested phase field models in Section 3.1.6.

To validate our model we investigate the sharp interface limit in Section 3.2 using matched asymptotic expansions. The analysis identifies all binary transmission conditions (and bulk equations) as proposed for the sharp interface ansatz in Section 3.1.1. Notably, this includes the Navier-slip condition as presented in Section 3.1.1.4. This result is novel, not only for ternary mixtures but also in the fundamental context of binary fluid–solid interfaces.

Based on the finite element method we introduce a numerical scheme for the δ-$2f1s$-model in Section 3.3 and illustrate the capabilities of the δ-$2f1s$-model by numerical examples in Section 3.4.

3.1 The Reactive Transport Problem for Multi-Phase Flow

3.1.1 The Sharp Interface Formulation

In this section we present the free boundary problem which is the basis for the phase field approach that is introduced in Section 3.1.2. While most of the governing equations and coupling conditions resemble standard choices, we introduce a novel ansatz for the momentum in the solid phase and for its coupling to the fluid phases. In Section 3.1.1.4 we show that this approach realizes a Navier-slip boundary condition for the fluid–solid interface.

Analogous to Chapter 2 we introduce a domain $\Omega \subset \mathbb{R}^N$, $N \in \{2, 3\}$, and assume that it is the disjoint union of domains $\Omega_1(t)$, $\Omega_2(t)$ and $\Omega_3(t)$ for all times $t \in [0, T]$. We interpret $\Omega_1(t)$, $\Omega_2(t)$, $\Omega_3(t)$ as bulk domains which are occupied by fluid phase 1 (e.g. water), fluid phase 2 (e.g. oil) and a solid phase, respectively. All bulk domains are time-dependent, as the fluid bulk domains can change by convection and the solid bulk domain by precipitation and dissolution processes. As displayed in Figure 3.1 we denote the interface between Ω_i and Ω_j by Γ_{ij} $(i < j)$. The normal unit vector $\mathbf{n} \in \mathbb{R}^N$ of the interface Γ_{ij} is supposed to point into Ω_j. We call Γ_{12} the fluid–fluid interface, and Γ_{13} and Γ_{23} fluid–solid interfaces. By $\nu \in \mathbb{R}$ we denote the normal velocity of the interface Γ_{ij}.

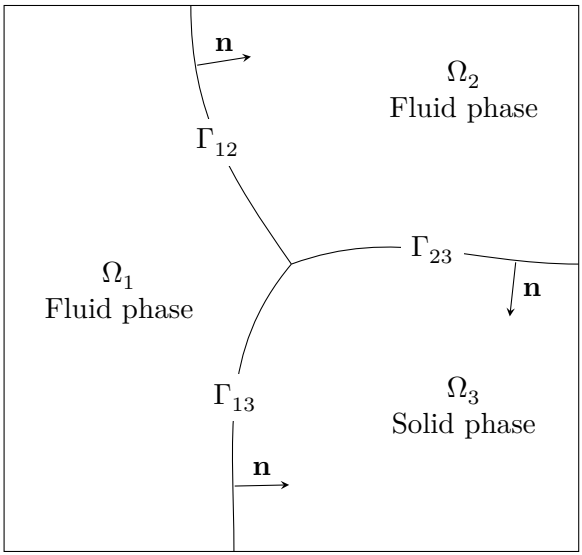

Figure 3.1: Partition of Ω into bulk domains Ω_1, Ω_2, Ω_3 and interfaces Γ_{12}, Γ_{13}, Γ_{23}.

3.1.1.1 The Bulk Equations

We consider the incompressible flow of the viscous fluid phase i in $\Omega_i(t)$, $i \in \{1,2\}$. Then, for a velocity field $\mathbf{v} = \mathbf{v}(t,\mathbf{x}) \in \mathbb{R}^N$ and pressure $p = p(t,\mathbf{x}) \in \mathbb{R}$ the dynamics is governed by the incompressible Navier–Stokes equations,

$$\nabla \cdot \mathbf{v} = 0, \tag{3.1}$$

$$\partial_t(\rho_i \mathbf{v}) + \nabla \cdot (\rho_i \mathbf{v} \otimes \mathbf{v}) + \nabla p = \nabla \cdot (2\gamma_i \nabla^s \mathbf{v}), \tag{3.2}$$

in $\Omega_i(t)$, $i \in \{1,2\}$, $t \in (0,T)$. Here, the fluid density $\rho_i > 0$ and the viscosity $\gamma_i > 0$ are assumed to be constant but are allowed to be different for each fluid phase. We choose $\rho_1 = \rho_3$, see Remark 3.1 for details. The symmetric Jacobian $\nabla^s \mathbf{v}$ is given by $\nabla^s \mathbf{v} = \frac{1}{2}\left(\nabla \mathbf{v} + (\nabla \mathbf{v})^\top\right)$.

Furthermore, we assume the presence of ions that can dissolve in fluid phase 1 but not in fluid phase 2. Thus, we account for the ion-concentration $c = c(t,\mathbf{x}) \geq 0$ in $\Omega_1(t)$ which is supposed to satisfy the standard transport-diffusion equation

$$\partial_t c + \nabla \cdot (\mathbf{v} c) - D\Delta c = 0 \tag{3.3}$$

in Ω_1, $t \in (0,T)$, using a constant diffusion rate $D > 0$. In the solid phase we assume to have a constant ion-concentration $c^* > 0$.

Albeit the solid phase should be immobile we impose an artificial velocity field $\mathbf{v} = \mathbf{v}(t,\mathbf{x})$ for it that is assumed to satisfy the elliptic law

$$\nabla \cdot (2\gamma_3 \nabla^s \mathbf{v}) - \rho_3 d_0 \mathbf{v} = 0 \tag{3.4}$$

in Ω_3, $t \in (0,T)$, with constants $\gamma_3, d_0 > 0$ and density of the solid phase $\rho_3 > 0$. Notably equation (3.4) has no physical meaning, but are essential to establish a slip condition for the tangential fluid velocity at the fluid–solid interfaces $\Gamma_{13}(t)$ and $\Gamma_{23}(t)$.

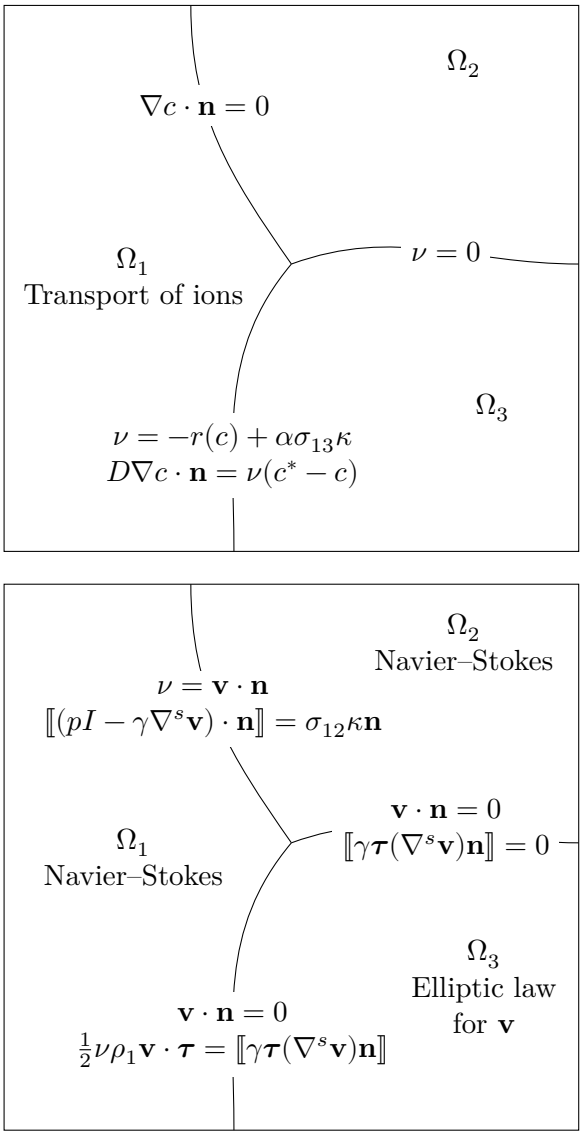

Figure 3.2: The bulk equations and interface conditions of the sharp interface model. Left: Equations for ion transport and surface reaction. Right: Flow equations and interface conditions, omitting the condition $[\![\mathbf{v}]\!] = 0$ that is valid at all interfaces.

3.1.1.2 The Interface Conditions

We proceed describing the interfacial dynamics between the bulk domains. The velocity field $\mathbf{v} : \Omega_1(t) \cup \Omega_2(t) \cup \Omega_3(t) \to \mathbb{R}^N$ is assumed to be continuous across all domains, i.e.,

$$[\![\mathbf{v}]\!] = 0 \quad \text{on } \Gamma_{12}, \Gamma_{13} \text{ and } \Gamma_{23}. \tag{3.5}$$

Here $[\![a]\!]$ is the jump of a quantity $a(\mathbf{x})$ across an interface Γ_{ij}, i.e.,

$$[\![a]\!](\mathbf{x}) = \lim_{\xi \to 0^+} (a(\mathbf{x} + \xi \mathbf{n}) - a(\mathbf{x} - \xi \mathbf{n})) \quad \text{for } \mathbf{x} \in \Gamma_{ij}.$$

The interface conditions between two fluids are determined by the balance laws for mass and momentum. They are given for the Navier–Stokes system by

$$\nu = \mathbf{v} \cdot \mathbf{n} \quad \text{on } \Gamma_{12}, \tag{3.6}$$

$$[\![(pI - 2\gamma \nabla^s \mathbf{v}) \cdot \mathbf{n}]\!] = \sigma_{12} \kappa \mathbf{n} \quad \text{on } \Gamma_{12}, \tag{3.7}$$

involving the normal velocity ν of the interface, the sum κ of principal curvatures (i.e., $N-1$ times the mean curvature) and the (constant) surface tension coefficient $\sigma_{12} > 0$ between the two fluids.

For the fluid–solid interfaces Γ_{13} and Γ_{23} we impose the conditions

$$\mathbf{v} \cdot \mathbf{n} = 0 \quad \text{on } \Gamma_{13} \text{ and } \Gamma_{23}, \tag{3.8}$$

$$\frac{1}{2} \nu \rho_1 \mathbf{v} \cdot \boldsymbol{\tau} = [\![2\gamma \boldsymbol{\tau} (\nabla^s \mathbf{v}) \mathbf{n}]\!] \quad \forall \boldsymbol{\tau} \in \mathbb{R}^N, \boldsymbol{\tau} \perp \mathbf{n} \quad \text{on } \Gamma_{13} \text{ and } \Gamma_{23}. \tag{3.9}$$

Condition (3.8) is the usual no-penetration condition for fluid flow. Condition (3.9) gives, together with (3.4), a slip condition for the tangential flow, see Section 3.1.1.4 for details.

Remark 3.1: *Instead of* (3.8) *one can impose the more general mass conservation* $-\mathbf{v}\rho_1 \cdot \mathbf{n} = \nu[\![\rho]\!]$ *on* Γ_{13}*. This allows for a volume change related to the reaction process. Under the assumption that the solid phase has the same density as fluid phase* 1*, i.e.,* $\rho_3 = \rho_1$*, there is no volume change, and we recover* (3.8)*. For the sake of simplicity we present the technically less involved computations resulting from* (3.8)*.*

It remains to fix the normal velocity of the fluid–solid interfaces Γ_{13} and Γ_{23}, which is given by the rates of precipitation and dissolution. We assume that reactions can only take place between fluid phase 1 and the solid phase, excluding reactions across Γ_{23}. Precisely, we choose

$$\nu = -r(c) + \alpha\sigma_{13}\kappa \quad \text{on } \Gamma_{13}, \tag{3.10}$$

$$\nu = 0 \quad \text{on } \Gamma_{23}. \tag{3.11}$$

Analogous to Chapter 2 the reaction rate function $r = r(c)$ depends only on the ion concentration c in fluid 1 and models both, dissolution and precipitation. We follow [Knabner et al. 1995], and assume $r(c)$ to be monotonically increasing in c.

Remark 3.2: *As already discussed in Chapter 2, a simple choice for a reaction rate* $r(c)$ *would be given by modeling the rate of precipitation using a quadratic mass action law and the rate of dissolution using a constant rate. With reaction rate* k*, equilibrium concentration* c_{eq} *(with* $c_{\text{eq}} < c^*$*), this means*

$$r(c) = r_p(c) - r_d = k\left(\frac{c^2}{c_{\text{eq}}^2} - 1\right).$$

The term $\alpha\sigma_{13}\kappa$ in (3.10) models curvature effects acting on the precipitation and dissolution process. While in previous works [Redeker et al. 2016] and in the Allen–Cahn–Navier–Stokes model of Chapter 2 the sharp interface limit of the phase field models required

a positive α, we also allow for $\alpha = 0$ in our analysis. We need to distinguish between the cases with and without curvature effects, i.e., $\alpha > 0$ and $\alpha = 0$, for the free energy functional in Section 3.1.5 and for the asymptotic analysis in Section 3.2.2.

Finally, we need a transmission condition that ensures the conservation of ions. Recall that we assume a constant ion concentration c^* in the solid bulk domain Ω_3. For Γ_{13} and Γ_{12} we thus impose the Rankine–Hugoniot like conditions

$$D\nabla c \cdot \mathbf{n} = \nu(c^* - c) \quad \text{on } \Gamma_{13}, \tag{3.12}$$

$$\nabla c \cdot \mathbf{n} = 0 \quad \text{on } \Gamma_{12}. \tag{3.13}$$

3.1.1.3 The Contact Angle Condition

The set of points where the three bulk domains $\Omega_1(t)$, $\Omega_2(t)$, $\Omega_3(t)$ meet consists of manifolds Γ_{123} with codimension 2. In the two-dimensional case the domains meet at isolated points, while in the three-dimensional case they meet at curves. Let us consider the two-dimensional case first.

Given the surface tension coefficients σ_{12}, σ_{13}, $\sigma_{23} > 0$ we impose the contact angle condition

$$\frac{\sin(\beta_1)}{\sigma_{23}} = \frac{\sin(\beta_2)}{\sigma_{13}} = \frac{\sin(\beta_3)}{\sigma_{12}}, \tag{3.14}$$

at Γ_{123}, where β_i is the contact angle of Ω_i at the contact point. Note that the β_i are uniquely determined through (3.14) and $\beta_1+\beta_2+\beta_3 = 2\pi$.

In the three-dimensional case, we impose condition (3.14) on the plane perpendicular to Γ_{123}, i.e., the plane with normal vector tangent to the contact curve.

With this, the description of the sharp interface formulation is complete. It consists of the bulk equations (3.1)–(3.4), the interface conditions (3.5)–(3.13) and the contact angle condition (3.14).

Classical results [Pukhnachev and Solonnikov 1982] show that prescribing both, a non-moving contact point and a contact angle, leads to an ill-posed model. It is therefore necessary for the well-posedness of the sharp interface formulation that we have the interface condition (3.9) instead of a no-slip condition. For $\beta_3 = \pi$ the contact point can move over a smooth solid phase Ω_3. We approximate this setting by choosing σ_{12} much smaller than σ_{13}, σ_{23}.

Additional boundary conditions have to be imposed on $\partial\Omega$, for example a Navier-slip condition for $\mathbf{v}$ and a homogeneous Neumann boundary condition for c. For the sake of brevity we do not consider expansions close to the boundary $\partial\Omega$ in the sharp interface limit in Section 3.2.

3.1.1.4 The Navier-Slip Condition

Before we conclude this section on the sharp interface model, we investigate the effect of the bulk equation (3.4) for $\mathbf{v}$ in the solid domain Ω_3 together with the boundary conditions (3.9) at the boundary of Ω_3. Given a slip length $L_{\text{slip}} > 0$, the Navier-slip condition reads

$$\mathbf{v} \cdot \boldsymbol{\tau} = -2L_{\text{slip}} \boldsymbol{\tau} (\nabla^s \mathbf{v}) \mathbf{n} \qquad \text{for all } \boldsymbol{\tau} \in \mathbb{R}^N,\ \boldsymbol{\tau} \perp \mathbf{n}, \tag{3.15}$$

at the interfaces Γ_{13} and Γ_{23}, where all variables are evaluated from the side of the fluid bulk phase. We show that classical solutions to the sharp interface formulation (3.1)–(3.14) approximately satisfy (3.15) with

$$L_{\text{slip}} = \gamma_1 \sqrt{\frac{2}{\rho_3 d_0 \gamma_3}}. \tag{3.16}$$

For the sake of simplicity we consider the simple geometry

$$\Omega_3 = \left\{ \mathbf{x} \in \mathbb{R}^N, \mathbf{x}_1 < 0 \right\}, \qquad \Omega_1 = \mathbb{R}^N \backslash \Omega_3, \qquad \Omega_2 = \emptyset,$$

and let all unknowns only depend on $\mathbf{x}_1$. Then (3.4) reads as

$$2\gamma_3 \partial_{\mathbf{x}_1}^2 \mathbf{v}(\mathbf{x}_1) - \rho_3 d_0 \mathbf{v}(\mathbf{x}_1) = 0.$$

Assuming a bounded velocity profile for $\mathbf{x}_1 \to -\infty$ we find

$$\mathbf{v} = \mathbf{C} e^{\sqrt{\frac{\rho_3 d_0}{2\gamma_3}}\mathbf{x}_1},$$

with some vector constant $\mathbf{C} \in \mathbb{R}^N$. In the solid bulk domain Ω_3 we find up to the boundary $\mathbf{x}_1 \to 0^-$

$$\partial_{\mathbf{n}}(\mathbf{v} \cdot \boldsymbol{\tau}) = -\partial_{\mathbf{x}_1}(\mathbf{v} \cdot \boldsymbol{\tau}) = -\sqrt{\frac{\rho_3 d_0}{2\gamma_3}} \mathbf{v} \cdot \boldsymbol{\tau}. \tag{3.17}$$

Assume that there is no reaction, so that (3.9) reduces on the half-space geometry to

$$[\![\gamma \partial_{\mathbf{n}}(\mathbf{v} \cdot \boldsymbol{\tau})]\!] = 0. \tag{3.18}$$

Recall that by (3.5) $\mathbf{v}$ is continuous across the interface Γ_{13}. Therefore, with (3.17) and (3.18) we find at the boundary of Ω_1, i.e., for $\mathbf{x}_1 \to 0^+$, the Navier-slip condition (3.15), (3.16).

In a more general geometry we also expect this behavior, as long as the exponential decay of $\mathbf{v}$ in the interior of Ω_3 is sufficiently fast. A lengthy calculation shows that for a radial Ω_3 with radius R we require $\rho_3 d_0/\gamma_3 \gg 1/R^2$. As both, $d_0 > 0$ and $\gamma_3 > 0$, are non-physical parameters, the slip length L_{slip} can be chosen while keeping a large quotient d_0/γ_3.

On the left-hand side of (3.9) we have the term $\frac{1}{2}\nu\rho_1 \mathbf{v} \cdot \boldsymbol{\tau}$. This term appears in the sharp interface limit in Section 3.2.3. In general, we expect the normal velocity ν of a fluid–solid interface to be small, so this term has minor influence on the slip length.

Remark 3.3: *To realize a no-slip condition one can choose a large d_0 in* (3.4)*. Recalling* (3.16)*, this leads to the slip length L_{slip}*

approaching zero. At the same time the quotient d_0/γ_3 becomes large and therefore $\mathbf{v}$ decays fast in the solid domain.

This is different to the approach considered in Chapter 2, where the choice $\gamma_3 = 0$ was made. Our analysis in this chapter does not hold in that case. Instead, Equation (3.4) directly results in $\mathbf{v} = 0$ in the solid domain Ω_3 and the continuity of $\mathbf{v}$ in (3.5) implies a no-slip condition for the fluid. When considering the sharp interface limit for $\gamma_3 = 0$ in Section 2.2, we do not get the tangential stress balance (3.9), as it would over-determine the system.

3.1.2 The $2f1s$-Phase Field Model

3.1.2.1 Preliminaries

To establish a phase field model in our case we introduce the fields

$$\phi_1(t, \mathbf{x}), \phi_2(t, \mathbf{x}), \phi_3(t, \mathbf{x}) : [0, T] \times \Omega \to \mathbb{R},$$

that approximate the indicator function of the respective phase in the sharp interface model. We summarize the fields in the vector-valued function $\boldsymbol{\Phi} = (\phi_1, \phi_2, \phi_3)^\top$ and call $\boldsymbol{\Phi} = \mathbf{e}_i$ a pure phase, with $\mathbf{e}_i \in \mathbb{R}^3$ being the i-th unit vector. In contrast to the sharp interface formulation, ϕ_i runs smoothly between 0 and 1 in a small layer around the interface. The width of this diffuse transition zone is controlled by a new parameter $\varepsilon > 0$. In the limit $\varepsilon \to 0$ the layer collapses to the interface, and we expect to regain the sharp interface formulation (3.1)–(3.14). For this we consider the sharp interface limit by asymptotic expansions in ε in Section 3.2.

Understanding the smooth phase field parameter ϕ_i as a volume fraction of the i-th phase we want to ensure that $\boldsymbol{\Phi}$ satisfies for all $t \in [0, T]$ and $\mathbf{x} \in \Omega$ the conservation constraint

$$\sum_{i=1}^{3} \phi_i(t, \mathbf{x}) = 1, \tag{3.19}$$

and additionally the range restriction $\phi_i(t, \mathbf{x}) \in [0, 1]$. However, the phase field dynamics relies on the fourth–order Cahn–Hilliard evolution, which does not satisfy a priori such a maximum principle. We enforce the relaxed constraint $\phi_i(t, \mathbf{x}) \in (-\delta, 1 + \delta)$ for some small $\delta > 0$ by using an unbounded potential function. To do so, we define first a double-well potential $W_{\mathrm{dw}}(\phi)$ by

$$W_{\mathrm{dw}}(\phi) = 450\phi^4(1-\phi)^4 + \delta\ell\left(\frac{\phi}{\delta}\right) + \delta\ell\left(\frac{1-\phi}{\delta}\right), \tag{3.20}$$

$$\ell(x) = \begin{cases} \frac{x^2}{1+x} & x \in (-1, 0), \\ 0 & x \geq 0, \end{cases}$$

see also Figure 3.3.

Remark 3.4: *Note that for $\delta \to 0$ the double-well function $W_{\mathrm{dw}}(\phi_i)$ converges point-wise to a potential of double-obstacle type, i.e.,*

$$W_{\mathrm{dw},0}(\phi) = 450\phi^4(1-\phi)^4 + \ell_o(\phi) + \ell_o(1-\phi),$$

$$\ell_o(x) = \begin{cases} \infty & x < 0, \\ 0 & x \geq 0, \end{cases}$$

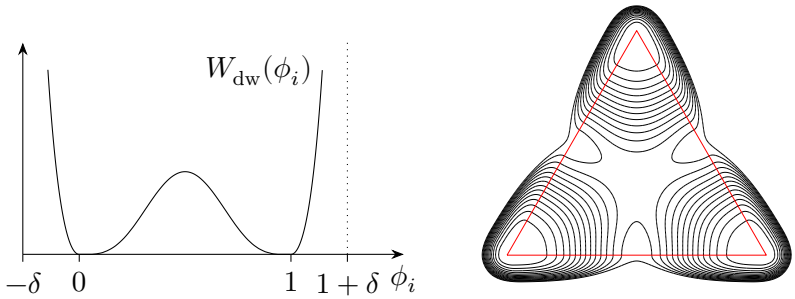

Figure 3.3: Left: Plot of the double well potential W_{dw}. Right: Contour plot of $W_0(\Phi)$ on the plane $\sum_i \phi_i = 1$ in barycentric coordinates.

and we need to interpret $W'_{\mathrm{dw},0}$ as a set-valued subderivative. The Cahn–Hilliard equation with double obstacle-potential has been thoroughly studied, see for example [Blowey and Elliott 1991]. This ansatz results in a model including variational inequalities, which we aim to avoid because of the merely technical complexity in the sharp interface limit and numerical implementation. Instead, we relate the non-dimensional δ and the dimensional ε in the sharp interface limit in Section 3.2 by $\varepsilon = L_{\mathrm{ref}}\delta$, where L_{ref} is a characteristic length scale independent of ε.

While we do not show the existence and uniqueness of solutions to the δ-2f1s-model presented in the upcoming Section 3.1.3, we expect the techniques of [Blowey and Elliott 1991] to also be applicable to W_{dw}.

Remark 3.5 (General properties of the double-well potential)**:** *The choice in* (3.20) *for W_{dw} is a specific one fitting the phase field model exactly to the sharp interface model, see the analysis in Section 3.2. In general W_{dw} should be symmetric, i.e., $W_{\mathrm{dw}}(\phi) = W_{\mathrm{dw}}(1-\phi)$, it should have minima at $\phi = 0$ (and $\phi = 1$) and satisfy $\lim_{\phi\to-\delta^+} W_{\mathrm{dw}}(\phi) = \infty$. Furthermore, we need $\frac{d}{d\phi}\sqrt{W_{\mathrm{dw}}(\phi)}\big|_{\phi=0^+} = 0$ to prevent bulk reactions in the leading order of the sharp interface limit in Section 3.2.1. This results in the use of a polynomial of degree eight.*

To define now the potential function $W(\boldsymbol{\Phi}) : \mathbb{R}^3 \to \mathbb{R}$ we note that its choice based on the double-well function W_{dw} induces different surface energies for each of the interfaces by different scalings (see also Remark 3.6). Based on [Boyer, Lapuerta, et al. 2010; Boyer and Lapuerta 2006] we consider

$$W_0(\boldsymbol{\Phi}) = \sum_{i=1}^{3} \Sigma_i W_{\mathrm{dw}}(\phi_i), \tag{3.21}$$

with scaling coefficients $\Sigma_i > 0$ $(i = 1, 2, 3)$, see also Figure 3.3. Because $W_0(\boldsymbol{\Phi})$ is only a reasonable choice for states $\boldsymbol{\Phi}$ from the

plane $\sum_i \phi_i = 1$ we introduce, as a generalization of [Zhang and Wang 2016], a projection P of $\mathbb{R}^3$ onto this plane by

$$P\boldsymbol{\Phi} = \boldsymbol{\Phi} + \Sigma_T(1-\phi_1-\phi_2-\phi_3)\begin{pmatrix}\Sigma_1^{-1}\\ \Sigma_2^{-1}\\ \Sigma_3^{-1}\end{pmatrix}, \quad \frac{1}{\Sigma_T} = \frac{1}{\Sigma_1}+\frac{1}{\Sigma_2}+\frac{1}{\Sigma_3}. \tag{3.22}$$

With the projection we finally define the potential $W(\boldsymbol{\Phi}) := W_0(P\boldsymbol{\Phi})$. Note that $W(\boldsymbol{\Phi}) : \mathbb{R}^3 \to \mathbb{R}$ is a function with a minimum in each of the pure phases $\boldsymbol{\Phi} = \mathbf{e}_i$. Moreover, the choice ensures in particular that $\boldsymbol{\Phi}$ satisfies the constraint (3.19). An equivalent formulation by introducing a Lagrange multiplier for the constraint is given in [Boyer and Lapuerta 2006].

Remark 3.6 (Relation of Σ_i and σ_{ij})**:** *Consider the two–phase case satisfying $\phi_i + \phi_j = 1$ for $i, j \in \{1,2,3\}, i \neq j$. In this case there are only transition zones between the pure phases $\boldsymbol{\Phi} = \mathbf{e}_i$ and $\boldsymbol{\Phi} = \mathbf{e}_j$. Then W reduces to the scaled double-well potential:*

$$W(\boldsymbol{\Phi}) = \Sigma_i W_{\mathrm{dw}}(\phi_i) + \Sigma_j W_{\mathrm{dw}}(\phi_j) = (\Sigma_i + \Sigma_j) W_{\mathrm{dw}}(\phi_i).$$

In the asymptotic analysis in Section 3.2.2 the scaling factor $\Sigma_i + \Sigma_j$ is identified as the surface energy σ_{ij} of the sharp interface formulation (3.1)–(3.14)*. We therefore have $\sigma_{ij} = \Sigma_i + \Sigma_j$, $i, j \in \{1,2,3\}$, which leads to*

$$\Sigma_i = \frac{1}{2}\left(\sigma_{ij} + \sigma_{ik} - \sigma_{jk}\right), \quad i,j,k \in \{1,2,3\}, \quad i \neq j \neq k \neq i. \tag{3.23}$$

In the literature, see e.g. [Harkins and Feldman 1922], $-\Sigma_i$ is known as wetting or spreading coefficient. In a more general setting than ours, a negative value of Σ_i implies $\sigma_{jk} > \sigma_{ij} + \sigma_{ik}$, i.e., an interface of phases j and k is energetically less favorable than a thin film of phase i in between these phases, phase i is "spreading".

In our model the surface energy σ_{12} induces surface tension effects between the two fluids and σ_{13} impacts the precipitation and dissolution process. A desirable setting for the contact angle condition (3.14) *was $\sigma_{12} \ll \sigma_{13}, \sigma_{23}$. This translates with* (3.23) *to the condition $\Sigma_3 \gg \Sigma_1, \Sigma_2$. Note that still $\Sigma_1, \Sigma_2, \Sigma_3 > 0$, and we satisfy the conditions posed in [Boyer and Lapuerta 2006] to avoid a mixture of all three phases in the transition regions.*

3.1.2.2 The $2f1s$-Model

We proceed to present the complete phase field model coupling the Cahn–Hilliard equations with the Navier–Stokes system, describing two fluid phases plus one solid phase ($2f1s$). The total fluid fraction ϕ_f and the ion–dissolving fluid fraction ϕ_c are given by

$$\phi_f(\boldsymbol{\Phi}) := \phi_1 + \phi_2, \qquad \phi_c := \phi_1. \tag{3.24}$$

Furthermore, we define the total density and the fluid density by

$$\rho(\boldsymbol{\Phi}) := \rho_1\phi_1 + \rho_2\phi_2 + \rho_3\phi_3, \qquad \rho_f(\boldsymbol{\Phi}) := \rho_1\phi_1 + \rho_2\phi_2. \tag{3.25}$$

To govern the three-phase dynamics we introduce for $\varepsilon > 0$ the $2f1s$-model

$$\nabla \cdot (\phi_f \mathbf{v}) = 0, \tag{3.26}$$

$$\begin{aligned}\partial_t(\rho_f\mathbf{v}) + \nabla\cdot((\rho_f\mathbf{v} + \mathbf{J}_f)\otimes\mathbf{v}) &= -\phi_f\nabla p + \nabla\cdot(2\gamma(\boldsymbol{\Phi})\nabla^s\mathbf{v}) \\ &\quad - \rho_3 d(\phi_f,\varepsilon)\mathbf{v} + \mathbf{S} + \frac{1}{2}\rho_1\mathbf{v}R_f,\end{aligned} \tag{3.27}$$

$$\partial_t(\phi_c c) + \nabla\cdot((\phi_c\mathbf{v} + \mathbf{J}_c)c) = D\nabla\cdot(\phi_c\nabla c) + R_c, \tag{3.28}$$

$$\partial_t\phi_i + \nabla\cdot(\phi_i\mathbf{v} + \mathbf{J}_i) = R_i, \qquad i \in \{1,2\}, \tag{3.29}$$

$$\partial_t\phi_3 + \nabla\cdot\mathbf{J}_3 = R_3, \tag{3.30}$$

$$\mu_i = \frac{\partial_{\phi_i} W(\boldsymbol{\Phi})}{\varepsilon} - \varepsilon\Sigma_i\Delta\phi_i, \qquad i \in \{1,2,3\}, \tag{3.31}$$

in $(0,T)\times\Omega$. The flux terms are given by

$$\mathbf{J}_i = -\frac{\varepsilon}{\Sigma_i}\nabla\mu_i, \quad \text{and} \quad \mathbf{J}_f = \rho_1\mathbf{J}_1 + \rho_2\mathbf{J}_2, \qquad \mathbf{J}_c = \mathbf{J}_1. \tag{3.32}$$

The reaction terms R_1, R_2, R_3, R_c, R_f modeling precipitation and dissolution of ions satisfy

$$R_3 = -R_1, \qquad R_2 = 0, \qquad \frac{1}{c^*}R_c = -R_3, \qquad R_f = R_1. \tag{3.33}$$

It remains to fix R_1, which will be derived in Section 3.1.5 as a constitutive relation from thermodynamical considerations.

The term $\mathbf{S}$ models the effective surface tension between the two fluids. There are a multitude of choices even for the two-phase case, see [Kim 2005] for an overview. As generalization to the three-phase case which assures thermodynamical consistency (see Theorem 3.1.5) we use

$$\mathbf{S} = -\mu_2\phi_f\nabla\left(\frac{\phi_1}{\phi_f}\right) - \mu_1\phi_f\nabla\left(\frac{\phi_2}{\phi_f}\right). \tag{3.34}$$

The $2f1s$-model (3.26)–(3.31) is complemented by initial conditions and is subject to the boundary conditions

$$\mathbf{v} = 0, \tag{3.35}$$
$$\nabla c\cdot\mathbf{n}_\Omega = 0, \tag{3.36}$$
$$\nabla\phi_i\cdot\mathbf{n}_\Omega = 0, \qquad i\in\{1,2,3\}, \tag{3.37}$$
$$\nabla\mu_i\cdot\mathbf{n}_\Omega = 0, \qquad i\in\{1,2,3\}, \tag{3.38}$$

on $(0,T)\times\partial\Omega$. Here $\mathbf{n}_\Omega\in\mathbb{R}^N$ is the outer normal unit vector on $\partial\Omega$.

3.1.2.3 Comments on the Incompressibility Equation (3.26)

As in Chapter 2, requiring $\phi_f\mathbf{v}$ to be divergence free replaces the usual incompressibility constraint on $\mathbf{v}$ alone. We follow here the

idea of volume averaging presented in [Abels, Garcke, et al. 2012], instead of the classical approach by [Lowengrub and Truskinovsky 1998]. The latter would not lead to a divergence-free formulation which we favor for numerical reasons. Note that $\mathbf{v}$ in (3.26) has then to be understood as the velocity of the fluid fraction instead of some average velocity of the full mixture. In particular, the ansatz prevents advection of the phase parameter ϕ_3 of the solid phase in the governing equation (3.30).

Remark 3.7: *We assume like in Section 3.1.1 that the densities* ρ_1 *and* ρ_3 *equal. Otherwise, the reaction process would lead to a change in volume, see also Remark 3.1, and we would lose the incompressibility constraint* (3.26)*. Note that the relation* $R_3 = -R_1$ *in* (3.33) *is a special case of the more general mass conservation relation* $R_1\rho_1 + R_3\rho_3 = 0$ *accounting for change in volume. Equation* (3.26) *would read in this case as*

$$\nabla \cdot (\phi_f \mathbf{v}) = R_1 + R_3.$$

3.1.2.4 Comments on the Momentum Equations (3.27)

The momentum equations are formulated for the combined momentum $\rho_f(\boldsymbol{\Phi})\mathbf{v}$ of the two fluid phases and involve the pressure-like term $\phi_f \nabla p$. Note that this term is not in divergence form anymore, due to the fact that the solid phase is assumed to be immobile and can thus act as a sink or source for momentum. This becomes clear by rewriting

$$\phi_f \nabla p = \nabla(\phi_f p) - p\nabla\phi_f.$$

The first term on the right-hand side is now in divergence form. The second term contributes in the interfacial region between the solid and the fluid phases, with $\nabla\phi_f$ being orthogonal to the interface here. It is therefore a normal force acting between the solid phase and the fluid phases.

The viscosity γ in (3.27) depends on the phase field parameter $\boldsymbol{\Phi}$. We choose harmonic averaging of the bulk viscosities from Section 3.1.1, i.e.,

$$\gamma(\boldsymbol{\Phi}) = \left(\phi_1\gamma_1^{-1} + \phi_2\gamma_2^{-1} + \phi_3\gamma_3^{-1}\right)^{-1}. \tag{3.39}$$

Whereas γ_1 and γ_2 are physical quantities, note that γ_3 does not represent a physical viscosity and is used for the Navier-slip condition instead.

Note that the viscosity term here is written as $\nabla \cdot (2\gamma(\boldsymbol{\Phi})\nabla^s \mathbf{v})$. This is in contrast to the Allen–Cahn–Navier–Stokes Model of Chapter 2, where this term was formulated as $\gamma_f\phi_f\nabla^2(\phi_f\mathbf{v})$. The term of the Allen–Cahn Model vanishes for $\phi_f = 0$, resulting in $\mathbf{v} = 0$ in the solid phase for the sharp interface limit. We choose here a term that does not vanish for $\phi_f = 0$ to realize the Navier-slip condition.

In [Abels, Garcke, et al. 2012] a thermodynamically consistent Cahn–Hilliard model for two-phase flow is constructed by adding a flux term in the momentum equations. We generalize this approach to an additional solid phase by the term $\nabla \cdot (\mathbf{J}_f \otimes \mathbf{v})$ and obtain a thermodynamically consistent model, see Theorem 3.1.1 below. The phase field parameter gets transported by both, the fluid fraction velocity $\mathbf{v}$ and the Cahn–Hilliard fluxes $\mathbf{J}_i$. This leads to an additional transport of the momentum of each fluid phase with its respective flux $\mathbf{J}_i$.

Next, we discuss the term $d(\phi_f, \varepsilon)\mathbf{v}$. As in Chapter 2, $d(\cdot, \varepsilon)$ can be any smooth, decreasing function with $d(1, \varepsilon) = 0$, $d(0, \varepsilon) = d_0 > 0$ for a constant d_0 independent of ε. This term ensures that $\mathbf{v}$ is small in the solid phase. Similar ideas have been used in [Beckermann et al. 1999; Garcke, Hinze, Kahle, and Fong Lam 2017]. While these works get $\mathbf{v} = 0$ in the solid phase, we use the variable to allow for slip at the fluid–solid interface instead, see Section 3.1.1.4. In practice, we choose $d(\phi_f, \varepsilon) = d_0(1 - \phi_f)^2$.

3.1.2.5 Comments on the Ion Transport Equation (3.28)

The equation for the dissolved ion concentration c consists of transport, diffusion and reaction. Analogously to the momentum equations, we introduce the additional term $\nabla \cdot (\mathbf{J}_c c)$ to account for the transport caused by the Cahn–Hilliard equation. The rate of diffusion scales with ϕ_c, such that there is no diffusion through other phases.

3.1.2.6 Comments on the Cahn–Hilliard Equations (3.29), (3.30), (3.31)

The phase field parameters ϕ_i are governed by a Cahn–Hilliard evolution. It is well known that one can interpret this evolution as a gradient flow to the Ginzburg–Landau free energy

$$f(\boldsymbol{\Phi}, \nabla\boldsymbol{\Phi}) = \frac{W(\boldsymbol{\Phi})}{\varepsilon} + \sum_{i=1}^{3} \frac{\varepsilon\Sigma_i}{2} |\nabla\phi_i|^2. \tag{3.40}$$

Pure phases $\boldsymbol{\Phi} = \mathbf{e}_i$ are minima of the potential $W(\boldsymbol{\Phi})$. Phase transitions, that are characterized by large gradients, are penalized in (3.40) through the term $|\nabla\phi_i|^2$. These two energy contributions get weighted by the parameter ε, resulting in phase transitions with a width of order ε. Following [Boyer, Lapuerta, et al. 2010; Boyer and Lapuerta 2006] the coefficients Σ_i have no influence on the width of the diffuse transition zone.

The Cahn–Hilliard equations (3.29), (3.30), (3.31) are coupled to the Navier–Stokes equations (3.26), (3.27) through the advection of ϕ_1 and ϕ_2. The solid phase ϕ_3 is not advected, leading to an effective total flow velocity of $\phi_f \mathbf{v}$, as described above.

As we show in Section 3.1.4, solutions to our model satisfy $\sum_{i=1}^{3} \phi_i = 1$ and $\sum_{i=1}^{3} \mu_i/\Sigma_i = 0$. As a consequence one of the equations for the three phase field parameters can be eliminated.

3.1.3 The δ-$2f1s$-Phase Field Model

For the $2f1s$-model we are not able to achieve thermodynamical consistency without the following modification. We need to avoid that quantities like ϕ_f and ρ_f from (3.24) and (3.25) can attain negative values, leading to a degeneration of the model. Therefore, we redefine these quantities using the small parameter δ which has been used to define the double-well potential in (3.20). This approach is analogous to the Regularized Allen–Cahn–Navier–Stokes model in Section 2.1.3, where we prevented degeneration of the model in the case $\phi_f = 0$. We define

$$\tilde{\phi}_f := \phi_1 + \phi_2 + 2\delta\phi_3, \tag{3.41}$$

$$\tilde{\rho}_f(\boldsymbol{\Phi}) := \rho_1\phi_1 + \rho_2\phi_2 + (\rho_1 + \rho_2)\delta, \tag{3.42}$$

$$\tilde{\gamma}(\boldsymbol{\Phi}) := (\phi_1\gamma_1^{-1} + \phi_2\gamma_2^{-1} + \phi_3\gamma_3^{-1} + (\gamma_1^{-1} + \gamma_2^{-1} + \gamma_3^{-1})\delta)^{-1}, \tag{3.43}$$

$$\tilde{\phi}_c := \phi_1 + \delta. \tag{3.44}$$

It is straightforward to see that these quantities are positive if $\phi_i > -\delta$ and (3.19) hold. Note that the double-well function $W_{\mathrm{dw}}(\phi_i)$ from (3.20) diverges at $\phi_i = -\delta$ and $\phi_i = 1 + \delta$. This implies $\phi_i \in (-\delta, 1+\delta)$ by establishing an energy estimate in Section 3.1.5.

We proceed to formulate the δ-$2f1s$-model by

$$\nabla \cdot (\tilde{\phi}_f \mathbf{v}) = 0, \tag{3.45}$$

$$\begin{aligned}\partial_t(\tilde{\rho}_f\mathbf{v}) + \nabla\cdot((\rho_f\mathbf{v} + \mathbf{J}_f)\otimes\mathbf{v}) = &-\tilde{\phi}_f\nabla p + \nabla\cdot(2\tilde{\gamma}(\boldsymbol{\Phi})\nabla^s\mathbf{v}) \\ &- \rho_3 d(\tilde{\phi}_f,\varepsilon)\mathbf{v} + \tilde{\mathbf{S}} + \frac{1}{2}\rho_1\mathbf{v}R_f,\end{aligned} \tag{3.46}$$

$$\partial_t(\tilde{\phi}_c c) + \nabla\cdot((\phi_c\mathbf{v} + \mathbf{J}_c)c) = D\nabla\cdot(\tilde{\phi}_c\nabla c) + R_c, \tag{3.47}$$

$$\partial_t\phi_i + \nabla\cdot(\phi_i\mathbf{v} + \mathbf{J}_i) = R_i, \qquad i \in \{1,2\}, \tag{3.48}$$

$$\partial_t\phi_3 + \nabla\cdot(2\delta\phi_3\mathbf{v} + \mathbf{J}_3) = R_3, \tag{3.49}$$

$$\mu_i = \frac{\partial_{\phi_i} W(\boldsymbol{\Phi})}{\varepsilon} - \varepsilon \Sigma_i \Delta \phi_i, \qquad i \in \{1,2,3\}, \tag{3.50}$$

in $(0,T)\times\Omega$. The modification also affects the surface tension term $\mathbf{S}$, such that we are led to replace $\mathbf{S}$ in (3.27) by $\tilde{\mathbf{S}}$ with

$$\tilde{\mathbf{S}} = -\mu_2 \tilde{\phi}_f \nabla \left(\frac{\phi_1}{\tilde{\phi}_f}\right) - \mu_1 \tilde{\phi}_f \nabla \left(\frac{\phi_2}{\tilde{\phi}_f}\right) - 2\delta\phi_3 \nabla(\mu_3 - \mu_1 - \mu_2). \tag{3.51}$$

From here on we consider only the δ-$2f1s$-model (3.45)–(3.50).

3.1.4 Conservation of Total Mass, Ions and Volume Fraction

Consider the δ-$2f1s$-model with boundary conditions (3.35)–(3.38). The phase field equations are written in divergence form, so it is easy to see that for classical solutions we have

$$\frac{d}{dt}\int_\Omega \phi_i \, d\mathbf{x} = \int_\Omega R_i \, d\mathbf{x},$$

i.e., the phase field variables are balanced by the reaction terms only. Using (3.33) this implies that the total mass $\rho(\boldsymbol{\Phi})$ from (3.25) is conserved,

$$\frac{d}{dt}\int_\Omega \rho(\boldsymbol{\Phi}) \, d\mathbf{x} = \int_\Omega \rho_1 R_1 + \rho_2 R_2 + \rho_1 R_3 \, d\mathbf{x} = 0.$$

Moreover, the total amount of ions, given by $\tilde{\phi}_c c + \phi_3 c^*$, is invariant because (3.33) implies

$$\frac{d}{dt}\int_\Omega \tilde{\phi}_c c + \phi_3 c^* \, d\mathbf{x} = \int_\Omega R_c + c^* R_3 \, d\mathbf{x} = 0.$$

Finally, classical solutions of the δ-$2f1s$-model obey also (3.19) provided (3.19) is satisfied initially. This is due to our construction of the

triple-well function $W(\boldsymbol{\Phi}) = W_0(P\boldsymbol{\Phi})$ with the projection P from in (3.22). The function W is constant in the direction $(\Sigma_1^{-1}, \Sigma_2^{-1}, \Sigma_3^{-1})^\top$, therefore

$$\begin{aligned}\sum_{i=1}^{3} \frac{\mu_i}{\Sigma_i} &= \frac{1}{\varepsilon} \sum_{i=1}^{3} \frac{\partial_{\phi_i} W(\boldsymbol{\Phi})}{\Sigma_i} - \varepsilon \Delta \sum_{i=1}^{3} \phi_i \\ &= \frac{\partial_{(\Sigma_1^{-1}, \Sigma_2^{-1}, \Sigma_3^{-1})^\top} W(\boldsymbol{\Phi})}{\varepsilon} - \varepsilon \Delta 1 = 0,\end{aligned} \tag{3.52}$$

and thus we get the desired conservation of volume fractions as

$$\frac{d}{dt} \sum_{i=1}^{3} \phi_i = \sum_{i=1}^{3} R_i - \nabla \cdot (\tilde{\phi}_f \mathbf{v}) + \varepsilon \Delta \sum_{i=1}^{3} \frac{\mu_i}{\Sigma_i} = 0.$$

3.1.5 Thermodynamical Consistency

Interpreting the Cahn–Hilliard equation as a gradient flow of the Ginzburg–Landau energy (3.40) and following the ideas in [Abels, Garcke, et al. 2012] the δ-$2f1s$-model can be shown to be thermodynamically consistent. We find a free energy functional satisfying a dissipation inequality along the evolution of the δ-$2f1s$-model. In our case it is

$$F(\boldsymbol{\Phi}, \nabla \boldsymbol{\Phi}, v, c) = \int_\Omega \frac{1}{2} \tilde{\rho}_f |\mathbf{v}|^2 + f(\boldsymbol{\Phi}, \nabla \boldsymbol{\Phi}) + \frac{1}{\tilde{\alpha}} g(c) \tilde{\phi}_c \, d\mathbf{x}. \tag{3.53}$$

This free energy functional consists of three parts: The kinetic energy of the fluid phases, the Ginzburg–Landau energy (3.40), and a third term $\tilde{\alpha}^{-1} g(c) \tilde{\phi}_c$. The last term represents the free energy associated with the fluid–ions mixture, depending only on the ion concentration. Note that even with no kinetic energy present, precipitation and dissolution can increase the surface area between the fluid and the solid phase (and thus the Ginzburg–Landau energy f), so they have to decrease the free mixture energy $g(c)$ at the same time.

With this in mind, we choose the specific form of the up to now unspecified function R_1 as

$$r(c) := g(c) + g'(c)(c^* - c), \qquad R_1 = -\frac{q(\boldsymbol{\Phi})}{\varepsilon}\left(r(c) + \tilde{\alpha}\mu_1 - \tilde{\alpha}\mu_3\right). \tag{3.54}$$

The choice of $r(c)$ is the result of the following argument. Consider (3.47)–(3.50) for the case that $\mathbf{v} \equiv 0$ and that $\boldsymbol{\Phi}$ and c are constant in space. From equations (3.47), (3.48) we can infer the conservation of ions $\partial_t(\tilde{\phi}_c c + (1-\tilde{\phi}_c)c^*) = 0$, and have therefore an implicit relation for $c = c(\tilde{\phi}_c)$. The reaction r is driven by the free energy $\tilde{\alpha}^{-1} g(c)\tilde{\phi}_c$ and should be given by the derivative of this term with respect to $\tilde{\phi}_c$, i.e.,

$$r = \frac{d}{d\tilde{\phi}_c}\Big(g(c(\tilde{\phi}_c))\tilde{\phi}_c\Big) = g(c) + g'(c)\tilde{\phi}_c \frac{d}{d\tilde{\phi}_c} c(\tilde{\phi}_c).$$

After direct calculation we recover the formula for $r(c)$ in (3.54). As stated in Section 3.1.1.2 we consider reaction terms $r(c)$ that are increasing in c. A short calculation shows that there is in fact a bijection between convex functions $g(c)$ and increasing functions $r(c)$. We therefore assume $g(c)$ to be convex in the following.

The reaction term R_1 does not only depend on r but also on the phase field potentials μ_1 and μ_3. These represent the influence of curvature effects on the reaction. As described in (3.10) this effect should scale with a chosen constant $\alpha \in [0, \infty)$. The case $\alpha = 0$ requires extra care. We therefore introduce a modified α as

$$\tilde{\alpha} = \begin{cases} \alpha & \text{for } \alpha > 0, \\ \delta & \text{for } \alpha = 0. \end{cases} \tag{3.55}$$

Furthermore, we localize the reaction to the fluid–solid interface by

choosing the non-negative function $q(\boldsymbol{\Phi})$ as

$$q(\boldsymbol{\Phi}) = \begin{cases} 30\phi_1^2\phi_3^2 & \text{for } \phi_1, \phi_3 \in [0,1], \\ 0 & \text{otherwise.} \end{cases}$$

Remark 3.8: *This is a similar choice as in [Redeker et al. 2016], where fluid motion is ignored. The situation is more intricate here. In general, we require $q = 0$ when $\phi_1 = 0$ or $\phi_3 = 0$. Furthermore, across an interface between phase $\boldsymbol{\Phi} = \mathbf{e}_1$ and phase $\boldsymbol{\Phi} = \mathbf{e}_3$ we require $q(\boldsymbol{\Phi}) = \sqrt{2W_{\mathrm{dw}}(\phi_1)}$, which results in the constant prefactor in $q(\boldsymbol{\Phi})$.*

To derive a thermodynamically consistent model we had to introduce the flux terms in (3.32) and the specific choice of the reaction R_1 in (3.54), and can now prove the following theorem.

Theorem 3.1.1. *Classical solutions to the δ-2f1s-model, which obey the boundary conditions* (3.35)–(3.38) *and satisfy $F(\boldsymbol{\Phi}, \nabla\boldsymbol{\Phi}, v, c) < \infty$ initially, fulfill for all $t \in (0, T]$ the free energy dissipation inequality*

$$\begin{aligned} &\frac{d}{dt}F(\boldsymbol{\Phi}, \nabla\boldsymbol{\Phi}, v, c) \\ &\quad= \int_\Omega -2\tilde{\gamma}(\boldsymbol{\Phi})\nabla\mathbf{v} : \nabla^s\mathbf{v} - \rho_3 d(\tilde{\phi}_f, \varepsilon)\mathbf{v}^2 - \varepsilon\sum_{i=1}^{3}\frac{1}{\Sigma_i}|\nabla\mu_i|^2 \\ &\qquad - \tilde{\alpha}^{-1}Dg''(c)\tilde{\phi}_c|\nabla c|^2 - \frac{q(\boldsymbol{\Phi})}{\varepsilon\tilde{\alpha}}\left(r(c) + \tilde{\alpha}\mu_1 - \tilde{\alpha}\mu_3\right)^2 d\mathbf{x} \\ &\quad\leq 0. \end{aligned}$$

Proof. We treat the time derivative of each of the terms in (3.53) separately. Let us start with $\partial_t(\tilde{\phi}_c g(c))$. Using integration by parts

and the homogeneous boundary conditions we have

$$\begin{aligned}\int_\Omega & g'(c)\nabla\cdot((\phi_c\mathbf{v}+\mathbf{J}_c)c)\,d\mathbf{x}\\ &= \int_\Omega (\nabla g(c))\cdot(\phi_c\mathbf{v}+\mathbf{J}_c) + g'(c)c\nabla\cdot(\phi_c\mathbf{v}+\mathbf{J}_c)\,d\mathbf{x} \qquad (3.56)\\ &= \int_\Omega -(g(c)-g'(c)c)\nabla\cdot(\phi_c\mathbf{v}+\mathbf{J}_c)\,d\mathbf{x}.\end{aligned}$$

Using (3.47), (3.48) and (3.56) we calculate

$$\begin{aligned}&\int_\Omega \partial_t(g(c)\tilde{\phi}_c)\,d\mathbf{x} \qquad (3.57)\\ &\quad= \int_\Omega g'(c)\partial_t(\tilde{\phi}_c c) + (g(c)-g'(c)c)\partial_t\tilde{\phi}_c\,d\mathbf{x}\\ &\quad= \int_\Omega g'(c)(R_c - \nabla\cdot((\phi_c\mathbf{v}+\mathbf{J}_c)c) + D\nabla\cdot(\tilde{\phi}_c\nabla c))\\ &\qquad\quad + (g(c)-g'(c)c)(R_1-\nabla\cdot(\phi_1\mathbf{v}+\mathbf{J}_1))\,d\mathbf{x}\\ &\quad= \int_\Omega g'(c)D\nabla\cdot(\tilde{\phi}_c\nabla c) + R_1(g(c)-g'(c)c+g'(c)c^*)\,d\mathbf{x}\\ &\quad= \int_\Omega g'(c)D\nabla\cdot(\tilde{\phi}_c\nabla c) + r(c)R_1\,d\mathbf{x}. \qquad (3.58)\end{aligned}$$

We require some results from vector calculus: For vector fields $\mathbf{A},\mathbf{B}$ we have

$$\begin{aligned}\nabla\cdot(\mathbf{A}\otimes\mathbf{B}) &= (\nabla\cdot\mathbf{A})\mathbf{B} + (\mathbf{A}\cdot\nabla)\mathbf{B},\\ \mathbf{B}\cdot\Big((\mathbf{A}\cdot\nabla)\mathbf{B}\Big) &= \frac{1}{2}(\mathbf{A}\cdot\nabla)|\mathbf{B}|^2.\end{aligned}$$

Using this and partial integration we get

$$\begin{aligned}
&\int_\Omega \mathbf{v} \cdot \Big(\nabla \cdot ((\rho_f \mathbf{v} + \mathbf{J}_f) \otimes \mathbf{v}) \Big)\, d\mathbf{x} \\
&\quad = \int_\Omega \mathbf{v} \cdot \Big((\nabla \cdot (\rho_f \mathbf{v} + \mathbf{J}_f))\mathbf{v} + ((\rho_f \mathbf{v} + \mathbf{J}_f) \cdot \nabla)\mathbf{v} \Big)\, d\mathbf{x} \\
&\quad = \int_\Omega \mathbf{v}^2 \nabla \cdot (\rho_f \mathbf{v} + \mathbf{J}_f) + \frac{1}{2}((\rho_f \mathbf{v} + \mathbf{J}_f) \cdot \nabla)\mathbf{v}^2 \, d\mathbf{x} \\
&\quad = \int_\Omega \frac{1}{2}\mathbf{v}^2 \nabla \cdot (\rho_f \mathbf{v} + \mathbf{J}_f)\, d\mathbf{x}.
\end{aligned} \tag{3.59}$$

Also, note that

$$\begin{aligned}
\partial_t \tilde{\rho}_f &= \rho_1 \partial_t \phi_1 + \rho_2 \partial_t \phi_2 \\
&= \rho_1 (R_1 - \nabla \cdot (\phi_1 \mathbf{v} + \mathbf{J}_1)) + \rho_2 (R_2 - \nabla \cdot (\phi_2 \mathbf{v} + \mathbf{J}_2)) \\
&= \rho_1 R_1 - \nabla \cdot (\rho_f \mathbf{v} + \mathbf{J}_f).
\end{aligned} \tag{3.60}$$

With (3.46), (3.59) and (3.60) we can calculate the time derivative of the kinetic energy as

$$\begin{aligned}
&\frac{d}{dt} \int_\Omega \frac{1}{2} \tilde{\rho}_f |\mathbf{v}|^2 \, d\mathbf{x} \\
&\quad = \int_\Omega \mathbf{v} \cdot \partial_t (\tilde{\rho}_f \mathbf{v}) - \frac{1}{2}\mathbf{v}^2 \partial_t \tilde{\rho}_f \, d\mathbf{x} \\
&\quad = \int_\Omega -\mathbf{v} \cdot (\nabla \cdot ((\rho_f \mathbf{v} + \mathbf{J}_f) \otimes \mathbf{v})) - \tilde{\phi}_f \mathbf{v} \cdot \nabla p \\
&\qquad\quad + \mathbf{v} \cdot (\nabla \cdot (2\tilde{\gamma}(\boldsymbol{\Phi}) \nabla^s \mathbf{v})) - \rho_3 d(\tilde{\phi}_f, \varepsilon)\mathbf{v}^2 + \tilde{\mathbf{S}} \cdot \mathbf{v} \\
&\qquad\quad + \mathbf{v} \cdot \frac{1}{2}\rho_1 \mathbf{v} R_f - \frac{1}{2}\mathbf{v}^2 \rho_1 R_1 + \frac{1}{2}\mathbf{v}^2 \nabla \cdot (\rho_f \mathbf{v} + \mathbf{J}_f)\, d\mathbf{x} \\
&\quad = \int_\Omega \mathbf{v} \cdot (\nabla \cdot (2\tilde{\gamma}(\boldsymbol{\Phi}) \nabla^s \mathbf{v})) - \rho_3 d(\tilde{\phi}_f, \varepsilon)\mathbf{v}^2 + \tilde{\mathbf{S}} \cdot \mathbf{v} \, d\mathbf{x}.
\end{aligned} \tag{3.61}$$

Next we consider the surface tension terms. Note that by (3.45)

$$0 = \nabla \cdot (\tilde{\phi}_f \mathbf{v}) = \nabla \cdot (\phi_1 \mathbf{v}) + \nabla \cdot (\phi_2 \mathbf{v}) + \nabla \cdot (2\delta \phi_3 \mathbf{v}),$$

and using this, partial integration and (3.51) we find

$$\begin{aligned}
&\int_\Omega \mu_1 \nabla\cdot(\phi_1\mathbf{v}) + \mu_2\nabla\cdot(\phi_2\mathbf{v}) + \mu_3\nabla\cdot(2\delta\phi_3\mathbf{v})\,d\mathbf{x}\\
&\quad= \int_\Omega -\mu_2\nabla\cdot(\phi_1\mathbf{v}) - \mu_1\nabla\cdot(\phi_2\mathbf{v})\\
&\qquad\qquad + (\mu_3-\mu_1-\mu_2)\nabla\cdot(2\delta\phi_3\mathbf{v})\,d\mathbf{x}\\
&\quad= \int_\Omega -\mu_2\tilde{\phi}_f\nabla\left(\frac{\phi_1}{\tilde{\phi}_f}\right)\cdot\mathbf{v} - \mu_1\tilde{\phi}_f\nabla\left(\frac{\phi_2}{\tilde{\phi}_f}\right)\cdot\mathbf{v}\\
&\qquad\qquad - 2\delta\phi_3\nabla(\mu_3-\mu_1-\mu_2)\cdot\mathbf{v}\,d\mathbf{x}\\
&\quad= \int_\Omega \tilde{\mathbf{S}}\cdot\mathbf{v}\,d\mathbf{x}.
\end{aligned} \tag{3.62}$$

With (3.62) we calculate the time derivative of the Ginzburg–Landau energy (3.40) to be

$$\begin{aligned}
\frac{d}{dt}\int_\Omega f(\boldsymbol{\Phi},\nabla\boldsymbol{\Phi})\,d\mathbf{x} &= \int_\Omega \sum_{i=1}^{3}\left(\frac{\partial f}{\partial\phi_i} - \nabla\cdot\frac{\partial f}{\partial\nabla\phi_i}\right)\partial_t\phi_i\,d\mathbf{x}\\
&= \int_\Omega \sum_{i=1}^{3}\mu_i\partial_t\phi_i\,d\mathbf{x}\\
&= \int_\Omega \sum_{i=1}^{3}\mu_i(R_i - \nabla\cdot\mathbf{J}_i) - \mu_1\nabla\cdot(\phi_1\mathbf{v})\\
&\qquad - \mu_2\nabla\cdot(\phi_2\mathbf{v}) - \mu_3\nabla\cdot(2\delta\phi_3\mathbf{v})\,d\mathbf{x}\\
&= \int_\Omega (\mu_1-\mu_3)R_1 - \sum_{i=1}^{3}\mu_i\nabla\cdot\mathbf{J}_i - \tilde{\mathbf{S}}\cdot\mathbf{v}\,d\mathbf{x}.
\end{aligned} \tag{3.63}$$

Finally, we calculate with (3.58), (3.61) and (3.63)

$$\begin{aligned}
&\frac{d}{dt}F(\boldsymbol{\Phi},\nabla\boldsymbol{\Phi},v,c)\,d\mathbf{x}\\
&\quad= \frac{d}{dt}\int_\Omega \frac{1}{2}\tilde{\rho}_f|\mathbf{v}|^2 + f(\boldsymbol{\Phi},\nabla\boldsymbol{\Phi}) + \tilde{\alpha}^{-1}g(c)\tilde{\phi}_c\,d\mathbf{x}
\end{aligned}$$

$$
\begin{aligned}
&= \int_\Omega \mathbf{v} \cdot (\nabla \cdot (2\tilde{\gamma}(\boldsymbol{\Phi})\nabla^s \mathbf{v})) - \rho_3 d(\tilde{\phi}_f, \varepsilon)\mathbf{v}^2 + \tilde{\mathbf{S}} \cdot \mathbf{v} \\
&\quad + (\mu_1 - \mu_3) R_1 - \sum_{i=1}^{3} \mu_i \nabla \cdot \mathbf{J}_i - \tilde{\mathbf{S}} \cdot \mathbf{v} \\
&\quad + \tilde{\alpha}^{-1} D g'(c) \nabla \cdot (\tilde{\phi}_c \nabla c) + \tilde{\alpha}^{-1} r(c) R_1 \, d\mathbf{x} \\
&= \int_\Omega -2\tilde{\gamma}(\boldsymbol{\Phi}) \nabla \mathbf{v} : \nabla^s \mathbf{v} - \rho_3 d(\tilde{\phi}_f, \varepsilon)\mathbf{v}^2 + \sum_{i=1}^{3} \nabla \mu_i \cdot \mathbf{J}_i \\
&\quad - \tilde{\alpha}^{-1} D g''(c) \tilde{\phi}_c |\nabla c|^2 + \tilde{\alpha}^{-1} \left(r(c) + \tilde{\alpha}\mu_1 - \tilde{\alpha}\mu_3 \right) R_1 \, d\mathbf{x}.
\end{aligned}
$$

A straightforward calculation shows $\nabla \mathbf{v} : \nabla^s \mathbf{v} \geq 0$. The assertion of the theorem follows by inserting the definitions of $\mathbf{J}_i$ (3.32) and R_1 (3.54). □

3.1.6 Algebraic Consistency

If one of the three phases is not present, we obtain simplified scenarios which reduce to phase field models that are partly known from literature.
We study the cases with one phase already absent initially. As in [Boyer and Lapuerta 2006] we first show that this phase does not appear at a later point in time. Afterwards we investigate the reduced two-phase models that arise from this simplification.

Let in the following $i, j, k \in \{1, 2, 3\}$, $i \neq j \neq k \neq i$. We consider the case $\phi_i = 0$ and $\phi_k + \phi_j = 1$. Using (3.21) and (3.22) we calculate

$$
\begin{aligned}
\partial_{\phi_i} W(\boldsymbol{\Phi}) &= \partial_{\phi_i} W_0(P\boldsymbol{\Phi}) \\
&= \left(1 - \frac{\Sigma_T}{\Sigma_i}\right) \partial_{\phi_i} W_0(\boldsymbol{\Phi}) - \frac{\Sigma_T}{\Sigma_j} \partial_{\phi_j} W_0(\boldsymbol{\Phi}) - \frac{\Sigma_T}{\Sigma_k} \partial_{\phi_k} W_0(\boldsymbol{\Phi}) \\
&= (\Sigma_i - \Sigma_T) \, \partial_{\phi_i} W_{\mathrm{dw}}(\phi_i) - \Sigma_T \partial_{\phi_j} W_{\mathrm{dw}}(\phi_j) \\
&\quad - \Sigma_T \partial_{\phi_k} W_{\mathrm{dw}}(\phi_k) \\
&= 0.
\end{aligned} \tag{3.64}
$$

For the last step recall the definition of W_{dw}, (3.20), to see that $\partial_{\phi_i} W_{\mathrm{dw}}(\phi_i) = 0$. Furthermore, with $\phi_k + \phi_j = 1$ and the symmetry of $W_{\mathrm{dw}}(\phi_i)$ with respect to $\phi_i = 1/2$ we have

$$\partial_{\phi_j} W_{\mathrm{dw}}(\phi_j) = \partial_{\phi_j} W_{\mathrm{dw}}(1-\phi_j) = -\partial_{\phi_k} W_{\mathrm{dw}}(\phi_k).$$

Using the calculation (3.64) we find $\phi_i \equiv 0$, $\mu_i \equiv 0$ as a solution to (3.48)/(3.49), (3.50) with homogeneous boundary conditions (3.35)–(3.38). Under the assumption of uniqueness this implies $\phi_i \equiv 0$ for all times if ϕ_i is not present in the initial data.

Before we consider special choices we point out another simplification for two-phase flow. With the two conditions $\phi_i = 0$ and $\phi_j + \phi_k = 1$ we can reduce the model to a model for a single phase-field variable, say ϕ_j. Using (3.21) and (3.22) we calculate

$$\begin{aligned}
\partial_{\phi_j} W(\boldsymbol{\Phi}) &= \partial_{\phi_j} W_0(P\boldsymbol{\Phi}) \\
&= \left(1 - \frac{\Sigma_T}{\Sigma_j}\right) \partial_{\phi_j} W_0(\boldsymbol{\Phi}) - \frac{\Sigma_T}{\Sigma_k} \partial_{\phi_k} W_0(\boldsymbol{\Phi}) - \frac{\Sigma_T}{\Sigma_i} \partial_{\phi_i} W_0(\boldsymbol{\Phi}) \\
&= \left(\Sigma_j - \Sigma_T\right) \partial_{\phi_j} W_{\mathrm{dw}}(\phi_j) - \Sigma_T \partial_{\phi_k} W_{\mathrm{dw}}(\phi_k) \\
&\quad - \Sigma_T \partial_{\phi_i} W_{\mathrm{dw}}(\phi_i) \\
&= \Sigma_j \partial_{\phi_j} W_{\mathrm{dw}}(\phi_j),
\end{aligned}$$

and define

$$\mu := \frac{\mu_j}{\Sigma_j} = \frac{\partial_{\phi_j} W_{\mathrm{dw}}(\phi_j)}{\varepsilon} - \varepsilon \Delta \phi_j.$$

3.1.6.1 Solid Phase plus one Fluid Phase (δ-$1f1s$)

We consider first the two cases $i = 1$ and $i = 2$, i.e., one of the two fluid phases is not present in the model. As a phase field variable we choose the indicator of the remaining fluid phase, meaning that for $i = 1$ we choose $j = 2$ and for $i = 2$ we choose $j = 1$. Note that

as calculated above $\mu_i = 0$ and $\mathbf{J}_i = 0$. The model δ-$2f1s$-model reduces to

$$\nabla \cdot (\tilde{\phi}_f \mathbf{v}) = 0, \tag{3.65}$$

$$\begin{aligned}\partial_t(\tilde{\rho}_f \mathbf{v}) + \nabla \cdot ((\phi_j \mathbf{v} - \varepsilon \nabla \mu) \otimes \rho_j \mathbf{v}) = &-\tilde{\phi}_f \nabla p + \nabla \cdot (2\tilde{\gamma}(\boldsymbol{\Phi}) \nabla^s \mathbf{v}) \\ &-\rho_3 d(\tilde{\phi}_f, \varepsilon)\mathbf{v} + \tilde{\mathbf{S}} + \frac{1}{2}\rho_1 \mathbf{v} R_f,\end{aligned} \tag{3.66}$$

$$\partial_t(\tilde{\phi}_c c) + \nabla \cdot ((\phi_c \mathbf{v} + \mathbf{J}_c)c) = D\nabla \cdot (\tilde{\phi}_c \nabla c) + R_c, \tag{3.67}$$

$$\partial_t \phi_j + \nabla \cdot (\phi_j \mathbf{v} - \varepsilon \nabla \mu) = R_j, \tag{3.68}$$

$$\mu = \frac{\partial_{\phi_j} W_{\mathrm{dw}}(\phi_j)}{\varepsilon} - \varepsilon \Delta \phi_j, \tag{3.69}$$

in $(0,T) \times \Omega$. This is a $1f1s$-model for a fluid fraction $\tilde{\phi}_f = 2\delta + (1 - 2\delta)\phi_j$. Previously suggested phase field models for single phase flow with precipitation [van Noorden and Eck 2011] and the model from Chapter 2 are based on the Allen–Cahn equation and were only able to ensure a global bound on but no dissipation of the free energy. By Theorem 3.1.1 the δ-$1f1s$-model (3.65)–(3.69) for single phase flow with precipitation/dissolution is also the first phase field model that ensures energy dissipation. We also refer to [Witterstein 2010; Witterstein 2011] for a two-phase flow model with phase change that satisfies a free energy inequality. By modeling the solid phase as a fluid with very high viscosity this model could also be used for the fluid–solid case.

The effective surface tension term reduces to

$$\tilde{\mathbf{S}} = -2\delta\phi_3 \nabla(\mu_3 - \mu_j) = 2\delta\sigma_{j3}(1 - \phi_j)\nabla\mu,$$

and is only there to keep consistency with the modified $\tilde{\phi}_f$.

In the case $i = 2$ this model is fully coupled. But for $i = 1$ there is no fluid present that dissolves the ions ($\phi_c = \phi_1 = 0$). Then $R_f = R_c = R_j = 0$ and the ion conservation law (3.67) is decoupled from the other equations and equals the diffusion equation $\delta\partial_t c = \delta D \Delta c$.

We use a modified version of the δ-$1f1s$ model (3.65)–(3.69) in Chapter 8 to model EICP in a micro-fluidic cell.

3.1.6.2 Two Fluid Phases (δ-$2f0s$)

We consider the case of two fluid phases. We have $\phi_3 = 0$ and reduce the model to the phase field variable ϕ_1. Note that $\phi_f = \tilde{\phi}_f = \phi_1 + \phi_2 = 1$ and $\Sigma_1^{-1}\mu_1 + \Sigma_2^{-1}\mu_2 = 0$. With this the δ-$2f1s$-model reduces to

$$\nabla \cdot \mathbf{v} = 0, \tag{3.70}$$

$$\partial_t(\tilde{\rho}_f \mathbf{v}) + \nabla \cdot ((\rho_f \mathbf{v} + \mathbf{J}_f) \otimes \mathbf{v}) + \nabla p = \nabla \cdot (2\tilde{\gamma}(\boldsymbol{\Phi})\nabla^s \mathbf{v}) + \tilde{\mathbf{S}}, \tag{3.71}$$

$$\partial_t(\tilde{\phi}_c c) + \nabla \cdot ((\phi_c \mathbf{v} + \mathbf{J}_c)c) = D\nabla \cdot (\tilde{\phi}_c \nabla c), \tag{3.72}$$

$$\partial_t \phi_1 + \mathbf{v} \cdot \nabla \phi_1 = \nabla \cdot (\varepsilon \nabla \mu), \tag{3.73}$$

$$\mu = \frac{\partial_{\phi_1} W_{\mathrm{dw}}(\phi_1)}{\varepsilon} - \varepsilon \Delta \phi_1. \tag{3.74}$$

Note that equation (3.72) does not couple back to the other equations, it is just an advection-diffusion equation for the ion concentration c.

Let us calculate

$$\mathbf{J}_f = \rho_1 \mathbf{J}_1 + \rho_2 \mathbf{J}_2 = -\varepsilon(\rho_1 \nabla \mu - \rho_2 \nabla \mu) = \varepsilon(\rho_2 - \rho_1)\nabla \mu,$$

and

$$\begin{aligned}
\tilde{\mathbf{S}} &= -\mu_2 \nabla \phi_1 - \mu_1 \nabla \phi_2 \\
&= \Sigma_2 \mu \nabla \phi_1 - \Sigma_1 \mu \nabla (1 - \phi_1) \\
&= \sigma_{12} \mu \nabla \phi_1 \\
&= \sigma_{12} \left(\frac{\partial_{\phi_1} W_{\mathrm{dw}}(\phi_1)}{\varepsilon} - \varepsilon \Delta \phi_1 \right) \nabla \phi_1
\end{aligned}$$

$$= \sigma_{12} \left(\frac{\nabla W_{\mathrm{dw}}(\phi_1)}{\varepsilon} + \varepsilon \nabla \left(\frac{|\nabla \phi_1|^2}{2} \right) - \varepsilon \nabla \cdot (\nabla \phi_1 \otimes \nabla \phi_1) \right).$$

We can absorb the first two terms by defining a modified pressure $\hat{p}$. Overall, the momentum equation can now be expressed as

$$\begin{aligned} &\partial_t(\tilde{\rho}_f \mathbf{v}) + \nabla \cdot (\rho_f \mathbf{v} \otimes \mathbf{v}) + \nabla \cdot ((\rho_2 - \rho_1)\varepsilon \nabla \mu \otimes \mathbf{v}) + \nabla \hat{p} \\ &\quad = \nabla \cdot (2\tilde{\gamma}(\boldsymbol{\Phi}) \nabla^s \mathbf{v}) - \sigma_{12} \varepsilon \nabla \cdot (\nabla \phi_1 \otimes \nabla \phi_1). \end{aligned}$$

The system is, except for the δ-modification of $\tilde{\rho}_f$ and $\tilde{\gamma}$, the diffuse-interface model proposed by [Abels, Garcke, et al. 2012] for two-phase flow.

3.2 The Sharp Interface Limit

We use matched asymptotic expansions to show that the formal asymptotic limit of the δ-$2f1s$-model for $\varepsilon \to 0$ is given by the sharp interface formulation (3.1)–(3.14) presented in Section 3.1.1. This technique for the sharp interface limit has been pioneered in [Caginalp and Fife 1988] and is explained in Section 1.3.

We assume now, that away from the interfaces we can write solutions to the δ-$2f1s$-model in terms of outer expansions of the unknowns $\boldsymbol{\Phi}$, $\mathbf{v}$, p, c, μ_1, μ_2, μ_3 as described in Section 1.3. Close to the interfaces we assume the existence of inner expansions in the same unknowns.

Analogous to Section 2.2 an important choice of scaling is $\delta = \varepsilon / L_{\mathrm{ref}}$, with a characteristic length scale L_{ref} independent of ε. With this choice the δ-modifications vanish in the sharp interface limit $\varepsilon \to 0$. Note that also the structure of the triple-well function $W(\boldsymbol{\Phi})$ now depends on ε. For ease of presentation we set $L_{\mathrm{ref}} = 1$.

We are interested in a regime of solutions where bulk phases, characterized through small gradients in the phase field parameter $\boldsymbol{\Phi}$, are separated by interfaces. In this regime we assume that μ_i is only of order $O(1)$, not of order $O(\varepsilon^{-1})$. This can be expected on

an $O(1)$-timescale, for a detailed discussion, see [Pego and Penrose 1989]. In this regime we also assume that the three bulk phases meet in the two-dimensional case at isolated points, called triple points. In the three-dimensional case they meet at curves, called contact lines.

We assume that we have classical solutions of the δ-$2f1s$-model with finite free energy (3.53). This implies in particular $\phi_i \in (-\delta, 1+\delta)$.

The minimizers of the Ginzburg–Landau free energy (3.40) that connect $\boldsymbol{\Phi} = \mathbf{e}_i$ with $\boldsymbol{\Phi} = \mathbf{e}_j$ only attain values along the edge between $\mathbf{e}_i$ and $\mathbf{e}_j$ because we followed the construction in [Boyer and Lapuerta 2006]. As in [Dunbar et al. 2019] we therefore assume that there are no third-phase contributions in the interfacial layers. See (3.76) below for the exact formulation of this assumption.

We first investigate the bulk phases of the system. For the interfaces between two phases we need to investigate leading order terms and first order terms of the inner expansions. In particular, we recover all transmission conditions between the phases as introduced in Section 3.1.1. Finally, we consider the triple point by a special expansion.

3.2.1 Outer Expansions

Expansion of (3.50)*,* $O(\varepsilon^{-1})$*:* We first note that $\phi_i^{\text{out}}(0,\cdot) \in [0,1]$, as otherwise a small ε would result in $W(\boldsymbol{\Phi}^{\text{out}}) = \infty$. With some lengthy calculations we find that stable solutions to the leading order are exactly the local minima of W on the plane $\sum_i \phi_i = 1$ as seen in Figure 3.3. Solutions are therefore the pure phases $\boldsymbol{\Phi}_0^{\text{out}} = \mathbf{e}_k$, $k \in \{1,2,3\}$. Additionally, we get from terms containing the diverging function ℓ in (3.20) the restriction $\phi_{i,1}^{\text{out}}, \phi_{j,1}^{\text{out}} \geq 0$, $\phi_{k,1}^{\text{out}} \leq 0$ $(i \neq j \neq k \neq i)$. The set of points where $\boldsymbol{\Phi}_0^{\text{out}} = \mathbf{e}_k$ corresponds to the bulk domain Ω_k of the sharp interface formulation described in Section 3.1.1.

Expansion of (3.45)*,* $O(1)$*:* Recall the definition of ϕ_f in (3.41). For the case $\boldsymbol{\Phi}_0^{\text{out}} = \mathbf{e}_3$ we do not retrieve any equation because $\phi_f = O(\varepsilon)$. Otherwise, we get

$$\nabla \cdot \mathbf{v}_0^{\text{out}} = 0,$$

which is equation (3.1) of the sharp interface formulation.

Expansion of (3.47)*,* $O(1)$*:* In the case $\boldsymbol{\Phi}_0^{\text{out}} = \mathbf{e}_1$ we have $\tilde{\phi}_c = 1 + O(\varepsilon)$. Also note that $q(\boldsymbol{\Phi}^{\text{out}}) = O(\varepsilon^2)$, as both $q(\boldsymbol{\Phi}_0^{\text{out}}) = 0$ and $\partial_{\phi_i} q(\boldsymbol{\Phi}_0^{\text{out}}) = 0$ for $i \in \{1, 2, 3\}$. With this we find

$$R_c = -c^* \frac{q(\boldsymbol{\Phi}^{\text{out}})}{\varepsilon} (r(c^{\text{out}}) + \tilde{\alpha}\mu_1^{\text{out}} - \tilde{\alpha}\mu_3^{\text{out}}) = O(\varepsilon).$$

The leading order terms of (3.47) are therefore

$$\partial_t c_0^{\text{out}} + \nabla \cdot (\mathbf{v}_0^{\text{out}} c_0^{\text{out}}) = D\Delta c_0^{\text{out}},$$

which is equation (3.3) of the sharp interface formulation. In the other cases $\boldsymbol{\Phi}_0^{\text{out}} = \mathbf{e}_2$, $\boldsymbol{\Phi}_0^{\text{out}} = \mathbf{e}_3$ we do not recover any equation.

Note that in Chapter 8 we will make a choice with $q(\boldsymbol{\Phi}) = 0$ in a neighborhood of the pure phases, to ensure that R_c vanishes, even if the reaction term $r(c^{\text{out}})$ scales as ε^{-1}.

Expansion of (3.46)*,* $O(1)$*:* For $\boldsymbol{\Phi}_0^{\text{out}} = \mathbf{e}_1$ or $\boldsymbol{\Phi}_0^{\text{out}} = \mathbf{e}_2$ we have $\tilde{\phi}_f = 1 + O(\varepsilon)$. With this we can expand the surface tension term $\tilde{\mathbf{S}}$ as

$$\begin{aligned}\tilde{\mathbf{S}} &= -\mu_{2,0}^{\text{out}} \varepsilon \nabla \phi_{1,1}^{\text{out}} - \mu_{1,0}^{\text{out}} \varepsilon \nabla \phi_{2,1}^{\text{out}} \\ &\quad - 2\varepsilon \phi_{3,0}^{\text{out}} \nabla(\mu_{3,0}^{\text{out}} - \mu_{1,0}^{\text{out}} - \mu_{2,0}^{\text{out}}) + O(\varepsilon^2) \\ &= O(\varepsilon).\end{aligned}$$

Analogous to R_c above we also have $R_f = O(\varepsilon)$ and by construction $d(\phi_f, \varepsilon) = O(\varepsilon)$. We retrieve the momentum equations (3.2), e.g. for $\boldsymbol{\Phi}_0^{\text{out}} = \mathbf{e}_1$

$$\partial_t(\rho_1 \mathbf{v}_0^{\text{out}}) + \nabla \cdot (\mathbf{v}_0^{\text{out}} \otimes (\rho_1 \mathbf{v}_0^{\text{out}})) + \nabla p_0^{\text{out}} = \nabla \cdot (2\gamma(\boldsymbol{\Phi}_0^{\text{out}}) \nabla^s \mathbf{v}_0^{\text{out}}).$$

On the other hand, for $\boldsymbol{\Phi}_0^{\text{out}} = \mathbf{e}_3$ the highest order terms result in

$$\nabla \cdot (2\gamma(\boldsymbol{\Phi}_0^{\text{out}}) \nabla^s \mathbf{v}_0^{\text{out}}) - \rho_3 d(0, \varepsilon) \mathbf{v}_0^{\text{out}} = 0,$$

which is equation (3.4) of the sharp interface formulation.

3.2.2 Inner Expansions, Leading Order

As seen in Section 3.2.1, there are three stable phases, namely $\boldsymbol{\Phi}_0^{\text{out}} = \mathbf{e}_1, \mathbf{e}_2, \mathbf{e}_3$. We therefore need to focus on the interfaces between these phases. To do so, we introduce

$$\Gamma_{ij}(t) = \left\{ \mathbf{x} \in \Omega : \phi_i(t, \mathbf{x}) = \phi_j(t, \mathbf{x}), \phi_i(t, \mathbf{x}) > 1/3 \right\}. \tag{3.75}$$

By our assumption, Γ_{ij} is a smooth $(d-1)$-dimensional manifold embedded in Ω and depending on time. We can apply the technique described in Section 1.3 to construct inner expansions of the unknowns $\boldsymbol{\Phi}$, $\mathbf{v}$, p, c, μ_1, μ_2, μ_3 for each of the three interfaces Γ_{12}, Γ_{13} and Γ_{23}.

Expansion of (3.50), $O(\varepsilon^{-1})$*:* As discussed at the beginning of Section 3.2 we assume no third-phase contributions in the interfacial layer. In detail, this means that at the interface Γ_{ij} we assume $\phi_{k,0}^{\text{in}} = 0$, where $k \neq i, k \neq j$ is the index of the third phase. We get

$$\phi_{i,0}^{\text{in}} + \phi_{j,0}^{\text{in}} = 1. \tag{3.76}$$

The leading order expansion of (3.50) for the third phase k reads

$$0 = (\Sigma_k - \Sigma_T)\ell'(\phi_{k,1}^{\mathrm{in}}) - \Sigma_T W'_{\mathrm{dw}}(\phi_{i,0}^{\mathrm{in}}) - \Sigma_T W'_{\mathrm{dw}}(\phi_{j,0}^{\mathrm{in}}).$$

As $\phi_{i,0}^{\mathrm{in}} + \phi_{j,0}^{\mathrm{in}} = 1$ we conclude $\ell'(\phi_{k,1}^{\mathrm{in}}) = 0$ and with this $\phi_{k,1}^{\mathrm{in}} \geq 0$. The asymptotic expansion of (3.50) for phase j results in

$$\begin{aligned} 0 &= \left(\Sigma_j - \Sigma_T\right) W'_{\mathrm{dw}}(\phi_{j,0}^{\mathrm{in}}) - \Sigma_T W'_{\mathrm{dw}}(\phi_{i,0}^{\mathrm{in}}) - \Sigma_T \ell'(\phi_{k,1}^{\mathrm{in}}) - \Sigma_j \partial_{zz}\phi_{j,0}^{\mathrm{in}} \\ &= \Sigma_j \left(W'_{\mathrm{dw}}(\phi_{j,0}^{\mathrm{in}}) - \partial_{zz}\phi_{j,0}^{\mathrm{in}}\right). \end{aligned} \tag{3.77}$$

The matching condition (1.28) implies $\phi_{j,0}^{\mathrm{in}}(-\infty) = 0$ and $\phi_{j,0}^{\mathrm{in}}(\infty) = 1$. Following from the definition of Γ_{ij} in (3.75) we also get $\phi_{j,0}^{\mathrm{in}}(0) = \frac{1}{2}$. With a lengthy calculation we find the unique solution to (3.77), implicitly given by

$$z = \frac{1}{30}\left(\frac{1}{1-\phi_{j,0}^{\mathrm{in}}} - \frac{1}{\phi_{j,0}^{\mathrm{in}}} + 2\log\left(\frac{\phi_{j,0}^{\mathrm{in}}}{1-\phi_{j,0}^{\mathrm{in}}}\right)\right). \tag{3.78}$$

Note that if we multiply (3.77) by $\partial_z \phi_{j,0}^{\mathrm{in}}$, integrate and use the matching conditions (1.28), (1.29) we find the equipartition of energy

$$W_{\mathrm{dw}}(\phi_{j,0}^{\mathrm{in}}) = \frac{1}{2}\left(\partial_z \phi_{j,0}^{\mathrm{in}}\right)^2. \tag{3.79}$$

The leading order expansion of the Ginzburg–Landau free energy (3.40) reads

$$\begin{aligned} &f(\boldsymbol{\Phi}^{\mathrm{in}}, \nabla\boldsymbol{\Phi}^{\mathrm{in}}) \\ &\quad = \varepsilon^{-1} W(\boldsymbol{\Phi}_0^{\mathrm{in}}) + \varepsilon^{-1}\Sigma_i \frac{1}{2}(\partial_z \phi_{i,0}^{\mathrm{in}})^2 + \varepsilon^{-1}\Sigma_j \frac{1}{2}(\partial_z \phi_{j,0}^{\mathrm{in}})^2 + O(1) \\ &\quad = \varepsilon^{-1}(\Sigma_i + \Sigma_j)\left(W_{\mathrm{dw}}(\phi_{j,0}^{\mathrm{in}}) + \frac{1}{2}(\partial_z \phi_{j,0}^{\mathrm{in}})^2\right) + O(1). \end{aligned}$$

We can define the surface energy σ_{ij} as the integral over the Ginzburg–Landau free energy,

$$\begin{aligned}\sigma_{ij} :&= \int_{-\infty}^{\infty} (\Sigma_i + \Sigma_j) \left(W_{\mathrm{dw}}(\phi_{j,0}^{\mathrm{in}}) + \frac{1}{2}(\partial_z \phi_{j,0}^{\mathrm{in}})^2 \right) dz \\ &= (\Sigma_i + \Sigma_j) \int_{-\infty}^{\infty} 2W_{\mathrm{dw}}(\phi_{j,0}^{\mathrm{in}})\, dz \\ &= (\Sigma_i + \Sigma_j) \int_0^1 \sqrt{2W_{\mathrm{dw}}(\phi_{j,0}^{\mathrm{in}})}\, d\phi_{j,0}^{\mathrm{in}} \\ &= \Sigma_i + \Sigma_j,\end{aligned} \tag{3.80}$$

where we have used (3.79), a coordinate transformation and an explicit calculation after inserting (3.20).

Expansion of (3.45)*,* $O(\varepsilon^{-1})$*:* Using the transformation rules, the leading order is

$$\partial_z(\phi_{f,0}^{\mathrm{in}} \mathbf{v}_0^{\mathrm{in}}) \cdot \mathbf{n} = 0.$$

Note that with the considerations above, we have $\phi_{f,0}^{\mathrm{in}} = \phi_{1,0}^{\mathrm{in}} + \phi_{2,0}^{\mathrm{in}} > 0$ across all interfaces. For Γ_{12} we find by integrating and using matching condition (1.28)

$$\mathbf{v}_0^{\mathrm{in}}(z) \cdot \mathbf{n} = \mathbf{v}_0^{\mathrm{out}}(t, \mathbf{x}_+) \cdot \mathbf{n} = \mathbf{v}_0^{\mathrm{out}}(t, \mathbf{x}_-) \cdot \mathbf{n} \quad \forall z \in (-\infty, \infty), \tag{3.81}$$

while for Γ_{13} and Γ_{23} we find with $\phi_{f,0}^{\mathrm{in}}(\infty) = 0$

$$\mathbf{v}_0^{\mathrm{in}}(z) \cdot \mathbf{n} = \mathbf{v}_0^{\mathrm{out}}(t, \mathbf{x}_-) \cdot \mathbf{n} = 0 \quad \forall z \in (-\infty, \infty). \tag{3.82}$$

This is equation (3.8) of the sharp interface formulation.

Expansion of (3.47)*,* $O(\varepsilon^{-2})$*:* We only consider the cases of Γ_{12} and Γ_{13}. Then $\tilde{\phi}_c^{\mathrm{in}} = \phi_{1,0}^{\mathrm{in}} + O(\varepsilon)$ and $\phi_{1,0}^{\mathrm{in}} > 0$. We note that R_c is

of order ε^{-1}. Therefore, we have in leading order

$$\partial_z(\phi_{1,0}^{\text{in}}\partial_z c_0^{\text{in}}) = 0.$$

Then the matching conditions (1.28), (1.29) at $z = -\infty$ imply

$$c_0^{\text{in}}(z) = c_0^{\text{out}}(t, \mathbf{x}_-) \quad \forall z \in (-\infty, \infty). \tag{3.83}$$

Expansion of (3.46)*,* $O(\varepsilon^{-2})$*:* Again, note that R_f is of order ε^{-1}. Expanding the surface tension term $\tilde{\mathbf{S}}$ we find

$$\begin{aligned}\tilde{\mathbf{S}} &= \varepsilon^{-1}\left(-\mu_{2,0}^{\text{in}}\phi_{f,0}^{\text{in}}\partial_z\left(\frac{\phi_{1,0}^{\text{in}}}{\phi_{f,0}^{\text{in}}}\right) - \mu_{1,0}^{\text{in}}\phi_{f,0}^{\text{in}}\partial_z\left(\frac{\phi_{2,0}^{\text{in}}}{\phi_{f,0}^{\text{in}}}\right)\right)\mathbf{n} + O(1)\\ &= O(\varepsilon^{-1}).\end{aligned}$$

With this the leading order expansion of (3.46) is

$$\begin{aligned}0 &= \partial_z\Big(\gamma(\boldsymbol{\Phi}_0^{\text{in}})((\partial_z\mathbf{v}_0^{\text{in}})\otimes\mathbf{n} + \mathbf{n}\otimes(\partial_z\mathbf{v}_0^{\text{in}}))\Big)\mathbf{n}\\ &= \partial_z(\gamma(\boldsymbol{\Phi}_0^{\text{in}})\partial_z\mathbf{v}_0^{\text{in}}).\end{aligned}$$

To get to the second line we have used that (3.81), (3.82) imply $\partial_z\mathbf{v}_0^{\text{in}}\cdot\mathbf{n} = 0$. Integrating and using the matching condition (1.29) gives

$$0 = \gamma(\boldsymbol{\Phi}_0^{\text{in}})\partial_z\mathbf{v}_0^{\text{in}}.$$

As $\gamma(\boldsymbol{\Phi}_0^{\text{in}})$ is positive, we find

$$\partial_z\mathbf{v}_0^{\text{in}} = 0. \tag{3.84}$$

With matching condition (1.28) we conclude

$$\mathbf{v}_0^{\text{in}}(z) = \mathbf{v}_0^{\text{out}}(t, \mathbf{x}_-) = \mathbf{v}_0^{\text{out}}(t, \mathbf{x}_+) \quad \forall z \in (-\infty, \infty). \tag{3.85}$$

This equation is the continuity of $\mathbf{v}$, given by (3.5), in the sharp interface formulation.

Expansion of (3.48), (3.49), $O(\varepsilon^{-1})$*:* We consider the interface Γ_{13}. We obtain for the phase field equations (3.49) for phase 3 and (3.48) for phase 1 in leading order

$$-\nu\partial_z\phi^{\text{in}}_{3,0} - \frac{1}{\Sigma_3}\partial_{zz}\mu^{\text{in}}_{3,0} = q(\boldsymbol{\Phi}^{\text{in}}_0)\left(r(c^{\text{in}}_0) + \tilde{\alpha}_0\mu^{\text{in}}_{1,0} - \tilde{\alpha}_0\mu^{\text{in}}_{3,0}\right),$$
$$-\nu\partial_z\phi^{\text{in}}_{1,0} - \frac{1}{\Sigma_1}\partial_{zz}\mu^{\text{in}}_{1,0} = -q(\boldsymbol{\Phi}^{\text{in}}_0)\left(r(c^{\text{in}}_0) + \tilde{\alpha}_0\mu^{\text{in}}_{1,0} - \tilde{\alpha}_0\mu^{\text{in}}_{3,0}\right).$$

Note that by (3.55) we have $\tilde{\alpha} = \alpha + O(\varepsilon)$. With the notation $\mu_{3-1} := \mu^{\text{in}}_{3,0} - \mu^{\text{in}}_{1,0}$ we get

$$\begin{aligned}-\nu\Sigma_3\partial_z\phi^{\text{in}}_{3,0} + \nu\Sigma_1\partial_z\phi^{\text{in}}_{1,0} - \partial_{zz}\mu_{3-1}\\ = (\Sigma_1+\Sigma_3)q(\boldsymbol{\Phi}^{\text{in}}_0)\left(r(c^{\text{in}}_0) - \alpha\mu_{3-1}\right).\end{aligned}$$

As there are no third-phase contributions in leading order we have $\partial_z\phi^{\text{in}}_{1,0} + \partial_z\phi^{\text{in}}_{3,0} = 0$. By construction of q (see Remark 3.8) and the equipartition of energy (3.79) it holds $q(\boldsymbol{\Phi}^{\text{in}}_0) = \partial_z\phi^{\text{in}}_{3,0}$. We have

$$-\nu(\Sigma_3+\Sigma_1)\partial_z\phi^{\text{in}}_{3,0} - \partial_{zz}\mu_{3-1} = (\Sigma_1+\Sigma_3)\partial_z\phi^{\text{in}}_{3,0}\left(r(c^{\text{in}}_0) - \alpha\mu_{3-1}\right). \tag{3.86}$$

We interpret (3.86) as an ordinary differential equation for μ_{3-1}. From the matching condition (1.29) we get the asymptotic boundary conditions $\partial_z\mu_{3-1}(-\infty) = \partial_z\mu_{3-1}(\infty) = 0$. Now we need to distinguish between the cases $\alpha = 0$ and $\alpha > 0$.

For $\alpha = 0$, integrating over equation (3.86) results in

$$-\nu(\Sigma_3+\Sigma_1) = (\Sigma_3+\Sigma_1)r(c^{\text{in}}_0). \tag{3.87}$$

This is a compatibility condition for the existence of solutions to (3.86) (note that $r(c^{\text{in}}_0)$ is constant because of (3.83)). When fulfilled, any constant function is a solution to (3.86).

For $\alpha > 0$ consider first the homogeneous part of (3.86),

$$\Big(-\partial_{zz} + (\Sigma_1+\Sigma_3)(\partial_z\phi^{\text{in}}_{3,0})\alpha\Big)\mu = 0.$$

This allows only for the solution $\mu = 0$. Therefore, the unique solution to (3.86) is given by

$$\mu_{3-1}(z) = \frac{1}{\alpha}(\nu + r(c_0^{\text{in}})).$$

Rearranging this, we can express the velocity of the interface as

$$\nu = \alpha\mu_{3-1}(z) - r(c_0^{\text{in}}). \tag{3.88}$$

Note that this expression also holds true for the case $\alpha = 0$, following from (3.87).

Expansion of (3.48)*,* $O(\varepsilon^{-1})$*:* Consider Γ_{23}. Arguing similar as above we find that the leading order expansion

$$-\nu\partial_z\phi_{2,0}^{\text{in}} - \frac{1}{\Sigma_1}\partial_{zz}\mu_{2,0}^{\text{in}} = 0$$

allows for each constant function $\mu_{2,0}^{\text{in}}$ as a solution, as long as the compatibility condition

$$\nu = 0 \tag{3.89}$$

is fulfilled. With the same argument applied to the equation for ϕ_1 we conclude $\mu_{1,0}^{\text{in}}$ to be constant.

The compatibility condition (3.89) corresponds to (3.11) in the sharp interface formulation.

Expansion of (3.48)*,* $O(\varepsilon^{-1})$*:* Consider Γ_{12}. Analogous to the result above we get the compatibility condition

$$\nu = \mathbf{v}_0^{\text{in}} \cdot \mathbf{n}, \tag{3.90}$$

and all constant functions $\mu_{1,0}^{\text{in}}$, $\mu_{2,0}^{\text{in}}$ are solutions.

The compatibility condition (3.90) corresponds to (3.6) in the sharp interface formulation.

3.2.3 Inner Expansions, First Order

Expansion of (3.47), $O(\varepsilon^{-1})$*:* We only consider the interfaces Γ_{12} and Γ_{13}. Substituting (3.33), (3.54) and the inner expansions we obtain with (3.83)

$$\begin{aligned} &-\nu\partial_z(\phi^{\text{in}}_{1,0}c^{\text{in}}_0) + \partial_z(\phi^{\text{in}}_{1,0}c^{\text{in}}_0\mathbf{v}^{\text{in}}_0)\cdot\mathbf{n} - \frac{1}{\Sigma_1}\partial_z(c^{\text{in}}_0\partial_z\mu^{\text{in}}_{1,0}) \\ &\quad = D\partial_z(\phi^{\text{in}}_{1,0}\partial_z c^{\text{in}}_1) - c^* q(\boldsymbol{\Phi}^{\text{in}}_0)(r(c^{\text{in}}_0) + \alpha\mu^{\text{in}}_{1,0} - \alpha\mu^{\text{in}}_{3,0}). \end{aligned} \tag{3.91}$$

In the case of the fluid–solid interface Γ_{13} we have $\mathbf{v}^{\text{in}}_0\cdot\mathbf{n} = 0$ and $q(\boldsymbol{\Phi}^{\text{in}}_0) = \sqrt{2W_{\text{dw}}(\phi^{\text{in}}_{1,0})} = \partial_z\phi^{\text{in}}_{3,0}$, so by integrating we conclude

$$\nu c^{\text{in}}_0 = -D\partial_z c^{\text{in}}_1(-\infty) - c^*(r(c^{\text{in}}_0) + \alpha\mu^{\text{in}}_{1,0} - \alpha\mu^{\text{in}}_{3,0}).$$

With (3.88) and matching condition (1.30) we get

$$\nu(c^* - c^{\text{in}}_0) = D\nabla c^{\text{out}}_0(t,\mathbf{x}_-)\cdot\mathbf{n}, \tag{3.92}$$

which describes (3.12) of the sharp interface formulation.

If we consider the fluid–fluid interface Γ_{12} instead, we have $q(\boldsymbol{\Phi}^{\text{in}}_0) = 0$ and conclude from (3.91)

$$c^{\text{in}}_0\Big((\mathbf{v}^{\text{in}}_0\cdot\mathbf{n} - \nu)\partial_z\phi^{\text{in}}_{1,0} - \frac{1}{\Sigma_1}\partial_{zz}\mu^{\text{in}}_{1,0}\Big) = D\partial_z(\phi^{\text{in}}_{1,0}\partial_z c^{\text{in}}_1).$$

With (3.90) and by integrating and matching conditions (1.29), (1.30)

$$0 = \nabla c^{\text{out}}_0(t,\mathbf{x}_-)\cdot\mathbf{n},$$

which corresponds to (3.13) of the sharp interface formulation.

Expansion of (3.50)*,* $O(1)$*:* At an interface Γ_{ij}, consider the difference $\mu_i - \mu_j$. With (3.50) we can write

$$\mu_i - \mu_j = \frac{1}{\varepsilon}\left(\Sigma_i W'_{\mathrm{dw}}(\phi_i) - \Sigma_j W'_{\mathrm{dw}}(\phi_j)\right) - \varepsilon\Sigma_i\Delta\phi_i + \varepsilon\Sigma_j\Delta\phi_j.$$

As $0 < \phi^{\mathrm{in}}_{i,0} < 1$ and $\phi^{\mathrm{in}}_{i,0} + \phi^{\mathrm{in}}_{j,0} = 1$ the $O(1)$ terms of this expansion are given by

$$\begin{aligned}
&\mu^{\mathrm{in}}_{i,0} - \mu^{\mathrm{in}}_{j,0} \\
&\quad = \Sigma_i W''_{\mathrm{dw}}(\phi^{\mathrm{in}}_{i,0})\phi^{\mathrm{in}}_{i,1} - \Sigma_j W''_{\mathrm{dw}}(\phi^{\mathrm{in}}_{j,0})\phi^{\mathrm{in}}_{j,1} \\
&\qquad - \Sigma_i\left(-\kappa\partial_z\phi^{\mathrm{in}}_{i,0} + \partial_{zz}\phi^{\mathrm{in}}_{i,1}\right) + \Sigma_j\left(-\kappa\partial_z\phi^{\mathrm{in}}_{j,0} + \partial_{zz}\phi^{\mathrm{in}}_{j,1}\right) \\
&\quad = \left(W''_{\mathrm{dw}}(\phi^{\mathrm{in}}_{i,0}) - \partial_{zz}\right)\left(\Sigma_i\phi^{\mathrm{in}}_{i,1} - \Sigma_j\phi^{\mathrm{in}}_{i,1}\right) + (\Sigma_i + \Sigma_j)\kappa\partial_z\phi^{\mathrm{in}}_{i,0}.
\end{aligned} \tag{3.93}$$

We want to multiply (3.93) by $\partial_z\phi^{\mathrm{in}}_{i,0}$ and integrate over z. For this we calculate

$$\begin{aligned}
&\int_{-\infty}^{\infty} (\partial_z\phi^{\mathrm{in}}_{i,0})\left(W''_{\mathrm{dw}}(\phi^{\mathrm{in}}_{i,0}) - \partial_{zz}\right)\left(\Sigma_i\phi^{\mathrm{in}}_{i,1} - \Sigma_j\phi^{\mathrm{in}}_{i,1}\right)\,dz \\
&\quad = \int_{-\infty}^{\infty} (\partial_z\phi^{\mathrm{in}}_{i,0})W''_{\mathrm{dw}}(\phi^{\mathrm{in}}_{i,0})\left(\Sigma_i\phi^{\mathrm{in}}_{i,1} - \Sigma_j\phi^{\mathrm{in}}_{i,1}\right) \\
&\qquad\quad - (\partial_{zzz}\phi^{\mathrm{in}}_{i,0})\left(\Sigma_i\phi^{\mathrm{in}}_{i,1} - \Sigma_j\phi^{\mathrm{in}}_{i,1}\right)\,dz \\
&\quad = \int_{-\infty}^{\infty} \partial_z\left(W'_{\mathrm{dw}}(\phi^{\mathrm{in}}_{i,0}) - \partial_{zz}\phi^{\mathrm{in}}_{i,0}\right)\left(\Sigma_i\phi^{\mathrm{in}}_{i,1} - \Sigma_j\phi^{\mathrm{in}}_{i,1}\right)\,dz \\
&\quad = 0,
\end{aligned}$$

where we have used integration by parts, equation (3.77) and matching conditions (1.28), (1.29) to get to the second line. The last equality follows from (3.77). Overall, we get from (3.93)

$$\int_{-\infty}^{\infty} (\mu^{\mathrm{in}}_{i,0} - \mu^{\mathrm{in}}_{j,0})\partial_z\phi^{\mathrm{in}}_{i,0}\,dz = \int_{-\infty}^{\infty} (\Sigma_i + \Sigma_j)\kappa(\partial_z\phi^{\mathrm{in}}_{i,0})^2\,dz.$$

Using the definition of σ_{ij} in (3.80) and the fact that $\mu^{\mathrm{in}}_{i,0} - \mu^{\mathrm{in}}_{j,0}$

does not depend on z (for Γ_{13} see (3.88), for Γ_{23} and Γ_{12} see the expansions of (3.48), $O(\varepsilon^{-1})$) we find

$$\mu_{j,0}^{\text{in}} - \mu_{i,0}^{\text{in}} = (\Sigma_i + \Sigma_j)\kappa = \sigma_{ij}\kappa. \tag{3.94}$$

With this the compatibility condition (3.88) for the reactive interface Γ_{13} reads

$$\nu = \alpha\sigma_{13}\kappa - r(c_0^{\text{in}}), \tag{3.95}$$

which is the interface condition (3.10) of the sharp interface formulation.

Expansion of (3.46), $O(\varepsilon^{-1})$*:* Let us look at the case of the fluid–fluid interface Γ_{12}. Condition (3.84) simplifies the analysis. In particular, we have

$$\begin{aligned}\nabla\cdot(2\tilde{\gamma}(\boldsymbol{\Phi}^{\text{in}})\nabla^s\mathbf{v}) = \frac{1}{\varepsilon}\partial_z\Big(\gamma(\boldsymbol{\Phi}_0^{\text{in}})\Big((\partial_z\mathbf{v}_1^{\text{in}})\otimes\mathbf{n} + \nabla_\Gamma\mathbf{v}_0^{\text{in}} \\ + \mathbf{n}\otimes(\partial_z\mathbf{v}_1^{\text{in}}) + (\nabla_\Gamma\mathbf{v}_0^{\text{in}})^\top\Big)\Big)\mathbf{n} + O(1),\end{aligned} \tag{3.96}$$

and the surface tension

$$\tilde{\mathbf{S}} = \frac{1}{\varepsilon}\left(-\mu_{2,0}^{\text{in}}\partial_z\phi_{1,0}^{\text{in}} - \mu_{1,0}^{\text{in}}\partial_z\phi_{2,0}^{\text{in}}\right)\mathbf{n} + O(1) = O(\varepsilon).$$

With this, equation (3.46) at order $O(\varepsilon^{-1})$ reads as

$$\begin{aligned}&-\nu\partial_z(\rho_{f,0}^{\text{in}}\mathbf{v}_0^{\text{in}}) + (\partial_z\rho_{f,0}^{\text{in}})(\mathbf{n}\cdot\mathbf{v}_0^{\text{in}})\mathbf{v}_0^{\text{in}} + \partial_z p_0^{\text{in}}\mathbf{n} \\ &\quad + \mu_{2,0}^{\text{in}}\partial_z\phi_{1,0}^{\text{in}}\mathbf{n} + \mu_{1,0}^{\text{in}}\partial_z\phi_{2,0}^{\text{in}}\mathbf{n} \\ &= \partial_z\Big(\gamma(\boldsymbol{\Phi}_0^{\text{in}})((\partial_z\mathbf{v}_1^{\text{in}})\otimes\mathbf{n} + \nabla_\Gamma\mathbf{v}_0^{\text{in}} + \mathbf{n}\otimes(\partial_z\mathbf{v}_1^{\text{in}}) + (\nabla_\Gamma\mathbf{v}_0^{\text{in}})^\top)\Big)\mathbf{n}.\end{aligned}$$

With (3.90) the first two terms cancel out. Using the fact that $\mu_{1,0}^{\text{in}}$ and $\mu_{2,0}^{\text{in}}$ are constant, integrating over z and applying matching

condition (1.31) yields

$$[\![p]\!]\mathbf{n} + \mu_{1,0}^{\text{in}}\mathbf{n} - \mu_{2,0}^{\text{in}}\mathbf{n} = [\![\gamma(\boldsymbol{\Phi}_0^{\text{out}})(\nabla \mathbf{v}_0^{\text{out}} + (\nabla \mathbf{v}_0^{\text{out}})^\top)]\!]\mathbf{n}.$$

We use (3.94) to conclude the interface condition

$$[\![pI - 2\gamma \nabla^s \mathbf{v}_0^{\text{out}}]\!]\mathbf{n} = \sigma_{12}\kappa\mathbf{n},$$

corresponding to (3.7) of the sharp interface formulation.

Expansion of (3.46)$\cdot\boldsymbol{\tau}$, $O(\varepsilon^{-1})$*:* Finally, for the fluid–solid interface Γ_{13}, we again use conditions (3.84) and (3.96). With this, equation (3.46) at order $O(\varepsilon^{-1})$ reads as

$$\begin{aligned}
&-\nu\partial_z(\rho_{f,0}^{\text{in}}\mathbf{v}_0^{\text{in}}) + \phi_{f,0}^{\text{in}}\partial_z p_0^{\text{in}}\mathbf{n} \\
&\quad - \mu_{2,0}^{\text{in}}\phi_{f,0}^{\text{in}}\partial_z\left(\frac{\phi_{1,0}^{\text{in}}}{\widetilde{\phi}_{f,0}^{\text{in}}}\right)\mathbf{n} - \mu_{1,0}^{\text{in}}\phi_{f,0}^{\text{in}}\partial_z\left(\frac{\phi_{2,0}^{\text{in}}}{\widetilde{\phi}_{f,0}^{\text{in}}}\right)\mathbf{n} \\
=&\partial_z\Big(\gamma(\boldsymbol{\Phi}_0^{\text{in}})((\partial_z\mathbf{v}_1^{\text{in}})\otimes\mathbf{n} + \nabla_\Gamma\mathbf{v}_0^{\text{in}} + \mathbf{n}\otimes(\partial_z\mathbf{v}_1^{\text{in}}) + (\nabla_\Gamma\mathbf{v}_0^{\text{in}})^\top)\Big)\mathbf{n} \\
&\quad + \frac{1}{2}\rho_1\mathbf{v}_0^{\text{in}}q(\boldsymbol{\Phi}_0^{\text{in}})\nu,
\end{aligned}$$

where we used (3.88), for the reaction term. We only consider the tangential component of this equation. For this, we multiply with an arbitrary vector $\boldsymbol{\tau} \perp \mathbf{n}$ and get

$$\begin{aligned}
&-\nu\partial_z(\rho_{f,0}^{\text{in}}\mathbf{v}_0^{\text{in}}\cdot\boldsymbol{\tau}) \\
=&\boldsymbol{\tau}\partial_z\Big(\gamma(\boldsymbol{\Phi}_0^{\text{in}})((\partial_z\mathbf{v}_1^{\text{in}})\otimes\mathbf{n} + \nabla_\Gamma\mathbf{v}_0^{\text{in}} + \mathbf{n}\otimes(\partial_z\mathbf{v}_1^{\text{in}}) + (\nabla_\Gamma\mathbf{v}_0^{\text{in}})^\top)\Big)\mathbf{n} \\
&\quad + \frac{1}{2}\nu\rho_1\partial_z\phi_{3,0}^{\text{in}}\mathbf{v}_0^{\text{in}}\cdot\boldsymbol{\tau}.
\end{aligned}$$

Integrating and using (1.28) and (1.31) we get the interface condition

$$\frac{1}{2}\nu\rho_1\mathbf{v}_0^{\text{out}}\cdot\boldsymbol{\tau} = [\![2\gamma\boldsymbol{\tau}(\nabla^s\mathbf{v}_0^{\text{out}})\mathbf{n}]\!], \tag{3.97}$$

which is condition (3.9) of the sharp interface formulation for Γ_{13}. For Γ_{23} the analogous calculation only differs by the vanishing reaction term and (3.89). The left-hand side of (3.97) vanishes, but as $\nu = 0$ on Γ_{23} the result (3.97) is valid on both Γ_{13} and Γ_{23}.

We remark that the left-hand side term in (3.97) exists due to the fact that the δ-$2f1s$-model preserves kinetic energy instead of momentum during precipitation and dissolution.

Remark 3.9: *Considering the normal component of* (3.46) *at a fluid–solid interface leads to*

$$\phi_{f,0}^{\mathrm{in}} \partial_z \left(p_0^{\mathrm{in}} - \mu_{2,0}^{\mathrm{in}} \frac{\phi_{1,0}^{\mathrm{in}}}{\tilde{\phi}_{f,0}^{\mathrm{in}}} - \mu_{1,0}^{\mathrm{in}} \frac{\phi_{2,0}^{\mathrm{in}}}{\tilde{\phi}_{f,0}^{\mathrm{in}}} \right) = \partial_z \Big(2\gamma(\boldsymbol{\Phi}_0^{\mathrm{in}}) \partial_z \mathbf{v}_1^{\mathrm{in}} \cdot \mathbf{n} \Big).$$

As we do not expect the right-hand side to vanish, $\phi_{f,0}^{\mathrm{in}} \partial_z p_0^{\mathrm{in}}$ has to balance this term. That means that in the region where $\phi_{f,0}^{\mathrm{in}}$ gets small, the assumption of $\partial_z p_0^{\mathrm{in}} = O(1)$ is no longer valid. Indeed, numerical simulations show that p can oscillate in the solid part of a fluid–solid interface.

3.2.4 Triple Point Expansions

As we have three bulk phases $\boldsymbol{\Phi}_0^{\mathrm{out}} = \mathbf{e}_1, \mathbf{e}_2, \mathbf{e}_3$ there are regions where these three phases meet. In the two-dimensional case we

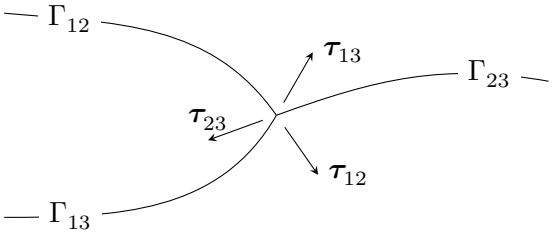

Figure 3.4: Vectors at the triple junction.

assume that the three phases meet at isolated points, called triple points. In the three-dimensional case we assume they meet at curves, called contact lines.

In two dimensions the analysis of the triple points

$$\Gamma_{123}(t) = \{\mathbf{x} \in \Omega : \boldsymbol{\Phi}(t, \mathbf{x}) = (1/3, 1/3, 1/3)^\top\}$$

can be done exactly as in [Bronsard and Reitich 1993; Garcke, Nestler, et al. 1998]. For this one introduces local coordinates around a $\hat{\mathbf{x}} \in \Gamma_{123}$ and assumes that solutions to the δ-$2f1s$-model can be written in terms of *triple point expansions* in these local coordinates. After matching the triple point expansions with the inner expansions of the three interfaces $\Gamma_{12}, \Gamma_{13}, \Gamma_{23}$ one obtains in leading order the condition

$$0 = \sum_{ij \in \{12,13,23\}} \sigma_{ij} \boldsymbol{\tau}_{ij}, \tag{3.98}$$

where $\boldsymbol{\tau}_{ij}$ is the tangential unit vector of Γ_{ij} at $\hat{\mathbf{x}}$, as shown in Figure 3.4.

Condition (3.98) is equivalent to the contact angle condition (3.14) in the sharp interface formulation.

For the three-dimensional case, the analysis of the contact lines can be done exactly as in [Dunbar et al. 2019]. We recover (3.14) on the plane perpendicular to the contact line.

3.3 Discretization and Implementation

We use a Galerkin finite element method on a conforming triangular mesh $\mathcal{T}$ to discretize the δ-$2f1s$-model (3.45)–(3.50) in space. For this we use Taylor–Hood elements [Taylor and Hood 1973] for $\mathbf{v}$ and p, i.e., Lagrange elements of order 2 for the velocity (with zero Dirichlet boundary conditions on $\partial\Omega$) and Lagrange elements of order 1 for the pressure (with zero mean value over Ω). We denote

these spaces by $\mathbf{v} \in (\mathcal{P}_{2,0}(\mathcal{T}))^N$ and by $p \in \mathcal{P}_{1,0}(\mathcal{T})$. For the ion concentration and phase field variables, we discretize with Lagrange elements of order 1 and solve for c, ϕ_1, ϕ_2, μ_1 and μ_2 in $\mathcal{P}_1(\mathcal{T})$. We recover ϕ_3 and μ_3 through the relations (3.19) and (3.52).

For the time discretization, we divide the time interval $[0,T]$ into subintervals $[t_n, t_{n+1}]$, $n = 0, \dots, N_t - 1$ with respective length $\Delta_{t,n} = t_{n+1} - t_n$. Given the values of p^n, $\mathbf{v}^n$, c^n, ϕ_1^n, ϕ_2^n, μ_1^n, μ_2^n at time t_n we search for functions p^{n+1}, $\mathbf{v}^{n+1}$, c^{n+1}, ϕ_1^{n+1}, ϕ_2^{n+1}, μ_1^{n+1}, μ_2^{n+1} in the respective finite element spaces. For this we discretize in time by the implicit Euler method. The weak formulation for the finite element method is then given as follows, and has to be satisfied for all test functions $\check{p} \in \mathcal{P}_{1,0}(\mathcal{T})$, $\check{\mathbf{v}} \in (\mathcal{P}_{2,0}(\mathcal{T}))^N$, $\check{c} \in \mathcal{P}_1(\mathcal{T})$, $\check{\phi}_1 \in \mathcal{P}_1(\mathcal{T})$, $\check{\phi}_2 \in \mathcal{P}_1(\mathcal{T})$, $\check{\mu}_1 \in \mathcal{P}_1(\mathcal{T})$, $\check{\mu}_2 \in \mathcal{P}_1(\mathcal{T})$

$$0 = \int_\Omega \check{p} \nabla \cdot (\tilde{\phi}_f^{n+1} \mathbf{v}^{n+1}) \, dx, \tag{3.99}$$

$$\begin{aligned} 0 = &\int_\Omega \tilde{\rho}_f^{n+1} \frac{\mathbf{v}^{n+1} - \mathbf{v}^n}{\Delta_{t,n}} \cdot \check{\mathbf{v}} \, dx \\ &+ \int_\Omega \left(\left(\left(\rho_f^{n+1} \mathbf{v}^{n+1} + \mathbf{J}_f^{n+1} \right) \cdot \nabla \right) \mathbf{v}^{n+1} \right) \cdot \check{\mathbf{v}} \, dx \\ &+ \int_\Omega \tilde{\phi}_f^{n+1} \nabla p^{n+1} \cdot \check{\mathbf{v}} \, dx + \int_\Omega 2\tilde{\gamma}(\boldsymbol{\Phi}^{n+1}) \nabla^s \mathbf{v}^{n+1} : \nabla \check{\mathbf{v}} \, dx \\ &+ \int_\Omega \rho_3 d(\tilde{\phi}_f^{n+1}, \varepsilon) \mathbf{v}^{n+1} \cdot \check{\mathbf{v}} \, dx - \int_\Omega \tilde{\mathbf{S}}^{n+1} \cdot \check{\mathbf{v}} \\ &+ \int_\Omega \frac{1}{2} \rho_1 R_f^{n+1} \mathbf{v}^{n+1} \cdot \check{\mathbf{v}} \, dx, \end{aligned} \tag{3.100}$$

$$
\begin{aligned}
0 = &\int_\Omega \frac{\tilde{\phi}_c^{n+1}(c^{n+1}-c^*) - \tilde{\phi}_c^{n}(c^{n}-c^*)}{\Delta_{t,n}} \check{c}\, dx \\
&+ \int_\Omega D\tilde{\phi}_c^{n+1} \nabla c^{n+1} \cdot \nabla \check{c}\, dx - \int_\Omega (c^{n+1}-c^*)\mathbf{J}_c^{n+1} \cdot \nabla \check{c}\, dx \\
&+ \int_\Omega \check{c} \nabla \cdot \left(\phi_c^{n+1}\mathbf{v}^{n+1}(c^{n+1}-c^*)\right)\, dx,
\end{aligned}
\tag{3.101}
$$

$$
\begin{aligned}
0 = &\int_\Omega \frac{\phi_i^{n+1}-\phi_i^n}{\Delta_{t,n}} \check{\phi}_i\, dx - \int_\Omega \mathbf{J}_i^{n+1} \cdot \nabla \check{\phi}_i\, dx \\
&+ \int_\Omega \check{\phi}_i \nabla \cdot \left(\phi_i^{n+1}\mathbf{v}^{n+1}\right)\, dx - \int_\Omega R_i^{n+1}\check{\phi}_i\, dx, \qquad i \in \{1,2\},
\end{aligned}
\tag{3.102}
$$

$$
\begin{aligned}
0 = &\int_\Omega \mu_i^{n+1}\check{\mu}_i\, dx - \int_\Omega \frac{\partial_{\phi_i} W(\Phi^{n+1})}{\varepsilon}\check{\mu}_i\, dx \\
&- \int_\Omega \varepsilon\Sigma_i \nabla\phi_i^{n+1}\nabla\check{\mu}_i\, dx, \qquad i \in \{1,2\},
\end{aligned}
\tag{3.103}
$$

together with the closure relations derived from (3.19) and (3.52)

$$
\begin{aligned}
\phi_3^{n+1} &= 1 - \phi_1^{n+1} - \phi_2^{n+1}, \\
\mu_3^{n+1} &= -\Sigma_3\left(\frac{\mu_1^{n+1}}{\Sigma_1} + \frac{\mu_2^{n+1}}{\Sigma_2}\right).
\end{aligned}
$$

Here the terms $\tilde{\phi}_f^{n+1}$, ρ_f^{n+1}, $\tilde{\rho}_f^{n+1}$, $\tilde{\phi}_c^{n+1}$, $\mathbf{J}_c^{n+1}$, $\mathbf{J}_i^{n+1}$, $\mathbf{J}_f^{n+1}$, R_i^{n+1}, $\tilde{\mathbf{S}}^{n+1}$ are to be understood as in their original definitions, with all variables replaced by the finite element functions at time t_{n+1}, e.g.

$$
\begin{aligned}
\tilde{\phi}_f^{n+1} &= \phi_1^{n+1} + \phi_2^{n+1} + 2\delta\phi_3^{n+1}, \\
\mathbf{J}_i^{n+1} &= -\frac{\varepsilon}{\Sigma_i}\nabla\mu_i^{n+1}, \\
R_1^{n+1} &= -\frac{q(\boldsymbol{\Phi}^{n+1})}{\varepsilon}\left(r(c^{n+1}) + \tilde{\alpha}\mu_1^{n+1} - \tilde{\alpha}\mu_3^{n+1}\right),
\end{aligned}
$$

$$\tilde{\mathbf{S}}^{n+1} = -\mu_2^{n+1}\tilde{\phi}_f^{n+1}\nabla\left(\frac{\phi_1^{n+1}}{\tilde{\phi}_f^{n+1}}\right) - \mu_1^{n+1}\tilde{\phi}_f^{n+1}\nabla\left(\frac{\phi_2^{n+1}}{\tilde{\phi}_f^{n+1}}\right) - 2\delta\phi_3^{n+1}\nabla(\mu_3^{n+1} - \mu_1^{n+1} - \mu_2^{n+1}).$$

In comparison to a fully implicit Euler discretization of (3.45)–(3.50), we have made two reformulations of the δ-$2f1s$-model. For the momentum equation (3.100) we first note that from (3.48) we find

$$\partial_t\tilde{\rho}_f + \nabla\cdot(\rho_f\mathbf{v} + \mathbf{J}_f) = \rho_1 R_f.$$

With this we rewrite (3.46) as

$$\tilde{\rho}_f\partial_t\mathbf{v} + ((\rho_f\mathbf{v} + \mathbf{J}_f)\cdot\nabla)\mathbf{v} = -\tilde{\phi}_f\nabla p + \nabla\cdot(2\tilde{\gamma}(\boldsymbol{\Phi})\nabla^s\mathbf{v}) - \rho_3 d(\tilde{\phi}_f,\varepsilon)\mathbf{v} + \tilde{\mathbf{S}} - \frac{1}{2}\rho_1\mathbf{v}R_f.$$

We use an implicit Euler discretization in time to obtain (3.100).

For the ion equation (3.101) we first reformulate the δ-$2f1s$-model so that there is no reaction term in the ion equation. For this we calculate (3.47)-c^*(3.48)

$$\partial_t(\tilde{\phi}_c(c-c^*)) + \nabla\cdot((\phi_c\mathbf{v} + \mathbf{J}_c)(c-c^*)) = D\nabla\cdot(\tilde{\phi}_c\nabla c).$$

Note that this formulation is very similar to the ion balance equation (2.5d) from Chapter 2. We discretize this formulation by implicit Euler to obtain (3.101).

Remark 3.10: *While the continuous δ-$2f1s$-model is equipped with a free energy that is decreasing in time, we can not prove the same for the FEM formulation* (3.99)–(3.103)*. Such energy decreasing schemes exist in literature for Cahn–Hilliard–Navier–Stokes systems (see e.g. [Grün and Klingbeil 2014; Minjeaud 2013]) and are much more intricate in the choice of discretization. The challenge in generalizing these schemes to the δ-$2f1s$ model is to include the fluid–ion mixture energy $g(c)$ and the reaction term $r(c)$, as they both depend non-linear on the ion concentration c.*

We solve the full system (3.99)–(3.103) either monolithically or using an operator splitting between the Navier–Stokes equations (3.99)–(3.100) and the Cahn–Hilliard equations (3.101)–(3.103), i.e., we solve for $\mathbf{v}^{n+1}$ and p^{n+1} while keeping the unknowns c^{n+1}, ϕ_1^{n+1}, ϕ_2^{n+1}, μ_1^{n+1}, μ_2^{n+1} fixed and vice versa. In the case of only one fluid phase present, the coupling between the two operators is rather weak, and the operator splitting scheme usually converges in two to four iterations. As such, it is faster than a monolithic solve of the full system, and we therefore prefer the operator splitting in applications with only one fluid phase (see Chapter 8). With two fluid phases present, there exists a fluid–fluid interface that gets transported with the fluid velocity, and therefore the Navier–Stokes and Cahn–Hilliard operators are coupled much stronger. In this case the monolithic solve is faster than iterating between the two operators.

While we do not prove the existence of solutions to the discrete system (3.99)–(3.103), we find in practice solutions for sufficiently small time step $\Delta_{t,n}$. We employ an adaptive time step, decreasing $\Delta_{t,n}$ in case our numerical solvers do not converge.

The implementation was done in the finite element framework PDELab [Bastian et al. 2010]. This has the advantage that we can use DUNE-ALUGrid [Alkämper et al. 2016] as a grid interface, which provides us with adaptive mesh refinement on an unstructured grid of simplices. We use $\nabla \boldsymbol{\Phi}^n$ as an indicator for refinement, and ensure that at least five grid cells are located across every interface. We solve the resulting non-linear system with Newton's method including the line search strategy, and use the GMRES method to solve the linear system in each Newton step, with ILU factorization as a preconditioner. The development of more suitable block-preconditioners for the linear system based on [Bosch et al. 2018; Garcke, Hinze, and Kahle 2016] should lead to a significant speed-up.

3.4 Numerical Investigation of the Phase Field Model

3.4.1 Nucleus in Channel Flow

For the first numerical example, let us illustrate the capability of the δ-$2f1s$-model. We consider initially a solid nucleus (ϕ_3, red) in a channel flow (ϕ_1, dark blue). Attached is a part of the second fluid phase (ϕ_2, light blue). The initial datum is displayed in Figure 3.5, top left. The upper and lower boundaries are impermeable, with boundary conditions (3.35)–(3.38). The left(right) boundary acts as an inflow(outflow) boundary. Due to a flow from the left, the second fluid phase gets pushed behind the nucleus (see Figure 3.5, top right/bottom left). Because the ion concentration at the inflow boundary is oversaturated, the nucleus begins to grow as can clearly be seen from the last graph in Figure 3.5. The contact angle at the triple junction is constant throughout the simulation, following (3.14). Notably, the new formulation of the Navier-slip condition leads to tangential flow around the nucleus.

3.4.2 Variable Slip Length

Next, we investigate the Navier-slip condition (3.15), (3.16). For this, we construct in $\Omega = [0, 1]^2$ a test case with a planar fluid–solid interface at $x = 1/4$, as shown in Figure 3.6. For the left boundary we impose boundary conditions (3.35)–(3.38), while we impose for the right boundary (3.36)–(3.38) together with the constant tangential velocity $\mathbf{v} = (0, 1)^\top$. The top and bottom boundary are chosen to be periodic. We choose $r(c) \equiv 0$ to have a stationary fluid–solid interface. This setting matches the one dimensional analysis in Section 3.1.1.4.

After a short time, the model evolves into a stationary state with a linear velocity profile in the fluid phase, as shown in Figure 3.6. In Figure 3.7 we plot a cross-section at $y = 1/2$ for two different

choices of $d(0)$. Note in particular that $\mathbf{v}$ decays exponentially in the solid phase, and this can happen over a width larger than ε (see Figure 3.7 on the right-hand side). Of course, the effective fluid flux $\mathbf{v}\phi_f$ still is approximately zero in the solid phase.

With equation (3.16) we can predict the slip length L_{slip} of the model. To compare the predicted slip length with the diffuse interface model, we calculate the velocity profile for a sharp interface at $x = 1/4$, with L_{slip} from (3.16). As seen in Figure 3.7 there is a good agreement between diffuse and sharp interface model, i.e., equation (3.16) predicts the slip length accurately.

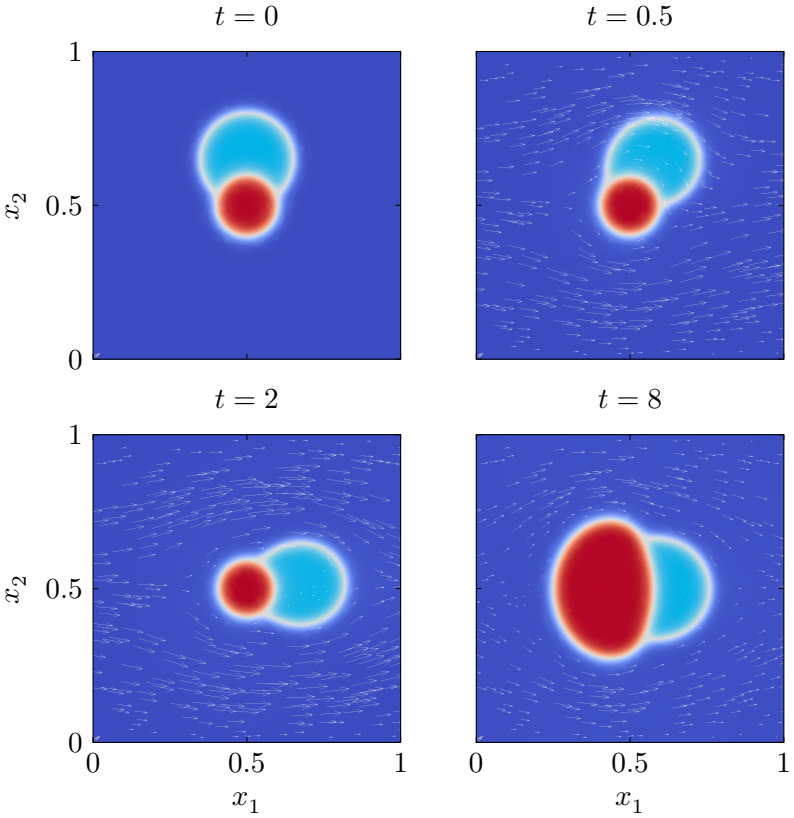

Figure 3.5: Growth of a solid nucleus in a channel flow, with attached fluid phase $\boldsymbol{\Phi} = \mathbf{e}_2$. Top left: initial data, top right: $t = 0.5$, bottom left: $t = 2$, bottom right: $t = 8$.

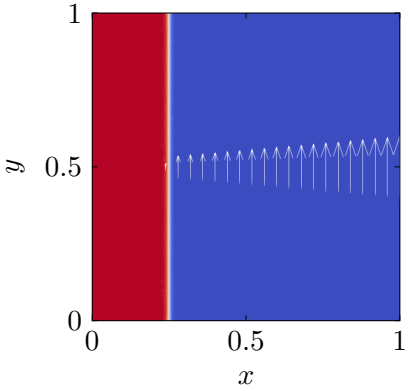

Figure 3.6: Navier-slip at a fluid–solid interface with solid phase (ϕ_3, red) on the left and first fluid phase (ϕ_1, blue) on the right side. The arrows show the fluid velocity $\mathbf{v}$ at the cross-section $y = 1/2$.

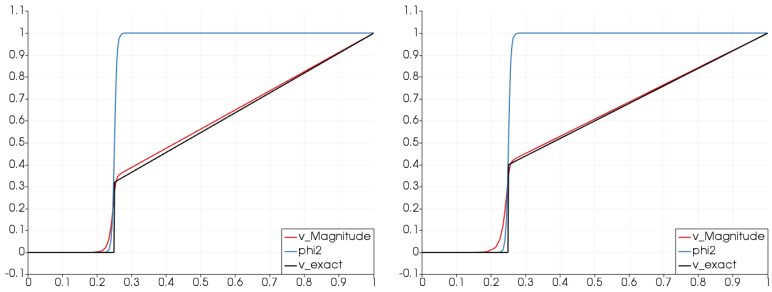

Figure 3.7: Cross-section $y = 0.5$ for $\varepsilon = 0.005$, $\gamma_1 = 0.5$, $\gamma_3 = 0.01$. Left: $d(0) = 400$, right: $d(0) = 200$. Plotted are ϕ_1 in blue, $|\mathbf{v}|$ in red and the velocity for the corresponding sharp interface in black.

The Cahn–Hilliard–Navier–Stokes Model as a Diffuse-Domain Model

4

On the pore-scale, flow induced by non-stationary fluid–fluid interfaces can occur on a time scale much faster than precipitation. For example, in the event of Haines jumps the fluid in pores is displaced in the time of milliseconds [Berg et al. 2013], while in contrast, EICP is changing the pore-scale geometry over several hours (see Chapter 8). This means in particular, that in some events the velocity of fluid–fluid interfaces can be much higher than the velocity of reactive fluid–solid interfaces. While the δ-$2f1s$-model from Chapter 3 is able to describe both flow and precipitation simultaneously, the difference in time scales provides a challenge: To describe the fast moving fluid–fluid interfaces, a high mobility in the Cahn–Hilliard equation is necessary. But then the evolution of fluid–solid interfaces is dominated by the Cahn–Hilliard equation instead of the slower precipitation, resulting e.g. in corners smoothing out over time (see Section 4.3 for an example).

To accommodate for the fast time scale, we propose in this chapter a model for the flow of two immiscible fluids together with a solid phase that does not change in time. For this we modify the δ-$2f1s$-model (3.45)–(3.50) from Chapter 3 to exclude any evolution of the solid phase. The resulting model, called DD-$2f1s$-model, is of diffuse-domain type. It consists of the two-phase Cahn–Hilliard–Navier–Stokes model (1.15)–(1.19) of [Abels, Garcke, et al. 2012] in a domain confined by a diffuse solid boundary.

The vision is to use the δ-$2f1s$-model and the DD-$2f1s$-model in a model-adaptive framework: The δ-$2f1s$-model is used to describe flow and precipitation on a slow time scale. In the case that surface tension effects lead to a fast evolution of fluid–fluid interfaces, one can switch to the DD-$2f1s$-model to describe such events until a stationary configuration of fluid–fluid interfaces is found. As both models describe all interfaces as diffuse interfaces, the phase field vector $\boldsymbol{\Phi}$ can be directly transferred between the models.

When describing a stationary solid phase, there are several advantages of the DD-$2f1s$-model compared to the δ-$2f1s$-model. Firstly, by construction the solid phase is stationary and does not change via Cahn–Hilliard evolution, see Section 4.3 for a comparison. Secondly it reduces the complexity of the model to a binary phase field model, leading to a smaller number of unknowns that have to be solved for. Finally, it allows for a contact angle condition with the angle of the solid phase being 180°. This can only be approximated by the δ-$2f1s$-model, see Section 3.1.1.3.

The idea to formulate the boundary conditions of a partial differential equation on a diffuse boundary leads to the diffuse domain approach of [Li et al. 2009]. Here the differential equation is reformulated on an enlarged domain, and the original boundary conditions are integrated through additional source terms. This method has been refined in recent years [Lervåg and Lowengrub 2015; Yu et al. 2020]. While we do not follow the diffuse domain approach here, our resulting model has many similarities to Cahn–Hilliard–Navier–Stokes models developed in the diffuse domain context.

In [Aland et al. 2010] model H (see (1.8)–(1.11) in the introduction) is formulated in a diffuse domain, using the techniques of [Li et al. 2009]. Analogously, in [Guo et al. 2021] the mass-averaged model by [Lowengrub and Truskinovsky 1998], allowing for different densities of the fluid phases, is formulated using the diffuse domain approach. Notably both models use a fixed contact angle at the boundary. It is not clear whether these models allow for a decreasing free energy. Both models have two phase field parameters ε and ε_ϕ for the Cahn–

Hilliard equation and the diffuse domain respectively. For constant ε and $\varepsilon_\phi \to 0$ model H (1.8)–(1.11) and the model of [Lowengrub and Truskinovsky 1998] are recovered in a sharp domain, but the sharp interface limit $\varepsilon = \varepsilon_\phi \to 0$ can not be shown. In contrast to this, in our model the choice $\varepsilon = \varepsilon_\phi$ is necessary, and we present the sharp interface limit in Section 4.2.

The structure of this chapter is as follows. After we briefly explain the underlying sharp interface ansatz in Section 4.1.1, we modify the δ-$2f1s$-model in Section 4.1.2 to derive the DD-$2f1s$-model. It still allows for a decreasing free energy, as shown in Section 4.1.3. To validate the DD-$2f1s$-model model we investigate the sharp interface limit in Section 4.2 using matched asymptotic expansions. Notably, using an expansion around the triple points we recover Young's equation for the contact angle. We illustrate the capabilities of the DD-$2f1s$-model by a numerical example in Section 4.3 and compare it to the δ-$2f1s$ model.

4.1 Multi-phase Flow in a Diffuse Domain

4.1.1 The Sharp Interface Formulation

In this section we present the free boundary problem underlying the DD-$2f1s$-model. We keep the notation introduced previously in Section 3.1.1. In particular, recall that the three domains $\Omega_1(t)$, $\Omega_2(t)$, Ω_3 are separated by the fluid–fluid interface $\Gamma_{12}(t)$ and the fluid–solid interfaces $\Gamma_{13}(t)$, $\Gamma_{23}(t)$. As the solid phase is assumed to be stationary, the domain Ω_3 does not depend on time. We assume the interface between Ω_3 and the fluid phases (i.e., $\overline{\Gamma_{13} \cup \Gamma_{23}}$) to be smooth. Figure 4.1 shows a summary of the bulk equations and interface conditions that are presented in the following.

4.1.1.1 The Bulk Equations

In Ω_1 and Ω_2 we consider the incompressible flow of a viscous fluid phase exactly as in Section 3.1.1. The dynamics of the velocity field $\mathbf{v}(t,\mathbf{x}) \in \mathbb{R}^N$ and pressure $p = p(t,\mathbf{x}) \in \mathbb{R}$ is governed by the incompressible Navier–Stokes equations (3.1), (3.2),

$$\nabla \cdot \mathbf{v} = 0, \tag{4.1}$$

$$\partial_t(\rho_i \mathbf{v}) + \nabla \cdot (\rho_i \mathbf{v} \otimes \mathbf{v}) + \nabla p = \nabla \cdot (2\gamma_i \nabla^s \mathbf{v}), \tag{4.2}$$

in $\Omega_i(t)$, $i \in \{1,2\}$, $t \in (0,T)$.

As in Section 3.1.1 we introduce in the immobile solid domain Ω_3 the artificial velocity field $\mathbf{v} = \mathbf{v}(t,\mathbf{x})$. This enables us to establish a Navier-slip condition at the fluid–solid interfaces Γ_{13} and Γ_{23}. The velocity field $\mathbf{v}$ in Ω_3 follows the elliptic law (3.4),

$$\nabla \cdot (2\gamma_3 \nabla^s \mathbf{v}) - \rho_3 d_0 \mathbf{v} = 0 \tag{4.3}$$

in Ω_3, $t \in (0,T)$.

In contrast to Chapter 3 we do not consider ions dissolved in the fluid, as we do not model the evolution of the solid phase due to precipitation and dissolution.

4.1.1.2 The Interface Conditions

The dynamics of the interfaces Γ_{12}, Γ_{13} and Γ_{23} is described by the following conditions. The velocity field $\mathbf{v} : \Omega \to \mathbb{R}^N$ is assumed to be continuous across all domains, i.e., $[\![\mathbf{v}]\!] = 0$ on Γ_{12}, Γ_{13} and Γ_{23}.

The interface Γ_{12} between the two fluids is described by the same balance laws for mass (3.6) and momentum (3.7) as in Chapter 3,

$$\nu = \mathbf{v} \cdot \mathbf{n} \quad \text{on } \Gamma_{12}, \tag{4.4}$$

$$[\![(pI - 2\gamma \nabla^s \mathbf{v}) \cdot \mathbf{n}]\!] = \sigma_{12} \kappa \mathbf{n} \quad \text{on } \Gamma_{12}. \tag{4.5}$$

The fluid–solid interfaces Γ_{13} and Γ_{23} do not move in normal direction because we assumed Ω_3 to be stationary, i.e.,

$$\nu = 0 \quad \text{on } \Gamma_{13} \text{ and } \Gamma_{23}.$$

We impose the no-penetration condition for fluid flow (3.8) together with the tangential stress balance law (3.9). This allows for a slip condition for the tangential flow, as described in Section 3.1.1.4. Because of $\nu = 0$ equation (3.9) simplifies to

$$0 = [\![2\gamma\boldsymbol{\tau}(\nabla^s \mathbf{v})\mathbf{n}]\!] \qquad \text{for all } \boldsymbol{\tau} \in \mathbb{R}^N, \boldsymbol{\tau} \perp \mathbf{n} \qquad \text{on } \Gamma_{13} \text{ and } \Gamma_{23}. \tag{4.6}$$

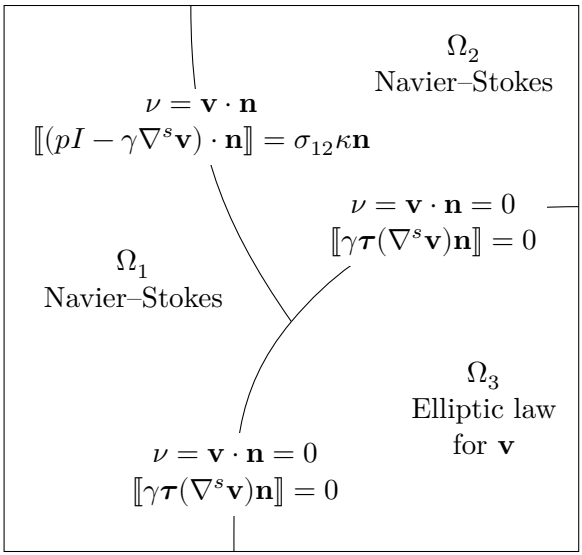

Figure 4.1: The bulk equations and interface conditions of the sharp interface model. The condition $[\![\mathbf{v}]\!] = 0$, being valid on all interfaces, is omitted. Starting from Figure 3.2, we obtain these conditions by setting $\nu = 0$ on Γ_{13} and Γ_{23}.

4.1.1.3 The Contact Angle Condition

We further impose a condition at the three-phase contact points. In the two-dimensional case these are isolated points, while in the three-dimensional case the three-phase contact points form one-dimensional contact lines. In the following we consider the two-dimensional case.

At the contact point we denote the contact angle of Ω_i by β_i. Assuming that the boundary of Ω_3 is smooth close to the contact point, we set $\beta_3 = \pi$. Given the constant coefficients Σ_1 and Σ_2, the contact angle β_1 satisfies the Young's equation

$$\Sigma_2 = \Sigma_1 + (\Sigma_1 + \Sigma_2)\cos\beta_1. \tag{4.7}$$

Then, we find β_2 through the relation $\beta_1 + \beta_2 + \beta_3 = 2\pi$. In the three dimensional case we impose the same conditions on the plane perpendicular to the contact curve, i.e., the plane with normal vector tangent to the contact curve.

Note that (4.7) is different to the contact angle condition (3.14) presented in Section (3.1.1.3). In particular, it is now possible to have a solid domain with $\beta_3 = \pi$, while this could only be approximated in Chapter 3.

Remark 4.1: *The coefficients Σ_1 and Σ_2 determine both the fluid–fluid surface energy σ_{12} and the contact angle β_1 through $\sigma_{12} = \Sigma_1 + \Sigma_2$ and (4.7) respectively. It is easy to check that the mapping*

$$\mathbb{R}^+ \times \mathbb{R}^+ \ni (\Sigma_1, \Sigma_2) \mapsto (\sigma_{12}, \beta_1) \in \mathbb{R}^+ \times (0, \pi)$$

is a bijection. Therefore, for a given surface energy σ_{12} and a given contact angle β_1 we can find values for Σ_1 and Σ_2.

4.1.2 The DD-$2f1s$-Phase Field Model

4.1.2.1 Preliminaries

Consider the three fields

$$\phi_1(t,\mathbf{x}), \phi_2(t,\mathbf{x}), \phi_3(\mathbf{x}) : [0,T] \times \Omega \to \mathbb{R}$$

approximating the indicator function of the respective phase in the sharp interface model. In contrast to the $2f1s$-model in Chapter 3 we view ϕ_3 as a given, constant field, and we gather only the unknown fields ϕ_1 and ϕ_2 in the vector-valued function $\boldsymbol{\Phi} = (\phi_1, \phi_2)^\top$.

The phase field variables ϕ_i are smooth and form diffuse transition zones with width determined by the parameter $\varepsilon > 0$. Understanding each ϕ_i as the volume fraction of the respective phase, we impose the condition

$$\phi_1(t,\mathbf{x}) + \phi_2(t,\mathbf{x}) = 1 - \phi_3(\mathbf{x}) \qquad \text{for all } t \in [0,T] \text{ and } \mathbf{x} \in \Omega. \tag{4.8}$$

Analogous to Section 3.1.2.1 we restrict ϕ_1 and ϕ_2 to the range $(-\delta, 1+\delta)$ for a small fixed parameter δ by using the double-well potential $W_{\text{dw}}(\phi)$ given by (3.20),

$$W_{\text{dw}}(\phi) = 450\phi^4(1-\phi)^4 + \delta\ell\left(\frac{\phi}{\delta}\right) + \delta\ell\left(\frac{1-\phi}{\delta}\right), \tag{4.9}$$

$$\ell(x) = \begin{cases} \frac{x^2}{1+x} & x \in (-1,0), \\ 0 & x \geq 0. \end{cases}$$

Remark 4.2: *The eighth-order polynomial in* (3.20) *was motivated by the need to prevent bulk precipitation in the sharp interface limit.*

As we do not model precipitation, we can also choose the simpler fourth-order double-well potential

$$W_{\mathrm{dw}}(\phi) = 18\phi^2(1-\phi)^2 + \delta\ell\left(\frac{\phi}{\delta}\right) + \delta\ell\left(\frac{1-\phi}{\delta}\right)$$

The triple-well potential function $W_0(\boldsymbol{\Phi}) : \mathbb{R}^2 \to \mathbb{R}$ can now be defined as

$$W_0(\boldsymbol{\Phi}) = \Sigma_1 W_{\mathrm{dw}}(\phi_1) + \Sigma_2 W_{\mathrm{dw}}(\phi_2), \tag{4.10}$$

with scaling coefficients $\Sigma_1, \Sigma_2 > 0$. This choice is motivated by [Boyer, Lapuerta, et al. 2010; Boyer and Lapuerta 2006] but in contrast to these works and the $2f1s$-model of Chapter 3 there is no contribution of the solid phase ϕ_3 to the potential (4.9).

The potential $W_0(\boldsymbol{\Phi})$ is reasonable for states $\boldsymbol{\Phi}$ on the affine space $\phi_1+\phi_2 = 1-\phi_3$. We introduce a projection P from $\mathbb{R}^2$ onto this plane. This projection is different to P in the $2f1s$-model in Section 3.1.2.1, as $\boldsymbol{\Phi}$ is now only two-dimensional. We define

$$P\boldsymbol{\Phi} = \boldsymbol{\Phi} + \Sigma_T(1-\phi_1-\phi_2-\phi_3)\begin{pmatrix}\Sigma_1^{-1}\\ \Sigma_2^{-1}\end{pmatrix}, \qquad \frac{1}{\Sigma_T} = \frac{1}{\Sigma_1} + \frac{1}{\Sigma_2}. \tag{4.11}$$

With the projection we finally define the potential $W(\boldsymbol{\Phi}) := W_0(P\boldsymbol{\Phi})$.

Remark 4.3: *We can find the construction of $W(\Phi)$ by modifying the Lagrange multiplier technique used in [Boyer and Lapuerta 2006]. For this we start with the system*

$$\begin{aligned}
\partial_t\phi_1 &= \nabla\cdot(M_1\nabla\mu_1),\\
\partial_t\phi_2 &= \nabla\cdot(M_2\nabla\mu_2),\\
\partial_t\phi_3 &= 0,\\
\mu_1 &= -\varepsilon\Sigma_1\Delta\phi_1 + \frac{\partial_{\phi_1}W_0(\boldsymbol{\Phi})}{\varepsilon} + \beta,
\end{aligned}$$

$$\mu_2 = -\varepsilon\Sigma_2\Delta\phi_2 + \frac{\partial_{\phi_2} W_0(\boldsymbol{\Phi})}{\varepsilon} + \beta,$$

with constant mobilities M_1, M_2 *yet to be determined. We use the Lagrange multiplier* β *to enforce the constraint* (4.8). *For initial data* $\boldsymbol{\Phi}$ *satisfying* $\phi_1(0,\mathbf{x}) + \phi_2(0,\mathbf{x}) = 1 - \phi_3(\mathbf{x})$ *this can be done by imposing* $\partial_t\phi_1 + \partial_t\phi_2 = 0$. *We calculate*

$$\begin{aligned} 0 &= \partial_t\phi_1 + \partial_t\phi_2 \\ &= \Delta\left(-\varepsilon M_1\Sigma_1\Delta\phi_1 - \varepsilon M_2\Sigma_2\Delta\phi_2 + \frac{M_1\partial_{\phi_1} W_0(\boldsymbol{\Phi})}{\varepsilon}\right. \\ &\qquad \left. + \frac{M_2\partial_{\phi_2} W_0(\boldsymbol{\Phi})}{\varepsilon} + (M_1+M_2)\beta\right). \end{aligned}$$

By choosing $M_1\Sigma_1 = M_2\Sigma_2 = M$ *for some constant* M *and using* $\Delta\phi_1 + \Delta\phi_2 = -\Delta\phi_3$ *as a consequence of* (4.8) *we have*

$$0 = M\Delta\left(\varepsilon\Delta\phi_3 + \frac{\partial_{\phi_1} W_0(\boldsymbol{\Phi})}{\Sigma_1\varepsilon} + \frac{\partial_{\phi_2} W_0(\boldsymbol{\Phi})}{\Sigma_2\varepsilon} + \frac{1}{\Sigma_T}\beta\right).$$

We therefore find the Lagrange multiplier β *to be equal to*

$$\beta = -\Sigma_T\varepsilon\Delta\phi_3 - \Sigma_T\frac{\partial_{\phi_1} W_0(\boldsymbol{\Phi})}{\Sigma_1\varepsilon} - \Sigma_T\frac{\partial_{\phi_2} W_0(\boldsymbol{\Phi})}{\Sigma_2\varepsilon},$$

and with this

$$\begin{aligned} \mu_1 &= -\varepsilon\Sigma_1\Delta\phi_1 - \Sigma_T\varepsilon\Delta\phi_3 \\ &\qquad + \frac{1}{\varepsilon}\left(\left(1 - \frac{\Sigma_T}{\Sigma_1}\right)\partial_{\phi_1} W_0(\boldsymbol{\Phi}) - \frac{\Sigma_T}{\Sigma_2}\partial_{\phi_2} W_0(\boldsymbol{\Phi})\right) \\ &= -\varepsilon\Sigma_1\Delta\phi_1 - \Sigma_T\varepsilon\Delta\phi_3 + \frac{\partial_{\phi_1} W(\boldsymbol{\Phi})}{\varepsilon}, \end{aligned}$$

and analogous for μ_2. *This last step motivates the exact choice of* P *in* (4.11).

4.1.2.2 The DD-$2f1s$-Model

We now present the diffuse domain $2f1s$-model. It can be seen as a modification of the δ-$2f1s$-model (3.45)–(3.50) presented in Section 3.1.3. For a fixed $\phi_3(\mathbf{x})$ it reads

$$\nabla \cdot (\phi_f \mathbf{v}) = 0, \tag{4.12}$$

$$\begin{aligned}\partial_t(\tilde{\rho}_f \mathbf{v}) + \nabla \cdot ((\rho_f \mathbf{v} + \mathbf{J}_f) \otimes \mathbf{v}) = &-\phi_f \nabla p + \nabla \cdot (2\tilde{\gamma}(\boldsymbol{\Phi}) \nabla^s \mathbf{v}) \\ &- \rho_3 d(\phi_f, \varepsilon)\mathbf{v} + \mathbf{S},\end{aligned} \tag{4.13}$$

$$\partial_t \phi_i + \nabla \cdot (\phi_i \mathbf{v} + \mathbf{J}_i) = 0, \qquad i \in \{1, 2\}, \tag{4.14}$$

$$\mu_i = \frac{\partial_{\phi_i} W(\boldsymbol{\Phi})}{\varepsilon} - \varepsilon \Sigma_i \Delta \phi_i - \varepsilon \Sigma_T \Delta \phi_3, \, i \in \{1, 2\}, \tag{4.15}$$

in $(0, T) \times \Omega$. As for the δ-$2f1s$-model, the total fluid fraction, fluid density, modified fluid density and modified fluid viscosity are given by

$$\begin{aligned}\phi_f(\boldsymbol{\Phi}) &:= \phi_1 + \phi_2, \\ \rho_f(\boldsymbol{\Phi}) &:= \rho_1 \phi_1 + \rho_2 \phi_2, \\ \tilde{\rho}_f(\boldsymbol{\Phi}) &:= \rho_1 \phi_1 + \rho_2 \phi_2 + (\rho_1 + \rho_2)\delta, \\ \tilde{\gamma}(\boldsymbol{\Phi}) &:= \left(\phi_1 \gamma_1^{-1} + \phi_2 \gamma_2^{-1} + \phi_3 \gamma_3^{-1} + (\gamma_1^{-1} + \gamma_2^{-1} + \gamma_3^{-1})\delta\right)^{-1},\end{aligned}$$

while the flux terms are given by

$$\mathbf{J}_i = -\frac{\varepsilon}{\Sigma_i} \nabla \mu_i, \quad \text{and} \quad \mathbf{J}_f = \rho_1 \mathbf{J}_1 + \rho_2 \mathbf{J}_2, \tag{4.16}$$

and the surface tension term reads

$$\mathbf{S} = -\mu_2 \phi_f \nabla \left(\frac{\phi_1}{\phi_f} \right) - \mu_1 \phi_f \nabla \left(\frac{\phi_2}{\phi_f} \right).$$

The DD-$2f1s$-model (4.12)–(4.15) is complemented by the boundary

conditions

$$\mathbf{v} = 0, \tag{4.17}$$

$$\nabla\phi_i \cdot \mathbf{n}_\Omega = 0, \qquad i \in \{1,2\}, \tag{4.18}$$

$$\nabla\mu_i \cdot \mathbf{n}_\Omega = 0, \qquad i \in \{1,2\}, \tag{4.19}$$

on $(0,T) \times \partial\Omega$. Here $\mathbf{n}_\Omega \in \mathbb{R}^N$ denotes the outer normal unit vector on $\partial\Omega$. Because of condition (4.8) the boundary condition (4.18) also restricts the choice of ϕ_3 to functions satisfying $\nabla\phi_3 \cdot \mathbf{n}_\Omega = 0$.

In contrast to the δ-$2f1s$-model we do not use a modification of ϕ_f. Because (4.8) implies $\phi_f = 1 - \phi_3$ we can ensure $\phi_f > 0$ by imposing the constraint $\phi_3 < 1$ for the given function $\phi_3(\mathbf{x})$. This choice also leads to an unmodified surface tension term $\mathbf{S}$. Equation (4.15) for the chemical potential μ_i is non-standard in the Cahn–Hilliard context, because of the additional term $-\varepsilon\Sigma_T\Delta\phi_3$. This choice is the result of the considerations made in Remark 4.3.

The DD-$2f1s$-model conserves mass in the sense that $\frac{d}{dt}\int_\Omega \phi_i \, d\mathbf{x} = 0$ and therefore $\frac{d}{dt}\int_\Omega \rho(\boldsymbol{\Phi}) \, d\mathbf{x} = 0$. By the construction in Remark 4.3 we also satisfy (4.8), provided ϕ_1 and ϕ_2 satisfy this condition initially.

4.1.3 Thermodynamical Consistency

Because we built the DD-$2f1s$-model on the δ-$2f1s$-model, we expect to recover the thermodynamical consistency described in Section 3.1.5. Indeed, the modifications here are chosen such that we find a similar free energy functional decreasing in time. The functional is given by

$$F(\boldsymbol{\Phi}, \nabla\boldsymbol{\Phi}, v) = \int_\Omega \frac{1}{2}\tilde{\rho}_f|\mathbf{v}|^2 + \sum_{i=1}^{2}\Sigma_i\left(\frac{W_{\mathrm{dw}}(\phi_i)}{\varepsilon} + \frac{1}{2}\varepsilon|\nabla\phi_i|^2\right) d\mathbf{x}. \tag{4.20}$$

The free energy functional consists of the kinetic energy of the fluid phases and the Ginzburg–Landau energy of the Cahn–Hilliard system. Note that following from our choice made in (4.10) there is no free energy associated to the solid phase ϕ_3. We can now proceed to formulate the thermodynamical consistency in the following theorem.

Theorem 4.1.1. *Consider a function $\phi_3(\mathbf{x})$ with $0 < \phi_3(\mathbf{x}) < 1$. Then classical solutions to the DD-2f1s-model* (4.12)–(4.15) *which obey the boundary conditions* (4.17)–(4.19) *and with initial conditions satisfying $F(\boldsymbol{\Phi}, \nabla\boldsymbol{\Phi}, v) < \infty$ fulfill for all $t \in (0, T]$ the free energy dissipation inequality*

$$\begin{aligned}
&\frac{d}{dt}F(\boldsymbol{\Phi}, \nabla\boldsymbol{\Phi}, v) \\
&\quad = \int_\Omega -2\tilde{\gamma}(\boldsymbol{\Phi})\nabla\mathbf{v} : \nabla^s\mathbf{v} - \rho_3 d(\phi_f, \varepsilon) - \varepsilon\sum_{i=1}^{2}\frac{1}{\Sigma_i}|\nabla\mu_i|^2\,d\mathbf{x} \\
&\quad \leq 0.
\end{aligned}$$

Proof. We first focus on the Ginzburg–Landau energy of (4.20). With partial integration and use of the homogeneous boundary conditions (4.18), (4.19) we find

$$\begin{aligned}
&\frac{d}{dt}\int_\Omega \sum_{i=1}^{2}\Sigma_i\left(\frac{W_{\mathrm{dw}}(\phi_i)}{\varepsilon} + \frac{1}{2}\varepsilon|\nabla\phi_i|^2\right)d\mathbf{x} \\
&\quad = \int_\Omega \sum_{i=1}^{2}\Sigma_i\left(\frac{W'_{\mathrm{dw}}(\phi_i)}{\varepsilon} - \varepsilon\Delta\phi_i\right)\partial_t\phi_i\,d\mathbf{x} \\
&\quad = \int_\Omega \sum_{i=1}^{2}\mu_i\partial_t\phi_i \\
&\qquad + \sum_{i=1}^{2}\left(\Sigma_T\Delta\phi_3 + \Sigma_T W'_{\mathrm{dw}}(\phi_1) + \Sigma_T W'_{\mathrm{dw}}(\phi_1)\right)\partial_t\phi_i\,d\mathbf{x}
\end{aligned}$$

$$
\begin{aligned}
&= \int_\Omega \sum_{i=1}^{2} \mu_i \partial_t \phi_i \, d\mathbf{x} \\
&= \int_\Omega - \sum_{i=1}^{2} \mu_i \nabla \cdot (\phi_i \mathbf{v} + \mathbf{J}_i) \, d\mathbf{x}.
\end{aligned}
\tag{4.21}
$$

We have used the equation for μ_i (4.15) and the definition of W in (4.10) and (4.11) to get to the third line in (4.21). The extra terms vanish because, by construction, we have $\partial_t \phi_1 + \partial_t \phi_2 = 0$.

Using the same calculation as in (3.61) we find for the kinetic energy of the fluid phases

$$
\begin{aligned}
&\frac{d}{dt} \int_\Omega \frac{1}{2} \tilde{\rho}_f |\mathbf{v}|^2 \, d\mathbf{x} \\
&\qquad = \int_\Omega \mathbf{v} \cdot (\nabla \cdot (2\tilde{\gamma}(\boldsymbol{\Phi}) \nabla^s \mathbf{v})) - \rho_3 d(\phi_f, \varepsilon) \mathbf{v}^2 + \mathbf{S} \cdot \mathbf{v} \, d\mathbf{x}.
\end{aligned}
\tag{4.22}
$$

Since $\nabla \cdot (\phi_f \mathbf{v}) = 0$ with $\phi_f = \phi_1 + \phi_2$, the surface tension term $\mathbf{S}$ calculates to

$$
\begin{aligned}
&\int_\Omega \mu_1 \nabla \cdot (\phi_1 \mathbf{v}) + \mu_2 \nabla \cdot (\phi_2 \mathbf{v}) \, d\mathbf{x} \\
&\qquad = \int_\Omega \left(-\mu_2 \nabla \cdot (\phi_1 \mathbf{v}) - \mu_1 \nabla \cdot (\phi_2 \mathbf{v}) \right) \, d\mathbf{x} \\
&\qquad = \int_\Omega \left(-\mu_2 \nabla \cdot \left(\frac{\phi_1}{\phi_f} \phi_f \mathbf{v} \right) - \mu_1 \nabla \cdot \left(\frac{\phi_2}{\phi_f} \phi_f \mathbf{v} \right) \right) \, d\mathbf{x} \\
&\qquad = \int_\Omega \left(-\mu_2 \phi_f \nabla \left(\frac{\phi_1}{\phi_f} \right) \cdot \mathbf{v} - \mu_1 \phi_f \nabla \left(\frac{\phi_2}{\phi_f} \right) \cdot \mathbf{v} \right) \, d\mathbf{x} \\
&\qquad = \int_\Omega \mathbf{S} \cdot \mathbf{v} \, d\mathbf{x}.
\end{aligned}
\tag{4.23}
$$

Finally, we combine (4.21), (4.22) and (4.23) to get

$$
\frac{d}{dt} F(\boldsymbol{\Phi}, \nabla \boldsymbol{\Phi}, v, c)
$$

$$
\begin{aligned}
&= \frac{d}{dt}\int_\Omega \frac{1}{2}\tilde{\rho}_f|\mathbf{v}|^2 + \sum_{i=1}^{2}\Sigma_i\left(\frac{W_{\mathrm{dw}}(\phi_i)}{\varepsilon} + \frac{1}{2}\varepsilon|\nabla\phi_i|^2\right) d\mathbf{x} \\
&= \int_\Omega \mathbf{v}\cdot(\nabla\cdot(2\tilde{\gamma}(\boldsymbol{\Phi})\nabla^s\mathbf{v})) - \rho_3 d(\phi_f,\varepsilon)\mathbf{v}^2 + \mathbf{S}\cdot\mathbf{v} \\
&\qquad - \sum_{i=1}^{2}\mu_i\nabla\cdot(\phi_i\mathbf{v} + \mathbf{J}_i)\, d\mathbf{x} \\
&= \int_\Omega -2\tilde{\gamma}(\boldsymbol{\Phi})\nabla\mathbf{v} : \nabla^s\mathbf{v} - \rho_3 d(\phi_f,\varepsilon)\mathbf{v}^2 + \sum_{i=1}^{2}\nabla\mu_i\cdot\mathbf{J}_i\, d\mathbf{x}.
\end{aligned}
$$

Since $\nabla\mathbf{v}{:}\nabla^s\mathbf{v} \geq 0$, using the definition of $\mathbf{J}_i$ in (4.16), the conclusion follows. □

4.2 The Sharp Interface Limit

In the following we briefly present the formal asymptotic limit of the DD-$2f1s$-model for $\varepsilon \to 0$. We use matched asymptotic expansions to show that the limit is the sharp interface formulation described in Section 4.1.1. As the arguments are mostly analogous to the sharp interface limit of the δ-$2f1s$-model in Section 3.2, we focus on the differences and additional assumptions needed for the DD-$2f1s$-model. In particular the argumentation at the triple point has to be adjusted to account for the fact that two of the three interfaces are stationary.

Let us summarize the assumptions that were already necessary for the sharp interface limit of the δ-$2f1s$-model. We choose the scaling $\delta = \varepsilon/L_{\mathrm{ref}}$ with $L_{\mathrm{ref}} = 1$ and assume the existence of a classical solution with finite free energy (4.20). We investigate a regime where the bulk phases are separated by interfaces that are characterized by a large gradient in $\boldsymbol{\Phi}$. Furthermore, we assume that we can write the solutions to the DD-$2f1s$-model in terms of outer and inner expansions of the unknowns $\boldsymbol{\Phi}$, $\mathbf{v}$, p, μ_1, μ_2, and also assume that μ_i is only of order $O(1)$. Finally, we assume that there are no third-phase contributions in the interfacial layers.

We now need to impose additional constraints on the given solid distribution $\phi_3(\mathbf{x})$. Assume that we have a one-parameter family of solid distributions $\phi_3(\mathbf{x}, \varepsilon)$ such that $\phi_3(\mathbf{x}, \varepsilon)$ can be written as outer and inner expansions in powers of ε. The leading order term of the outer expansion of ϕ_3 is given by the indicator function of the sub-domain Ω_3. We assume that the inner boundary $\partial\Omega_3 \backslash \partial\Omega$ is smooth. The leading order term of the inner expansion of ϕ_3 satisfies as a compatibility condition the equipartition of energy

$$W_{\mathrm{dw}}(\phi_{3,0}^{\mathrm{in}}) = \frac{1}{2}\left(\partial_z \phi_{3,0}^{\mathrm{in}}\right)^2 . \tag{4.24}$$

With these assumptions, we start by investigating the bulk phases of the system. Afterwards we investigate the interfaces to recover the transmission conditions and the triple point to recover Young's equation (4.7).

4.2.1 Outer Expansions

Expansion of (4.15)*,* $O(\varepsilon^{-1})$*:* As we assumed that $\phi_{3,0}^{\mathrm{out}}$ is the indicator function of Ω_3 we distinguish the following two cases.

For the case $\phi_{3,0}^{\mathrm{out}} = 1$, the only solution with finite energy is given by $\phi_{1,0}^{\mathrm{out}} = \phi_{2,0}^{\mathrm{out}} = 0$. The diverging part ℓ of the double well potential W_{dw} in (3.20) additionally implies that $\phi_{1,1}^{\mathrm{out}}, \phi_{2,1}^{\mathrm{out}} \geq 0$.

For the case $\phi_{3,0}^{\mathrm{out}} = 0$ a short calculation shows that there are two stable solutions $\boldsymbol{\Phi}_0^{\mathrm{out}} = (1,0)^\top$ and $\boldsymbol{\Phi}_0^{\mathrm{out}} = (0,1)^\top$. For the first solution we get the additional restriction $\phi_{1,1}^{\mathrm{out}} \leq 0$ and $\phi_{2,1}^{\mathrm{out}} \geq 0$. For the second solution the sign on these restrictions is flipped. We identify the set where $\boldsymbol{\Phi}_0^{\mathrm{out}} = \mathbf{e}_i, i \in \{1,2\}$ with the bulk domain Ω_i in the sharp interface formulation (4.1.1).

Expansion of (4.12)*,* $O(1)$*:* Analogous to the δ-$2f1s$-model we recover the incompressibility equation (3.1) of the sharp interface formulation.

Expansion of (4.13)*,* $O(1)$*:* Analogous to the δ-$2f1s$-model we recover the momentum equation (3.2) of the sharp interface formulation in Ω_1 and Ω_2 and the elliptic law for $\mathbf{v}$ (3.4) in Ω_3.

4.2.2 Inner Expansions, Leading Order

We introduce the three interfaces Γ_{12}, Γ_{13} and Γ_{23} through

$$\begin{aligned}\Gamma_{12}(t) &= \{\mathbf{x} \in \Omega : \phi_1(t,\mathbf{x}) = \phi_2(t,\mathbf{x}),\ \phi_1(t,\mathbf{x}) > 1/4\}\,,\\ \Gamma_{i3}(t) &= \left\{\mathbf{x} \in \Omega : \phi_3(\mathbf{x}) = 1/2,\ \phi_i(t,\mathbf{x}) > \phi_{(2-i)}(t,\mathbf{x})\right\},\end{aligned} \tag{4.25}$$

for $i \in \{1,2\}$. By our assumption, Γ_{ij} is a smooth $(d-1)$-dimensional manifold embedded in Ω and depending on time. On the other hand, as ϕ_3 does not depend on time, the total solid interface $\Gamma_3 := \overline{\Gamma_{13}(t) \cup \Gamma_{23}(t)}$ does not depend on time. As described in Section 1.3 we construct inner expansions of the unknowns $\boldsymbol{\Phi}$, $\mathbf{v}$, p, μ_1, μ_2 for each of the three interfaces Γ_{12}, Γ_{13} and Γ_{23}.

Expansion of (4.15)*,* $O(\varepsilon^{-1})$*:* As mentioned at the beginning of Section 3.2 we assume that there are no third-phase contributions in the interfacial layers. This means that we assume $\phi^{\text{in}}_{k,0} = 0$ at the interface Γ_{ij}, where $k \in \{1,2,3\}$, $k \neq i, k \neq j$ is the index of the third phase.

For the fluid–fluid interface Γ_{12} we can argue exactly as for the δ-$2f1s$-model in Section 3.2.2 and find that the $\phi^{\text{in}}_{1,0}$ is given implicitly by

$$z = \frac{1}{30}\left(\frac{1}{1-\phi^{\text{in}}_{1,0}} - \frac{1}{\phi^{\text{in}}_{1,0}} + 2\log\left(\frac{\phi^{\text{in}}_{1,0}}{1-\phi^{\text{in}}_{1,0}}\right)\right). \tag{4.26}$$

For the fluid–solid interfaces Γ_{i3} the distribution of $\Phi^{\text{in}}_{i,0}$ across the interface is already fully determined by the given $\phi^{\text{in}}_{3,0}$ and the assumption that there is no third-phase contribution, i.e., $\phi^{\text{in}}_{i,0} + \phi^{\text{in}}_{3,0} = 1$. We nevertheless check that the leading order terms match, as otherwise

our assumption of no third phase contribution would not be justified. For $0 \leq \phi_{i,0}^{\text{in}} \leq 1$ the leading order expansion of (4.15) for μ_i reads

$$\begin{aligned} 0 &= (\Sigma_i - \Sigma_T)\, W'_{\text{dw}}(\phi_{i,0}^{\text{in}}) - \Sigma_i \partial_{zz}\phi_{i,0}^{\text{in}} - \Sigma_T \partial_{zz}\phi_{3,0}^{\text{in}} \\ &= (\Sigma_i - \Sigma_T)\left(W'_{\text{dw}}(\phi_{i,0}^{\text{in}}) - \partial_{zz}\phi_{i,0}^{\text{in}}\right). \end{aligned} \tag{4.27}$$

Note that with the same arguments as for the fluid–fluid interface this leads to the same interface shape (4.26). By multiplying (4.27) with $\partial_z \phi_{i,0}^{\text{in}}$, integrating and using the matching conditions (1.28), (1.29) we recover the equipartition of energy

$$W_{\text{dw}}(\phi_{i,0}^{\text{in}}) = \frac{1}{2}\left(\partial_z \phi_{i,0}^{\text{in}}\right)^2.$$

As $\phi_{i,0}^{\text{in}} + \phi_{3,0}^{\text{in}} = 1$ it is also necessary that the equipartition of energy for $\phi_{3,0}^{\text{in}}$ holds. This is exactly requirement (4.24) we introduced at the beginning of this section. Indeed, numerical experiments show that for a general $\phi_{3,0}^{\text{in}}$ not fulfilling (4.24) there are third phase contributions in the fluid–solid interfaces.

Expansion of (4.12)*,* $O(\varepsilon^{-1})$*:* Analogous to the δ-$2f1s$-model we recover the continuity of $\mathbf{v}_0^{\text{out}} \cdot \mathbf{n}$ across the fluid–fluid interface Γ_{12} and the no-penetration condition $\mathbf{v}_0^{\text{out}} \cdot \mathbf{n} = 0$ at the fluid–solid interfaces Γ_{13} and Γ_{23}.

Expansion of (4.13)*,* $O(\varepsilon^{-2})$*:* Analogous to the δ-$2f1s$-model we recover the continuity of $\mathbf{v}_0^{\text{out}}$ across all interfaces.

Expansion of (4.14)*,* $O(\varepsilon^{-1})$*:* We can use the same arguments as for the δ-$2f1s$-model, but in a much simpler setting, because there is no reaction as a right-hand side term. We find as a compatibility condition the normal velocity of the interface equal to

$$\nu = \mathbf{v}_0^{\text{out}} \cdot \mathbf{n},$$

which simplifies to $\nu = 0$ in case of the fluid–solid interfaces Γ_{13} and Γ_{23}. If the compatibility condition is fulfilled, all constant functions $\mu^{\text{in}}_{1,0}$ and $\mu^{\text{in}}_{2,0}$ are solutions to the leading order terms of (4.14).

4.2.3 Inner Expansions, First Order

Expansion of (4.15)*,* $O(1)$*:* We only consider the fluid–fluid interface Γ_{12}. For this interface we can argue analogous to the δ-$2f1s$-model when investigating the difference $\mu_2 - \mu_1$. We find

$$\mu^{\text{in}}_{2,0} - \mu^{\text{in}}_{1,0} = (\Sigma_2 + \Sigma_1)\kappa = \sigma_{12}\kappa. \tag{4.28}$$

Expansion of (4.13)*,* $O(\varepsilon^{-1})$*:* We can again use arguments analogous to the δ-$2f1s$-model, in a simpler version. Note that there is no reaction term and no modification of the surface tension term $\mathbf{S}$. For the fluid–fluid interface Γ_{12} we recover the stress balance (3.7) of the sharp interface formulation. For the fluid–solid interfaces we only match the tangential component of the momentum equation, and we find

$$0 = [\![2\gamma\boldsymbol{\tau}(\nabla^s \mathbf{v}^{\text{out}}_0)\mathbf{n}]\!],$$

which is equal to (4.6) of the sharp interface formulation.

4.2.4 Triple Point Expansions

As a last step we investigate the three-phase contact points. In the two-dimensional case the three bulk phases meet at triple points, which we assume to be isolated points. In the three-dimensional case they meet at curves, called contact lines. In this section we analyze the two-dimensional case based on the ideas in [Bronsard and Reitich 1993; Garcke, Nestler, et al. 1998] and recover Young's equation (4.7) for the contact angle. For the three-dimensional case one can follow [Dunbar et al. 2019] and use the arguments of the two-dimensional case on the plane perpendicular to the contact line.

For the *DD*-2*f*1*s*-model this results in Young's equation (4.7) on the plane perpendicular to the contact line.

We define the set of triple points as

$$\Gamma_{123}(t) = \left\{\mathbf{x} \in \Omega : \boldsymbol{\Phi}(t,\mathbf{x}) = (1/4, 1/4)^\top\right\}.$$

This implies $\phi_3(\mathbf{x}) = 1/2$ at the triple points and therefore matches our definition of the interfaces Γ_{ij} in (4.25).

For a triple point $\hat{\mathbf{x}}(t) \in \Gamma_{123}(t)$ we introduce local coordinates around $\hat{\mathbf{x}}$ by

$$\mathbf{y}(t,\mathbf{x}) = \frac{\mathbf{x} - \hat{\mathbf{x}}(t)}{\varepsilon}.$$

For a generic scalar variable u this transformation yields

$$\nabla_{\mathbf{x}} u = \frac{1}{\varepsilon}\nabla_{\mathbf{y}} u + O(1), \tag{4.29}$$

$$\Delta_{\mathbf{x}} u = \frac{1}{\varepsilon^2}\Delta_{\mathbf{y}} u + O(\varepsilon). \tag{4.30}$$

We assume that close to the triple point $\hat{\mathbf{x}}(t)$ we can write solutions to the *DD*-2*f*1*s*-model (4.12)–(4.15) in terms of *triple point expansions* of the form

$$\boldsymbol{\Phi}^{\mathrm{tp}}(t,\mathbf{y}) = \boldsymbol{\Phi}_0^{\mathrm{tp}}(t,\mathbf{y}) + \varepsilon\boldsymbol{\Phi}_1^{\mathrm{tp}}(t,\mathbf{y}) + \dots,$$

and similarly for all other unknowns. The functions $\boldsymbol{\Phi}_k^{\mathrm{tp}}$, $k \in \mathbb{N}_0$ do not depend on ε. Note that the triple point expansion is already written in the rescaled local coordinates $\mathbf{y}$.

In the triple point $\hat{\mathbf{x}}$, the three interfaces $\Gamma_{12}, \Gamma_{13}, \Gamma_{23}$ meet. We therefore have three additional coordinate systems $(z_{ij}, \mathbf{s}_{ij})$, $i < j$, from the inner expansions used in the interfaces. Note that we are in the two-dimensional case and $\mathbf{s}_{ij}$ is therefore a scalar. We choose the local parametrization of the interfaces such that $z_{ij} = 0$, $\mathbf{s}_{ij} = 0$ coincides with $\hat{\mathbf{x}}$ and that $\mathbf{s}_{ij} > 0$ on the interface Γ_{ij}. Furthermore,

for the interface Γ_{ij}, $i < j$, the direction of positive z_{ij} is oriented towards Ω_j. Denote by

$$\mathbf{n}_{ij}(t) = \partial_z \mathbf{x}(t, \mathbf{s}_{ij} = 0, z)\big|_{z=0}$$

the normal unit vector of Γ_{ij} at the triple point, and by

$$\boldsymbol{\tau}_{ij}(t) = \partial_{\mathbf{s}} \mathbf{x}(t, \mathbf{s}, z_{ij} = 0)\big|_{\mathbf{s}=0}$$

the tangential vector of Γ_{ij} pointing away from $\hat{\mathbf{x}}$. Since we assumed that the boundary of Ω_3 around a triple point is smooth we have

$$\mathbf{n}_{13} = \mathbf{n}_{23} \quad \text{and} \quad \boldsymbol{\tau}_{13} = -\boldsymbol{\tau}_{23}, \tag{4.31}$$

see Figure 4.2 for an illustration.

Let t be fixed and denote the limit of $\boldsymbol{\Phi}^{\text{in}}(t, \mathbf{s}_{ij}, z)$ for positive $\mathbf{s}_{ij} \to 0$ by $\boldsymbol{\Phi}^{\text{in}}(t, 0_+, z)$. We match the triple point expansions with the inner

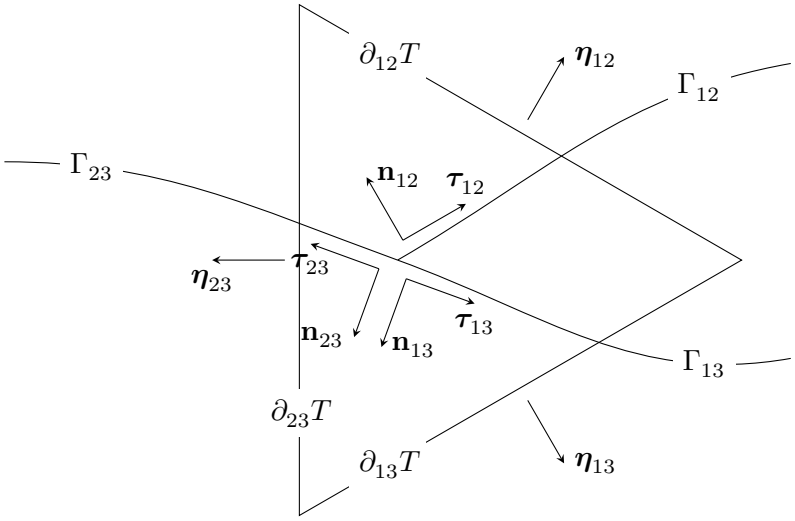

Figure 4.2: Vectors at the triple junction.

expansions at $\boldsymbol{\Phi}^{\text{in}}(t, 0_+, z)$ by the *matching conditions*

$$\lim_{\zeta\to\infty} \boldsymbol{\Phi}_0^{\text{tp}}(t, \zeta\boldsymbol{\tau}_{ij} + z\mathbf{n}_{ij}) = \boldsymbol{\Phi}_0^{\text{in},ij}(t, 0_+, z), \tag{4.32}$$

$$\lim_{\zeta\to\infty} \nabla_{\mathbf{y}}\boldsymbol{\Phi}_0^{\text{tp}}(t, \zeta\boldsymbol{\tau}_{ij} + z\mathbf{n}_{ij}) = \partial_z\boldsymbol{\Phi}_0^{\text{in},ij}(t, 0_+, z) \otimes \mathbf{n}_{ij}, \tag{4.33}$$

where $\boldsymbol{\Phi}^{\text{in},ij}$ is the inner solution on Γ_{ij}. Note that for (4.33) it is essential that both $\mathbf{y}$ and z scale the same with ε. A direct consequence of (4.33) is that, for the directional derivative along a vector $\mathbf{e} \in \mathbb{R}^N$,

$$\lim_{\zeta\to\infty} \partial_{\mathbf{e}}\boldsymbol{\Phi}_0^{\text{tp}}(t, \zeta\boldsymbol{\tau}_{ij} + z\mathbf{n}_{ij}) = \partial_z\boldsymbol{\Phi}_0^{\text{in},ij}(t, z, 0_+)(\mathbf{n}_{ij} \cdot \mathbf{e}). \tag{4.34}$$

Finally, we introduce an equilateral triangle T with center $\hat{\mathbf{x}}$ and side length $R = \varepsilon^{1/2}$. Measured in the coordinate system $\mathbf{y}$, this triangle has the side length $R_{\mathbf{y}} = \varepsilon^{-1/2}$. The orientation is chosen such that each side is intersected by exactly one of the interfaces Γ_{ij}. We denote the side intersecting Γ_{ij} by $\partial_{ij}T$ and call its outer normal unit vector $\boldsymbol{\eta}_{ij}$. For an illustration see Figure 4.2.

Expansion of (4.15), $O(\varepsilon^{-1})$*:* The leading order expansion of (4.15) for μ_i, $i \in \{1, 2\}$ reads

$$0 = \partial_{\phi_i} W(\boldsymbol{\Phi}_0^{\text{tp}}) - \Sigma_i\Delta_{\mathbf{y}}\phi_{i,0}^{\text{tp}} - \Sigma_T\Delta_{\mathbf{y}}\phi_{3,0}^{\text{tp}}. \tag{4.35}$$

We have again used the assumption that μ_i is not of order $O(\varepsilon^{-1})$. We are interested in the change of energy along the solid interface, i.e., in direction $\boldsymbol{\tau}_{13}$, and therefore calculate

$$\begin{aligned}
\partial_{\boldsymbol{\tau}_{13}} W(\boldsymbol{\Phi}_0^{\text{tp}}) &= \sum_{i=1}^{2} \partial_{\phi_i} W(\boldsymbol{\Phi}_0^{\text{tp}})\partial_{\boldsymbol{\tau}_{13}}\phi_{i,0}^{\text{tp}} \\
&= \sum_{i=1}^{2} \left(\Sigma_i\Delta_{\mathbf{y}}\phi_{i,0}^{\text{tp}} + \Sigma_T\Delta_{\mathbf{y}}\phi_{3,0}^{\text{tp}}\right)\partial_{\boldsymbol{\tau}_{13}}\phi_{i,0}^{\text{tp}} \\
&= \sum_{i=1}^{2} \Sigma_i\Delta_{\mathbf{y}}\phi_{i,0}^{\text{tp}}\partial_{\boldsymbol{\tau}_{13}}\phi_{i,0}^{\text{tp}} - \Sigma_T\Delta_{\mathbf{y}}\phi_{3,0}^{\text{tp}}\partial_{\boldsymbol{\tau}_{13}}\phi_{3,0}^{\text{tp}}.
\end{aligned} \tag{4.36}$$

Here we have used (4.35) to get to the second line, and $\partial_{\boldsymbol{\tau}_{13}}\phi^{\mathrm{tp}}_{1,0} + \partial_{\boldsymbol{\tau}_{13}}\phi^{\mathrm{tp}}_{2,0} = -\partial_{\boldsymbol{\tau}_{13}}\phi^{\mathrm{tp}}_{3,0}$ as a consequence of (4.8) to get to the third line. With the notation $\hat{\Sigma}_1 := \Sigma_1$, $\hat{\Sigma}_2 := \Sigma_2$, $\hat{\Sigma}_3 := -\Sigma_T$, we can write (4.36) as

$$\partial_{\boldsymbol{\tau}_{13}} W(\boldsymbol{\Phi}^{\mathrm{tp}}_0) = \sum_{k=1}^{3} \hat{\Sigma}_k \Delta_{\mathbf{y}} \phi^{\mathrm{tp}}_{k,0} \partial_{\boldsymbol{\tau}_{13}} \phi^{\mathrm{tp}}_{k,0}.$$

We now integrate over T and use Green's first identity to calculate

$$\begin{aligned}
\int_T \partial_{\boldsymbol{\tau}_{13}} W(\boldsymbol{\Phi}^{\mathrm{tp}}_0)\, d\mathbf{y} &= \sum_{k=1}^{3} \hat{\Sigma}_k \int_T \Delta_{\mathbf{y}} \phi^{\mathrm{tp}}_{k,0} \partial_{\boldsymbol{\tau}_{13}} \phi^{\mathrm{tp}}_{k,0}\, d\mathbf{y} \\
&= \sum_{k=1}^{3} \hat{\Sigma}_k \left(\int_{\partial T} \left(\nabla_{\mathbf{y}} \phi^{\mathrm{tp}}_{k,0} \cdot \boldsymbol{\eta} \right) \partial_{\boldsymbol{\tau}_{13}} \phi^{\mathrm{tp}}_{k,0}\, dS_{\mathbf{y}} \right. \\
&\qquad \left. - \int_T \nabla_{\mathbf{y}} \phi^{\mathrm{tp}}_{k,0} \cdot \nabla_{\mathbf{y}} \left(\partial_{\boldsymbol{\tau}_{13}} \phi^{\mathrm{tp}}_{k,0} \right) d\mathbf{y} \right) \\
&= \sum_{k=1}^{3} \hat{\Sigma}_k \left(\int_{\partial T} \left(\nabla_{\mathbf{y}} \phi^{\mathrm{tp}}_{k,0} \cdot \boldsymbol{\eta} \right) \partial_{\boldsymbol{\tau}_{13}} \phi^{\mathrm{tp}}_{k,0}\, dS_{\mathbf{y}} \right. \\
&\qquad \left. - \int_T \frac{1}{2} \partial_{\boldsymbol{\tau}_{13}} \left| \nabla_{\mathbf{y}} \phi^{\mathrm{tp}}_{k,0} \right|^2 d\mathbf{y} \right),
\end{aligned}$$

where $\boldsymbol{\eta}$ is the outer normal unit vector of T. As all integrals over T only contain directional derivatives, we can also rewrite them to integrals over ∂_T and get

$$\begin{aligned}
0 = &\int_{\partial T} W(\boldsymbol{\Phi}^{\mathrm{tp}}_0) \left(\boldsymbol{\tau}_{13} \cdot \boldsymbol{\eta} \right) dS_{\mathbf{y}} \\
&+ \sum_{k=1}^{3} \hat{\Sigma}_k \left(\int_{\partial T} \frac{1}{2} \left| \nabla_{\mathbf{y}} \phi^{\mathrm{tp}}_{k,0} \right|^2 \left(\boldsymbol{\tau}_{13} \cdot \boldsymbol{\eta} \right) dS_{\mathbf{y}} \right. \\
&\qquad \left. - \int_{\partial T} \left(\nabla_{\mathbf{y}} \phi^{\mathrm{tp}}_{k,0} \cdot \boldsymbol{\eta} \right) \partial_{\boldsymbol{\tau}_{13}} \phi^{\mathrm{tp}}_{k,0}\, dS_{\mathbf{y}} \right).
\end{aligned} \tag{4.37}$$

We can split each integral over the boundary ∂T into integrals over the three sides $\partial_{ij} T$. As $\varepsilon \to 0$, we have the side length $R_{\mathbf{y}} = \varepsilon^{-1/2} \to \infty$.

Therefore, we use the matching conditions (4.32), (4.33) and (4.34).

Let us first focus on a single side $\partial_{ij}T$ of the triangle, and only on the first term on the right-hand side of (4.37). It is easy to see that the integral exists and is uniformly bounded for $R_{\mathbf{y}} \to \infty$. Using the matching condition (4.32),

$$\begin{aligned}\lim_{R_{\mathbf{y}}\to\infty} \int_{\partial_{ij}T} W(\boldsymbol{\Phi}_0^{\mathrm{tp}}) \left(\boldsymbol{\tau}_{13} \cdot \boldsymbol{\eta}_{ij}\right) \, dS_{\mathbf{y}} \\ = \frac{1}{\boldsymbol{\tau}_{ij} \cdot \boldsymbol{\eta}_{ij}} \int_{-\infty}^{\infty} W(\boldsymbol{\Phi}_0^{\mathrm{in},ij}(t,z,0_+)) \left(\boldsymbol{\tau}_{13} \cdot \boldsymbol{\eta}_{ij}\right) \, dz_{ij}.\end{aligned} \tag{4.38}$$

Here the factor $1/(\boldsymbol{\tau}_{ij} \cdot \boldsymbol{\eta}_{ij})$ is introduced through the coordinate transformation from the arc length $dS_{\mathbf{y}}$ to the coordinate z_{ij}. With the matching conditions (4.33) and (4.34), we can use the same arguments on the other terms of (4.37). For the sum over all sides of ∂T we get

$$\begin{aligned}0 = \sum_{ij\in\{12,13,23\}} \frac{1}{\boldsymbol{\tau}_{ij} \cdot \boldsymbol{\eta}_{ij}} \Bigg[\int_{-\infty}^{\infty} W(\boldsymbol{\Phi}_0^{\mathrm{in},ij}) \left(\boldsymbol{\tau}_{13} \cdot \boldsymbol{\eta}_{ij}\right) \, dz_{ij} \\ + \sum_{k=1}^{3} \hat{\Sigma}_k \int_{-\infty}^{\infty} \frac{1}{2} \left|\partial_z \phi_k^{\mathrm{in},ij}\right|^2 \left(\boldsymbol{\tau}_{13} \cdot \boldsymbol{\eta}_{ij}\right) \, dz_{ij} \\ - \sum_{k=1}^{3} \hat{\Sigma}_k \int_{-\infty}^{\infty} \left(\partial_z \phi_k^{\mathrm{in},ij}\right)^2 (\mathbf{n}_{ij} \cdot \boldsymbol{\eta}_{ij})(\mathbf{n}_{ij} \cdot \boldsymbol{\tau}_{13}) \, dz_{ij} \Bigg].\end{aligned} \tag{4.39}$$

Recall that we have calculated the exact shape of $\phi_k^{\mathrm{in},ij}(z)$ in the inner expansions (4.26), and by equipartition of energy (3.79), (4.24) and construction of W_{dw} (see (3.80)) we have

$$\begin{aligned}\int_{-\infty}^{\infty} W_{\mathrm{dw}}(\phi_k^{\mathrm{in},ij}) \, dz_{ij} &= \int_{-\infty}^{\infty} \frac{1}{2} \left(\partial_z \phi_k^{\mathrm{in},ij}\right)^2 \, dz_{ij} \\ &= \begin{cases} \frac{1}{2} & \text{if } k = i \text{ or } k = j, \\ 0 & \text{else.} \end{cases}\end{aligned}$$

Together with the construction of W in (4.10) we write (4.39) as

$$\begin{aligned}
0 =& \frac{1}{\boldsymbol{\tau}_{12}\cdot\boldsymbol{\eta}_{12}}\Big(\frac{1}{2}(\Sigma_1+\Sigma_2)(\boldsymbol{\tau}_{13}\cdot\boldsymbol{\eta}_{12})+\frac{1}{2}(\Sigma_1+\Sigma_2)(\boldsymbol{\tau}_{13}\cdot\boldsymbol{\eta}_{12})\\
&\qquad -(\Sigma_1+\Sigma_2)(\mathbf{n}_{12}\cdot\boldsymbol{\eta}_{12})(\mathbf{n}_{12}\cdot\boldsymbol{\tau}_{13})\Big)\\
&+\frac{1}{\boldsymbol{\tau}_{13}\cdot\boldsymbol{\eta}_{13}}\Big(\frac{1}{2}\Sigma_1(\boldsymbol{\tau}_{13}\cdot\boldsymbol{\eta}_{13})+\frac{1}{2}(\Sigma_1-\Sigma_T)(\boldsymbol{\tau}_{13}\cdot\boldsymbol{\eta}_{13})\\
&\qquad -(\Sigma_1-\Sigma_T)(\mathbf{n}_{13}\cdot\boldsymbol{\eta}_{13})(\mathbf{n}_{13}\cdot\boldsymbol{\tau}_{13})\Big)\\
&+\frac{1}{\boldsymbol{\tau}_{23}\cdot\boldsymbol{\eta}_{23}}\Big(\frac{1}{2}\Sigma_2(\boldsymbol{\tau}_{13}\cdot\boldsymbol{\eta}_{23})+\frac{1}{2}(\Sigma_2-\Sigma_T)(\boldsymbol{\tau}_{13}\cdot\boldsymbol{\eta}_{23})\\
&\qquad -(\Sigma_2-\Sigma_T)(\mathbf{n}_{23}\cdot\boldsymbol{\eta}_{23})(\mathbf{n}_{23}\cdot\boldsymbol{\tau}_{13})\Big).
\end{aligned}$$

With $\mathbf{n}_{13}\cdot\boldsymbol{\tau}_{13}=0$, $\mathbf{n}_{23}\cdot\boldsymbol{\tau}_{13}=0$ and $\boldsymbol{\tau}_{13}=-\boldsymbol{\tau}_{12}$ this simplifies to

$$\begin{aligned}
0 =& \frac{\Sigma_1+\Sigma_2}{\boldsymbol{\tau}_{12}\cdot\boldsymbol{\eta}_{12}}\Big((\boldsymbol{\tau}_{13}\cdot\boldsymbol{\eta}_{12})-(\mathbf{n}_{12}\cdot\boldsymbol{\eta}_{12})(\mathbf{n}_{12}\cdot\boldsymbol{\tau}_{13})\Big)\\
&+(\Sigma_1-\frac{1}{2}\Sigma_T)-(\Sigma_2-\frac{1}{2}\Sigma_T).
\end{aligned}$$

As $\boldsymbol{\tau}_{12}$ and $\mathbf{n}_{12}$ are perpendicular, we have $\boldsymbol{\eta}_{12}=(\boldsymbol{\tau}_{12}\cdot\boldsymbol{\eta}_{12})\boldsymbol{\tau}_{12}+(\mathbf{n}_{12}\cdot\boldsymbol{\eta}_{12})\mathbf{n}_{12}$, and we can conclude

$$\begin{aligned}
0 =& \frac{\Sigma_1+\Sigma_2}{\boldsymbol{\tau}_{12}\cdot\boldsymbol{\eta}_{12}}\Big((\boldsymbol{\tau}_{13}\cdot\boldsymbol{\tau}_{12})(\boldsymbol{\tau}_{12}\cdot\boldsymbol{\eta}_{12})+(\boldsymbol{\tau}_{13}\cdot\mathbf{n}_{12})(\mathbf{n}_{12}\cdot\boldsymbol{\eta}_{12})\\
&\qquad -(\mathbf{n}_{12}\cdot\boldsymbol{\eta}_{12})(\mathbf{n}_{12}\cdot\boldsymbol{\tau}_{13})\Big)+(\Sigma_1-\frac{1}{2}\Sigma_T)-(\Sigma_2-\frac{1}{2}\Sigma_T)\\
=&(\boldsymbol{\tau}_{13}\cdot\boldsymbol{\tau}_{12})(\Sigma_1+\Sigma_2)+\Sigma_1-\Sigma_2,
\end{aligned}$$

which is Young's equation (4.7), as $\boldsymbol{\tau}_{13}\cdot\boldsymbol{\tau}_{12}=\cos\beta_1$.

4.3 Numerical Investigation

In the following, we illustrate the capabilities of DD-$2f1s$-model by a numerical example. We discretize the DD-$2f1s$-model analogous to the discretization of the δ-$2f1s$-model described in Section 3.3. We employ a Galerkin FEM scheme, with Taylor–Hood elements for $\mathbf{v}$ and p, and Lagrange elements of order 1 for ϕ_1 and μ_1. We discretize in time by implicit Euler. Again, the implementation was done in PDELab [Bastian et al. 2010] using DUNE-ALUGrid [Alkämper et al. 2016] for adaptive grid generation.

As a numerical example we consider a droplet in the corner of a solid phase. As boundary conditions, we choose (4.17)–(4.19) for the left and bottom boundary, and symmetry boundary conditions for the right and top boundary. The droplet is initialized with 90 degree contact angle to the solid phase (ϕ_3, red), see Figure 4.3. The choice $\Sigma_1 = 1$, $\Sigma_2 = 20$ leads to a wetting first fluid phase (ϕ_1, dark blue) with contact angle $\beta_1 = 25.2°$, using (4.7). The system therefore evolves to a stationary state with this contact angle. In the steady state, we can calculate the capillary pressure as the pressure difference in the two fluid phases ϕ_1 and ϕ_2.

When we use the δ-$2f1s$-model in the same setting, the solid phase is also evolving. This leads to the corner of the solid phase smoothing out over time. In Figure 4.4 the final state of simulations is compared between the DD-$2f1s$-model and the δ-$2f1s$-model. For the δ-$2f1s$-model we choose $\Sigma_1 = 1$, $\Sigma_2 = 20$, $\Sigma_3 = 200$, resulting in $\beta_1 = 27.3°$, $\beta_2 = 155.2°$ and $\beta_3 = 177.5°$, using (3.14). For the comparison, the reaction terms of the δ-$2f1s$-model are set to zero, i.e., $R_1 = 0$.

As an application for the DD-$2f1s$-model, we want to predict the transmissibility of pore throats in a pore network model. A pore network model resolves the pore-scale of a porous medium in a simplified form. It consists of an undirected graph depicting the connectivity of the porous medium. The vertices of the graph are called pore bodies and contain information about the volume of each pore. The edges of the graph are called pore throats and contain

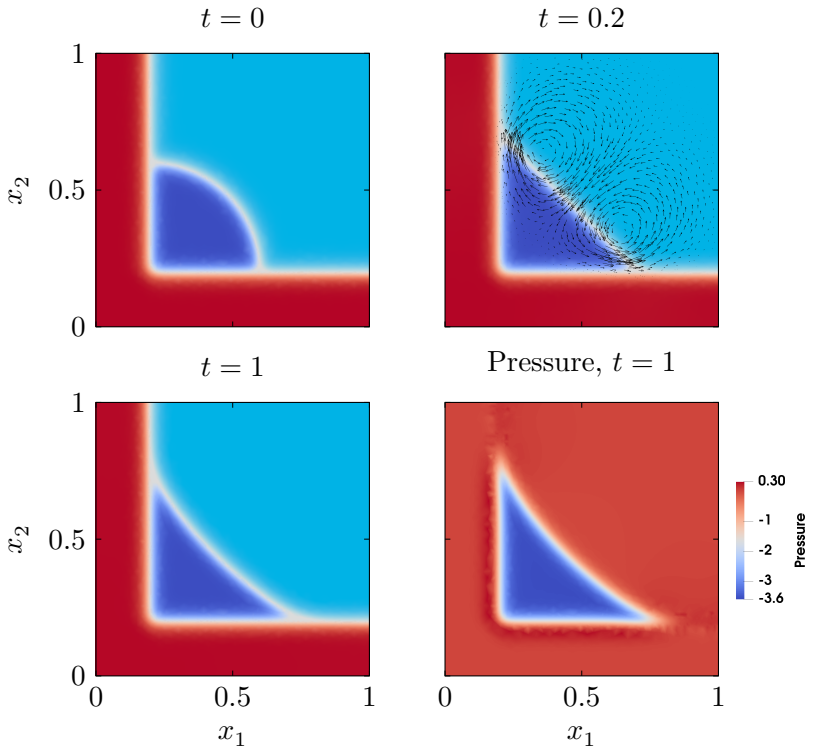

Figure 4.3: Droplet in the corner of a pore throat with square cross-section. Top left: Initial data, top right: velocity field for $t = 0.2$, bottom left: $t = 1$ (stationary state), bottom right: $p\phi_f$ in non-dimensional form at $t = 1$.

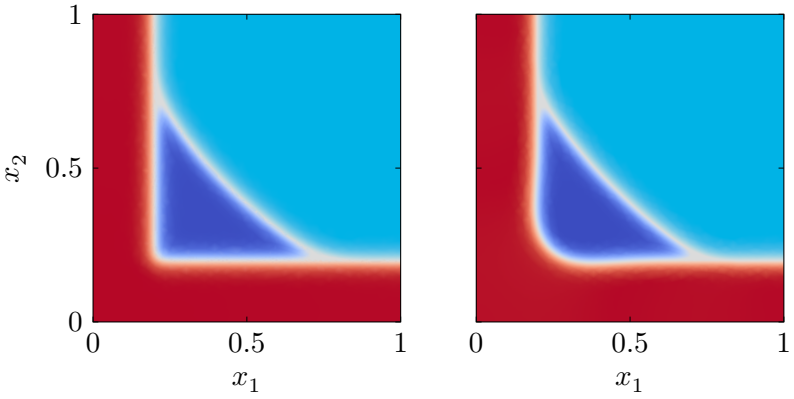

Figure 4.4: Droplet in the corner of a pore throat with square cross-section at $t = 1$. Left: DD-2f1s-model, right: δ-2f1s-model.

information about the transmissibility, i.e., the flow resistance. All degrees of freedom in a pore network model are placed in the pore bodies. In the case of one-phase flow, only the pressure in each pore body is unknown, and by predicting the transmissibility with a Hagen–Poiseuille law one can solve for the pressure in each pore body and the resulting flow rate through the pore throats. For two-phase flow, the saturation in each pore body enters as a new unknown, and a constitutive relation between capillary pressure and saturation is assumed. We refer to [Weishaupt 2020] for an introduction into two-phase pore network models.

For two-phase flow and for a general pore throat geometry it is not straightforward to determine the transmissibility, as it depends on the distribution of the fluid phases in the pore throat. We assume that the pore throat geometry and the fluid distribution are constant in longitudinal direction, and consider therefore only a transversal cross-section of the pore throat. To determine the transmissibility for a given saturation, a stationary fluid distribution for this saturation has to be found. We therefore use the *DD*-2f1s-model to find these stationary fluid distributions. In this context the example in

Figure 4.3 can be seen as the cross-section of a pore throat.

To obtain the transmissibility we consider the steady state, and solve (4.13) under the assumption that there is no flow in transversal direction and the pressure gradient in longitudinal direction is constant. We obtain the flow profile and can integrate over the transversal cross-section to obtain a non-dimensional transmissibility.

For this application, the advantage of the DD-$2f1s$-model over the δ-$2f1s$-model is twofold. For one, we have to solve for fewer phase field variables, as we can use (4.8) to only keep ϕ_1 and μ_1 as unknowns. More importantly, the fact that the solid phase does not evolve in time means that steady states for different saturations are comparable, as they have exactly the same solid phase distribution. This allows us to iterate the example in Figure 4.3 for different saturations to obtain a relation between capillary pressure and saturation, as well as a relation between transmissibility and saturation.

While Figure 4.3 shows the simple case of a pore throat with square cross-section, this approach works for general cross-sections. In combination with the δ-$2f1s$-model the precipitation in pore throats can be predicted, resulting in cross-sections that change over time.

Part II
Upscaling of Reactive Flow

Upscaling the Allen–Cahn Model Using Periodic Homogenization

5

In this chapter we consider the regularized Allen–Cahn phase field model from Chapter 2, Equations (2.5) to be defined in a periodic porous medium. The pore-scale, where grain, mineral and fluid-filled void space are explicitly separated, is the microscale, and we derive a macroscale model describing the effective behavior of the system in Section 5.1. After this we use numerical examples to study the behavior of the upscaled model parameters in terms of the diffuse interface parameter in Section 5.2.

5.1 Upscaling

We consider a domain $\mathcal{D}$ containing small, periodically distributed grains, as sketched in Figure 5.1. In a porous medium, $\mathcal{D}$ represents the union of the void space, mineral space and the grain space, where the grains are considered as perforations. We refer to the union of the void space and mineral space as the pore space. The grains are impermeable for fluid and no reactions take place there. Hence, the phase field model (2.5) is not defined in the grain space but only in the pore space of $\mathcal{D}$. The grains do not change with time, while the moving boundary between mineral and fluid, located in the pore space of $\mathcal{D}$, is still handled by the phase field equation as a diffuse interface. We assume that the mineral precipitates on the boundary of the perforations or at already existing minerals, and not inside the

void space. Another important assumption is that the void space in $\mathcal{D}$ is connected and that the mineral never grows in such a way that the pore space is clogged.

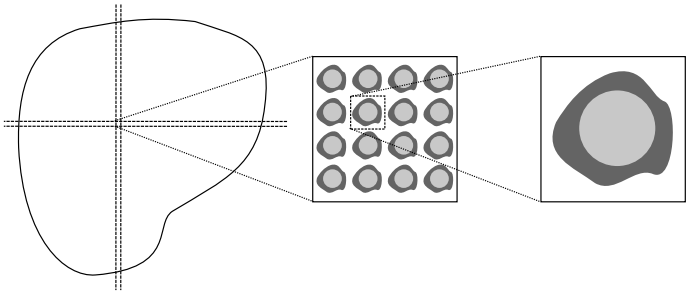

Figure 5.1: Structure of porous medium. Fluid-filled void space is marked with white, mineral is dark gray, and non-reactive grain is light gray. The pore space is the union of the void space and mineral space.

The porous medium $\mathcal{D}$ contains many periodically repeating grains. This means that the phase field model (2.5) is defined on a domain of high complexity. In such cases, the averaged behavior of the system is of primary interest. In consequence, we apply periodic homogenization techniques to find effective equations valid at a larger scale, where the microscale oscillations are no longer visible, but their effect is still taken into account. This is done by identifying a scale separation and applying asymptotic expansions on non-dimensional versions of the model equations, see Section 1.4 for an overview.

When non-dimensionalizing the model (2.5), one must address the size of the appearing non-dimensional numbers (e.g. Reynolds, Péclet, Cahn and Damköhler). In particular, their order of magnitude determines the regime we consider. In the following, we consider a regime in the range of Darcy's law [Hornung 1996] and where time scales for macroscale solute diffusion, advection and reaction are approximately the same size. As we show in the following, this leads to diffusion dominating at the pore-scale. Finally, we want the phase field to appear as a local, microscale variable, and we

address the choices necessary to achieve so. Note that other choices for the non-dimensional numbers are possible, but result in different upscaled models, as discussed in Section 1.4.

5.1.1 The Scale Separation

In the dimensional setting we let ℓ be a typical length scale at the microscale (i.e., the pore-scale), e.g., the width of the right-most box in Figure 5.1) and L a typical length scale at the macroscale, e.g. the width of the domain $\mathcal{D}$ or of the Darcy-scale, as commonly made for homogenization [Davit et al. 2013; Hornung 1996]. With this we define $\beta = \ell/L$, reflecting the ratio between the micro- and macroscale and hence giving us the scale separation. We assume that ℓ is much smaller than L, hence β is a small number. We mention that in [van Duijn and Pop 2004, Remark 1.2] a different definition of the scale separation is discussed, and how this leads to the same non-dimensional model is then shown.

A third, even smaller length scale is given by the diffuse interface width ε. As the interfaces have to be resolved on the microscale, we require ε to be much smaller than ℓ. We define the ratio $\bar{\varepsilon} = \varepsilon/\ell$ to express the interface width in comparison to the microscale. Overall, we obtain the three length scales $L \gg \ell \gg \varepsilon$.

In what follows we rewrite the model in non-dimensional form. In doing so we introduce a local unit cell $Y = [0,1]^N$, as seen in Figure 5.2, where $N \in \{2,3\}$, depending on spatial dimension, and we let the local variable $\mathbf{y} \in (0,1)^N$ describe points within Y. The local cell consists of the fluid part F and mineral part M, and the grain part G as sketched in Figure 5.2. Hence, locally the phase field model is defined in the pore space $P = F \cup M$, while G defines the perforation. The boundary Γ_P defines the (stationary) internal boundary between perforation and the domain for the phase field model. The boundary ∂Y denotes the outer boundary of the unit cell Y. At this boundary we will later apply periodic boundary conditions

allowing to decouple the unit cells from each other. However, when referring to internal boundaries, the boundary Γ_P is meant.

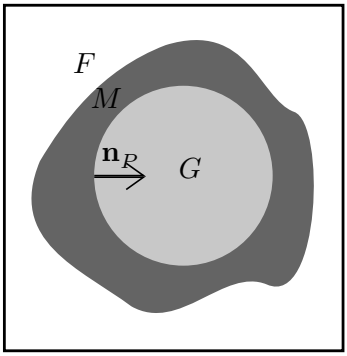

Figure 5.2: Local pore $Y = [0,1]^N$. The fluid part (white) is F, mineral part (dark gray) is M and grain part (light gray) is G, along with a normal vector $\mathbf{n}_P$ at the internal boundary Γ_P. The outer boundary of the local pore, ∂Y, is marked with black.

To distinguish between the two scales in the model we use $\mathbf{x}$ as the variable at the macroscale, which is then connected to the local, microscale variable $\mathbf{y}$ through $\mathbf{y} = \beta^{-1}\mathbf{x}$. This can be interpreted as $\mathbf{x}$ only seeing the macroscale behavior, while the zoomed-in $\mathbf{y}$ sees the microscale rapid changes in a single cell. Hence, for each macroscale point $\mathbf{x}$, we can identify a unit cell, with its own local variable $\mathbf{y}$.

With this we have that the perforated domain of the phase field model is the union of all the local pores P, scaled by β. This means that the domain depends on β and can be written as

$$\Omega^\beta = \cup_{w \in W_\mathcal{D}} \{\beta(w + P)\},$$

where $W_\mathcal{D}$ is a subset of $\mathbb{Z}^N$ satisfying $\mathcal{D} = \cup_{w \in W_\mathcal{D}} \{\beta(w+Y)\}$, which is the complete (non-perforated) medium domain seen to the left in Figure 5.1. We use β as a superscript to indicate dependence on β.

The union of all internal boundaries Γ_P is denoted by

$$\Gamma^\beta = \cup_{w \in W_\mathcal{P}} \{\beta(w + \Gamma_P)\}.$$

5.1.2 Non-Dimensional Model Equations

For identifying which terms are dominating in the model and hence are important for the upscaling, we first non-dimensionalize the model equations (2.5). The assumptions made below on the typical flow rate, viscosity and pressure difference, ensure that we are in the range of Darcy's law, which means that at the macroscale the conservation of momentum equation (2.5c) becomes a Darcy-like law. Also, we ensure that the diffuse interface (i.e., the transition between mineral and fluid) stays within a local pore. Non-dimensional variables and quantities are denoted with a hat and are defined as shown in Table 5.1

Note the superscript β for the variables having a highly oscillatory behavior. The relations between the reference quantities are given through several non-dimensional numbers. The size of these non-dimensional numbers describes which regime we consider. As already mentioned, we are here interested in the regime where Darcy's law is valid and where solute advection, diffusion and reaction time scales are about the same order of magnitude. Darcy's law is valid when fluid flow is laminar and when the pressure drop dominates the flow behavior. This corresponds to the Reynolds and Euler numbers being

$$\mathrm{Re} = \rho_{\mathrm{ref}} v_{\mathrm{ref}} L / \gamma_{\mathrm{ref}} = O(\beta^0), \quad \mathrm{Eu} = p_{\mathrm{ref}} / v_{\mathrm{ref}}^2 \rho_{\mathrm{ref}} = O(\beta^{-2}),$$

respectively. Different choices can e.g. lead to the Forchheimer law [Chen et al. 2001]. The observation time scale t_{ref} is set to be equal to the time scale of solute advection, $t_{\mathrm{adv}} = L/v_{\mathrm{ref}}$. With this we have $v_{\mathrm{ref}} = x_{\mathrm{ref}}/t_{\mathrm{ref}}$ as shown in Table 5.1. Diffusion and reaction time scales are identified as $t_{\mathrm{diff}} = L^2/D_{\mathrm{ref}}$ and $t_{\mathrm{react}} = c_{\mathrm{ref}}\ell/k_{\mathrm{ref}}$, respectively. These time scales are assumed to be about the same

Table 5.1: Variables, reference values and non-dimensional quantities for the non-dimensionalization.

Variable	Reference value	Non-dimensional variable
time	t_{ref}	$\hat{t} = t/t_{\text{ref}}$
space	$x_{\text{ref}} = L$,	$\hat{x} = x/x_{\text{ref}}$
	$y_{\text{ref}} = \ell$,	$\hat{y} = y/y_{\text{ref}}$
	$\varepsilon_{\text{ref}} = \varepsilon$	$\hat{\varepsilon} = 1$
velocity	$v_{\text{ref}} = x_{\text{ref}}/t_{\text{ref}}$	$\hat{\mathbf{v}}^\beta = \mathbf{v}/v_{\text{ref}}$
density	ρ_{ref}	$\hat{\rho}_1 = \rho_1/\rho_{\text{ref}}$
viscosity	γ_{ref}	$\hat{\gamma}_f = \gamma_f/\gamma_{\text{ref}}$
pressure	p_{ref}	$\hat{p}^\beta = p/p_{\text{ref}}$
momentum dissipation rate	K_{ref}	$\hat{K} = K/K_{\text{ref}}$
molar concentration	c_{ref}	$\hat{c}^\beta = c/c_{\text{ref}}$
		$\hat{c}^* = c^*/c_{\text{ref}}$
diffusion coefficient	D_{ref}	$\hat{D} = D/D_{\text{ref}}$
reaction rate	k_{ref}	$\hat{k} = k/k_{\text{ref}}$
Allen–Cahn mobility	α_{ref}	$\hat{\alpha} = \alpha/\alpha_{\text{ref}}$

as the advection time scale, meaning that advection, diffusion and reaction are equally important, which corresponds to the Péclet and Damköhler number being

$$\text{Pe} = t_{\text{diff}}/t_{\text{adv}} = O(\beta^0), \quad \text{Da} = t_{\text{adv}}/t_{\text{react}} = O(\beta^0),$$

respectively. Upscaled models have also been derived for other regimes w.r.t. the Péclet and the Damköhler numbers by employing either homogenization [Allaire and Hutridurga 2012; Bringedal, Berre, et al. 2016b; Choquet and Mikelić 2009; Kumar, van Noorden, et al. 2011; Mikelić, Devigne, et al. 2006; van Duijn, Mikelić, et al. 2008] or volume averaging techniques [Wood et al. 2011; Wood 2007].

For reference quantities and parameters affecting the phase-field variable, we assume that the diffuse interface width is proportional

to the pore size ℓ by the constant factor $\bar{\varepsilon} = \varepsilon/\ell$. In particular, $\bar{\varepsilon}$ should be independent of β. This corresponds to the Cahn number being

$$\mathrm{Ca} = \varepsilon_{\mathrm{ref}}/L = \beta\bar{\varepsilon}.$$

This way, the interface width is small relative to the pore size, but remains a microscale quantity without approaching its sharp-interface limit as β approaches zero. Similar choices are made in the upscaling of the phase field models found in [Daly and Roose 2015; Metzger and Knabner 2021; Redeker et al. 2016], while an interface width that is large compared to the pore size is upscaled in [Schmuck et al. 2013; Schmuck et al. 2012]. In the latter two papers, the phase field appears as a macroscale variable in the upscaled model.

The microscale diffusive time scale of the phase field, i.e., $t_{\mathrm{diff},\alpha} = \ell^2/\alpha_{\mathrm{ref}}$, is chosen to be comparable with the reactive time scale, but where $\hat{\alpha}$ is still allowed to be small but independent of β (i.e., $O(\beta^0)$). Hence, the diffusive Damköhler number of the phase field is

$$\mathrm{Da}_{AC} = t_{\mathrm{diff},\alpha}/t_{\mathrm{react}} = O(\beta^0).$$

This choice supports the phase-field variable as a microscale variable, without affecting the sharp-interface limit as β approaches zero. Finally, the reference value K_{ref} is chosen in relation to the other flow-related reference values to ensure low velocities in the diffuse transition zone as β approaches zero. Interpreting K_{ref} as viscosity divided by a slip length, this corresponds to the Navier number being

$$\mathrm{Na} = \ell_s/L = O(\beta),$$

where $\ell_s = \gamma_{\mathrm{ref}}/K_{\mathrm{ref}}$ is the associated slip length.

For readability, in the following we let the non-dimensional numbers that are equal to $O(\beta^k)$ be exactly equal to β^k, but other choices for the proportionality constants are straightforward. Hence, we now have that $\mathrm{Re} = 1$, $\mathrm{Eu} = \beta^{-2}$, etc. This corresponds to letting $\gamma_{\mathrm{ref}} = \rho_{\mathrm{ref}} L v_{\mathrm{ref}}$ and $p_{\mathrm{ref}} = v_{\mathrm{ref}}^2 \rho_{\mathrm{ref}} L^2/\ell^2$. From the Péclet and Damköhler numbers we get $k_{\mathrm{ref}} = c_{\mathrm{ref}}\ell/t_{\mathrm{ref}}$ and $D_{\mathrm{ref}} = L^2/t_{\mathrm{ref}}$. With this

choice of k_{ref}, the non-dimensional reaction rate can be defined as $\hat{r}(\hat{c}) = \hat{k}(\hat{c}^2/\hat{c}_{\text{eq}}^2 - 1)$. $\text{Da}_{AC} = 1$ corresponds to $\alpha_{\text{ref}} = \ell^2/t_{\text{ref}}$. Finally, $\text{Na} = \beta$ means that $K_{\text{ref}} = \rho_{\text{ref}} v_{\text{ref}} L/\ell$.

Table 5.2 summarizes the choices made in the non-dimensionalization.

Table 5.2: Non-dimensional quantities and their relation to the upscaling parameter β.

Dimensionless number	Definition	Size w.r.t. β
Scale separation	$\beta = \ell/L$	β
Reynolds number	$\text{Re} = \rho_{\text{ref}} v_{\text{ref}} L/\gamma_{\text{ref}}$	β^0
Euler number	$\text{Eu} = p_{\text{ref}}/v_{\text{ref}}^2 \rho_{\text{ref}}$	β^{-2}
Péclet number	$\text{Pe} = L v_{\text{ref}}/D_{\text{ref}}$	β^0
Damköhler number	$\text{Da} = k_{\text{ref}} L/c_{\text{ref}} v_{\text{ref}} \ell$	β^0
Cahn number	$\text{Ca} = \varepsilon_{\text{ref}}/L$	β
Phase field Damköhler number	$\text{Da}_{AC} = k_{\text{ref}} \ell/\alpha_{\text{ref}} c_{\text{ref}}$	β^0
Navier number	$\text{Na} = \gamma_{\text{ref}}/K_{\text{ref}} L$	β

Remark 5.1: *The (non-dimensional) diffuse-interface width $\bar{\varepsilon}$, phase-field mobility $\hat{\alpha}$ and regularization parameter δ are all small, positive numbers that are independent of β. That means, they remain fixed as $\beta \to 0$ in the following section. These three numbers affect the behavior of the phase field model. In particular, $\hat{\varepsilon}$ is the microscale diffuse interface width, $\hat{\alpha}$ dictates the equilibration speed of the diffuse interface, while δ assures the model not being degenerate. These numbers are chosen small in the numerical examples, but do not rely on any internal ordering nor depend on each other.*

Since from now on we only use non-dimensional variables, we skip the hat on all variables. With this, the dimensionless model reads in

Ω^β

$$\bar{\varepsilon}^2\partial_t\phi^\beta + \alpha W'(\phi^\beta) = \beta^2\alpha\bar{\varepsilon}^2\nabla^2\phi^\beta - 4\bar{\varepsilon}\phi^\beta(1-\phi^\beta)\frac{1}{c^*}r(c^\beta), \tag{5.1a}$$

$$\nabla\cdot((\phi^\beta+\delta)\mathbf{v}^\beta) = 0, \tag{5.1b}$$

$$\begin{aligned}&\beta^2\rho_1\Big(\partial_t((\phi^\beta+\delta)\mathbf{v}^\beta) - \frac{1}{2}\mathbf{v}^\beta\partial_t\phi^\beta + \nabla\cdot((\phi^\beta+\delta)\mathbf{v}^\beta\otimes\mathbf{v}^\beta)\Big)\\ &= -(\phi^\beta+\delta)\nabla p^\beta + \beta^2\gamma_f(\phi^\beta+\delta)\nabla^2((\phi^\beta+\delta)\mathbf{v}^\beta) - \frac{K}{\bar{\varepsilon}}\frac{(1-\phi^\beta)n}{\phi^\beta+n}\mathbf{v}^\beta,\end{aligned} \tag{5.1c}$$

$$\partial_t((\phi^\beta+\delta)(c^\beta-c^*)) + \nabla\cdot((\phi^\beta+\delta)\mathbf{v}^\beta c^\beta) = D\nabla\cdot((\phi^\beta+\delta)\nabla c^\beta), \tag{5.1d}$$

with boundary conditions on Γ^β given by

$$\nabla\phi^\beta\cdot\mathbf{n}^\beta = 0, \tag{5.1e}$$

$$(\phi^\beta+\delta)\nabla c^\beta\cdot\mathbf{n}^\beta = 0, \tag{5.1f}$$

$$\mathbf{v}^\beta = 0. \tag{5.1g}$$

Remark 5.2: *Note that the analysis below remains unchanged if $\delta = 0$, when clogging is not considered. In other words, including an β-independent regularization parameter δ does not affect the upscaling. The presence of $\delta > 0$ ensures that the resulting model is not degenerate, which is important for the numerical examples.*

5.1.3 The Formal Asymptotic Expansions

We apply the homogenization ansatz, namely we assume that the unknowns can be written as a series expansion in terms of β with

explicit dependence on the micro- and macroscale variables. For the phase field ϕ^β this reads

$$\phi^\beta(t,\mathbf{x}) = \phi_0(t,\mathbf{x},\mathbf{y}) + \beta\phi_1(t,\mathbf{x},\mathbf{y}) + \beta^2\phi_2(t,\mathbf{x},\mathbf{y}) + \dots, \tag{5.2}$$

where the functions $\phi_i(t,\mathbf{x},\mathbf{y})$ are Y-periodic in $\mathbf{y}$. Similar expansions are assumed for all dependent variables. The introduction of the microscale variable $\mathbf{y}$ is an important aspect: While the ϕ^β needs to resolve both the microscale and macroscale behavior, we assume that the functions in the series expansion can separate between slow variability through $\mathbf{x}$ and fast variability through $\mathbf{y}$. Further, the series expansion allows to capture the dominating behavior in ϕ_0, while lower order behavior is captured through the subsequent terms. Also note that macroscale $\mathbf{x}$ is defined in the entire (non-perforated) domain $\mathcal{D}$, while $\mathbf{y}$ is defined locally in a pore P.

As $\mathbf{y}$ is a local variable behaving like $\mathbf{y} = \beta^{-1}\mathbf{x}$, the spatial derivatives need to be rewritten accordingly. Hence, for a generic variable v one has

$$\nabla v(\mathbf{x},\mathbf{y}) = \nabla_\mathbf{x} v(\mathbf{x},\mathbf{y}) + \frac{1}{\beta}\nabla_\mathbf{y} v(\mathbf{x},\mathbf{y}), \tag{5.3}$$

where $\nabla_\mathbf{x}$ and $\nabla_\mathbf{y}$ are the gradients w.r.t. $\mathbf{x}$ and $\mathbf{y}$, respectively. We insert the asymptotic expansions (5.2) and the rescaled derivatives (5.3) into the model equations (5.1), and equate terms of same order with respect to β to isolate the behavior of the system on different scales. In the regularized equations, the term $\phi_0 + \delta$ appears frequently, and we use the notation $\phi_0^\delta = \phi_0 + \delta$ in this case. Note that $\phi_0^\delta > 0$.

5.1.3.1 Phase Field Equation

Equating the dominating $O(1)$ terms in the phase field equation (5.1a), gives

$$\bar{\varepsilon}^2\partial_t\phi_0 + \alpha W'(\phi_0) = \alpha\bar{\varepsilon}^2\nabla_\mathbf{y}^2\phi_0 - 4\bar{\varepsilon}\phi_0(1-\phi_0)\frac{1}{c^*}r(c_0).$$

The dominating term of the corresponding boundary condition (5.1e) gives $\nabla_{\mathbf{y}}\phi_0 \cdot \mathbf{n}_P = 0$. Observe that the above equation is similar to the original (5.1a), but involves only spatial derivatives w.r.t. $\mathbf{y}$. Although ϕ_0 still depends on $\mathbf{x}$, $\mathbf{x}$ only appears as a parameter as no derivatives w.r.t. $\mathbf{x}$ are involved. Recalling the Y-periodicity in $\mathbf{y}$, ϕ_0 solves the following *cell problem* for the phase field:

$$\begin{aligned} \bar{\varepsilon}^2\partial_t\phi_0 + \alpha W'(\phi_0) &= \alpha\bar{\varepsilon}^2\nabla_{\mathbf{y}}^2\phi_0 - 4\bar{\varepsilon}\phi_0(1-\phi_0)\frac{1}{c^*}r(c_0) && \text{in } P, \\ \nabla_{\mathbf{y}}\phi_0 \cdot \mathbf{n}_P &= 0 && \text{on } \Gamma_P, \\ \text{Periodicity in } \mathbf{y} & && \text{across } \partial Y. \end{aligned} \tag{5.4}$$

These cell problems are defined for each macroscale $\mathbf{x}$, meaning thus for each pore as in Figure 5.2. However, the cell problems are decoupled locally due to the periodicity requirement.

5.1.3.2 Mass Conservation Equation

The dominating $O(\beta^{-1})$ term in (5.1b) gives

$$\nabla_{\mathbf{y}} \cdot (\phi_0^\delta \mathbf{v}_0) = 0 \text{ in } P, \tag{5.5}$$

which is needed in the derivation for the momentum and ion conservation equations. Next, the $O(1)$ terms provide

$$\nabla_{\mathbf{x}} \cdot (\phi_0^\delta \mathbf{v}_0) + \nabla_{\mathbf{y}} \cdot (\phi_0^\delta \mathbf{v}_1 + \phi_1 \mathbf{v}_0) = 0.$$

Integrating w.r.t. $\mathbf{y}$ over P, applying the Gauss theorem and the boundary conditions $\mathbf{v}_0 = \mathbf{v}_1 = 0$ on Γ_P together with periodicity, one gets

$$\nabla_{\mathbf{x}} \cdot \overline{(\phi_0^\delta \mathbf{v}_0)} = 0 \text{ in } \mathcal{D}. \tag{5.6}$$

The overline-notation indicates a quantity averaged over the microscale. Formally, one can extend the quantities defined in the pore space P by 0 inside the perforations G, allowing for an average over the entire cell Y. For a scalar variable $v(t, \mathbf{x}, \mathbf{y})$ we define

$\overline{v}(t,\mathbf{x}) = \frac{1}{|Y|}\int_Y v(t,\mathbf{x},\mathbf{y})d\mathbf{y} = \int_P v(t,\mathbf{x},\mathbf{y})d\mathbf{y}$. Note that $|Y|$, the volume of Y, is 1. In this way, the average of the highest order term of the phase field, $\overline{\phi_0}(t,\mathbf{x})$, corresponds to the porosity at time t at the macroscale location $\mathbf{x}$.

5.1.3.3 Momentum Conservation Equation

The dominating $O(\beta^{-1})$ term in (5.1c) yields

$$\phi_0^\delta \nabla_{\mathbf{y}} p_0 = 0,$$

meaning that $p_0 = p_0(t,\mathbf{x})$ is independent of $\mathbf{y}$. The $O(1)$ terms give

$$\phi_0^\delta(\nabla_{\mathbf{x}} p_0 + \nabla_{\mathbf{y}} p_1) = \gamma_f \phi_0^\delta \nabla_{\mathbf{y}}^2(\phi_0^\delta \mathbf{v}_0) - \frac{K}{\bar{\varepsilon}}\frac{(1-\phi_0)n}{\phi_0+n}\mathbf{v}_0. \tag{5.7}$$

We use the linearity of the equation and determine p_1 and $\mathbf{v}_0$ in terms of (the gradient of) p_0. With $\Pi^j(t,\mathbf{x},\mathbf{y})$ and $\mathbf{w}^j(t,\mathbf{x},\mathbf{y})$ solving the cell problems

$$\begin{aligned}
\phi_0^\delta(\mathbf{e}_j + \nabla_{\mathbf{y}}\Pi^j) + \gamma_f \phi_0^\delta \nabla_{\mathbf{y}}^2(\phi_0^\delta \mathbf{w}^j) = \frac{K}{\bar{\varepsilon}}\frac{(1-\phi_0)n}{\phi_0+n}\mathbf{w}^j \quad &\text{in } P,\\
\nabla_{\mathbf{y}}\cdot(\phi_0^\delta \mathbf{w}^j) = 0 \quad &\text{in } P,\\
\mathbf{w}^j = 0 \quad &\text{on } \Gamma_P,\\
\text{Periodicity in } \mathbf{y} \text{ across } \partial Y,\ j \in \{1,\dots,N\},&
\end{aligned} \tag{5.8}$$

we observe that

$$\begin{aligned}
p_1(t,\mathbf{x},\mathbf{y}) &= \sum_{j=1}^N \Pi^j(t,\mathbf{x},\mathbf{y})\partial_{x_j} p_0(t,\mathbf{x}),\\
\mathbf{v}_0(t,\mathbf{x},\mathbf{y}) &= -\sum_{j=1}^N \mathbf{w}^j(t,\mathbf{x},\mathbf{y})\partial_{x_j} p_0(t,\mathbf{x}),
\end{aligned}$$

now fulfill (5.5) and (5.7). The boundary condition for $\mathbf{w}^j$ on Γ_P follows from $\mathbf{v}_0 = 0$ on Γ_P. Note that the cell problem is solved in $\mathbf{y}$

for a fixed $\mathbf{x}$. Hence, as with the phase field cell problem, one can solve for single pores independently.

Multiplying with ϕ_0^δ in the last equality and averaging over Y gives

$$\overline{\phi_0^\delta \mathbf{v}_0} = -\mathcal{K}\nabla_{\mathbf{x}} p_0 \text{ in } \mathcal{D}, \tag{5.9}$$

where the components of the permeability tensor $\mathcal{K}(t, \mathbf{x})$ are given by

$$k_{ij}(t, \mathbf{x}) = \int_P \phi_0^\delta w_i^j d\mathbf{y}, \qquad \text{with } i, j \in \{1, \dots, N\}.$$

Here, w_i^j are the components of $\mathbf{w}^j$, which are the solutions of the cell problems (5.8) with the continuous extension $\mathbf{w}^j = 0$ inside the grain.

5.1.3.4 Ion Conservation Equation

The dominating $O(\beta^{-2})$ term from the ion conservation equation (5.1d) and dominating $O(\beta^{-1})$ term from the corresponding boundary condition (5.1f) give

$$\begin{aligned} \nabla_{\mathbf{y}} \cdot (\phi_0^\delta \nabla_{\mathbf{y}} c_0) &= 0 && \text{in } P, \\ \phi_0^\delta \nabla_{\mathbf{y}} c_0 \cdot \mathbf{n}_P &= 0 && \text{on } \Gamma_P, \end{aligned}$$

along with periodicity in $\mathbf{y}$. This implies that $c_0 = c_0(t, \mathbf{x})$ is independent of $\mathbf{y}$.

Further, the $O(\beta^{-1})$ terms from (5.1d) and $O(1)$ terms from (5.1f) give

$$\begin{aligned} \nabla_{\mathbf{y}} \cdot (\phi_0^\delta (\nabla_{\mathbf{x}} c_0 + \nabla_{\mathbf{y}} c_1)) &= 0 && \text{in } P, \\ \phi_0^\delta (\nabla_{\mathbf{x}} c_0 + \nabla_{\mathbf{y}} c_1) \cdot \mathbf{n}_P &= 0 && \text{on } \Gamma_P, \end{aligned}$$

where we used (5.5) for the convective term. We exploit again the linearity of the problem and formulate $c_1(t, \mathbf{x}, \mathbf{y})$ in terms of (the

derivatives of) $c_0(t, \mathbf{x})$. We let the weight functions $\omega^j(t, \mathbf{x}, \mathbf{y})$ solve the cell problems

$$\begin{aligned} \nabla_{\mathbf{y}} \cdot (\phi_0^\delta(\nabla_{\mathbf{y}}\omega^j + \mathbf{e}_j)) &= 0 && \text{in } P, \\ \phi_0^\delta(\nabla_{\mathbf{y}}\omega^j + \mathbf{e}_j) \cdot \mathbf{n}_P &= 0 && \text{on } \Gamma_P, \\ \text{Periodicity in } \mathbf{y} &\text{ across } \partial Y, && j \in \{1, \dots, N\}, \end{aligned} \tag{5.10}$$

As earlier, the cell problems are solved in $\mathbf{y}$ for a fixed $\mathbf{x}$. Then, for an arbitrary $\tilde{c}_1 = \tilde{c}_1(t, \mathbf{x})$ we obtain that

$$c_1(t, \mathbf{x}, \mathbf{y}) = \tilde{c}_1(t, \mathbf{x}) + \sum_{j=1}^{N} \omega^j(t, \mathbf{x}, \mathbf{y}) \partial_{x_j} c_0(t, \mathbf{x}).$$

As follows from (5.11) below, only $\nabla_{\mathbf{y}} c_1$ is needed for obtaining the upscaled model, therefore the function $\tilde{c}_1$ plays no role in the upscaling, and it is not necessary to specify it.

The $O(1)$ terms from (5.1d) and $O(\beta)$ terms from (5.1f) give

$$\begin{aligned} &\partial_t(\phi_0^\delta(c_0 - c^*)) + \nabla_{\mathbf{x}} \cdot (\phi_0^\delta \mathbf{v}_0 c_0) + \nabla_{\mathbf{y}} \cdot \mathbf{A} \\ &\quad = D(\nabla_{\mathbf{y}} \cdot \mathbf{B} + \nabla_{\mathbf{x}} \cdot (\phi_0^\delta(\nabla_{\mathbf{x}} c_0 + \nabla_{\mathbf{y}} c_1)) \quad \text{in } \mathcal{D} \times P, \\ &\mathbf{B} \cdot \mathbf{n}_P = 0 \qquad \text{on } \Gamma_P, \end{aligned} \tag{5.11}$$

where $\mathbf{A} = \phi_1 \mathbf{v}_0 c_0 + \phi_0^\delta \mathbf{v}_1 c_0 + \phi_0^\delta \mathbf{v}_0 c_1$ and $\mathbf{B} = \phi_0^\delta \nabla_{\mathbf{x}} c_1 + \phi_0^\delta \nabla_{\mathbf{y}} c_2 + \phi_1 \nabla_{\mathbf{x}} c_0 + \phi_1 \nabla_{\mathbf{y}} c_1$. The above equation contains derivates in both $\mathbf{x}$ and $\mathbf{y}$. To find the upscaled model we integrate in $\mathbf{y}$ over the domain P, apply Gauss' theorem in $\mathbf{y}$, use the boundary condition on Γ_P and the periodicity requirement to remove the $\nabla_{\mathbf{y}} \cdot \mathbf{A}$ and $\nabla_{\mathbf{y}} \cdot \mathbf{B}$ terms. For the velocity terms in $\mathbf{A}$, we also apply the boundary condition (5.1g), which gives $\mathbf{v}_0 = \mathbf{v}_1 = 0$ on Γ_P. This leads to the upscaled reaction-advection-diffusion equation

$$\partial_t(\overline{\phi_0^\delta}(c_0 - c^*)) + \nabla_{\mathbf{x}} \cdot (\overline{\phi_0^\delta \mathbf{v}_0} c_0) = D \nabla_{\mathbf{x}} \cdot (\mathcal{A} \nabla_{\mathbf{x}} c_0) \text{ in } \mathcal{D}. \tag{5.12}$$

The component of the matrix $\mathcal{A}(t, \mathbf{x})$ are

$$a_{ij}(t, \mathbf{x}) = \int_P \phi_0^\delta(\delta_{ij} + \partial_{y_i}\omega^j)d\mathbf{y}, \qquad \text{with } i, j \in \{1, \dots, N\},$$

where ω^j is the solution of the cell problem (5.10). Hence, the upscaled ion conservation equation (5.12) is to be solved for $\mathbf{x} \in \mathcal{D}$ only, but receiving information from the microscale $\mathbf{y}$ through the effective diffusion matrix and the effective velocity.

5.1.4 The Upscaled Allen–Cahn–Navier–Stokes Model

To summarize, the upscaled system of equations consist of the three equations (5.6), (5.9) and (5.12) on the macroscale, for the unknowns $\overline{\phi\mathbf{v}_0}(t, \mathbf{x})$, $p_0(t, \mathbf{x})$ and $c_0(t, \mathbf{x})$. The upscaled system is completed by three supplementary cell problems (5.4), (5.8) and (5.10) to be solved locally in each single pore, providing effective properties for the upscaled system.

The regularization δ was kept throughout the upscaling procedure for consistency. We introduced this regularization for avoiding a degeneracy in the system, which would create difficulties in the numerical implementations. For the upscaled model, these difficulties are encountered in the cell problems. Hence, we only consider ϕ_0^δ in the effective properties and set $\delta = 0$ in (5.6), (5.9) and (5.12). Then, for macroscale $\mathbf{x} \in \mathcal{D}$, and for $t > 0$,

$$\begin{aligned}
\nabla_{\mathbf{x}} \cdot (\overline{\phi_0\mathbf{v}_0}) &= 0 && \text{in } \mathcal{D},\\
\overline{\phi_0\mathbf{v}_0} &= -\mathcal{K}\nabla_{\mathbf{x}} p_0 && \text{in } \mathcal{D},\\
\partial_t(\overline{\phi_0}(c_0 - c^*)) + \nabla_{\mathbf{x}} \cdot (\overline{\phi_0\mathbf{v}_0}c_0) &= D\nabla_{\mathbf{x}} \cdot (\mathcal{A}\nabla_{\mathbf{x}} c_0) && \text{in } \mathcal{D},
\end{aligned}$$

where the phase field $\phi_0(t, \mathbf{x}, \mathbf{y})$ is updated locally in each pore by

solving

$$\begin{aligned} \bar{\varepsilon}^2 \partial_t \phi_0 + \alpha W'(\phi_0) &= \alpha \bar{\varepsilon}^2 \nabla_{\mathbf{y}}^2 \phi_0 - 4\bar{\varepsilon}\phi_0(1-\phi_0)\frac{1}{c^*} r(c_0) && \text{in } P, \\ \nabla_{\mathbf{y}} \phi_0 \cdot \mathbf{n}_P &= 0 && \text{on } \Gamma_P, \end{aligned}$$

for all $\mathbf{x} \in \mathcal{D}$ and $t > 0$. The effective matrices $\mathcal{K}(t, \mathbf{x})$ and $\mathcal{A}(t, \mathbf{x})$ are found through

$$k_{ij}(t, \mathbf{x}) = \int_P \phi_0^\delta w_i^j d\mathbf{y}, \text{ where}$$

$$\begin{aligned} \phi_0^\delta(\mathbf{e}_j + \nabla_{\mathbf{y}} \Pi^j) + \gamma_f \phi_0^\delta \nabla_{\mathbf{y}}^2(\phi_0^\delta \mathbf{w}^j) &= \frac{K}{\bar{\varepsilon}} \frac{(1-\phi_0)n}{\phi_0 + n} \mathbf{w}^j && \text{in } P, \\ \nabla_{\mathbf{y}} \cdot (\phi_0^\delta \mathbf{w}^j) &= 0 && \text{in } P, \\ \mathbf{w}^j &= 0 && \text{on } \Gamma_P, \end{aligned}$$

and

$$a_{ij}(t, \mathbf{x}) = \int_P \phi_0^\delta(\delta_{ij} + \partial_{y_i} \omega^j) d\mathbf{y}, \text{ where}$$

$$\begin{aligned} \nabla_{\mathbf{y}} \cdot (\phi_0^\delta(\nabla_{\mathbf{y}} \omega^j + \mathbf{e}_j) &= 0 && \text{in } P, \\ \phi_0^\delta(\nabla_{\mathbf{y}} \omega^j + \mathbf{e}_j) \cdot \mathbf{n}_P &= 0 && \text{on } \Gamma_P, \end{aligned}$$

for $i, j \in \{1, \dots, N\}$. The unknowns $\mathbf{w}^j(t, \mathbf{x}, \mathbf{y})$, $\Pi^j(t, \mathbf{x}, \mathbf{y})$ and $\omega^j(t, \mathbf{x}, \mathbf{y})$ fulfill periodicity requirements in $\mathbf{y}$ across ∂Y.

5.2 Numerical Investigation for the Upscaled Model

To illustrate the behavior of the phase field model and its dependence on the diffuse interface width and on the upscaling parameter, we solve the cell problems for various choices of $\bar{\varepsilon}$ and compare to the corresponding sharp-interface solution, showing how the effective

ion diffusivity and the flow permeability depend on the width of the diffuse interface. Note that in all examples we solve the corresponding non-dimensional model and that all specified parameters are also non-dimensional.

5.2.1 Solutions to Cell Problems

For sharp-interface models, cell problems for flow and diffusion using a level set formulation have been derived in [Bringedal, Berre, et al. 2016a; van Noorden 2009a]. Note that in both formulations, the local reaction rate is uniform inside each pore as the local ion concentration is constant (cf. Section 5.1.3.4). Hence, if the minerals are initially shaped as circles (or as cylinders), the mineral layer evolves in a radially symmetric manner and the mineral remains a circle (or cylinder), see [van Noorden 2009a]. Hence, the level set formulation can be rewritten into an equation for the radius $R(t, \mathbf{x})$ of the solid (grain and mineral), where the cell problems depend on $R(t, \mathbf{x})$ [Bringedal and Kumar 2017; van Noorden 2009a]. In the radially symmetric case, the effective ion diffusivity and the permeability are scalar quantities.

We adopt a similar approach here, by solving the cell problems (5.8) and (5.10) to determine the effective permeability and ion diffusivity by assuming that the phase field has a smooth transition (of $O(\bar{\varepsilon})$) at some distance R from the center of the cell. We do not attempt to determine permeability and diffusivity curves as functions of R as in [Bringedal and Kumar 2017; van Noorden 2009a] (see e.g. Figure 3 in [van Noorden 2009a]), but instead choose some values of R and investigate the behavior as we let the diffuse interface width $\bar{\varepsilon}$ vary.

The cell problems (5.8) and (5.10) are discretized using a control volume method on a staggered Cartesian grid as in Section 2.3, where the cell problem unknowns ω^j and Π^j are defined in the centers of the control volumes, and the vectors $\mathbf{w}^j$ are at the edges. The grid is uniform and quadratic with 800 grid cells in each direction, so that we have at least 8 grid cells through the diffuse transition zone for

the smallest $\bar{\varepsilon}$. Note that the size of the non-reactive part G does not affect the resulting values of the effective variables as long G is well within the mineral phase. For all the cell problems we use a regularization of $\delta = 10^{-8}$.

Remark 5.3: *Specifying a phase field corresponding to a circular mineral with radius R is not straightforward as no analytical expression exist. An approximate phase field can be found by assuming radial symmetry and considering the reaction-free version of* (5.4) *in polar coordinates. We seek $\phi(t, r)$ solving*

$$\bar{\varepsilon}^2 \partial_t \phi + \alpha W'(\phi) = \alpha \bar{\varepsilon}^2 \frac{1}{r} \partial_r (r \partial_r \phi). \tag{5.13}$$

Because of the non-conservative property of the Allen–Cahn equation, a radially symmetric phase field drop always shrinks towards the center due to curvature effects. Using this, we consider the initial condition

$$\phi(t = 0, r) = \frac{1}{1 + \exp(-4(r - R_0)/\bar{\varepsilon})}, \tag{5.14}$$

where R_0 is larger than the radius R, which is the mineral radius we seek a phase field for. Following from the curvature-driven movement, the mineral shrinks according to the radial Allen–Cahn equation (5.13)*. The simulation is stopped when the radius of the transition region reaches R, more precisely when $\phi = 0.5$ at $r = R$. This resulting phase field is hence used when solving the cell problems. As boundary conditions we apply $\phi = 0$ at $r = 0$ and $\phi = 1$ at $r = 1$. It could be tempting to directly specify* (5.14) *with $R_0 = R$ as the phase field, but this would not fulfill the steady-state version of* (5.13)*. Although* (5.14) *has similar structure as* (2.6)*, which is the solution of the one-dimensional steady-state version of the Allen–Cahn equation, this finding cannot be extended to the radially symmetric case due to the structure of the Laplace operator in polar coordinates. This also means that the initial condition* (5.14) *is only an approximate initial condition.*

5.2.1.1 Permeability

For the cell problem (5.8) providing the permeability we consider mineral radii of $R = 0.2,\ 0.3,\ 0.4$. The corresponding permeability values for these mineral radii are $\mathcal{K} = 3.3 \times 10^{-2},\ 1.1 \times 10^{-2},\ 1.8 \times 10^{-3}$, respectively [Bringedal and Kumar 2017]. The applied values of $\bar{\varepsilon}$ in (5.14) are $\bar{\varepsilon} = 0.05,\ 0.04,\ 0.03,\ 0.02,\ 0.01,\ 0.0075,\ 0.005$. In Figure 5.3, the phase field permeability values are compared to the permeability values resulting from the corresponding sharp interface models. It becomes clear that the phase field permeability values are approaching the ones for the sharp interface models as the values of $\bar{\varepsilon}$ are decreasing. However, the relative errors are large, and are for $\bar{\varepsilon} = 0.01$ equal to 5%, 7% and 15% for $R = 0.2,\ 0.3,\ 0.4$, respectively. These deviations can be explained by the fact that flow takes place in the diffuse transition zone, which enhances the flow through the entire cell, and hence overestimates the permeability. This effect is diminished when the parameter K in the phase field cell problem (5.8) is increased, but larger values of K could also lead to an underestimation of the permeability if $\bar{\varepsilon}$ is large. For the results in Figure 5.3, $K = 25$ was used. Hence, finding a good choice for the interpolation function $d(\phi, \bar{\varepsilon})$ in (2.5c) is essential in the numerical implementation.

5.2.1.2 Effective Ion Diffusivity

For the effective diffusivity cell problem (5.10) we consider the same values for R and $\bar{\varepsilon}$. The effective diffusivities for the sharp-interface model are, for these three values of R, $\mathcal{A} = 0.78,\ 0.56,\ 0.32$, respectively. These values have been found by solving the corresponding sharp-interface cell problems for the diffusion tensor, whose formulation can be found e.g. in [van Noorden 2009a], using the PDE toolbox in Matlab on recursively finer grids until four digits of accuracy are obtained. The phase field effective diffusion values are compared to the corresponding sharp interface effective diffusion values in Figure 5.4. Although the phase field values seemingly

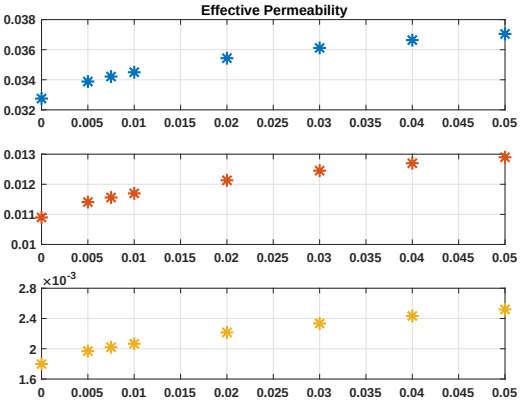

Figure 5.3: Permeability values for $R = 0.2$ (top), $R = 0.3$ (middle) and $R = 0.4$ (bottom), plotted over various values of $\bar{\varepsilon}$. The sharp interface values are plotted at $\bar{\varepsilon} = 0$.

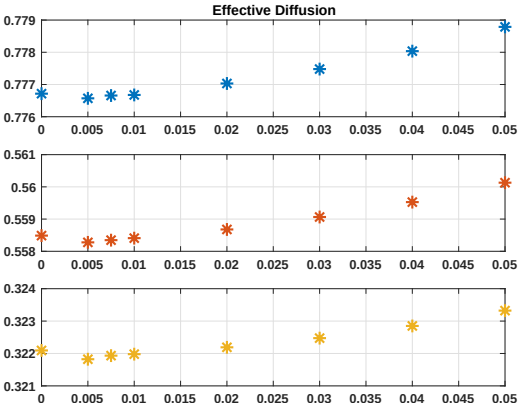

Figure 5.4: Effective diffusion values for $R = 0.2$ (top), $R = 0.3$ (middle) and $R = 0.4$ (bottom), plotted over various values of $\bar{\varepsilon}$. The sharp interface values are plotted at $\bar{\varepsilon} = 0$.

converge towards a slightly different value than the value provided by the sharp interface model, it is worth noting that the relative errors are rather small ($< 0.3\%$ in all cases), hence the effective diffusion tensors are well approximated even for large values of $\bar{\varepsilon}$. Note that when defining the transition zone to being where $\phi = 0.5$, leads to a slightly over-estimated size of the grain as the transition zone spreads out radially, which can explain why the diffusion values approaches a slightly too low value. For example, for $R = 0.3$ the relative difference between the true porosity and the one found through Remark 5.3 using $\bar{\varepsilon} = 0.01$ is 0.03%. Other potential sources of errors would be difference in numerical solvers between the diffuse and sharp-interface discretizations.

Upscaling the Allen–Cahn Model in a Thin Strip

6

A simple but instructive averaged model can be obtained by considering the non-dimensional Allen–Cahn model from Chapter 5, Equations (5.1) in a two-dimensional thin strip, mimicking the flow through a long pore. In this case, the scale separation is defined through the ratio $\beta = \ell/L$ between the width ℓ and the length L of the strip. Sharp interface formulations for models in a thin strip and considering reactive transport leading to changes in the pore geometry have been formulated and upscaled in [Bringedal, Berre, et al. 2015; Bringedal, Berre, et al. 2016b; Kumar, van Noorden, et al. 2011; van Noorden 2009b]. The advantage of formulating such sharp interface models in the geometry of a thin strip is that mineral phase can easily be described by its width, depending on the location along the strip.

This chapter is organized as follows. In Section 6.1 we derive the resulting effective model for the thin strip through asymptotic expansions and transversal averaging of the non-dimensional model equations. We then proceed with numerical experiments in Section 6.2 to compare this model to a sharp interface model and the original two-dimensional formulation.

6.1 Upscaling

We set the domain of the thin strip as $\Omega = (0, L) \times (0, \ell)$, such that $\beta = \ell/L$ defines the scale separation. For the non-dimensional case we rescale the domain of the thin strip as $(x, y) \in (0, 1)^2$. Note that y now plays the role of the transversal variable, and not a local one, but is still scaled by the factor β and represents the direction where rapid changes are occurring. Derivatives in the y-direction (across the strip) are scaled with $1/\beta$. Hence, for a dummy variable $v(x, y)$ one gets

$$\nabla v(x, y) = \partial_x v \, \mathbf{e}_x + \frac{1}{\beta} \partial_y v \, \mathbf{e}_y,$$

where $\mathbf{e}_x$ and $\mathbf{e}_y$ are unit vectors in the directions along and across the thin strip.

As a starting point, we use the non-dimensional model equations (5.1) in the domain of the thin strip. For this, we make exactly the same assumptions on the scaling of non-dimensional numbers as in Section 5.1.2.

6.1.1 Transversal Averaging

We assume symmetry along $y = 1/2$ and only consider the lower half of the strip. We assume the existence of asymptotic expansions in the form

$$\phi^\beta(t, \mathbf{x}) = \phi_0(t, x, y) + \beta \phi_1(t, x, y) + \dots, \tag{6.1}$$

for all variables.

As seen analogous to the sharp interface limit, Equation (2.6), a leading order solution to the phase field equation (5.1a) approaching value 1 in the fluid part and 0 in the mineral part is given by

$$\phi_0(t, x, y) = \frac{1}{1 + e^{-4(y-d)/\bar{\varepsilon}}}, \tag{6.2}$$

where $y = d(t,x)$ defines the interface between fluid and mineral through $\phi_0 = 1/2$. This formulation uses $d(t,x)$ as an unknown, analogous to sharp-interface models for the thin strip [Bringedal, Berre, et al. 2015; Bringedal, Berre, et al. 2016b; Kumar, van Noorden, et al. 2011; van Noorden 2009b]. Equation (6.2) still incorporates a phase field variable that affects the model formulation. However, as ϕ_0 in (6.2) does not fulfill the zero Neumann and symmetry boundary conditions, we are making a small error by using this phase field (for $d \approx 0$ and $d \approx 1/2$, this error in can also be large). Under the assumption that no clogging appears, there are no problems with degeneracy in the equations for the resulting thin strip model. We therefore let $\delta = 0$. It is possible to do the transversal averaging also with $\delta > 0$, and would only require the phase field ϕ being replaced with $\phi + \delta$ in the ion and mass conservation equations.

We take a different approach in Chapter 7, where we do not find an explicit solution to the phase field equation, but instead keep the phase field equation as a one-dimensional cell-problem, that has to be solved for. This also means that we can not set $\delta = 0$ in Chapter 7, as this would lead to a possibly degenerate cell-problem.

6.1.1.1 Equation for $d(t,x)$

The equation for $d(t,x)$ is obtained by inserting (6.2) into the phase field equation (5.1a) and collecting the lowest order terms in β, $O(\beta^0)$. This results in

$$\bar{\varepsilon}^2 \partial_t \phi_0 + \alpha W'(\phi_0) = \alpha \bar{\varepsilon}^2 \partial_y^2 \phi_0 - 4\bar{\varepsilon}\phi_0(1-\phi_0)\frac{1}{c^*} r(c_0).$$

We show in Section 6.1.1.5 that c_0 is independent of y. Inserting (6.2) for ϕ_0 and using the equalities

$$\partial_t \phi_0 = -\frac{4}{\bar{\varepsilon}}\phi_0(1-\phi_0)\partial_t d,$$

$$\partial_y^2 \phi_0 = \frac{4^2}{\bar{\varepsilon}^2}\phi_0(1-\phi_0)(1-2\phi_0),$$

and cancelling equal terms and common factors, results in

$$\partial_t d = \frac{1}{c^*} r(c_0). \tag{6.3}$$

Hence, the phase field $\phi_0(t, x, y)$ is given by (6.2), where the mineral width $d(t, x)$ follows from (6.3).

Note that the resulting equation for $d(t, x)$ is the same model equation as used in the sharp interface thin strip formulations as [Bringedal, Berre, et al. 2015; van Noorden 2009b]. However, the phase field $\phi(t, x, y)$ still appears in the upscaled solute transport and flow equations. This allows to illustrate the behavior of the phase field model with respect to $\bar{\varepsilon}$ and β in a simple setting.

6.1.1.2 Equation for the Averaged Phase Field

The transversally averaged phase field is needed in the upscaled thin strip model. In view of the symmetry, the transversal average of (6.2) is

$$\begin{aligned}\overline{\phi}_0 &= 2\int_0^{1/2} \frac{1}{1 + e^{-4(y-d)/\bar{\varepsilon}}} dy \\ &= 1 + \frac{\bar{\varepsilon}}{2} \log\left(1 + e^{-\frac{4}{\bar{\varepsilon}}(0.5-d)}\right) - \frac{\bar{\varepsilon}}{2} \log\left(1 + e^{\frac{4}{\bar{\varepsilon}}d}\right).\end{aligned}$$

6.1.1.3 Equation for Mass Conservation

The lowest order term arising from the mass conservation equation (5.1b) yields

$$\partial_y(\phi_0 \mathbf{v}_0^y) = 0,$$

which together with the boundary condition (5.1g) gives that the lowest order transversal velocity component $\mathbf{v}_0^y$ is independent of y. The next order provides

$$\partial_x(\phi_0 \mathbf{v}_0^x) + \partial_y(\phi_0 \mathbf{v}_1^y) = 0,$$

where $\mathbf{v}_0^x$ is the lowest order along-strip velocity component and $\mathbf{v}_1^y$ is the first order transversal velocity component. This equation is integrated in y from 0 to 1/2, which together with boundary condition (5.1g) at $y = 0$ and symmetry at $y = 1/2$ gives

$$\partial_x(\overline{\phi_0 \mathbf{v}_0^x}) = 0.$$

6.1.1.4 Equation for Average Flow Rate

Inserting asymptotic expansions into (5.1c), from the lowest order term one gets

$$\phi_0 \partial_y p_0 = 0.$$

As $\phi_0 > 0$ this implies that $p_0 = p_0(t, x)$ is independent of y. The longitudinal (along the strip) component of the $O(1)$ terms provides

$$0 = -\phi_0 \partial_x p_0 + \gamma_f \phi_0 \partial_y^2(\phi_0 \mathbf{v}_0^x) - \frac{K}{\bar{\varepsilon}} \frac{(1-\phi_0)n}{\phi_0 + n} \mathbf{v}_0^x.$$

We let $q = \phi_0 \mathbf{v}_0^x$ represent the unknown and insert the expression for ϕ_0, (6.2) when necessary. Then,

$$\gamma_f \partial_y^2 q - \frac{K}{\bar{\varepsilon}} \frac{n e^{-4(y-d)/\bar{\varepsilon}} (1 + e^{-4(y-d)/\bar{\varepsilon}})^2}{1 + n(1 + e^{-4(y-d)/\bar{\varepsilon}})} q = \partial_x p_0, \tag{6.4}$$

The variables t and x appearing in d and p are considered parameters. Hence, we have an inhomogeneous, second-order, linear ODE with non-constant coefficients. Finding simple analytical expressions for the solution of q is not straightforward. Instead, a boundary condition $\overline{\phi_0 \mathbf{v}_0^x} = 1$ at $x = 0$ and $x = 1$ can be used to resolve the flow through the strip together with mass conservation. This means that we do not need to solve for the pressure p and flow profile q inside the thin strip, but instead just use mass conservation for the upscaled model.

6.1.1.5 Equation for Ion Concentration

Inserting (6.2) for ϕ_0 and the asymptotic expansion of c^β into (5.1d) and equating the lowest order terms yields

$$\partial_y(\phi_0 \partial_y c_0) = 0.$$

Together with the lowest order boundary condition $\phi_0 \partial_y c_0 = 0$ at $y = 0$ and $y = 1$, and that $\phi > 0$, it follows that c_0 is independent of the transversal variable y, i.e.,

$$c_0 = c_0(t, x).$$

Integrating (5.1d) in y from 0 to 1/2, and applying boundary conditions (5.1f) and (5.1g) on the lower boundary and symmetry conditions on $y = 1/2$, results in

$$\begin{aligned}\int_0^{1/2} \partial_t(\phi(c^\beta - c^*))dy + \int_0^{1/2} \partial_x(\phi \mathbf{v}^{\beta,x}(c^\beta - c^*))dy \\ = D \int_0^{1/2} \partial_x(\phi \partial_x(c^\beta - c^*))dy,\end{aligned}$$

where $\mathbf{v}^{\beta,x}$ is the along-strip component of the $\mathbf{v}^\beta$. Using the asymptotic expansions and using that c_0 is independent of y leads to

$$\partial_t(\overline{\phi}_0(c_0 - c^*)) + \partial_x(\overline{\phi_0 \mathbf{v}_0^x}(c_0 - c^*)) = D\partial_x(\overline{\phi}_0 \partial_x(c_0 - c^*).$$

6.1.2 The Averaged Allen–Cahn–Navier–Stokes Model

We can now summarize the results of the transversal averaging. With the unknowns $d(t, x)$, $\overline{\phi_0}(t, x)$, $c_0(t, x)$, and $\overline{\phi_0 \mathbf{v}_0^x}(t, x)$, the upscaled

equations obtained by transversal averaging are

$$\partial_t d = \frac{1}{c^*} r(c_0), \tag{6.5a}$$

$$\overline{\phi_0} = 1 + \frac{\bar{\varepsilon}}{2} \log\left(1 + e^{-4(0.5-d)/\bar{\varepsilon}}\right) - \frac{\bar{\varepsilon}}{2} \log\left(1 + e^{4d/\bar{\varepsilon}}\right), \tag{6.5b}$$

$$\overline{\phi_0 \mathbf{v}_0^x} = 1, \tag{6.5c}$$

$$\partial_t(\overline{\phi_0}(c_0 - c^*)) = -\partial_x(\overline{\phi_0 \mathbf{v}_0^x}(c_0 - c^*)) + D\partial_x(\overline{\phi_0}\partial_x(c_0 - c^*)), \tag{6.5d}$$

for $x \in (0, 1)$ and $t > 0$. Note the absence of a momentum conservation equation, and hence the pressure is not obtained here.

6.2 Numerical Investigation

The original equations (5.1) are formulated on the scaled strip $(x, y) \in [0, 1]^2$, but using symmetry at $y = 0.5$. Therefore, only half of the strip needs to be considered. For both the original system (5.1) and the transversally averaged system (6.5), we design an example including dissolution. We let $c_0(t = 0) = c^\beta(t = 0) = 0.5$ in the entire domain initially, and inject an ion concentration of $c_0 = c^\beta = 0.25$ at $x = 0$. At the outlet $x = 1$ we assume zero Neumann condition for the ion concentration. The reaction rate is chosen to be $r(c) = c^2/0.5^2 - 1$, corresponding to an equilibrium concentration of $c_{\text{eq}} = 0.5$. Hence, net dissolution occurs when injecting a lower ion concentration. Initially the strip is assumed to be halfway filled with a mineral layer at top and bottom, i.e., $d(t = 0) = 0.25$. The phase field in the original equations is initialized with (6.2) using $d = 0.25$. Also, we apply a zero Neumann condition for the phase field at both inlet and outlet. The original model (5.1) is initialized with constant pressure and zero velocity. In the upscaled system (6.5), the inlet condition $\overline{\phi \mathbf{v}_0^x} = 1$ also gives the flow through the strip. For the original equations (5.1), the inlet condition for the along-strip component of the flow rate $\mathbf{v}^\beta$, $\mathbf{v}^{\beta,x}$, is formulated using a time-dependent parabolic

profile such that $\mathbf{v}_x^\beta = 0$ at $y = d(t,0)$, $\partial_y \mathbf{v}^{\beta,x} = 0$ at the symmetry line $y = 0.5$, and $\overline{\phi^\beta \mathbf{v}^{\beta,x}} = 1$ is fulfilled. The outlet condition for pressure is a zero Neumann condition.

The following (non-dimensional) constants have been used in the simulations:

$$D = 1, \quad c^* = 1, \quad \alpha = 0.0075, \quad K = 25, \quad \rho_1 = 1, \quad \gamma_f = 1.$$

The value of α is chosen small to ensure low surface curvature effects, while the value of K is chosen large to avoid too much flow in the diffuse transition zone. Also note that the mineral concentration is chosen artificially low so that large changes in the mineral width occur [van Noorden 2009b]. We let $\delta = 10^{-6}$ in the original model (5.1) for all simulations.

Similar as in Section 5.2.1 and Section 2.3, both the original equations (5.1) and the averaged system (6.5) are discretized using a control volume method on a staggered Cartesian grid where ion concentration, pressure and phase field are defined in the centers of the control volumes, and the velocities across the edges. For the original equations rectangular grids are used, where the resolution in the transversal direction is fine enough to resolve the diffuse transition zone properly.

6.2.1 Comparison to the Sharp Interface Formulation

For the upscaled system of equations (6.5), we can compare the obtained solution with similar upscaled models based on a sharp interface formulation, such as the ones found in [Bringedal, Berre, et al. 2015; van Noorden 2009b]. Discretizing the sharp interface model with the same method, and choosing same initial and boundary conditions, we can investigate the effect of the diffuse interface $\bar{\varepsilon}$ on the model variables.

There are some minor differences in ion concentration c_0, and accordingly in the value of mineral width d as the reaction rate depends

on c_0. Figure 6.1 shows the ion concentrations in the sharp interface model and in the phase field model for various values of $\bar{\varepsilon}$ at $t = 0.5$. For smaller values of $\bar{\varepsilon}$, the ion concentration approaches the values found through the sharp interface model. The differences in values for the mineral width are small (the largest absolute difference for $\bar{\varepsilon} = 0.05$ is 0.003).

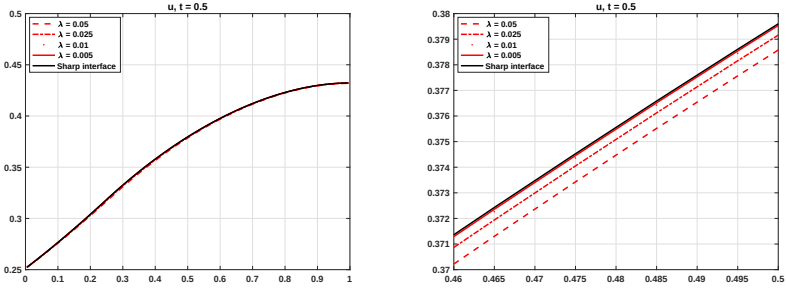

Figure 6.1: Ion concentration inside thin strip at $t = 0.5$. Right figure shows zoomed in view near the middle of the strip, where the largest differences between the model runs are found.

6.2.2 Comparison to the Original Two-Dimensional Formulation

We can also check the quality of the upscaling procedure; namely, whether the transversal averages of the output from the original equations (5.1) approaches the model output found by the upscaled model (6.5) as β approaches zero. For this comparison we fix a value of $\bar{\varepsilon}$ and let β vary. For simplicity, we consider $\bar{\varepsilon} = 0.05,\ 0.01$, and $\beta = 0.1,\ 0.05,\ 0.025,\ 0.01,\ 0.005$, where the latter corresponds to a strip that is 200 times longer than its width. A typical snapshot from a simulation, with $\bar{\varepsilon} = 0.05$ and $\beta = 0.1$ is seen in Figure 6.2. Even for such a "large" value of β, the derivatives with respect to y of e.g. ion concentration, is practically zero. The flow field is found through solving Navier–Stokes, and the along-strip component shows

a parabola-like profile as expected for this regime. Some flow inside the diffuse interface can be seen.

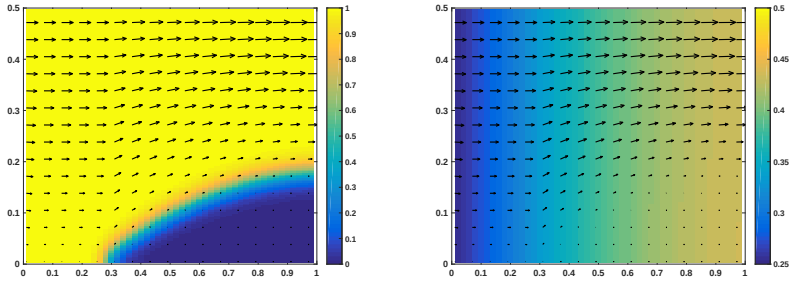

Figure 6.2: Phase field (left) and ion concentration (right) in thin strip at $t = 0.5$. Note that the y-axis is scaled to fit between 0 and 0.5, but should be between 0 and 0.5β. Velocity field is given as vector overlay and is mainly along the strip. The transversal component of the velocity field has been scaled with $1/\beta$. For this simulation, $\beta = 0.1$ and $\bar{\varepsilon} = 0.05$. The domain was discretized with 50 control volumes in the x-direction and 150 control volumes in the y-direction.

By vertically averaging the results from the original equations (5.1) and comparing to the results from the already upscaled model (6.5), we find in general good correspondence. There is little variability in the transversal direction for ion concentration already for relatively large values of β, as illustrated in Figure 6.2 for $\beta = 0.1$. Hence, the averaged ion concentration does not deviate much when decreasing β. However, some difference is found in the dissolution of the mineral between the two-dimensional model (5.1) and the upscaled model (6.5). These differences do not change with smaller β. The upscaled system of equations uses directly $\partial_t d = r(c)/c^*$, which is equivalent to the reaction rate found in a sharp interface model, while the original phase field equation still has an effect from the interface width $\bar{\varepsilon}$ in the reaction rate.

Also, the upscaled model uses an approximated phase field which does

not fulfill the boundary conditions at the top and lower boundaries, and in particular makes a big error in the boundary conditions for $d \approx 0$, i.e., the point where the fluid–solid interface meets the outer boundary. However, as seen from Figure 6.3 and Figure 6.4, the differences in d and c are small already for $\bar{\varepsilon} = 0.05$.

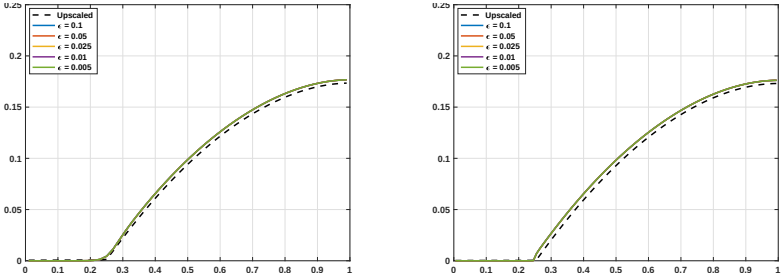

Figure 6.3: Width of mineral layer $d(t, x)$ inside (the lower half of) the thin strip at $t = 0.5$ for $\bar{\varepsilon} = 0.05$ (left) and $\bar{\varepsilon} = 0.01$ (right). Note that the colored lines, corresponding to averaged results from the original equations (5.1)*, are (almost) on top of each other. The mineral width is found through the phase field by* $(0.5 - 0.5\overline{\phi}^{\beta})$.

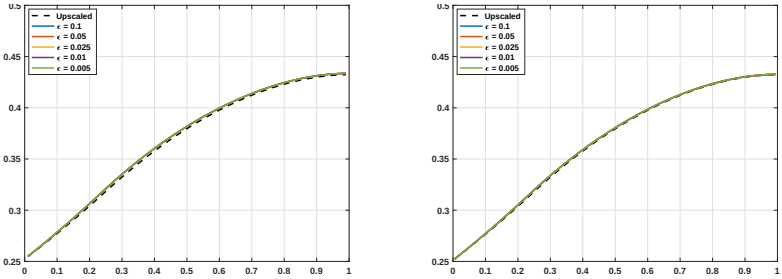

Figure 6.4: Transversally averaged ion concentration inside thin strip at $t = 0.5$ for $\bar{\varepsilon} = 0.05$ (left) and $\bar{\varepsilon} = 0.01$ (right). Note that the colored lines, corresponding to averaged results from the original equations (5.1)*, are (almost) on top of each other.*

Upscaling the Cahn–Hilliard Model in a Thin Strip

7

As in the previous chapter, we are interested in the behavior of our models in the simplified geometry of a thin strip. We now consider the full Cahn–Hilliard Model from Chapter 3, including two fluid phases. Compared to Chapter 6, this introduces additional complexity and requires a more refined strategy.

This chapter is organized as follows. First we bring the δ-$2f1s$-model from Chapter 3 to a non-dimensional form in Section 7.1. In Section 7.2 we derive its upscaled counterpart by considering a thin strip geometry. The upscaled model still uses phase-field variables to locate the diffuse interfaces. In Section 7.3 we identify the sharp-interface limit of the upscaled model. Notably the upscaling and the sharp-interface limit commute. The numerical examples discussed in Section 7.5 conclude this chapter.

7.1 Non-dimensionalization

We proceed by bringing the δ-$2f1s$-model (3.45)–(3.50) to a non-dimensional form, and derive an upscaled counterpart of it by employing asymptotic expansion and averaging techniques. We consider a simplified geometric setting, and start by introducing a thin strip having length L and width $\ell \ll L$, as shown in Figure 7.1.

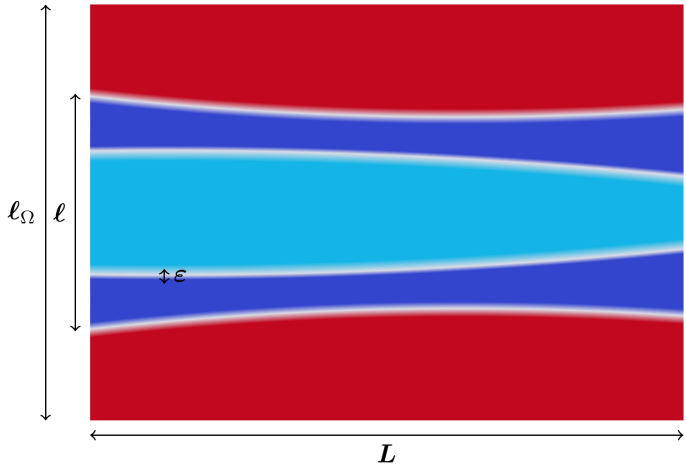

Figure 7.1: Setting of the thin strip: The strip with length L and width ℓ consists of solid walls (red, $\boldsymbol{\Phi} \approx (0,0,1)^\top$) and fluid phases (light blue, dark blue). The diffuse interface width ε is smaller than ℓ.

With a chosen domain width $\ell_\Omega > \ell$, the domain $\Omega = (0, L) \times (-\ell_\Omega/2, \ell_\Omega/2)$ includes the thin strip mentioned above, which is identified as $[0, L] \times [-\ell/2, \ell/2]$. The region outside the strip is occupied by the mineral, so $\boldsymbol{\Phi} \approx (0,0,1)^t$ there. As an important difference to the construction in Chapter 6 we do not allow for $\ell_\Omega = \ell$, i.e., dissolution of the mineral up to the boundary of Ω. The diffuse interfaces are located in regions of width ε. We assume here that the diffuse-interface regions remain clearly separated inside the thin strip, hence $\varepsilon \ll \ell$.

Three length scales can be identified, $L \gg \ell \gg \varepsilon$. These are related through the aspect ratio $\beta = \ell/L$ and the Cahn-Number $Cn = \varepsilon/L$, both assumed small. Observe that, in fact, $Cn \ll \beta \ll 1$.

The reference quantities used in the non-dimensionalization procedure are listed in Table 7.1. Non-dimensional values are then identified by a hat. Note that we relate only few reference values directly to each other. In particular, we do relate reference values

when we want to emphasize an explicit dependence on y_{ref}, as seen for p_{ref}, d_{ref} and μ_{ref}. The choices are motivated as follows. To obtain an upscaled macroscopic velocity of order $v_{\text{ref}} = x_{\text{ref}}/t_{\text{ref}}$, the pressure drop in the thin strip has to scale with $1/(y_{\text{ref}})^2$ (this means that the Euler number scales with β^{-2}). Also, the slip length L_{slip} is supposed to be of order ℓ and not L, which is achieved by a momentum dissipation scaling $1/(y_{\text{ref}})^2$.

We rewrite the Cahn number introduced above in terms of reference quantities, and define other dimensionless numbers that are used below to relate the reference quantities: the Reynolds number, Capillary number, Damköhler number and Péclet numbers of the phase field and ion concentration,

$$\begin{aligned} Re &= \frac{\rho_{\text{ref}} v_{\text{ref}} x_{\text{ref}}}{\gamma_{\text{ref}}}, & Ca &= \frac{\gamma_{\text{ref}} v_{\text{ref}}}{\Sigma_{\text{ref}}}, & Cn &= \frac{\varepsilon_{\text{ref}}}{x_{\text{ref}}}, \\ Da &= \frac{r_{\text{ref}} x_{\text{ref}}}{v_{\text{ref}}}, & Pe_{CH} &= \frac{v_{\text{ref}} x_{\text{ref}}}{M_{\text{ref}}}, & Pe_c &= \frac{v_{\text{ref}} x_{\text{ref}}}{D_{\text{ref}}}. \end{aligned} \tag{7.1}$$

Clearly, the non-dimensionalization also affects the spatial and temporal derivatives, namely

$$\hat{\nabla} = x_{\text{ref}} \nabla, \quad \text{and} \quad \partial_{\hat{t}} = t_{\text{ref}} \partial_t. \tag{7.2}$$

We now can insert the non-dimensional variables of Table 7.1, the non-dimensional numbers (7.1) and the non-dimensional operators in (7.2) into the δ-$2f1s$-model (3.45)–(3.50).

For the reaction terms we use the equation

$$R_1 = -q(\boldsymbol{\Phi}) \left(r(c) + \tilde{\alpha}\mu_1 - \tilde{\alpha}\mu_3 \right)$$

instead of (3.54), as we will impose the relation between the reaction term R_1 and $\bar{\varepsilon}$ through the Damköhler number Da.

Table 7.1: Variables, reference values and non-dimensional quantities for the non-dimensionalization.

Variable	Reference value	Non-dimensional variable
time	$t_{\mathrm{ref}} = T$	$\hat{t} = t/t_{\mathrm{ref}}$
space	$x_{\mathrm{ref}} = L$,	$\hat{x} = x/x_{\mathrm{ref}}$
	$y_{\mathrm{ref}} = \ell$,	$\hat{y} = y/y_{\mathrm{ref}}$
	$\varepsilon_{\mathrm{ref}} = \varepsilon$	$\hat{\varepsilon} = 1$
velocity	$v_{\mathrm{ref}} = x_{\mathrm{ref}}/t_{\mathrm{ref}}$	$\hat{\mathbf{v}} = \mathbf{v}/v_{\mathrm{ref}}$
density	$\rho_{\mathrm{ref}} = \rho_1$	$\hat{\rho}_i = \rho_i/\rho_{\mathrm{ref}}$, $i \in \{1,2,3\}$
		$\hat{\rho}_f = \rho_f/\rho_{\mathrm{ref}}$
		$\hat{\tilde{\rho}}_f = \tilde{\rho}_f/\rho_{\mathrm{ref}}$
viscosity	$\gamma_{\mathrm{ref}} = \gamma_1$	$\hat{\gamma}_i = \gamma_i/\gamma_{\mathrm{ref}}$, $i \in \{1,2,3\}$
		$\hat{\tilde{\gamma}} = \tilde{\gamma}/\gamma_{\mathrm{ref}}$
pressure	$p_{\mathrm{ref}} = \gamma_{\mathrm{ref}} v_{\mathrm{ref}} x_{\mathrm{ref}} y_{\mathrm{ref}}^{-2}$	$\hat{p} = p/p_{\mathrm{ref}}$
momentum dissipation rate	$d_{\mathrm{ref}} = \gamma_{\mathrm{ref}}/(\rho_{\mathrm{ref}} y_{\mathrm{ref}}^2)$	$\hat{d} = d/d_{\mathrm{ref}}$
surface energy	$\Sigma_{\mathrm{ref}} = \Sigma_1$	$\hat{\Sigma}_i = \Sigma_i/\Sigma_{\mathrm{ref}}$, $i \in \{1,2,3\}$
CH mobility	$M_{\mathrm{ref}} = M$	$\hat{M} = 1$
CH chemical potential	$\mu_{\mathrm{ref}} = \Sigma_{\mathrm{ref}}/y_{\mathrm{ref}}$	$\hat{\mu} = \mu/\mu_{\mathrm{ref}}$
CH triple-well potential	$W_{\mathrm{ref}} = \Sigma_{\mathrm{ref}}$	$\hat{W} = W/\Sigma_{\mathrm{ref}}$
molar concentration	$c_{\mathrm{ref}} = c^*$	$\hat{c} = c/c_{\mathrm{ref}}$
diffusion coefficient	$D_{\mathrm{ref}} = D$	$\hat{D} = 1$
reaction rate	r_{ref}	$\hat{r}(\hat{c}) = r(c)/r_{\mathrm{ref}}$
AC mobility	$\alpha_{\mathrm{ref}} = r_{\mathrm{ref}}/\mu_{\mathrm{ref}}$	$\hat{\alpha} = \alpha/\alpha_{\mathrm{ref}}$

With this, the non-dimensional equations become

$$\hat{\nabla}\cdot(\tilde{\hat{\phi}}_f\hat{\mathbf{v}})=0, \tag{7.3}$$

$$\begin{aligned}\partial_{\hat{t}}(\tilde{\hat{\rho}}_f\hat{\mathbf{v}})+\hat{\nabla}\cdot(\hat{\rho}_f\hat{\mathbf{v}}\otimes\hat{\mathbf{v}})+\frac{Cn}{\beta Pe_{CH}}\hat{\nabla}\cdot((\hat{\rho}_1\hat{\mathbf{J}}_1+\hat{\rho}_2\hat{\mathbf{J}}_2)\otimes\hat{\mathbf{v}})\\ =-\frac{1}{\beta^2 Re}\tilde{\hat{\phi}}_f\hat{\nabla}\hat{p}+\frac{1}{Re}\hat{\nabla}\cdot(2\tilde{\hat{\gamma}}(\boldsymbol{\Phi})\hat{\nabla}^s\hat{\mathbf{v}})\\ -\frac{1}{\beta^2 Re}\hat{\rho}_3\hat{d}(\tilde{\hat{\phi}}_f)\hat{\mathbf{v}}+\frac{1}{\beta Re}\frac{1}{Ca}\hat{\tilde{\mathbf{S}}}+Da\frac{1}{2}\hat{\rho}_1\hat{\mathbf{v}}\hat{R},\end{aligned} \tag{7.4}$$

for the flow,

$$\partial_{\hat{t}}(\tilde{\hat{\phi}}_c\hat{c})+\hat{\nabla}\cdot(\phi_c\hat{\mathbf{v}}\hat{c})+\frac{Cn}{\beta Pe_{CH}}\hat{\nabla}\cdot(\hat{\mathbf{J}}_1\hat{c})=\frac{1}{Pe_c}\hat{\nabla}\cdot(\tilde{\hat{\phi}}_c\hat{\nabla}\hat{c})+Da\hat{R}, \tag{7.5}$$

for the ion transport-diffusion-reaction, while for the Cahn–Hilliard evolution one gets

$$\partial_{\hat{t}}\phi_1+\hat{\nabla}\cdot(\phi_1\hat{\mathbf{v}})+\frac{Cn}{\beta Pe_{CH}}\hat{\nabla}\cdot\hat{\mathbf{J}}_1=Da\hat{R}, \tag{7.6}$$

$$\partial_{\hat{t}}\phi_2+\hat{\nabla}\cdot(\phi_2\hat{\mathbf{v}})+\frac{Cn}{\beta Pe_{CH}}\hat{\nabla}\cdot\hat{\mathbf{J}}_2=0, \tag{7.7}$$

$$\partial_{\hat{t}}\phi_3+\hat{\nabla}\cdot(2\delta\phi_3\hat{\mathbf{v}})+\frac{Cn}{\beta Pe_{CH}}\hat{\nabla}\cdot\hat{\mathbf{J}}_3=-Da\hat{R}, \tag{7.8}$$

$$\hat{\mathbf{J}}_i=-\frac{1}{\hat{\Sigma}_i}\hat{\nabla}\hat{\mu}_i,\qquad i\in\{1,2,3\}, \tag{7.9}$$

$$\frac{\hat{\mu}_i}{\beta}=\frac{\partial_{\phi_i}\hat{W}(\boldsymbol{\Phi})}{Cn}-Cn\hat{\Sigma}_i\hat{\nabla}^2\phi_i,\quad i\in\{1,2,3\}. \tag{7.10}$$

All equations are defined in the dimensionless time-space domain $(0,1]\times\hat{\Omega}$, where $\hat{\Omega}=(0,1)\times(-\hat{\ell}_\Omega/2,\hat{\ell}_\Omega/2)$. The surface tension

and reaction are given as

$$\hat{\tilde{\mathbf{S}}} = -\hat{\mu}_2 \tilde{\phi}_f \hat{\nabla} \left(\frac{\phi_1}{\tilde{\phi}_f} \right) - \hat{\mu}_1 \tilde{\phi}_f \hat{\nabla} \left(\frac{\phi_2}{\tilde{\phi}_f} \right) - 2\delta\phi_3 \hat{\nabla}(\hat{\mu}_3 - \hat{\mu}_1 - \hat{\mu}_2),$$
$$\hat{R} = -q(\boldsymbol{\Phi})(\hat{r}(\hat{c}) + \hat{\tilde{\alpha}}\hat{\mu}_1 - \hat{\tilde{\alpha}}\hat{\mu}_3).$$

From here on, we only work with the non-dimensional model and therefore the hats are left out in the notation.

7.2 Upscaling in a Thin Strip

We now proceed by deriving the upscaled model, obtained when passing to the limit $\beta \to 0$. This means that the thin strip reduces to a one-dimensional object, as its width is vanishing compared to its length.

Analogous to Chapter 6 we introduce new coordinates (x, y) such that $\mathbf{x} = (x, \beta y)$. In the thin strip we expect all variables to vary in longitudinal direction $\mathbf{e}_x$ on the length scale $L = x_{\text{ref}}$ and in transversal direction $\mathbf{e}_y$ on the length scale $\ell = y_{\text{ref}} = \beta x_{\text{ref}}$. In particular this results in $\nabla = \mathbf{e}_x \partial_x + \beta^{-1} \mathbf{e}_y \partial_y$.

7.2.1 Scaling of Non-Dimensional Numbers

The upscaled model also depends on the scaling of the dimensionless numbers (7.1) with respect to β. We consider the following behavior

of these numbers with respect to β

$$Re = \bar{Re}, \tag{7.11}$$
$$Ca = \bar{Ca}, \tag{7.12}$$
$$Cn = \beta\bar{\varepsilon}, \tag{7.13}$$
$$Da = \bar{Da}/\bar{\varepsilon}, \tag{7.14}$$
$$Pe_{CH} = 1/(\beta^2\bar{M}), \tag{7.15}$$
$$Pe_c = \bar{Pe}_c, \tag{7.16}$$

where $\bar{Re}$, $\bar{Ca}$, $\bar{\varepsilon}$, $\bar{Da}$, $\bar{M}$, $\bar{Pe}_c$ are constants independent of β. In detail, these choices are motivated as follows.

- The moderate Reynolds number (7.11) leads to a parabolic flow profile in the thin strip, we expect laminar flow.
- As the curvature of the fluid–fluid interface is of order $O(\beta)$, choosing a moderate capillary number Ca in (7.12) leads to the same pressure in both fluids, thus the capillary pressure becomes 0 (for sharp-interface models see also [Lunowa et al. 2021; Sharmin, Bringedal, et al. 2020]). Note that this is a major difference to the three-dimensional case, see e.g. [Mikelić 2009], where we expect a curvature of $O(\beta^{-1})$ leading to a non-zero capillary pressure.
- The scaling of the Cahn number Cn in (7.13) can be reformulated to $\bar{\varepsilon} = \varepsilon/\ell$. Therefore, the interface width ε scales with the width of the thin strip, ℓ. At the same time, the diffuse interface regions are assumed to be localized inside the thin strip, therefore we require $\varepsilon \ll \ell$. This translates into a fixed, small $\bar{\varepsilon}$, i.e., $\bar{\varepsilon} \ll 1$. In the numerical experiments presented in Section 7.5 we choose $\bar{\varepsilon} = 0.03$.
- We consider a moderate Damköhler number (7.14). In the sharp-interface model, this would ensure that the interfaces move with moderate velocity inside the thin strip, proportional to ℓ/T. In the diffuse-interface model, the reaction is only active in the diffuse-interface region, which has an area scaling with ε.

Therefore, Da is divided by $\bar{\varepsilon}$, and expect to have fluid–solid or fluid–fluid interfaces evolving over the length scale ℓ. A dominating Damköhler regime like $Da = O(\beta^{-1})$ would instead lead to equilibrium-type reactions in the upscaled model, but the evolution of the interfaces should remain moderate. This can be achieved by assuming that the molar density of the species in the precipitate is sufficiently high to compensate the fast reaction kinetics.

- The high Péclet number (7.15) for the phase field assures that the evolution of the phase field remains within the transversal length scale ℓ in an $O(1)$ time scale.
- The moderate Péclet number of the ion diffusion (7.16) results in a macroscopic diffusion of ions, while the ion distribution in transversal direction equilibrates faster than the $O(1)$ time scale.

Lastly, the small, non-dimensional number $\delta > 0$ appears in the δ-$2f1s$-model. It is used as a regularization parameter, to ensure the positivity of volume fractions, density and viscosity. Here we assume that δ is constant and independent of β.

7.2.2 Asymptotic Expansions

We assume that we can write solutions to the non-dimensional δ-$2f1s$-model (7.3)–(7.10) in terms of an asymptotic expansion in β of $\boldsymbol{\Phi}$, $\mathbf{v}$, p, c, μ_1, μ_2, μ_3. To be precise, we assume expansions of the form

$$\boldsymbol{\Phi}(t, \mathbf{x}) = \boldsymbol{\Phi}_0(t, x, y) + \beta \boldsymbol{\Phi}_1(t, x, y) + \beta^2 \boldsymbol{\Phi}_2(t, x, y) + \dots \ ,$$

where $\boldsymbol{\Phi}_k$, $k \in \mathbb{N}_0$ do not depend on β. In particular, we also use this notation for other variables. Inserting these asymptotic expansions into the non-dimensional δ-$2f1s$-model we group by powers of β.

Remark 7.1: *Note that the asymptotic expansions are written depending on the new coordinates x and y. This means that in the* $\mathbf{e}_x$

direction variables can not vary on the (non-dimensional) length scale β, because a non-trivial function $f(x/\beta)$ can not be expanded in the form $f(x/\beta) = f_0(x) + \beta f_1(x) + \ldots$. In particular this implies that there are no phase-field interfaces possible perpendicular to the thin strip, as they would change the value of $\boldsymbol{\Phi}$ over the length $Cn = \beta\bar{\varepsilon}$.

The assumption is also violated for triple points, where all three phases meet, and for points where interfaces meet the boundary of Ω at $y = \pm\ell_\Omega/2$. Therefore, ℓ_Ω has to be chosen big enough, such that the width of the thin strip does not reach ℓ_Ω.

Our ansatz for ϕ_0 in Chapter 6, Equation (6.2) introduces a big error in the boundary conditions for the case that $d \approx 0$, i.e., for the point where the fluid–solid interface meets the outer boundary of the domain. The numerical investigation in Section 6.2.2 shows that in this case this does not translate into a big error in the upscaled model. In contrast, the numerical example in Section 7.5.1 shows that violating the assumption of slow variation in $\mathbf{e}_x$ direction for fluid–fluid interfaces leads to a big error in the upscaled model.

The non-dimensional domain is given by $\Omega = (0,1) \times (-\ell_\Omega/2, \ell_\Omega/2)$, and we choose as boundary conditions at $y = \pm\ell_\Omega/2$ for the upscaling

$$\partial_y \boldsymbol{\Phi}(t,x,\pm\ell_\Omega/2) = 0, \tag{7.17}$$

$$\partial_y \mu(t,x,\pm\ell_\Omega/2) = 0, \tag{7.18}$$

$$\partial_y c(t,x,\pm\ell_\Omega/2) = 0, \tag{7.19}$$

$$\mathbf{v}(t,x,\pm\ell_\Omega/2) = 0. \tag{7.20}$$

Expansion of (7.3), $O(\beta^{-1})$: Recall that $\nabla = \mathbf{e}_x\partial_x + \beta^{-1}\mathbf{e}_y\partial_y$. Therefore, the leading order terms of (7.3) are of order $O(\beta^{-1})$, we have

$$\partial_y(\tilde{\phi}_{f,0}\mathbf{v}_0)\cdot\mathbf{e}_y = 0.$$

We denote components of $\mathbf{v}$ as $\mathbf{v}^{(1)} = \mathbf{v} \cdot \mathbf{e}_x$ and $\mathbf{v}^{(2)} = \mathbf{v} \cdot \mathbf{e}_y$. Note that $\tilde{\phi}_{f,0} > 0$ by construction in (3.41), so after integrating and using the leading order of boundary condition (7.20) we can divide by $\tilde{\phi}_{f,0}$ and obtain

$$\mathbf{v}_0^{(2)} = 0. \tag{7.21}$$

As expected, there is no leading order flow perpendicular to the thin strip.

Expansion of (7.3)*,* $O(1)$*:* With (7.21) we get in first order

$$\partial_x(\tilde{\phi}_{f,0}\mathbf{v}_0^{(1)}) + \partial_y(\tilde{\phi}_{f,0}\mathbf{v}_1^{(2)}) = 0. \tag{7.22}$$

The $O(\beta)$ term of boundary condition (7.20) reads $\mathbf{v}_1(y = \pm\ell_\Omega/2) = 0$. After integrating (7.22) in y we can use this to get

$$\partial_x \int_{-\ell_\Omega/2}^{\ell_\Omega/2} \tilde{\phi}_{f,0}\mathbf{v}_0^{(1)}\, dy = 0. \tag{7.23}$$

Here, $\tilde{\phi}_{f,0}\mathbf{v}_0^{(1)}$ is the flux in $\mathbf{e}_x$ direction, so (7.23) implies that the total flux in $\mathbf{e}_x$ direction is conserved.

Expansion of (7.10)*,* $O(\beta^{-1})$*:* We get with $Cn = \beta\bar{\varepsilon}$ three terms in leading order

$$\mu_{i,0} = \frac{\partial_{\phi_i} W(\boldsymbol{\Phi}_0)}{\bar{\varepsilon}} - \bar{\varepsilon}\Sigma_i \partial_y^2 \phi_{i,0}. \tag{7.24}$$

Notably from the Laplacian only derivatives in $\mathbf{e}_y$-direction remain. In the upscaled model this leads to a Cahn–Hilliard evolution only acting in $\mathbf{e}_y$ direction.

Expansion of (7.6), (7.7), (7.8), $O(1)$*:* Note that with (7.13), (7.14) and (7.15) we can write

$$\frac{Cn}{\beta Pe_{CH}} = \beta^2 \bar{\varepsilon}\bar{M} \qquad \text{and} \qquad Da = \frac{\bar{Da}}{\bar{\varepsilon}}. \tag{7.25}$$

We insert (7.9) into (7.6), (7.7), (7.8), as we do not treat $\mathbf{J}_i$ as a primary variable. Together with (7.21) we have in leading order $O(1)$

$$\partial_t \phi_{1,0} + \partial_x(\phi_{1,0}\mathbf{v}_0^{(1)}) + \partial_y(\phi_{1,0}\mathbf{v}_1^{(2)}) - \frac{\bar{\varepsilon}\bar{M}}{\Sigma_1}\partial_y^2 \mu_{1,0} = \frac{\bar{Da}}{\bar{\varepsilon}} R_0, \tag{7.26}$$

$$\partial_t \phi_{2,0} + \partial_x(\phi_{2,0}\mathbf{v}_0^{(1)}) + \partial_y(\phi_{2,0}\mathbf{v}_1^{(2)}) - \frac{\bar{\varepsilon}\bar{M}}{\Sigma_2}\partial_y^2 \mu_{2,0} = 0, \tag{7.27}$$

$$\partial_t \phi_{3,0} + \partial_x(2\delta\phi_{3,0}\mathbf{v}_0^{(1)}) + \partial_y(2\delta\phi_{3,0}\mathbf{v}_1^{(2)}) - \frac{\bar{\varepsilon}\bar{M}}{\Sigma_3}\partial_y^2 \mu_{3,0} = -\frac{\bar{Da}}{\bar{\varepsilon}} R_0, \tag{7.28}$$

where the leading order term of the reaction is given by

$$R_0 = -q(\boldsymbol{\Phi}_0)(r(c_0) + \tilde{\alpha}\mu_{1,0} - \tilde{\alpha}\mu_{3,0}). \tag{7.29}$$

Note that as in (7.24) only the y-derivatives of the Laplacian remain in the leading order.

Expansion of (7.5), $O(\beta^{-2})$*:* We obtain in leading order only one $O(\beta^{-2})$ term

$$\frac{1}{\bar{Pe}_c}\partial_y(\tilde{\phi}_{c,0}\partial_y c_0) = 0.$$

Integrating in y and using the leading order term of boundary condition (7.19) results in

$$\tilde{\phi}_{c,0}\partial_y c_0 = 0.$$

Because by construction $\tilde{\phi}_{c,0} > 0$, we conclude

$$\partial_y c_0 = 0. \tag{7.30}$$

Therefore, c_0 is constant in $\mathbf{e}_y$ direction, and we write $c_0 = c_0(t,x)$ to emphasize that c_0 only depends on the x coordinate.

Expansion of (7.5), $O(\beta^{-1})$*:* As we found $\partial_y c_0 = 0$ in (7.30), we get in first order only the term

$$\frac{1}{\bar{Pe}_c}\partial_y(\tilde{\phi}_{c,0}\partial_y c_1) = 0.$$

With analogous argumentation to the $O(\beta^{-2})$ case we get $\partial_y c_1 = 0$ and can write $c_1 = c_1(t,x)$ to show that c_1 is independent of y.

Expansion of (7.5), $O(1)$*:* Similar to the $O(1)$ expansion of (7.6), (7.7), (7.8), we insert the Cahn–Hilliard flux $\mathbf{J}_i$ (7.9) and the non-dimensional numbers (7.25) into the equation, and use (7.21). We obtain the second order terms

$$\begin{aligned}\partial_t(\tilde{\phi}_{c,0}c_0) + \partial_x(\phi_{c,0}\mathbf{v}_0^{(1)}c_0) + \partial_y(\phi_{c,0}\mathbf{v}_1^{(2)}c_0) - \frac{\bar{\varepsilon}\bar{M}}{\Sigma_1}\partial_y(c_0\partial_y\mu_{1,0})\\ = \frac{1}{\bar{Pe}_c}\partial_x(\tilde{\phi}_{c,0}\partial_x c_0) + \frac{1}{Pe_c}\partial_y(\tilde{\phi}_{c,0}\partial_y c_2) + \frac{\bar{D}a}{\bar{\varepsilon}}R_0,\end{aligned}$$

where R_0 is given by (7.29). After integrating in y we can use the boundary conditions (7.18), (7.19), (7.20) to eliminate the terms containing a y derivative. We obtain

$$\begin{aligned}\frac{d}{dt}\left(c_0\int_{-\ell_\Omega/2}^{\ell_\Omega/2}\tilde{\phi}_{c,0}\,dy\right) + \partial_x\left(c_0\int_{-\ell_\Omega/2}^{\ell_\Omega/2}\phi_{c,0}\mathbf{v}_0^{(1)}\,dy\right)\\ = \frac{1}{\bar{Pe}_c}\partial_x\left(\left(\int_{-\ell_\Omega/2}^{\ell_\Omega/2}\tilde{\phi}_{c,0}\,dy\right)\partial_x c_0\right) + \frac{\bar{D}a}{\bar{\varepsilon}}\int_{-\ell_\Omega/2}^{\ell_\Omega/2}R_0\,dy.\end{aligned} \tag{7.31}$$

Here we have written c_0 outside the integrals to emphasize that c_0 does not depend on y. Equation (7.31) is a transport-diffusion-reaction equation for $c_0(x,t)$, where the coefficients still depend on the exact distribution of $\boldsymbol{\Phi}_0$ in the $\mathbf{e}_y$ direction.

Expansion of (7.4)*,* $O(\beta^{-3})$*:* The only term of order $O(\beta^{-3})$ is

$$-\frac{1}{\bar{R}e}\tilde{\phi}_{f,0}\mathbf{e}_y\partial_y p_0 = 0.$$

As $\tilde{\phi}_{f,0}$ is positive by construction, we conclude that p_0 does not depend on y and write $p_0 = p_0(t,x)$.

Expansion of (7.4)$\cdot\mathbf{e}_x$*,* $O(\beta^{-2})$*:* We investigate in the first order only the equation for the x-component. With (7.21) and $p_0 = p_0(t,x)$ the remaining terms are

$$-\frac{1}{\bar{R}e}\tilde{\phi}_{f,0}\partial_x p_0 + \frac{1}{\bar{R}e}\partial_y(\tilde{\gamma}(\boldsymbol{\Phi}_0)\partial_y \mathbf{v}_0^{(1)}) - \frac{1}{\bar{R}e}\rho_3 d(\tilde{\phi}_{f,0})\mathbf{v}_0^{(1)} = 0.$$

We can interpret this as a linear differential equation for $\mathbf{v}_0^{(1)}$ with boundary conditions (7.20). In particular, we can use the linearity to write

$$\mathbf{v}_0^{(1)}(t,x,y) = -w(t,x,y)\partial_x p_0(t,x), \tag{7.32}$$

where w is the solution to the cell problem

$$\rho_3 d(\tilde{\phi}_{f,0})w - \partial_y(\tilde{\gamma}(\boldsymbol{\Phi}_0)\partial_y w) = \tilde{\phi}_{f,0}, \tag{7.33}$$

$$w(t,x,\pm\ell_\Omega/2) = 0. \tag{7.34}$$

For a given $\boldsymbol{\Phi}$ the function w calculates the parabolic flow profile in the cross-section of the thin strip. As we expect from a Darcy-type flow, the fluid velocity is proportional to $-\partial_x p_0$, shown in (7.32).

Remark 7.2: *We note that by construction* $\tilde{\gamma} > 0$ *and therefore the cell problem* (7.33), (7.34) *has a unique solution.*

7.2.3 The Upscaled δ-$2f1s$-Model

Let us summarize the results of the upscaling. Except for $\mathbf{v}$ we only need the leading order term of each unknown, and therefore drop the subscript 0. We call the model (7.35)–(7.50) the upscaled δ-$2f1s$-model.

From (7.23) and (7.32) we have the macroscopic continuity equation for the total flux Q_f and the Darcy-equation for the pressure p, and the macroscopic transport-diffusion-reaction equation for the ion concentration c (7.31)

$$\partial_x Q_f = 0, \tag{7.35}$$

$$Q_f = -K_f \partial_x p, \tag{7.36}$$

$$\frac{d}{dt}\left(\tilde{\phi}_{c,\text{total}} c\right) + \partial_x\left((-K_c \partial_x p) c\right) = \frac{1}{\bar{Pe}_c}\partial_x\left(\tilde{\phi}_{c,\text{total}} \partial_x c\right) + \frac{\bar{Da}}{\bar{\varepsilon}} R_{\text{total}}. \tag{7.37}$$

These equations are macroscopic in the sense that the unknowns Q_f, p and c depend only on x and t, but not on y. The parameters in these equations are upscaled quantities, depending on the exact distribution of the phases in y direction

$$\tilde{\phi}_{c,\text{total}} = \int_{-\ell_\Omega/2}^{\ell_\Omega/2} \tilde{\phi}_c \, dy, \tag{7.38}$$

$$K_f(t,x) = \int_{-\ell_\Omega/2}^{\ell_\Omega/2} \tilde{\phi}_f w \, dy, \tag{7.39}$$

$$K_c(t,x) = \int_{-\ell_\Omega/2}^{\ell_\Omega/2} \tilde{\phi}_c w \, dy, \tag{7.40}$$

$$R_{\text{total}} = \int_{-\ell_\Omega/2}^{\ell_\Omega/2} R \, dy. \tag{7.41}$$

For the phase-field parameters we still have to solve the fully coupled two-dimensional problem (7.24), (7.26), (7.27), (7.28),

$$\partial_t \phi_1 + \partial_x(\phi_1 \mathbf{v}_0^{(1)}) + \partial_y(\phi_1 \mathbf{v}_1^{(2)}) - \frac{\bar{\varepsilon}\bar{M}}{\Sigma_1}\partial_y^2 \mu_1 = \frac{\bar{D}a}{\bar{\varepsilon}} R, \tag{7.42}$$

$$\partial_t \phi_2 + \partial_x(\phi_2 \mathbf{v}_0^{(1)}) + \partial_y(\phi_2 \mathbf{v}_1^{(2)}) - \frac{\bar{\varepsilon}\bar{M}}{\Sigma_2}\partial_y^2 \mu_2 = 0, \tag{7.43}$$

$$\partial_t \phi_3 + \partial_x(2\delta\phi_3 \mathbf{v}_0^{(1)}) + \partial_y(2\delta\phi_3 \mathbf{v}_1^{(2)}) - \frac{\bar{\varepsilon}\bar{M}}{\Sigma_3}\partial_y^2 \mu_3 = -\frac{\bar{D}a}{\bar{\varepsilon}} R, \tag{7.44}$$

$$\mu_i = \frac{\partial_{\phi_i} W(\boldsymbol{\Phi})}{\bar{\varepsilon}} - \bar{\varepsilon}\Sigma_i \partial_y^2 \phi_i, \qquad i \in \{1,2,3\}, \tag{7.45}$$

with the reaction term

$$R = -q(\boldsymbol{\Phi})(r(c) + \tilde{\alpha}\mu_1 - \tilde{\alpha}\mu_3). \tag{7.46}$$

Note that in contrast to the non-dimensional model (7.3)–(7.10) the Cahn–Hilliard evolution acts only in $\mathbf{e}_y$ direction. The only term acting in $\mathbf{e}_x$ direction is the transport of the fluid phases. This enables us in Section 7.4 to develop a numerical model that uses explicit upwinding for the fluid transport and can therefore decouple cell-problems for different values of x.

For the flow it suffices to solve the cell problem (7.33), (7.34)

$$\rho_3 d(\tilde{\phi}_f) w - \partial_y(\tilde{\gamma}(\boldsymbol{\Phi})\partial_y w) = \tilde{\phi}_f, \tag{7.47}$$

$$\lim_{y \to \pm \ell_\Omega/2} w = 0, \tag{7.48}$$

and recover the flow $\mathbf{v}_0^{(1)}$, $\mathbf{v}_1^{(2)}$ by (7.32) and (7.22)

$$\mathbf{v}_0^{(1)} = -w\partial_x p, \tag{7.49}$$

$$\partial_x(\tilde{\phi}_f \mathbf{v}_0^{(1)}) + \partial_y(\tilde{\phi}_f \mathbf{v}_1^{(2)}) = 0. \tag{7.50}$$

7.3 Sharp-Interface Limit of the Upscaled δ-$2f1s$-Model

In the previous section we have investigated the scale separation $\beta = \ell/L \to 0$. A different limit process is the sharp-interface limit $\varepsilon \to 0$. In Section 3.2 this limit is analyzed for the δ-$2f1s$-model (3.45)–(3.50), resulting in the sharp-interface evolution described in Section 3.1.1.

Because the upscaled δ-$2f1s$-model (7.35)–(7.50) still contains a Cahn–Hilliard evolution, depending on the small number $\bar{\varepsilon} = \varepsilon/\ell$, we can investigate the sharp-interface limit $\bar{\varepsilon} \to 0$ of the upscaled δ-$2f1s$-model in the non-dimensional domain $\Omega = (0,1) \times (-\ell_\Omega/2, \ell_\Omega/2)$. This means that we are interested in the limit process of vanishing diffuse interface width ε compared to the width ℓ of the thin strip. In the following we use matched asymptotic expansions to analyze this limit, the argumentation is mostly analogous to Section 3.2.

7.3.1 Assumptions and Scaling of Non-Dimensional Numbers

To derive the sharp-interface limit $\bar{\varepsilon} \to 0$, we assume that $\bar{Pe}_c, \bar{Da}, \bar{M}$ are constant and independent of $\bar{\varepsilon}$. This choice of scaling allows for a reasonable limit process, with physical properties independent of the diffuse interface width.

Analogous to Section 3.1.1 the scaling $\delta = \bar{\varepsilon}$ is important. The regularization parameter δ is introduced in the δ-$2f1s$ model to ensure the positivity of e.g. the density $\tilde{\rho}_f(\boldsymbol{\Phi})$ in (3.42). This δ-regularization is not necessary for the sharp-interface formulation, and the choice $\delta = \bar{\varepsilon}$ leads to δ vanishing in the sharp-interface limit.

As a basic assumption we expect to have solutions that form bulk phases, characterized by nearly constant $\boldsymbol{\Phi}$, and interfaces, characterized by a large gradient of $\boldsymbol{\Phi}$. We also assume that μ_i, $i \in \{1,2,3\}$ is of order $O(1)$, not of order $O(\bar{\varepsilon}^{-1})$, as equation (7.45) would suggest.

For a discussion of why this assumption is reasonable on an $O(1)$ time scale, see [Pego and Penrose 1989].

We also assume that in an interface between phase $\boldsymbol{\Phi} = \mathbf{e}_i$ and $\boldsymbol{\Phi} = \mathbf{e}_j$ the third phase is not present. This assumption is reasonable because with our construction of W in Section 3.1.2.1 minimizers of the Ginzburg–Landau energy $W(\boldsymbol{\Phi}) + \sum_i \Sigma_i \Delta\phi_i$ that connect $\boldsymbol{\Phi} = \mathbf{e}_i$ and $\boldsymbol{\Phi} = \mathbf{e}_j$ satisfy $\phi_k = 0$, $k \in \{1,2,3\} \setminus \{i,j\}$.

7.3.2 Outer Expansions

For the bulk phases we assume that we can write solutions to the upscaled δ-$2f1s$-model (7.35)–(7.50) in terms of an outer asymptotic expansion in $\bar{\varepsilon}$ for the variables $\boldsymbol{\Phi}$, w, $\mathbf{v}_0^{(1)}$, $\mathbf{v}_1^{(2)}$, p, c, μ_1, μ_2, μ_3, as described in Section 1.3, i.e., we assume expansions of the form

$$\boldsymbol{\Phi}(t,x,y) = \boldsymbol{\Phi}_0^{out}(t,x,y) + \bar{\varepsilon}\boldsymbol{\Phi}_1^{out}(t,x,y) + \bar{\varepsilon}^2\boldsymbol{\Phi}_2^{out}(t,x,y) + \dots .$$

The expansions for the macroscopic variables $p(x), c(x)$ do not depend on y. We insert these expansions into the upscaled δ-$2f1s$-model and group by orders of $\bar{\varepsilon}$.

Outer Expansion of (7.45)*,* $O(\beta^{-1})$*:* As in Section 3.2.1 we find that the only stable solutions to the leading order terms are $\boldsymbol{\Phi}_0^{out} = \mathbf{e}_k$, $k \in \{1,2,3\}$ with the restriction $\phi_{k,1}^{out} \leq 0$ and $\phi_{i,1}^{out}, \phi_{j,1}^{out} \geq 0$ for $\{i,j\} = \{1,2,3\} \setminus \{k\}$. The additional restriction stems from the fact that the triple well potential W depends on $\delta = \bar{\varepsilon}$.

We define the set $\Omega_k(t)$ to be the set of (x,y) where $\boldsymbol{\Phi}_0^{out}(t,x,y) = \mathbf{e}_k$. In the sharp interface formulation, $\Omega_k(t)$ represents the domain of phase k.

Outer Expansion of (7.47)*,* $O(1)$*:* In Ω_3, i.e., in case $\boldsymbol{\Phi}_0^{out} = \mathbf{e}_3$, we have $\tilde{\phi}_{f,0}^{out} = 0$ and the leading order reads

$$\rho_3 d_0 w_0^{out} - \partial_y(\gamma_3 \partial_y w_0^{out}) = 0, \tag{7.51}$$

where $d_0 = d(0) > 0$. In the fluid phases Ω_i, $i \in \{1,2\}$, we have $\boldsymbol{\Phi}_0^{out} = \mathbf{e}_i$ and therefore $\tilde{\phi}_{f,0}^{out} = 1$. Note that by construction $d(1) = 0$. With this we obtain in leading order

$$-\partial_y(\gamma_i \partial_y w_0^{out}) = 1. \tag{7.52}$$

Outer Expansion of (7.50)*,* $O(1)$*:* In the fluid phases $\boldsymbol{\Phi}_0^{out} = \mathbf{e}_i$, $i \in \{1,2\}$ we have $\tilde{\phi}_{f,0}^{out} = 1$ and obtain

$$\partial_x(\mathbf{v}_{0,0}^{(1),out}) + \partial_y(\mathbf{v}_{1,0}^{(2),out}) = 0. \tag{7.53}$$

Outer Expansion of (7.35)*,* (7.36)*,* $O(1)$*:* We now consider the macroscopic equations. The equations for the flow (7.35), (7.36) upscale trivially, the leading order reads

$$\partial_x Q_{f,0}^{out} = 0, \tag{7.54}$$

$$Q_{f,0}^{out} = -K_{f,0}^{out} \partial_x p_0^{out}, \tag{7.55}$$

where the parameter $K_{f,0}^{out}$ is the leading order expansion of K_f, using (7.39)

$$K_{f,0}^{out} = \int_{-\ell_\Omega/2}^{\ell_\Omega/2} \phi_{f,0}^{out} w_{f,0}^{out}\, dy. \tag{7.56}$$

Note that the leading order expansion of $\tilde{\phi}_f$ is $\phi_{f,0}^{out}$ as the δ-modification is of order $O(\bar{\varepsilon})$ because of the scaling choice $\delta = \bar{\varepsilon}$.

Outer Expansion of (7.37)*,* $O(1)$*:* For the transport-diffusion-reaction equation for c let us first investigate the reaction term. We have

with (7.41) and (7.46)

$$\frac{\bar{Da}}{\bar{\varepsilon}} R_{\text{total}} = -\frac{\bar{Da}}{\bar{\varepsilon}} \int_{-\ell_\Omega/2}^{\ell_\Omega/2} q(\boldsymbol{\Phi})(r(c) + \tilde{\alpha}\mu_1 - \tilde{\alpha}\mu_3)\, dy.$$

As $q(\boldsymbol{\Phi}^{out}) = O(\varepsilon^2)$ in the bulk phases $\phi_0^{out} = \mathbf{e}_k$, $k \in \{1,2,3\}$, there is no contribution of the reaction term in the bulk at leading order. Note that there is a contribution of this term in the interface regions, see Section 7.3.3. Overall we have for (7.37) in leading order

$$\begin{aligned} &\frac{d}{dt}\left(\phi_{c,\text{total},0}^{out} c_0^{out}\right) + \partial_x\left((-K_{c,0}^{out}\partial_x p_0^{out}) c_0^{out}\right) \\ &\quad = \frac{1}{\bar{Pe}_c}\partial_x\left(\phi_{c,\text{total},0}^{out}\partial_x c_0^{out}\right) + \bar{Da} R_{\text{interface},0}, \end{aligned} \tag{7.57}$$

with coefficients

$$\phi_{c,\text{total},0}^{out} = \int_{-\ell_\Omega/2}^{\ell_\Omega/2} \phi_{c,0}^{out}\, dy, \tag{7.58}$$

$$K_{c,0}^{out} = \int_{-\ell_\Omega/2}^{\ell_\Omega/2} \phi_{c,0}^{out} w_{f,0}^{out}\, dy, \tag{7.59}$$

and $R_{\text{interface},0}$ as a placeholder for the interface contributions of the reaction term.

7.3.3 Inner Expansions

We have shown in Section 7.3.2 that the domain is partitioned into Ω_1, Ω_2 and Ω_3. We locate the interfaces between the phases as

$$\Gamma_{ij}(t) = \left\{(x,y) \in \Omega : \phi_i(t,x,y) = \phi_j(t,x,y) \geq 1/3\right\}. \tag{7.60}$$

We assume that Γ_{ij} is a smooth, one-dimensional manifold. As explained in Remark 7.1 we do not consider triple-points, where all three phases meet, and do not allow for the interfaces to touch the boundary of Ω at $y = \pm\ell_\Omega/2$. Also, interfaces can not occur perpen-

dicular to the thin strip and therefore there exists locally around an interface Γ_{ij} a unique mapping $s(t,x)$ such that $(x, s(t,x)) \in \Gamma_{ij}$.

We use this mapping to introduce a new coordinate z close to the interface

$$z(x,t) = \frac{y - s(t,x)}{\bar{\varepsilon}}.$$

Because we expect the interface width to be of size $\bar{\varepsilon}$, the coordinate z is scaled by ε^{-1}. The velocity of Γ_{ij} at (x,s) in y-direction is given by

$$\nu(x) = \partial_t s(t,x).$$

We use the new coordinates (t,x,z) as the coordinates to describe the interfaces Γ_{ij}. For a generic function $f(t,x,y) = f^{in}(t,x,z)$ we obtain the transformation rules

$$\partial_t f = -\frac{1}{\varepsilon}\nu\partial_z f^{in} + \partial_t f^{in}, \tag{7.61}$$

$$\partial_y f = \frac{1}{\varepsilon}\partial_z f^{in}, \tag{7.62}$$

$$\partial_x f = -\frac{1}{\varepsilon}(\partial_x s)\partial_z f^{in} + \partial_x f^{in}. \tag{7.63}$$

We assume that close to an interface Γ_{ij} we can write solutions to the upscaled δ-$2f1s$-model (7.35)–(7.50) in terms of an inner asymptotic expansion in $\bar{\varepsilon}$ for the variables $\boldsymbol{\Phi}$, w, $\mathbf{v}_0^{(1)}$, $\mathbf{v}_1^{(2)}$, μ_1, μ_2, μ_3. We assume expansions of the form

$$\boldsymbol{\Phi}(t,x,y) = \boldsymbol{\Phi}_0^{in}(t,x,z) + \bar{\varepsilon}\boldsymbol{\Phi}_1^{in}(t,x,z) + \bar{\varepsilon}^2\boldsymbol{\Phi}_2^{in}(t,x,z) + \dots,$$

with coefficients $\boldsymbol{\Phi}_k^{in}$ independent of $\bar{\varepsilon}$. In contrast to the outer asymptotic expansions, the inner asymptotic expansions depend on the (t,x,z) coordinates. This leads to different terms being of the highest order when inserting the expansions into the upscaled δ-$2f1s$-model. We do not use inner expansions of the macroscopic variables p and c, as they are constant across all interfaces.

To relate inner and outer expansions, we match the limit value of inner expansions for $z \to \pm\infty$ with the limit value of the outer expansions at s (from the respective side). We use matching conditions analogous to Section 1.3

$$\lim_{z\to\pm\infty} \boldsymbol{\Phi}_0^{in}(t,x,z) = \lim_{y\to 0^+} \boldsymbol{\Phi}_0^{out}(t,x,s\pm y), \tag{7.64}$$

$$\lim_{z\to\pm\infty} \partial_z \boldsymbol{\Phi}_0^{in}(t,x,z) = 0, \tag{7.65}$$

$$\lim_{z\to\pm\infty} \partial_z \boldsymbol{\Phi}_1^{in}(t,x,z) = \lim_{y\to 0^+} \partial_y \boldsymbol{\Phi}_0^{out}(t,x,s\pm y). \tag{7.66}$$

Inner Expansion of (7.45), $O(\bar{\varepsilon}^{-1})$*:* Consider an interface between bulk phases $\boldsymbol{\Phi}_0^{out} = \mathbf{e}_i$ and $\boldsymbol{\Phi}_0^{out} = \mathbf{e}_j$. With matching condition (7.64) this means

$$\lim_{z\to-\infty} \boldsymbol{\Phi}_0^{in} = \mathbf{e}_i \qquad \text{and} \qquad \lim_{z\to\infty} \boldsymbol{\Phi}_0^{in} = \mathbf{e}_j. \tag{7.67}$$

With the same argument as in Section 3.2.2 we find that $\phi_{j,0}^{in}$ is implicitly given by

$$z = \frac{1}{30}\left(\frac{1}{1-\phi_{j,0}^{in}} - \frac{1}{\phi_{j,0}^{in}} + 2\log\left(\frac{\phi_{j,0}^{in}}{1-\phi_{j,0}^{in}}\right)\right). \tag{7.68}$$

Also, $\phi_{i,0}^{in}$ is given by $\phi_{i,0}^{in} = 1 - \phi_{j,0}^{in}$.

Inner Expansion of (7.50), $O(\bar{\varepsilon}^{-1})$*:* Using the coordinate transformations (7.62) and (7.63), we get in leading order

$$-(\partial_x s)\partial_z(\phi_{f,0}^{in}\mathbf{v}_{0,0}^{(1),in}) + \partial_z(\phi_{f,0}^{in}\mathbf{v}_{1,0}^{(2),in}) = 0.$$

Note that $\partial_x s(t,x)$ does not depend on z and therefore

$$-(\partial_x s)\phi_{f,0}^{in}\mathbf{v}_{0,0}^{(1),in} + \phi_{f,0}^{in}\mathbf{v}_{1,0}^{(2),in} = const. \tag{7.69}$$

with respect to z. Across the interface Γ_{12} we have $\phi_{f,0}^{in} = 1$ and thus with matching condition (7.64) we get for all $z \in \mathbb{R}$

$$\begin{aligned} &- (\partial_x s)\mathbf{v}_{0,0}^{(1),in}(t,x,z) + \mathbf{v}_{1,0}^{(2),in}(t,x,z) \\ &\quad = \lim_{z\to\pm\infty} -(\partial_x s)\mathbf{v}_{0,0}^{(1),in}(t,x,z) + \mathbf{v}_{1,0}^{(2),in}(t,x,z) \\ &\quad = \lim_{y\to 0^+} -(\partial_x s)\mathbf{v}_{0,0}^{(1),out}(t,x,s\pm y) + \mathbf{v}_{1,0}^{(2),out}(t,x,s\pm y). \end{aligned} \tag{7.70}$$

In particular, this means that the term $-(\partial_x s)\mathbf{v}_{0,0}^{(1),out} + \mathbf{v}_{1,0}^{(2),out}$ is continuous across the Γ_{12} interface.

When matching (7.69) at the fluid–solid interfaces Γ_{13} and Γ_{23}, $\phi_{f,0}^{in}$ vanishes in the limit towards the solid phase, we can conclude

$$-(\partial_x s)\phi_{f,0}^{in}\mathbf{v}_{0,0}^{(1),in} + \phi_{f,0}^{in}\mathbf{v}_{1,0}^{(2),in} = 0. \tag{7.71}$$

Using matching condition (7.64) we find

$$-(\partial_x s)\mathbf{v}_{0,0}^{(1),out} + \mathbf{v}_{1,0}^{(2),out} = 0 \tag{7.72}$$

for the fluid velocity. This condition therefore allows only for fluid flow parallel to the fluid–solid interfaces.

Inner Expansion of (7.42), (7.43), (7.44), $O(\bar{\varepsilon}^{-1})$*:* We argue analogous to Section 3.2.2. The leading order expansions for (7.42), (7.43) and (7.44) are given by

$$\begin{aligned} &- \nu\partial_z\phi_{1,0}^{in} - (\partial_x s)\partial_z(\phi_{1,0}^{in}\mathbf{v}_{0,0}^{(1),in}) + \partial_z(\phi_{1,0}^{in}\mathbf{v}_{1,0}^{(2),in}) - \frac{\bar{M}}{\Sigma_1}\partial_z^2\mu_{1,0}^{in} \\ &\quad = -\bar{D}a\, q(\boldsymbol{\Phi}_0^{in})(r(c_0^{out}) + \alpha\mu_{1,0}^{in} - \alpha\mu_{3,0}^{in}), \end{aligned} \tag{7.73}$$

$$- \nu\partial_z\phi_{2,0}^{in} - (\partial_x s)\partial_z(\phi_{2,0}^{in}\mathbf{v}_{0,0}^{(1),in}) + \partial_z(\phi_{2,0}^{in}\mathbf{v}_{1,0}^{(2),in}) - \frac{\bar{M}}{\Sigma_2}\partial_z^2\mu_{2,0}^{in} = 0, \tag{7.74}$$

$$-\nu\partial_z\phi^{in}_{3,0} - \frac{\bar{M}}{\Sigma_3}\partial_z^2\mu^{in}_{3,0} = +\bar{Da}\, q(\boldsymbol{\Phi}^{in}_0)(r(c^{out}_0) + \alpha\mu^{in}_{1,0} - \alpha\mu^{in}_{3,0}). \tag{7.75}$$

Let us first consider the interface Γ_{13}, with Ω_1 being in the negative z direction. Here $\phi^{in}_{1,0} = \phi^{in}_{f,0}$ and with (7.71) the advection terms vanish from (7.73). We also have no third phase contributions and therefore $\phi^{in}_{1,0} + \phi^{in}_{3,0} = 1$. With notation $\mu_{3-1} := \mu^{in}_{3,0} - \mu^{in}_{1,0}$ we calculate $\Sigma_3 \cdot$ (7.75) $-\Sigma_1 \cdot$ (7.73) to be

$$\begin{aligned} &-(\Sigma_1+\Sigma_3)\nu\partial_z\phi^{in}_{3,0} - \bar{M}\partial_z^2\mu_{3-1} \\ &\quad = (\Sigma_1+\Sigma_3)\bar{Da}\, q(\boldsymbol{\Phi}^{in}_0)(r(c^{out}_0) - \alpha\mu_{3-1}). \end{aligned} \tag{7.76}$$

By construction of q (see Remark 3.8) the identity $q(\boldsymbol{\Phi}^{in}_0) = \partial_z\phi^{in}_{3,0}$ holds. We can interpret (7.76) as an ordinary differential equation for μ_{3-1} with boundary conditions $\lim_{z\to\pm\infty}\partial_z\mu_{3-1} = 0$ (by using matching condition (7.65)).

In the case $\alpha = 0$ all constant functions μ_{3-1} are solutions to the differential equation, under the compatibility condition

$$\nu = -\bar{Da}\, r(c^{out}_0). \tag{7.77}$$

In case $\alpha > 0$ the unique solution to (7.76) is given by the constant function

$$\mu_{3-1} = \alpha^{-1}(\nu + \bar{Da}\, r(c^{out}_0)). \tag{7.78}$$

We can combine (7.77) and (7.78), and also consider the case that the fluid and solid side of the Γ_{13} interface is switched. Overall we conclude

$$\nu = \begin{cases} \alpha(\mu^{in}_{1,0} - \mu^{in}_{3,0}) + \bar{Da}\, r(c) & \text{if } \lim_{z\to-\infty}\boldsymbol{\Phi}^{in}_0 = \mathbf{e}_3 \\ & \text{and } \lim_{z\to\infty}\boldsymbol{\Phi}^{in}_0 = \mathbf{e}_1 \\ \alpha(\mu^{in}_{3,0} - \mu^{in}_{1,0}) - \bar{Da}\, r(c) & \text{if } \lim_{z\to-\infty}\boldsymbol{\Phi}^{in}_0 = \mathbf{e}_1 \\ & \text{and } \lim_{z\to\infty}\boldsymbol{\Phi}^{in}_0 = \mathbf{e}_3 \end{cases} \tag{7.79}$$

For Γ_{23} we can argue analogous to the Γ_{13} case. Because there is no precipitation, i.e., $q(\boldsymbol{\Phi}_0^{in}) = 0$, we obtain

$$\mu_{3,0}^{in} - \mu_{2,0}^{in} = const. \qquad \text{and} \qquad \nu = 0. \tag{7.80}$$

Lastly, we consider the fluid–fluid interface Γ_{12}, with Ω_1 in the direction of negative z. There is no precipitation process, so with $q(\boldsymbol{\Phi}_0^{in}) = 0$ we integrate over (7.73) and use matching conditions (7.64) for $\phi_{1,0}^{in}$ and (7.65) for $\partial_z \mu_{1,0}^{in}$ and obtain

$$\nu = -(\partial_x s)\mathbf{v}_{0,0}^{(1),in} + \mathbf{v}_{1,0}^{(2),in}. \tag{7.81}$$

Furthermore, $\mu_{1,0}^{in}$ has to be constant in z, and with analogous argumentation using (7.74) also $\mu_{2,0}^{in}$ is constant.

Inner Expansion of (7.45)*,* $O(1)$*:* We consider the interface Γ_{ij} with Ω_i in negative z direction. We assume the absence of a third phase, i.e., $\phi_{k,0}^{in} = 0$, $k \in \{1,2,3\} \setminus \{i,j\}$, and find by construction of W in Section 3.1.2.1 that $\partial_{\phi_i} W'(\boldsymbol{\Phi}_0^{in}) = W'_{\mathrm{dw}}(\phi_{i,0}^{in})$. We examine the difference $\mu_i - \mu_j$ at first order and find

$$\begin{aligned} \mu_{i,0}^{in} - \mu_{j,0}^{in} = \Sigma_i W''_{\mathrm{dw}}(\phi_{i,0}^{in})\phi_{i,1}^{in} - \Sigma_i \partial_z^2 \phi_{i,1}^{in} \\ - \Sigma_j W''_{\mathrm{dw}}(\phi_{j,0}^{in})\phi_{j,1}^{in} + \Sigma_j \partial_z^2 \phi_{j,1}^{in}. \end{aligned} \tag{7.82}$$

In absence of a third phase $\phi_{i,0}^{in} + \phi_{j,0}^{in} = 1$, and by construction $W_{\mathrm{dw}}(\phi)$ is symmetric around $\phi = 1/2$. Therefore, $W''_{\mathrm{dw}}(\phi_{i,0}^{in}) = W''_{\mathrm{dw}}(\phi_{j,0}^{in})$, and we rewrite (7.82) as

$$\mu_{i,0}^{in} - \mu_{j,0}^{in} = \left(W''_{\mathrm{dw}}(\phi_{j,0}^{in}) - \partial_z^2\right)\left(\Sigma_i \phi_{i,1}^{in} - \Sigma_j \phi_{j,1}^{in}\right).$$

Recall that $\mu_{i,0}^{in} - \mu_{j,0}^{in}$ is constant across the interface Γ_{ij}. After multiplying with $\partial_z \phi_{j,0}^{in}$ and integrating over z we calculate

$$\mu_{i,0}^{in} - \mu_{j,0}^{in} = \int_{-\infty}^{\infty} \left(\partial_z \phi_{j,0}^{in}\right)\left(\mu_{i,0}^{in} - \mu_{j,0}^{in}\right) dz$$

$$
\begin{aligned}
&= \int_{-\infty}^{\infty} \left(\partial_z \phi_{j,0}^{in}\right) \left(W''_{\mathrm{dw}}(\phi_{j,0}^{in}) - \partial_z^2\right) \left(\Sigma_i \phi_{i,1}^{in} - \Sigma_j \phi_{j,1}^{in}\right) dz \\
&= \int_{-\infty}^{\infty} \left(W''_{\mathrm{dw}}(\phi_{j,0}^{in}) \partial_z \phi_{j,0}^{in} - \partial_z^3 \phi_{j,0}^{in}\right) \left(\Sigma_i \phi_{i,1}^{in} - \Sigma_j \phi_{j,1}^{in}\right) dz \\
&= \int_{-\infty}^{\infty} \partial_z \left(W'_{\mathrm{dw}}(\phi_{j,0}^{in}) - \partial_z^2 \phi_{j,0}^{in}\right) \left(\Sigma_i \phi_{i,1}^{in} - \Sigma_j \phi_{j,1}^{in}\right) dz \\
&= 0.
\end{aligned}
$$

We have used partial integration to get to the third line, the boundary terms vanish with matching condition (7.66) and the structure of $\phi_{j,0}^{in}$ (7.68). The fourth line evaluates to zero with the equipartition of energy. Note that compared to Section 3.2.3 there is no curvature term in this calculation, as the Cahn–Hilliard evolution acts only in the y-direction.

We conclude

$$\mu_{i,0}^{in} = \mu_{j,0}^{in}, \tag{7.83}$$

and (7.79) simplifies to

$$\nu = \begin{cases} +\bar{Da}\, r(c) & \text{for } \lim_{z\to-\infty} \boldsymbol{\Phi}_0^{in} = \mathbf{e}_3 \text{ and } \lim_{z\to\infty} \boldsymbol{\Phi}_0^{in} = \mathbf{e}_1, \\ -\bar{Da}\, r(c) & \text{for } \lim_{z\to-\infty} \boldsymbol{\Phi}_0^{in} = \mathbf{e}_1 \text{ and } \lim_{z\to\infty} \boldsymbol{\Phi}_0^{in} = \mathbf{e}_3. \end{cases} \tag{7.84}$$

Inner Expansion of (7.47), $O(\bar{\varepsilon}^{-2})$*:* At leading order the equation reads

$$\partial_z(\gamma(\boldsymbol{\Phi}_0^{in}) \partial_z w_0^{in}) = 0.$$

After integrating in y we use matching condition (7.65) divide by $\gamma(\boldsymbol{\Phi}_0^{in}) > 0$ and find

$$\partial_z w_0^{in} = 0, \tag{7.85}$$

so w is constant across the interface. With matching condition (7.65) this implies

$$\lim_{y\to 0^+} w_0^{out}(t,x,s+y) = \lim_{y\to 0^+} w_0^{out}(t,x,s-y). \tag{7.86}$$

Inner Expansion of (7.47)*,* $O(\bar{\varepsilon}^{-1})$*:* With (7.85) the first order term of (7.47) reads

$$\partial_z(\gamma(\boldsymbol{\Phi}_0^{in})\partial_z w_1^{in}) = 0.$$

We integrate and with matching conditions (7.64), (7.66) we get

$$\begin{aligned}\lim_{y\to 0^+} &\left(\gamma(\boldsymbol{\Phi}_0^{out}(t,x,s+y))\partial_y w_0^{out}(t,x,s+y)\right)\\ &= \lim_{y\to 0^+} \left(\gamma(\boldsymbol{\Phi}_0^{out}(t,x,s-y))\partial_y w_0^{out}(t,x,s-y)\right).\end{aligned} \tag{7.87}$$

Inner Expansion of (7.37)*,* $O(1)$*:* We only need to investigate the reaction term

$$\frac{\bar{Da}}{\bar{\varepsilon}} R_{\text{total}} = -\frac{\bar{Da}}{\bar{\varepsilon}} \int_{-\ell_\Omega/2}^{\ell_\Omega/2} q(\boldsymbol{\Phi})(r(c) + \tilde{\alpha}\mu_1 - \tilde{\alpha}\mu_3)\, dy.$$

On Γ_{12} and Γ_{23} we have $q(\boldsymbol{\Phi}^{in}) = O(\bar{\varepsilon}^2)$ and therefore no leading order contribution. Let us consider Γ_{13} with Ω_1 in negative z direction. Using (7.83) the leading order term of the integrand is $q(\boldsymbol{\Phi}_0^{in})r(c_0^{out})$. Transforming the integral to the z coordinate results in the leading order term of $O(1)$

$$-\bar{Da}\; r(c_0^{out}) \int_{-\infty}^{\infty} q(\boldsymbol{\Phi}_0^{in})\, dz.$$

By construction of q we have with the equipartition of energy that $q(\boldsymbol{\Phi}_0^{in}) = d_z\phi_{3,0}^{in}$. With matching condition (7.64) the integral evaluates to one. When considering Γ_{13} with Ω_1 in positive z direction we get the same result.

There might be multiple Γ_{13} interfaces contributing to the macroscopic reaction term. Therefore, the total contribution to (7.37) at order $O(1)$ is

$$\bar{Da}\, R_{\text{interface}} = -\bar{Da} N(\Gamma_{13}) r(c_0^{out}), \tag{7.88}$$

with $N(\Gamma_{13})$ being the number of Γ_{13} interfaces for a fixed x.

7.3.4 The Upscaled Sharp-Interface Model

We summarize the results of the matched asymptotic expansions. For this we drop the subscript 0 and the superscript *out* for ease of notation. We call (7.89)–(7.107) the upscaled sharp-interface model.

The macroscopic equations for the unknowns Q_f, p and c are given by (7.54), (7.55) and (7.57),

$$\partial_x Q_f = 0, \tag{7.89}$$

$$Q_f = -K_f \partial_x p, \tag{7.90}$$

$$\begin{aligned} \frac{d}{dt}\left(\phi_{c,\text{total}} c\right) + \partial_x\left((-K_c \partial_x p) c\right) \\ = \frac{1}{\bar{Pe}_c} \partial_x\left(\phi_{c,\text{total}} \partial_x c\right) + \bar{Da}\, R_{\text{interface}}. \end{aligned} \tag{7.91}$$

The coefficients of the upscaled equations depend on the distribution of the phases in the thin strip. In contrast to the upscaled phase field model (7.35)–(7.50) the sharp-interface limit does not depend on the phase-field variables $\boldsymbol{\Phi}$. Instead, the three disjoint domains $\Omega_1(t)$, $\Omega_2(t)$ and $\Omega_3(t)$ are used to locate the phases. The interface between Ω_i and Ω_j is denoted by Γ_{ij}. We introduce the notation $\Omega_i|_x = \{y \in [-\ell_\Omega/2, \ell_\Omega/2] : (x, y) \in \Omega_i(t)\}$, and write $N(\Gamma_{13})$ for the

number of Γ_{13} interfaces at a given x. With (7.58), (7.56), (7.59), (7.88) we can calculate the coefficients of (7.89)–(7.91) as

$$\phi_{c,\text{total}}(x) = \text{vol}\,(\Omega_1|_x)\,, \tag{7.92}$$

$$K_f(t,x) = \int_{\Omega_1|_x \cup \Omega_2|_x} w\,dy, \tag{7.93}$$

$$K_c(t,x) = \int_{\Omega_1|_x} w\,dy, \tag{7.94}$$

$$R_{\text{interface}} = -N(\Gamma_{13})r(c). \tag{7.95}$$

We describe the evolution of the phases with the interface velocity ν. This velocity in y direction is given by (7.84), (7.80), (7.81), summarized as

$$\nu = \pm \bar{D}a\; r(c) \qquad \text{on } \Gamma_{13}, \text{ with } \Omega_1 \text{ in } \pm y \text{ direction}, \tag{7.96}$$

$$\nu = 0 \qquad \text{on } \Gamma_{23}, \tag{7.97}$$

$$\nu = -(\partial_x s)\mathbf{v}_0^{(1)} + \mathbf{v}_1^{(2)} \qquad \text{on } \Gamma_{12}. \tag{7.98}$$

For the flow profile we solve at each x and t a cell problem for the unknown w. Summarizing (7.51), (7.52), (7.86), (7.87) and the boundary condition (7.48), the unknown w is given by the second order differential equation

$$-\partial_y(\gamma_1 \partial_y w) = 1 \qquad \text{in } \Omega_1|_x, \tag{7.99}$$

$$-\partial_y(\gamma_2 \partial_y w) = 1 \qquad \text{in } \Omega_2|_x, \tag{7.100}$$

$$\rho_3 d_0 w - \partial_y(\gamma_3 \partial_y w) = 0 \qquad \text{in } \Omega_3|_x, \tag{7.101}$$

$$[\![w]\!] = 0 \qquad \text{at } \Gamma_{12}, \Gamma_{13}, \Gamma_{23}, \tag{7.102}$$

$$[\![\gamma \partial_y w]\!] = 0 \qquad \text{at } \Gamma_{12}, \Gamma_{13}, \Gamma_{23}, \tag{7.103}$$

$$w = 0 \qquad \text{at } y = \pm \ell_\Omega/2. \tag{7.104}$$

For the transport of the fluid–fluid interface Γ_{12} in (7.98) we need the flow velocities $\mathbf{v}_0^{(1)}$ and $\mathbf{v}_1^{(2)}$. We then get the horizontal flow

velocity $\mathbf{v}_0^{(1)}$ from (7.49),

$$\mathbf{v}_0^{(1)} = -w\partial_x p_0. \tag{7.105}$$

For the vertical flow velocity $\mathbf{v}_1^{(2)}$ one has to solve (7.53), (7.70) and (7.72), summarized

$$\partial_x(\mathbf{v}_0^{(1)}) + \partial_y(\mathbf{v}_1^{(2)}) = 0 \qquad \text{in } \Omega_1 \cup \Gamma_{12} \cup \Omega_2, \tag{7.106}$$

$$-(\partial_x s)\mathbf{v}_0^{(1)} + \mathbf{v}_1^{(2)} = 0 \qquad \text{on } \Gamma_{13} \text{ and } \Gamma_{23}. \tag{7.107}$$

7.3.5 The Upscaled Sharp-Interface Model in a Simplified Geometry with Symmetry

The upscaled sharp-interface model (7.89)–(7.107) uses no assumption on how the phases are distributed. When these are appearing in a fixed order, the model simplifies. In this case, there is no need to consider a general subdomain Ω_i for the phase i, it is sufficient to know the width of the phase i layer in the y direction. These widths become unknowns of the model.

We assume here the following simplified geometry. The solid phase (in Ω_3) is covered by a film of fluid 1 (occupying Ω_1). The second fluid (in Ω_2) is located in the middle of the thin strip. For simplicity, we assume symmetry around the x-axis. An illustration of the geometry is given in Figure 7.2.

With functions $d_1(t,x) > 0$, $d_2(t,x) > 0$, representing the width in y direction of the fluid phase 1, respectively 2, we can describe this situation by defining

$$\begin{aligned}
\Omega_2(t) &= \{(x,y) : -d_2(t,x) < y < d_2(t,x)\}, \\
\Omega_1(t) &= \{(x,y) : -d_1(t,x) - d_2(t,x) < y < -d_2(t,x)\} \\
&\quad \cup \{(x,y) : d_2(t,x) < y < d_1(t,x) + d_2(t,x)\}, \\
\Omega_3(t) &= \{(x,y) : -\ell_\Omega/2 < y < -d_1(t,x) - d_2(t,x)\} \\
&\quad \cup \{(x,y) : d_1(t,x) + d_2(t,x) < y < \ell_\Omega/2\}.
\end{aligned}$$

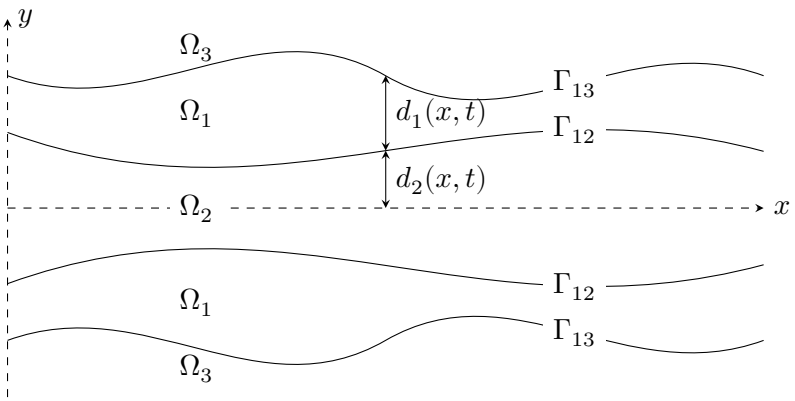

Figure 7.2: Symmetric geomery of two fluid phases in a thin strip

In this geometry the solution w to the cell problem (7.99)–(7.104) depends only on the variables d_1 and d_2, and on the choice of ℓ_Ω. With a lengthy calculation we find that the terms depending on ℓ_Ω decay exponentially fast for big ℓ_Ω, and we drop them in the following. The remaining terms lead to

$$K_f = \frac{2}{\gamma_1}\left(\frac{(d_1+d_2)^3}{3} + \left(\frac{\gamma_1}{\gamma_2}-1\right)\frac{d_2^3}{3} + L_{\text{slip}}(d_1+d_2)^2\right),$$
$$K_c = \frac{2}{\gamma_1}\left(\frac{d_1^3}{3} + \frac{d_1^2 d_2}{2} + L_{\text{slip}} d_1(d_1+d_2)\right),$$

with the slip length L_{slip} given by

$$L_{\text{slip}} = \frac{\gamma_1}{\sqrt{\rho_3 d_0 \gamma_3}}.$$

We can relate $\partial_t d_1$ and $\partial_t d_2$ with the interface velocities (7.96)–(7.98). Considering the fluid–solid interface Γ_{13} we get with (7.96)

$$\partial_t\,(d_1+d_2) = \nu = -\bar{D}a\; r(c), \tag{7.108}$$

while for the fluid–fluid interface Γ_{12} we calculate with (7.98), (7.106), (7.107)

$$\begin{aligned}
\partial_t d_2 &= -(\partial_x d_2)\mathbf{v}_0^{(1)}(t,x,d_2) + \mathbf{v}_1^{(2)}(t,x,d_2) \\
&\quad + (\partial_x(d_1+d_2))\mathbf{v}_0^{(1)}(t,x,d_1+d_2) - \mathbf{v}_1^{(2)}(t,x,d_1+d_2) \\
&= (\partial_x(d_2+d_1))\mathbf{v}_0^{(1)}(t,x,d_1+d_2) - (\partial_x d_2)\mathbf{v}_0^{(1)}(t,x,d_2) \\
&\quad - \int_{d_2}^{d_2+d_1} \partial_y \mathbf{v}_1^{(2)}(t,x,y)\,dy \\
&= (\partial_x(d_2+d_1))\mathbf{v}_0^{(1)}(t,x,d_1+d_2) - (\partial_x d_2)\mathbf{v}_0^{(1)}(t,x,d_2) \\
&\quad + \int_{d_2}^{d_2+d_1} \partial_x \mathbf{v}_0^{(1)}(t,x,y)\,dy \\
&= \partial_x \left(\int_{d_2}^{d_2+d_1} \mathbf{v}_0^{(1)}(t,x,y)\,dy \right).
\end{aligned}$$

The integral equals the total fluid flux in x direction in the upper half of Ω_1. We use (7.105), (7.94) and the symmetry of w around $y=0$ to further calculate

$$\begin{aligned}
\partial_t d_2 &= \partial_x \left(\int_{d_2}^{d_2+d_1} \mathbf{v}_0^{(1)}\,dy \right) = -\partial_x \left((\partial_x p) \int_{d_2}^{d_2+d_1} w\,dy \right) \\
&= -\frac{1}{2}\partial_x \left(K_c \partial_x p \right).
\end{aligned} \tag{7.109}$$

We can now summarize (7.89), (7.90), (7.91), (7.108) and (7.108) as an upscaled model for the unknowns d_1, d_2, p, Q_f and c

$$\partial_t d_1 + \partial_t d_2 = -\bar{D}a\; r(c(t,x)), \tag{7.110}$$

$$\partial_t d_2 = -\frac{1}{2}\partial_x \left(K_c(d_1,d_2)\partial_x p \right), \tag{7.111}$$

$$Q_f = -K_f(d_1,d_2)\partial_x p, \tag{7.112}$$

$$\partial_x Q_f = 0, \tag{7.113}$$

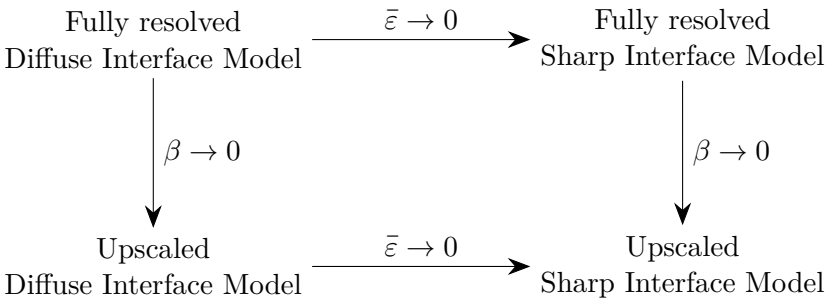

Figure 7.3: Models obtained by upscaling ($\beta \to 0$) and sharp interface limit ($\bar{\varepsilon} \to 0$).

$$\frac{d}{dt}\left(2d_1 c\right) + \partial_x\left(\left(-K_c(d_1,d_2)\partial_x p\right)c\right) = \frac{1}{Pe_c}\partial_x\left(2d_1\partial_x c\right) - 2\bar{D}a\, r(c). \tag{7.114}$$

Remark 7.3: *We can rewrite* (7.111), (7.112) *to highlight the hyperbolicity of the model. As discussed in Remark 7.1 one assumption for the upscaling is that there is no occurrence of triple points. Therefore, we assume* $d_1 > 0$ *and* $d_2 > 0$ *and deduce* $K_f > 0$, $K_c > 0$. *We can now calculate*

$$\partial_t d_2 = \frac{1}{2} Q_f \partial_x \left(\frac{K_c(d_1,d_2)}{K_f(d_1,d_2)} \right). \tag{7.115}$$

The unknown d_2 *gets transported with flux* $Q_f K_c/K_f$ *and can show hyperbolic behavior, such as the formation of discontinuities.*

7.3.6 Asymptotic Consistency

In Section 7.2 we have investigated the limit process $\beta \to 0$, while in Section 7.3 we examined $\bar{\varepsilon} \to 0$. A common question is under which circumstances there is asymptotic consistency, i.e., these two limit processes commute. In Figure 7.3 all limit processes are shown in a commutative diagram.

We investigate asymptotic consistency with non-dimensional numbers chosen as in (7.11)–(7.16) with $\bar{Re}$, $\bar{Ca}$, $\bar{Da}$, $\bar{M}$, $\bar{Pe}_c$ constant and independent of $\bar{\varepsilon}$ and β. The non-dimensional δ is chosen as $\delta = \bar{\varepsilon}$.

When starting with the fully-resolved diffuse-interface model, given by (7.3)–(7.10), the limit $\bar{\varepsilon} \to 0$ results in a sharp-interface model as described in Section 3.1.1.

When we assume the geometry of Section 7.3.5 we can proceed to upscale the fully-resolved sharp-interface model after introducing d_1 and d_2. While the process is tedious, the main ideas are analogous to the calculations in [Sharmin, Bringedal, et al. 2020]. In particular the asymptotic expansion of interface conditions, normal vectors and curvature has to be handled with care, as the coordinates $\mathbf{x} = (x, \beta y)$ depend on β. For sake of brevity we skip this calculation here.

With the geometry of Section 7.3.5 we find asymptotic consistency, i.e., the limit processes $\beta \to 0$ and $\bar{\varepsilon} \to 0$ commute. The result of the upscaling of the fully-resolved sharp-interface model is exactly given by (7.110)–(7.114).

Remark 7.4: *In more general geometries, asymptotic consistency does not necessarily hold. This is due to the following observation. When upscaling a fully-resolved diffuse-interface model, the parameter δ is constant and independent of β. This leads to $\tilde{\phi}_f > 0$ and $\tilde{\phi}_c > 0$ everywhere. Because of this, we obtain upscaled equations for p and c without further assumptions on the geometry. The upscaled variables p and c do not depend on y, even if the geometry consists of two parallel channels separated by a solid region with $\boldsymbol{\Phi} \approx \mathbf{e}_3$. On the other hand, when upscaling the fully-resolved diffuse-interface model, the δ-modifications have already vanished, as $\delta = \bar{\varepsilon}$. In this case, it is possible to have a different pressure p in each channel, i.e., in each connected part of $\overline{\Omega_1|_x \cup \Omega_2|_x}$. Also, it is possible to have a different ion concentration c in each connected part of $\Omega_1|_x$.*

We conclude that we have asymptotic consistency under the condition that there is only one flow channel, i.e., $\overline{\Omega_1|_x \cup \Omega_2|_x}$ is connected for every x, and that the first fluid phase is connected, i.e., $\Omega_1|_x$ is

connected for every x. It is also possible to consider the symmetric case as in Section 7.3.5 and have two symmetric connected parts of fluid one.

7.4 Numerical Scheme for the Upscaled δ-$2f1s$-Model

The upscaled δ-$2f1s$-model consists of multiple coupled problems. The upscaled equations (7.35)–(7.37) for the unknowns Q_f, p and c have parameters (7.38)–(7.41) that depend on the distribution of phases in y-direction. This distribution is described by the fully coupled two-dimensional problem (7.42)–(7.45) for the Cahn–Hilliard variables ϕ_1, ϕ_2, ϕ_3, μ_1, μ_2, μ_3. Furthermore, the flow profile has to be calculated by the cell problem (7.47), (7.48).

For simplicity, we present the numerical scheme for equidistant time steps $t_n = n\Delta t$ and equidistant discretization in x by $x_k = k\Delta x$. Let also $x_{k+1/2} = (x_k + x_{k+1})/2$. For each t_n, x_k we discretize the one-dimensional unknown $\phi^n_{1,k}(y) = \phi_1(t_n, x_k, y)$ with linear Lagrange elements, and analogous for $\phi^n_{2,k}$, $\phi^n_{3,k}$, $\mu^n_{1,k}$, $\mu^n_{2,k}$, $\mu^n_{3,k}$, $\mathbf{v}^{(1),n}_{0,k}$, $\mathbf{v}^{(2),n}_{1,k}$, w^n_k. Again, we also use this notation for other variables such as $\tilde{\phi}^n_{f,k}$.

We discretize the macroscopic unknown $c(t,x)$ with a finite volume scheme, so $c^n(x) = c(t_n, x)$ is piecewise constant with $c(t_n, x) = c^n_k$ for $x \in (x_{k-1/2}, x_{k+1/2})$. The pressure $p^n(x) = p(t_n, x)$ is discretized using linear Lagrange elements with nodes $x_{k+1/2}$. Therefore, $\partial_x p$ is constant on each finite volume cell $(x_{k-1/2}, x_{k+1/2})$.

Algorithm 7.5 (Two-Scale Scheme for Upscaled δ-$2f1s$-Model)**:** *Given $\boldsymbol{\Phi}^n_k$, c^n_k for all x_k at time t_n, we calculate $\boldsymbol{\Phi}^{n+1}_k$, c^{n+1}_k with the following steps.*

1. *For each x_k use (7.47), (7.48) to solve for $w^n_k(y)$. Here we use $\boldsymbol{\Phi} = \boldsymbol{\Phi}^n_k$ and the finite element method to discretize the*

equation. The equations for different x_k are independent and can be solved in parallel.

2. *For each x_k calculate $K^n_{f,k}$ and $K^n_{c,k}$ by*

$$K^n_{f,k} = \int_{-\ell_\Omega/2}^{\ell_\Omega/2} \tilde{\phi}^n_{f,k} w^n_k \, dy, \qquad K^n_{c,k} = \int_{-\ell_\Omega/2}^{\ell_\Omega/2} \tilde{\phi}^n_{c,k} w^n_k \, dy.$$

3. *Solve for $p^n(x)$ using the finite element method with*

$$\partial_x(-K^n_f \partial_x p^n) = 0.$$

Here $K^n_f(x) = K^n_{f,k}$ for $x \in (x_{k-1/2}, x_{k+1/2})$. As $K^n_f > 0$, the pressure p is either a monotone increasing or monotone decreasing function, depending on the boundary conditions. We assume from here on $\partial_x p^n \leq 0$ and therefore fluid flow in positive x direction. In case $\partial_x p^n \geq 0$ the upwind schemes in Steps 5 and 7 have to be modified.

4. *For each x_k calculate $\mathbf{v}^{(1),n}_{0,k}(y) = -w^n_k(y)\partial_x p^n(x_k)$.*

5. *Next, for each x_k we solve for $\mathbf{v}^{(2),n}_{1,k}$ and the Cahn–Hilliard variables $\phi^{n+1}_{2,k}$, $\phi^{n+1}_{3,k}$, $\mu^{n+1}_{1,k}$, $\mu^{n+1}_{2,k}$, $\mu^{n+1}_{3,k}$. For $\mathbf{v}^{(2),n}_{1,k}$ we use* (7.50) *the with an explicit upwind scheme for the x-derivative, i.e.,*

$$\partial_y(\tilde{\phi}^{n+1}_{f,k} \mathbf{v}^{(2),n}_{1,k}) = -\frac{\tilde{\phi}^n_{f,k} \mathbf{v}^{(1),n}_{0,k} - \tilde{\phi}^n_{f,k-1} \mathbf{v}^{(1),n}_{0,k-1}}{\Delta x}. \tag{7.116}$$

This equation is coupled with the Cahn–Hilliard cell problems (7.42)–(7.45)*. We again use an explicit upwinding scheme for*

the x-derivative,

$$\begin{aligned}
&\frac{\phi_{1,k}^{n+1}-\phi_{1,k}^{n}}{\Delta t}+\frac{\phi_{1,k}^{n}\mathbf{v}_{0,k}^{(1),n}-\phi_{1,k-1}^{n}\mathbf{v}_{0,k-1}^{(1),n}}{\Delta x}\\
&\quad+\partial_y(\phi_{1,k}^{n+1}\mathbf{v}_{1,k}^{(2),n})-\frac{\bar{\varepsilon}\bar{M}}{\Sigma_1}\partial_y^2\mu_{1,k}^{n+1} \qquad (7.117)\\
&\quad=-\frac{\bar{D}a}{\bar{\varepsilon}}q(\boldsymbol{\Phi}_k^{n+1})\left(r(c^n(x_k))+\tilde{\alpha}\mu_{1,k}^{n+1}-\tilde{\alpha}\mu_{3,k}^{n+1}\right),\\
&\frac{\phi_{2,k}^{n+1}-\phi_{2,k}^{n}}{\Delta t}+\frac{\phi_{2,k}^{n}\mathbf{v}_{0,k}^{(1),n}-\phi_{2,k-1}^{n}\mathbf{v}_{0,k-1}^{(1),n}}{\Delta x}\\
&\quad+\partial_y(\phi_{2,k}^{n+1}\mathbf{v}_{1,k}^{(2),n})-\frac{\bar{\varepsilon}\bar{M}}{\Sigma_1}\partial_y^2\mu_{2,k}^{n+1}=0, \qquad (7.118)\\
&\phi_{3,k}^{n+1}=1-\phi_{1,k}^{n+1}-\phi_{2,k}^{n+1}, \qquad (7.119)\\
&\mu_{1,k}^{n+1}=\frac{\partial_{\phi_1}W(\boldsymbol{\Phi}_k^{n+1})}{\bar{\varepsilon}}-\bar{\varepsilon}\Sigma_i\partial_y^2\phi_{1,k}^{n+1}, \qquad (7.120)\\
&\mu_{2,k}^{n+1}=\frac{\partial_{\phi_2}W(\boldsymbol{\Phi}_k^{n+1})}{\bar{\varepsilon}}-\bar{\varepsilon}\Sigma_i\partial_y^2\phi_{2,k}^{n+1}, \qquad (7.121)\\
&\mu_{3,k}^{n+1}=-\mu_{1,k}^{n+1}-\mu_{2,k}^{n+1}. \qquad (7.122)
\end{aligned}$$

Note that we do not use (7.44) *and* (7.45) *for* $\phi_{3,k}^{n+1}$ *and* $\mu_{3,k}^{n+1}$. *Instead, we use that by construction* $\phi_1+\phi_2+\phi_3=1$ *and* $\mu_1+\mu_2+\mu_3=0$.

We use the finite element method to discretize (7.116)–(7.122) *and Newtons method to solve the resulting nonlinear system. This step has by far the highest computational cost. With the explicit upwinding scheme for the x derivatives, the cell problems for each k fully decouple and can be solved in parallel. This leads to a significant speed-up in comparison to discretizing the Cahn–Hilliard evolution* (7.42)–(7.45) *naively as a two-dimensional problem.*

6. *Calculate* $\tilde{\phi}^{n+1}_{c,total,k}$ *and* $R^{n+1}_{total,k}$ *as*

$$\tilde{\phi}^{n+1}_{c,total,k} = \int_{-\ell_\Omega/2}^{\ell_\Omega/2} \phi^{n+1}_{c,k}\, dy, \tag{7.123}$$

$$R^{n+1}_{total,k} = -\int_{-\ell_\Omega/2}^{\ell_\Omega/2} q(\boldsymbol{\Phi}^{n+1}_k)\left(r(c^n(x_k)) + \tilde{\alpha}\mu^{n+1}_{1,k} - \tilde{\alpha}\mu^{n+1}_{3,k}\right) dy. \tag{7.124}$$

We also set $\tilde{\phi}^{n+1}_{c,total,k+1/2} = (\tilde{\phi}^{n+1}_{c,total,k} + \tilde{\phi}^{n+1}_{c,total,k+1})/2$.

7. *Finally, we solve for* c *using* (7.37) *discretized by the finite volume method. We use an implicit upwinding scheme for the transport in* x*-direction*

$$\begin{aligned}
&\frac{\tilde{\phi}^{n+1}_{c,total,k}c^{n+1}_k - \tilde{\phi}^{n}_{c,total,k}c^{n}_k}{\Delta t} \\
&\quad - \frac{K^n_{c,k}\partial_x p^n(x_k)c^{n+1}_k - K^n_{c,k-1}\partial_x p^n(x_{k-1})c^{n+1}_{k-1}}{\Delta x} \\
&= \frac{1}{\bar{Pe}_c}\frac{1}{\Delta x}\left(\tilde{\phi}^{n+1}_{c,total,k+1/2}\frac{c^{n+1}_{k+1} - c^{n+1}_k}{\Delta x}\right. \\
&\qquad \left. -\phi^{n+1}_{c,total,k-1/2}\frac{c^{n+1}_k - c^{n+1}_{k-1}}{\Delta x}\right) + \frac{\bar{Da}}{\bar{\varepsilon}}R^{n+1}_{total,k}.
\end{aligned} \tag{7.125}$$

7.5 Numerical Investigation

We now compare the upscaled δ-$2f1s$-model (7.35)–(7.50) to the fully-resolved δ-$2f1s$-model (7.3)–(7.10). Remark 7.3 suggests that shock fronts can form in the upscaled model. Note that in this case the assumptions for the upscaling in Section 7.2 are no longer valid, and we expect different behaviors from the two models.

For the fully-resolved δ-$2f1s$-model we use the framework described in Section 3.3.

7.5.1 Comparison: Formation of an N-Wave

As our first numerical example we choose a geometry as described in Section 7.3.5, with the computational domain $(x, y) \in [0, 1] \times [-1, 0]$. For $x = 0$ and $x = 1$ we choose periodic boundary conditions for all variables except the pressure p. For $y = -1$ we use the trivially upscaled versions of the boundary conditions (7.17)–(7.20) and for $y = 0$ we choose boundary conditions according to the symmetry assumption.

We compare the non-dimensional δ-$2f1s$-model with the upscaled δ-$2f1s$-model (7.35)–(7.50). For simplicity, we choose $\gamma_1 = \gamma_2$ and d_0 sufficiently big such that $L_{\text{slip}} \approx 0$. We choose the phase-field parameter $\bar{\varepsilon} = 0.03$ and $\delta = \bar{\varepsilon}$ as in Section 7.3.

We want to focus on the hyperbolic behavior of d_2 as described in Remark 7.3. Therefore, we choose c in the initial conditions such that $r(c) = 0$. This leads to no precipitation or dissolution in the model, and the fluid–solid interface does not change over time. We choose

$$d_1 + d_2 \equiv 0.7 \qquad \text{and} \qquad d_1(x) = 0.4 + 0.15 \sin(2\pi x).$$

This corresponds to a plane fluid–solid interface and a sine-shaped fluid–fluid interface. An image of these initial conditions is given in Figure 7.4.

By applying a pressure difference as Dirichlet boundary condition at $x = 0$ and $x = 1$, the two fluid phases move in positive x-direction. The fluid velocity $\mathbf{v}_0^{(1)}$ is higher in the center of the channel. As shown in Figure 7.4 this leads to a steeper fluid–fluid interface over time. At a time $t^* > 0$ the upscaled δ-$2fs$ model has a fluid–fluid interface that is perpendicular to the thin strip. As discussed in Remark 7.1, the assumptions for the upscaling in Section 7.2 are no longer valid. For times $t > t^*$ the fluid–fluid interface rolls over, leading to multiple layers of fluid phase 1 at the same x coordinate.

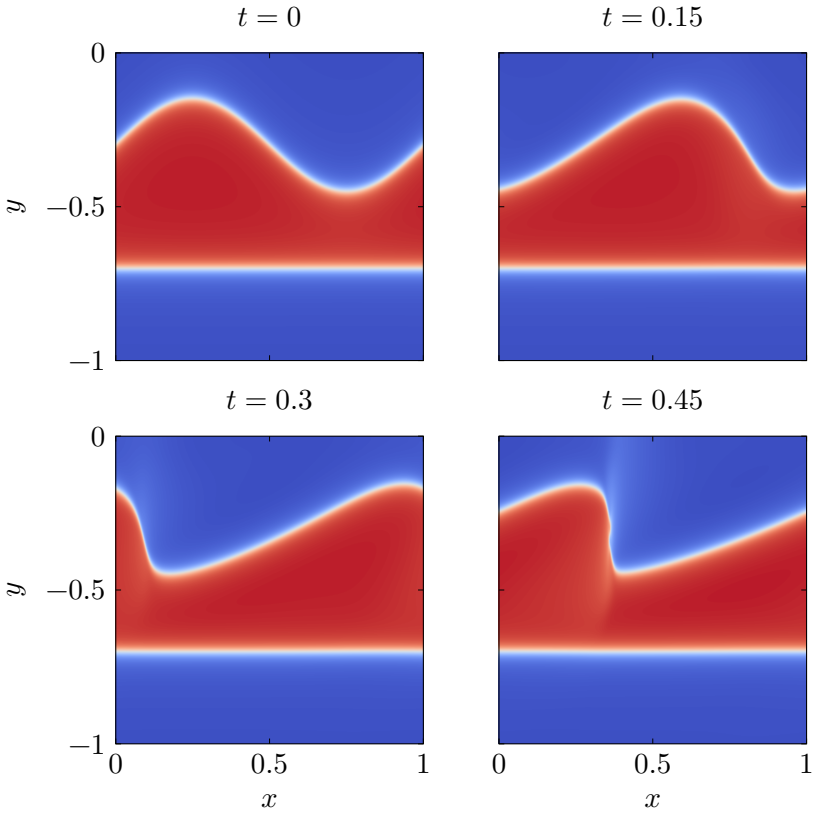

Figure 7.4: Evolution of the upscaled δ-2f1s-model on the domain $[0, 1] \times [-1, 0]$. Shown in red is fluid phase one, with fluid phase two above and the solid phase below.

We can compare this behavior with the non-dimensional δ-$2f1s$-model in a thin strip for different values of β. As shown in Figure 7.5, for times $t < t^*$ there is a good agreement between the non-dimensional δ-$2f1s$-model with small values of β and the upscaled δ-$2f1s$-model.

In contrast to the upscaled δ-$2f1s$-model, the non-dimensional δ-$2f1s$-model does not evolve to a fluid–fluid interface perpendicular to the thin strip, as shown in Figure 7.5. Instead, when reaching a steep fluid–fluid interface there are regions of high curvature at the beginning and end of the steep passage. In these regions of high curvature the surface tension leads to a pressure difference between the fluid phases, counteracting the interface getting steeper. For smaller β the fluid–fluid interface allows for a steeper passage in (x, y) coordinates, as this effect depends on the curvature in the $\mathbf{x}$ coordinates, which are not scaled with β.

7.5.2 Comparison: Precipitation

In the second numerical example we study precipitation in the thin strip. We use the same domain and boundary conditions as in the previous example. Again, we choose $\gamma_1 = \gamma_2$, and a d_0 large enough so that $L_{\text{slip}} \approx 0$. We further choose $\bar{\varepsilon} = 0.03$ and $\delta = \bar{\varepsilon}$. We use a simple, linear reaction rate $r(c) = c - 0.5$ and choose the ion concentration to be in equilibrium initially, i.e., $c = 0.5$ everywhere. With $d_1(x) = 0.4$ and $d_2(x) = 0.3$ in the initial conditions correspond to the phases being layered in the thin strip, without depending on x. To induce precipitation we add a source term $s(x)$ to the ion conservation equation (7.5), it now reads

$$\begin{aligned}\partial_t(\tilde{\phi}_c c) + \nabla \cdot (\phi_c \mathbf{v} c) + \frac{Cn}{\beta Pe_{CH}} \nabla \cdot (\mathbf{J}_1 c) \\ = \frac{1}{Pe_c} \nabla \cdot (\tilde{\phi}_c \nabla c) + DaR + \tilde{\phi}_c s(x).\end{aligned}$$

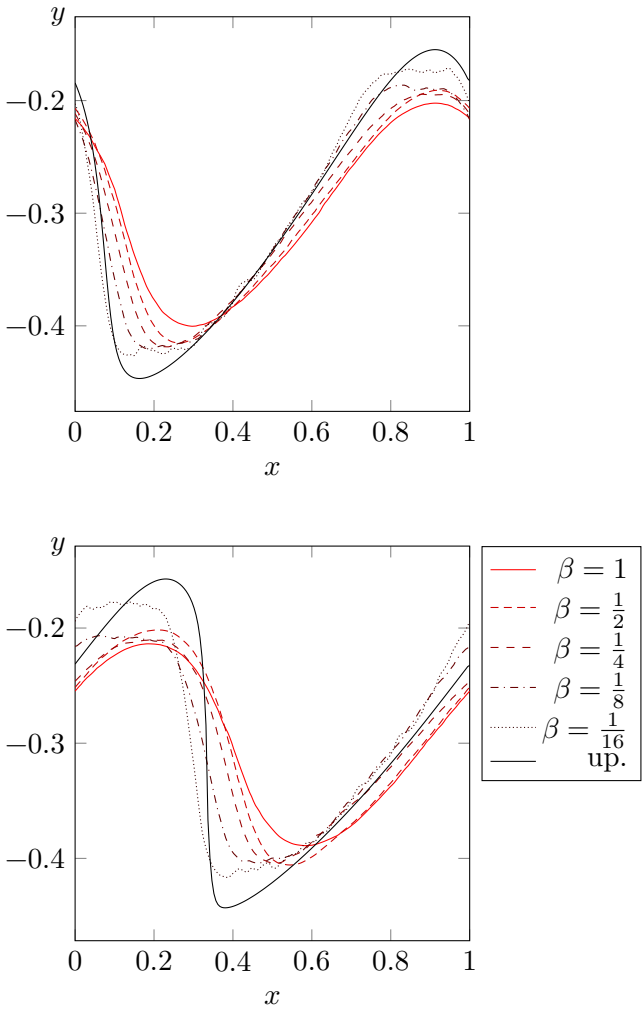

Figure 7.5: Fluid–fluid interface locations for the non-dimensional δ-$2f1s$-model with varying β, and for the up-scaled δ-$2f1s$-model. The interface is located through the condition $\phi_1 = \phi_2$. Top: $t = 0.3$, Bottom: $t = 0.44$.

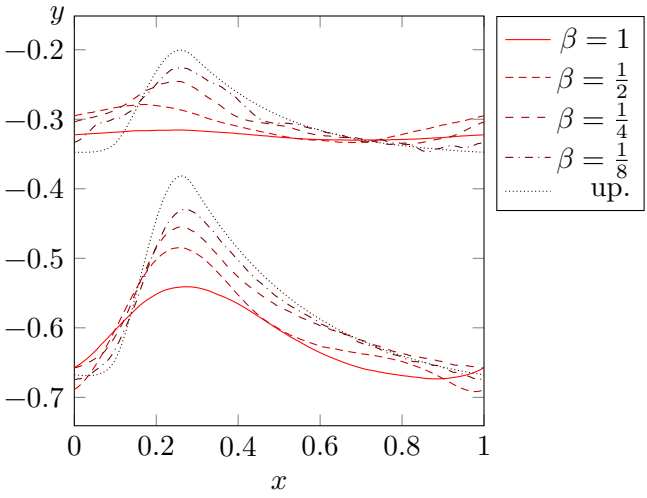

Figure 7.6: Interface locations at time $t = 2.4$ for the non-dimensional δ-$2f1s$-model with varying β, and for the upscaled δ-$2f1s$-model. The fluid–fluid interface can be seen in the upper half and is located by the condition $\phi_1 = \phi_2$. The fluid–solid interface in the lower half is located by $\phi_1 = \phi_3$.

The source terms upscales trivially at order $O(\beta^0)$, and the upscaled ion conservation equation (7.37) is now given by

$$\frac{d}{dt}\left(\tilde{\phi}_{c,\text{total}} c\right) + \partial_x\left((-K_c \partial_x p) c\right) = \frac{1}{\bar{Pe}_c}\partial_x\left(\tilde{\phi}_{c,\text{total}} \partial_x c\right) + \frac{\bar{Da}}{\bar{\varepsilon}} R_{\text{total}} + \tilde{\phi}_{c,\text{total}} s(x).$$

We choose the ion source to be located between $x = 0.1$ and $x = 0.3$, in detail

$$s(x) = \max(0, 62.5(x - 0.1)(0.3 - x)).$$

Figure 7.6 shows a comparison between the non-dimensional δ-$2f1s$-model with different values of β, and the upscaled δ-$2f1s$-model. There is a good agreement between the full model with small values

of β and the upscaled model. For large values of β there is less precipitation in the thin strip. This is due to the ion concentration c not being constant in y-direction. The source term $\tilde{\phi}_c s(x)$ generates ions everywhere in the first fluid phase, but precipitation removes ions from the first fluid phase only at the fluid–solid interface. This leads to an oversaturation $c > 0.5$ further away from the fluid–solid interface. For smaller values of β the diffusion in y-direction results in more ions precipitating and therefore a smaller oversaturation of ions in the fluid phase.

Figure 7.6 also shows the influence of a non-constant width of the thin strip on the flow inside the thin strip. The fluid–fluid interfaces are pushed towards the center of the thin strip, where flow velocities are higher.

Part III
Applications

Investigation of Crystal Growth in Enzymatically Induced Calcite Precipitation

8

In this chapter we develop a phase field model for EICP based on the δ-$1f1s$-model of Chapter 3. We then proceed to use this model in a comparative study with an experiment of EICP in a micro-fluidic cell [Weinhardt et al. 2020a]. For this we first give an overview over the performed experiments in Section 8.1 and over the phase field model in Section 8.2. We then compare the model to the experiment in Section 8.3.

As described briefly in Section 1.1.1, EICP in a porous medium can be used to alter strength, stiffness, porosity and permeability of the porous medium. It can be used similarly to other methods of inducing mineral precipitation, such as e.g. microbially induced calcium carbonate precipitation (MICP), to seal high-permeable leakage pathways. This has been demonstrated for MICP in various studies, [Cunningham et al. 2019; Cuthbert et al. 2013; Phillips, Gerlach, et al. 2013; Phillips, Lauchnor, et al. 2013; Phillips, Cunningham, et al. 2016]. Applications for soil stabilization are described in [Mujah et al. 2017; van Paassen et al. 2010; Whitaker et al. 2018], for co-precipitation of heavy metals in [Lauchnor et al. 2013; Mitchell and Ferris 2005], or for building or monument restoration in [Minto, Tan, et al. 2018]. EICP itself has already been applied for dust control [Hamdan and Kavazanjian 2016; Woolley et al. n.d.], soil strengthening [Neupane et al. 2013], or to modify permeability [Nemati and Voordouw 2003].

Successful sealing results from a complex interplay between the transport of chemicals and urease, determined by fluid dynamics, the ureolysis as well as the precipitation reaction leading to clogging and thus a change in the transport-determining porous medium properties. Numerical modeling can employ conceptual ideas for these individual processes and mechanisms, and account for complex interactions between different processes. As such it improves process-understanding, optimizes experimental and field setups, and predicts e.g. the outcome of the application of EICP.

Field-scale applications require a Darcy-scale approach to be able to account for the large domain sizes. The Darcy-scale models of EICP or MICP, e.g. [Cunningham et al. 2019; Hommel, Akyel, et al. 2020; Hommel, Coltman, et al. 2018; Minto, Lunn, et al. 2019; Nassar et al. 2018; van Wijngaarden et al. 2016] currently rely on simple parametrizations of the effects of precipitation on porous-medium properties, such as permeability. Especially for the sealing applications of EICP or MICP, the correct prediction of permeability is of outstanding importance. To improve on the simplistic relations currently used to describe the change in porous-medium Darcy-scale properties due to EICP or MICP, the pore-scale needs to be considered, as here Darcy-scale properties can be observed and described as changes in geometry. This is experimentally possible due to advances in imaging technologies, e.g. [Blunt et al. 2013; Wildenschild and Sheppard 2013].

In this chapter we develop a pore-scale model for EICP that reproduces the patterns observed in the experiments such as preferential growth towards the higher concentration gradient on the upstream side or in advection-dominated flow in pore throats. Perspectively, within a multi-scale approach, pore-scale models might inform Darcy-scale models what relation to use for predicting the change in Darcy-scale hydraulic properties and how to parameterize those relations.

For the reactions of the pore-scale model, we adopt simplifying assumptions of a constant ureolysis rate, calculated for the experi-

mental conditions of [Weinhardt et al. 2020b] based on the ureolysis kinetics of [Hommel, Akyel, et al. 2020]. The precipitation process is assumed to be an equilibrium reaction, therefore crystal growth is limited by the diffusion of ions to the crystal interface from the aqueous bulk liquid, which is oversaturated due to ureolysis. Note, that the developed model does not have any additional calibration parameters; the model estimates the calcite oversaturation due to enzymatic ureolysis in the inlet region using the jack bean-meal (JBM) extract ureolysis kinetics of [Hommel, Akyel, et al. 2020].

Experimental and modeling investigations complement each other. The very small dimensions of the experimental setup do not allow for reliable measurements of local concentrations. Only minuscule volumes would be available for analysis and the volume of the inlet and outlet structures as well as the tubing are much larger than the volume of the region of interest.

Using complementary modeling, detailed concentration distributions, crystal growth rates and growth directions within the region of interest can be predicted reliably. The distribution of crystal aggregates and their growth over time is a measure available in both the experiment and the numerical simulation, allowing for a validation of the developed model by comparison of the model predictions with the experimental data.

In this study, we show that the developed model reproduces the following observations of pore-scale experiments:

- Crystal aggregates grow faster on their upstream side than on their downstream side, leading to a shift of the center of mass in the upstream direction.
- Crystal aggregates grow faster in places of high flow velocity.

8.1 Micro-Fluidic Experiments

8.1.1 Experimental Setup and Procedure

In this section, the micro-fluidic experiment is briefly described. More detailed information about the procedure and the setup can be found in [Weinhardt et al. 2020b]. The micro-fluidic cells were produced by following the standard workflow of soft lithography [Karadimitriou, Musterd, et al. 2013; Xia and Whitesides 1998]. The design of the micro-fluidic cell is shown in Figure 8.1 and consists of an inlet channel, an outlet channel, and the actual domain of interest, which is a series of four identical circular pore bodies connected by rectangular pore throats. The details of the channels connected to the pressure sensors are not pictured here since the pressure measurements have been analyzed in detail in [Weinhardt et al. 2020b] and are not in the focus of the present study here. There are two syringe pumps which induce the flow: Syringe 1 (S_1) is filled with an urea/calcium-chloride solution with equimolar concentrations of 1/3 $^{\mathrm{mol}}/_{\mathrm{L}}$. Syringe 2 ($S_2$) is filled with a solution extracted from a 5 $^{\mathrm{g}}/_{\mathrm{L}}$ JBM suspension by filtering through a 0.45 μm cellulose membrane. The reactive solutions mix in the T-junction, before entering the micro-fluidic cell via an inlet tube of the length 10 cm and an inner diameter of 0.5 mm.

The whole system was initially saturated with deionized water. The inlet tube, the inlet channel, the porous domain and the outlet channel were subsequently saturated with the reactant solutions. The pressure sensors end up in a dead end. Therefore, there is no flow in the channels connected to the pressure sensors. Once the micro-fluidic cell was saturated with the reactive solutions, a constant flow rate of 0.01 μL/s was applied at both syringes for 5 hours. The flow direction is indicated with blue arrows in Figure 8.1. The transparent nature of Polydimethylsiloxane (PDMS) allowed the direct visualization of the processes taking place in the pore space by using transmitted light microscopy. A description of the microscope used can be found in [Karadimitriou, Joekar-Niasar, et al. 2012]. In

Table 8.1, the concentrations of the reactive solutions, as well as the flow rates are summarized. The ambient temperature was 23°C throughout the experiment.

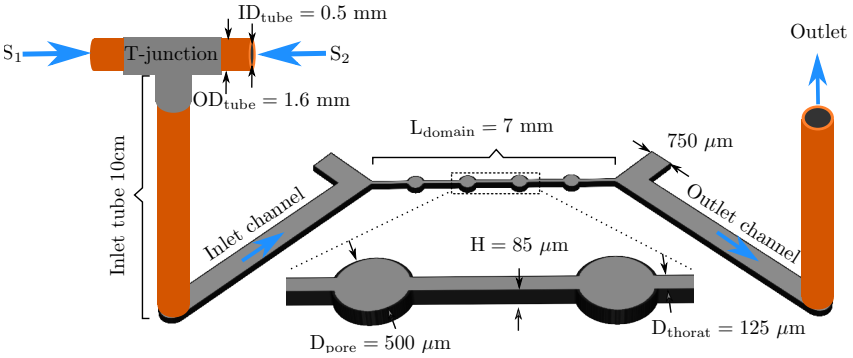

Figure 8.1: Schematic sketch of the micro-fluidic cell and its dimensions: It includes the inlet and outlet tubes (orange) connected to the inlet and outlet channels. The domain of interest consists of four pore bodies connected with pore throats. A part of it is shown enlarged in the bottom of the figure. The blue arrows indicate the flow direction of the reactive solutions, induced by the syringe pumps S_1 *and* S_2*, filled with urea calcium chloride solution and filtered JBM suspension respectively. Sketch based on [Weinhardt et al. 2020b]*

8.1.2 Kinetics of Urea Hydrolysis

The hydrolysis of urea can be assumed to follow a first-order kinetic reaction with respect to the concentration of urea c_{urea} (8.1) [Feder et al. 2020; Hommel, Akyel, et al. 2020]. In this case the reaction rate r_{u} is a function of the molar concentration of urea c_{urea} as well as the mass concentration of JBM extract, C_{JBM},

$$r_{\text{u}} = -\frac{dc_{\text{urea}}}{dt} = k_{\text{u}} c_{\text{urea}} C_{\text{JBM}}. \tag{8.1}$$

Table 8.1: Concentrations and flow rate of the reactive solutions (based on [Weinhardt et al. 2020b])

Solution	c_{urea} [mol/L]	c_{CaCl_2} [mol/L]	C_{JBM} [g/L]	Q [μL/s]
S_1	1/3	1/3	0	0.01
S_2	0	0	5	0.01
Mixed	1/6	1/6	2.5	0.02

According to [Feder et al. 2020] and [Hommel, Akyel, et al. 2020], the temperature-dependent rate coefficient for enzymatic ureolysis, k_{u}, can be calculated using Arrhenius-type exponential relations. The expression (8.2) below is based on the experimental investigations of [Feder et al. 2020], with $a_{\text{u,0}}$ being the pre-exponential factor and $a_{\text{u,T}}$ being a lumped exponent describing the temperature dependence of the rate coefficient,

$$k_{\text{u}} = a_{\text{u,0}} e^{\left(\frac{a_{\text{u,T}}}{T}\right)}. \tag{8.2}$$

By integrating Equation (8.1) over time, the concentration of urea can explicitly be calculated at a certain time t, based on an initial concentration of urea, $c_{\text{urea,0}}$,

$$c_{\text{urea}}(t) = c_{\text{urea,0}}\, e^{-(k_{\text{u}}\, C_{\text{JBM}}\, t)}. \tag{8.3}$$

Consequentially, also the reaction rate can be determined explicitly at a certain time or, likewise, since the flow rate is constant, at a point along the flow path. The reaction takes place once the two solutions, as described in the previous section, mix. The mixing happens in the inlet tube, right after the T-junction (see Figure 8.1). The residence time in the inlet tube, which is determined by the flow rate and the geometry of the inlet tube, is approximately 16 minutes. Since the residence time in the micro-fluidic cell is only a few seconds, we assume that the changes of the urea concentration are negligible. Therefore, the ureolysis reaction rate can be assumed to be constant throughout the micro-fluidic cell, while it is determined by the residence time in the inlet tube. Table 8.2 gives the relevant

parameters to determine the ureolysis rate in the cell, assuming that there is no accumulation or inactivation of urease in the inlet tubing and the porous domain and the urease concentration is constant at the injected concentration of $C_{\mathrm{JBM}} = 2.5\mathrm{g/L}$.

Table 8.2: Kinetic and other parameters to estimate the ureolysis rate based on Equation (8.1)

Symbol	Parameter	Value	Unit
$a_{\mathrm{u},0}$	Arrhenius-type kinetics coefficient	462.74	[L/(g s)]
$a_{\mathrm{u,T}}$	Arrhenius-type kinetics coefficient	-4263.108	[K]
T	Temperature	296.15	[K]
C_{JBM}	Mass concentration of suspended urease	2.5	[g/L]
k_{u}	Rate coefficient at 296.15 K	2.592E-4	[L/(g s)]
t_{tube}	Residence time in the tube	16.36	[min]
$c_{\mathrm{urea},0}$	Initial molar concentration at the T-junction	0.167	[mol/L]
$\mathrm{c}_{\mathrm{urea,cell}}$	Molar concentration of urea in the cell	0.088	[mol/L]
$r_{\mathrm{u,cell}}$	Ureolysis rate in the cell	5.716E-5	[mol/(L s)]

8.2 Phase Field Model for EICP

8.2.1 Modifications to the δ-1f1s Model

To model the growth of crystal aggregates in the micro-fluidic cell, we modify the δ-1f1s-model of Section 3.1.6.1. To present the modified model, we introduce as unknowns the phase-field parameter ϕ, the fluid velocity $\mathbf{v}$, the pressure p, and the inorganic carbon

concentration c in the fluid. The model couples the equation for the transport, diffusion, and reaction of inorganic carbon

$$\partial_t(\tilde{\phi}c) + \nabla \cdot ((\phi\mathbf{v} + J)c) = \nabla \cdot (D\tilde{\phi}\nabla c) + \tilde{\phi}r_{\text{u,cell}} - r_{\text{precip}}(\phi, c), \tag{8.4}$$

with the Navier–Stokes equations in the fluid phase, given by

$$\nabla \cdot (\tilde{\phi}\mathbf{v}) = 0, \tag{8.5}$$

$$\begin{aligned}\partial_t(\rho\tilde{\phi}\mathbf{v}) + \nabla \cdot (\rho(\phi\mathbf{v} + J) \otimes \mathbf{v}) = &-\tilde{\phi}\nabla p + \nabla \cdot (2\gamma\nabla^s\mathbf{v}) \\ &- \frac{12\gamma}{h^2}\mathbf{v} - d(\tilde{\phi})\mathbf{v}.\end{aligned} \tag{8.6}$$

The phase field parameter ϕ is determined by the Cahn–Hilliard evolution

$$\partial_t\phi + \nabla \cdot J = -\frac{r_{\text{precip}}(\phi, c)}{c^*}, \tag{8.7}$$

$$J = -M\nabla\mu, \tag{8.8}$$

$$\mu = \frac{W'_{\text{dw}}(\phi)}{\varepsilon} - \varepsilon\nabla^2\phi. \tag{8.9}$$

Here, ρ is the fluid density, γ is the fluid viscosity, D is the diffusion coefficient of carbonate ions, and c^* is the molar density of the precipitated calcium carbonate. Values are taken from literature and listed in Table 8.1. From the Cahn–Hilliard evolution, we have the phase-field mobility M and a double-well potential W_{dw} from (3.20) with minima at 0 and 1. For the modification $\tilde{\phi} = \phi + \delta$ we choose $\delta =$ 5E-03 to keep the numerical system stable while barely perturbing the solution.

The Equations (8.5), (8.6) are the Navier–Stokes equations, modified as follows from the δ-$1f1s$-model. The model is employed only in the two-dimensional geometry of the micro-fluidic cell. From the assumption of a parabolic flow profile across the height h of the cell, an additional drag term enters the Navier–Stokes equation, analogous to the derivation of a Hele–Shaw flow [Lamb 1932]. As a second

modification we do not let γ depend on ϕ. In the δ-$1f1s$ model this would coincide with $\gamma_1 = \gamma_3$. To ensure a no-slip condition between the solid and fluid phase we choose the drag term

$$d(\phi) = d_0(1-\phi)^2,$$

with a constant d_0 sufficiently large, see also Remark 3.3.

Equation (8.4) has two reaction terms on the right-hand side. The term $r_{\text{u,cell}}$ describes the hydrolysis of urea. As discussed in Section 8.1.2, this depends on temperature, activity of urea, and mass concentration of enzyme. These values are assumed to be approximately constant in the micro-fluidic cell, as the time for fluid to pass through the cell is in the order of seconds. The value for $r_{\text{u,cell}}$ was determined in Section 8.1.2 and is given in Table 8.2. In the δ-$1f1s$-model no such bulk-reaction term is considered, but the extension of the analysis to the case with constant $r_{\text{u,cell}}$ is straightforward. The second reaction term, r_{precip}, models the precipitation of calcium carbonate and is given by

$$r_{\text{precip}}(\phi, c) = \left(k_{\text{precip}}(c - c_{\text{eq}}) + \delta\mu\right) \max\left(\phi(1-\phi) - 0.1\ ,\ 0\right). \tag{8.10}$$

This is analogous to the Term R_f for the δ-$1f1s$-model, with $\alpha = 0$, a reaction rate $r(c)$ proportional to the oversaturation $c - c_{\text{eq}}$ of inorganic carbon and a function $q(\phi) = \max\left(\phi(1-\phi) - 0.1\ ,\ 0\right)$. Note that this q does not satisfy the requirements stated in Remark 3.8, and the sharp interface limit does therefore not recover the Navier-slip condition. This choice in q is necessary because of the following consideration. As the precipitation process is fast in comparison to the hydrolysis of urea, it is assumed to be an equilibrium reaction. The choice for k_{precip} is therefore not from literature, but instead big enough that equilibrium conditions can be observed at the interface at all times. This also means that in this regime k_{precip} can not be viewed as an $O(\varepsilon^0)$ term, and a q chosen as in Remark 3.8 would result in precipitation in the bulk regimes (compare Section 3.2.1).

Table 8.3: Parameters for the phase field model

Symbol	Parameter	Value	Unit
c^*	Molar density of $CaCO_3$	27.1	[mol/L]
c_{eq}	Fully saturated carbonate concentration	1.4E-04	[mol/L]
D	Diffusion coefficient	8.04E-10	[m^2/s]
ρ	Density of water	0.997E03	[kg/m^3]
γ	Viscosity of water	1.01E-03	[kg/(m s)]
d_0	Momentum dissipation in solid phase	1E06	[kg/(m^3 s)]
$r_{\text{u,cell}}$	Reaction rate of urea hydrolysis	5.716E-05	[mol/(L s)]
h	Height of micro-fluidic cell	8.5E-05	[m]
k_{precip}	Precipitation rate	200	[1/s]
ε	Interface width	2E-06	[m]
M	Phase field mobility	1E-05	-
δ	Phase field modification	5E-03	-

8.2.2 Numerical Implementation

The equations are discretized by a Finite-Element Method, with Taylor–Hood elements for velocity $\mathbf{v}$ and pressure p, and second-order Lagrange elements for concentration c and phase-field parameter ϕ. All equations are discretized fully implicit in time, i.e., by implicit Euler method. We do not solve the system monolithically, but instead iterate between solving the Navier–Stokes equations (8.5), (8.6) and equations (8.4)–(8.9) until convergence.

The implementation was done in Dune-PDELab [Bastian et al. 2010] using ALUGrid [Alkämper et al. 2016]. This comes with the benefit of adaptive grid generation. The phase field model requires small grid cells to resolve the diffuse interface, while grid cells at larger distance to the interfaces can be considerably larger. Figure 8.2 shows a section of the grid containing one crystal aggregate. The grid is adapted after each timestep to account for the evolving interfaces.

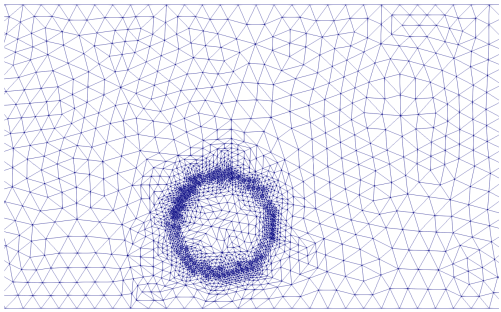

Figure 8.2: Part of the grid used for the simulation in Section 8.3. The grid is refined at the interface between the fluid phase and the precipitated calcium carbonate.

One major challenge for the simulation is the relatively fast flow in the order of mm/s compared to the total runtime of the experiment of multiple hours. The flow regime introduces a severe restriction on the timestep dt. For the simulation of the full system, including the flow, small timesteps of size $dt = 0.01s$ are used, making the simulation computationally demanding. To tackle this problem, a special timestepping is introduced; small timesteps are needed to resolve the interplay between transport, diffusion, and reaction. After a few seconds in the simulation, transport, diffusion and reaction balance each other and all unknowns change on the time-scale of minutes. This is facilitated by the laminar flow regime. At this stage, the only process leading to a change in unknowns is the growth of precipitated calcium carbonate. This growth happens rather slowly, i.e., on a larger time scale, and it is now possible to only update the phase field ϕ using

$$\partial_t \phi = -\frac{r_{\text{precip}}(\phi, c)}{c^*}, \tag{8.11}$$

with a larger timestep $dt = 10s$, while keeping all other unknowns constant. After this big timestep, smaller timesteps with the full system are again performed until a quasi-static state is reached. A sketch of such a timestepping procedure can be seen in Figure 8.3

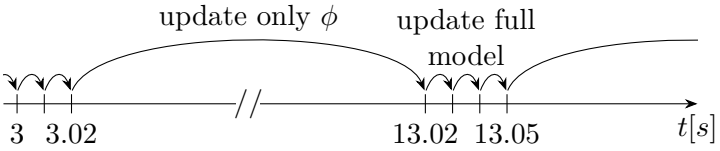

Figure 8.3: Sketch of the timestepping algorithm, with small and big timesteps.

8.2.3 Calculation of the Inflow Conditions

The simulation of the experiment is performed on the domain consisting of pore throats and pore bodies, without the inlet and outlet region of the micro-fluidic cell, see Figure 8.1. At the inflow boundary of the simulation domain, both fluid velocity $\mathbf{v}_{\text{in}}$ and inorganic carbon concentration c_{in} have to be prescribed. The velocity is chosen as a parabolic flow profile with total flow rate of 0.02 μL/s. In contrast, it is more difficult to determine the inorganic-carbon concentration c_{in} at the inflow boundary.

The hydrolysis of urea begins as soon as the reactant solutions mix in the T-junction before the inlet tube. Due to the residence time in the tube of 16 min, see Table 8.2, the inorganic carbon produced in this time can not be neglected. While integrating the reaction rate (8.1) over the residence time gives an upper bound for c_{in}, the actual value is much lower because of precipitation in the inflow tube and the inlet area of the micro-fluidic cell.

Therefore, to determine the concentration c_{in}, we have to take into consideration the distribution of precipitated carbonate in the inlet area of the micro-fluidic cell. We use the knowledge about the model reaching a quasi-static state as described in Section 8.2.2. In case the inlet area is long enough, this state is reached before the inflow boundary of the main simulation. Figure 8.4 shows a picture of the inlet area taken at the end of the experiment. For the simulation, a section S of the inlet area is used as representative for the whole inlet area. This justifies using periodic boundaries at inflow and

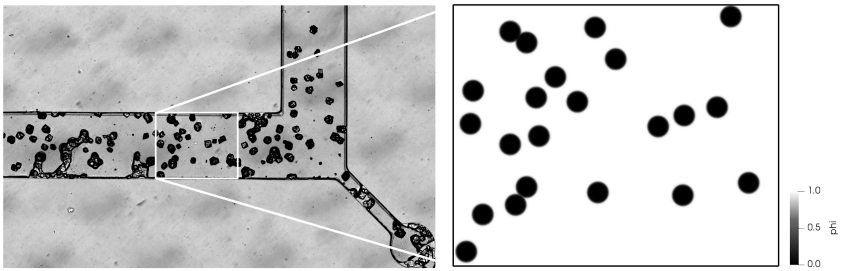

Figure 8.4: Left: Calcite precipitation in the inlet area after the experimental run. A representative section S is highlighted by a white-colored boundary. Right: Simplified precipitate distribution in the section S used for simulation.

outflow boundary of S. Now, the flow profile around the precipitated carbonate can be calculated by solving for steady-state solutions of (8.5), (8.6) in S. Next, the inorganic-carbon concentration c in the inlet section is determined by

$$\nabla \cdot (\phi \mathbf{v} c) = \nabla \cdot (D\phi \nabla c) + \phi r_{\mathrm{u,cell}} - r_{\mathrm{precip}}(\phi, c). \tag{8.12}$$

This equation is a steady state version of (8.4). The concentration c_{in} is then calculated as the flux average

$$c_{\mathrm{in}} = \frac{\int_S c\phi \mathbf{v} \cdot \mathbf{e}_1 dx}{\int_S \phi \mathbf{v} \cdot \mathbf{e}_1 dx},$$

where $\mathbf{e}_1$ is the unit vector pointing from inflow to outflow boundary of S. We obtain the slightly oversaturated inflow condition $c_{\mathrm{in}} = 3.150E-04 \mathrm{mol}/\mathrm{l}$.

8.3 Results and Discussion

We compare results [Weinhardt et al. 2020a] of the experiment described in Section 8.1.1 with the mathematical model of Section 8.2.

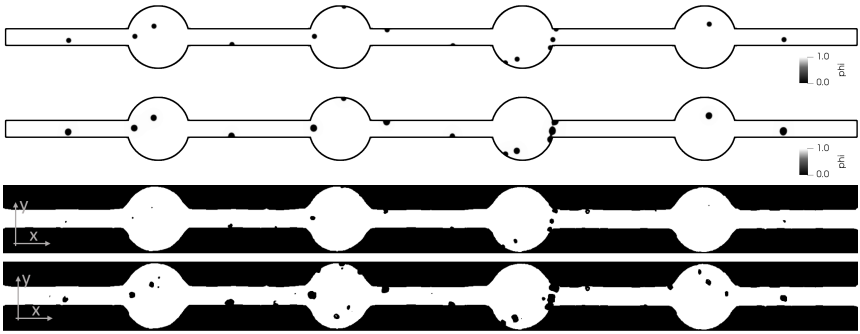

Figure 8.5: Top: Fluid volume fraction ϕ in initial and final state of the simulation. Bottom: Corresponding states of the experimental run.

The exact locations of the points of nucleation are different for each repetition of the experiment; they are obviously subject to effects which we have to denote for now as random since we attribute them to conditions that are not easy to analyze in the details, such as impurities of the PDMS surface as hypothesized in [Weinhardt et al. 2020b]. In any case, we cannot determine or predict the points of nucleation a-priori, thus we use here data from an experimental run 52 min after start to determine the initial nuclei for the simulation model.

The model leaves its range of validity in approaching conditions of clogging; it is therefore stopped shortly before clogging. We compare the results of the final state of the simulation with a corresponding state of the experimental run that shows similar clogging behavior. In the comparison, we characterize crystal aggregates by centroid and volume.

Figure 8.5 shows the initial and the final distribution of precipitated calcite in both experiment and simulation. All crystal aggregates show some growth, and we observe near-clogging at the end of the third pore body. For further investigation and more convenient referencing, we number the crystal aggregates from left to right, as shown in Figure 8.6. The three crystal aggregates at the end of the third

pore body are excluded from the comparison and thus numbering, since they merged during the experiment. Also, new nucleation points forming after the initial 52 min are not considered, as they would have to be placed into the running simulation. The black dot in the pore throat between the third and the fourth pore body is an impurity of the micro-fluidic cell and not a calcite crystal.

While the final state of the simulation and the corresponding state of the experimental run match fairly well, the elapsed time in experiment and model is different. The pictures of the experiment shown in Figure 8.5 are at 52 min and 112 min after the start of the experiment. Compared to the elapsed 60 min, the simulation reaches its final state after 287 min. There are several reasons for this. Firstly, the model is two-dimensional and therefore cannot capture all effects of flow around the precipitates. In particular, it assumes that crystal aggregates span the whole height of the micro-fluidic cell, i.e., they form cylindrical shapes. The work [Weinhardt et al. 2020b] shows that this is not true and this is discussed further in Section 8.3.2. Secondly, the model neglects electrodiffusion, which has been shown to enhance the precipitation process in similar models, see [Zhang and Klapper 2011]. Lastly, both the ureolysis rate $r_{\mathrm{u,cell}}$ and the determination of the inorganic carbon concentration c_{in} at the inflow boundary are subject to uncertainty. We find from multiple simulation runs that the crystal-growth rate is approximately reciprocal to $r_{\mathrm{u,cell}}$.

8.3.1 Movement of Centroids

We determine the centroid of each crystal aggregate in the simulation by integrating over an area containing the crystal aggregate. For the experimental data, the same is done after image segmentation. In Figure 8.6, the evolution of the centroids relative to the initial position is shown.

In both experiment and simulation, it can be observed that the values of the x-coordinate of the centroids decrease over time, i.e., the

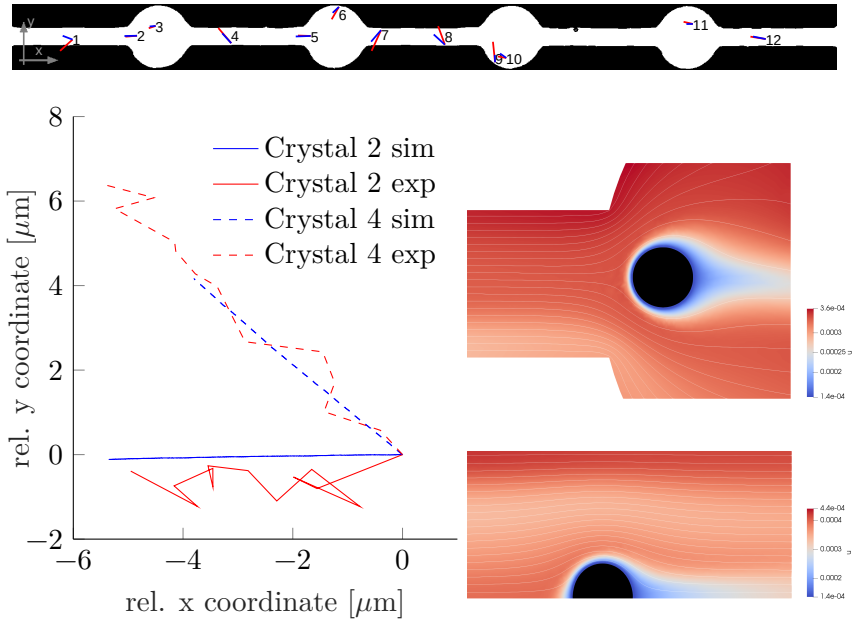

Figure 8.6: Growth of precipitates; top: Change of the position of the centroids as vector (20 times enlarged) for simulation (blue) and the experiment (red); bottom left: change of the position of centroids relative to the initial location for the crystal aggregates 2 and 4; bottom right: streamlines and inorganic carbon concentration c around the crystal aggregates 2 and 4, obtained from the simulation.

crystal aggregates grow in upstream direction. To comprehend this, we exemplarily consider crystal aggregates with numbers 2 and 4. In Figure 8.6 the inorganic carbon concentration around crystal aggregate 5 is shown. The oversaturated calcium carbonate gets transported to the upstream side of the aggregate and precipitates there due to the fast time scale of precipitation. When the fluid reaches the downstream side of the aggregate, little oversaturation of calcium carbonate is left and therefore nearly no precipitation is observed at this side.

We conclude from the simulation that the growth process is governed by the interplay of transport and diffusion close to the crystal aggregate. A lower flow rate and more diffusion lead to a less pronounced growth in the upstream direction. Indeed, this can be observed when comparing pore throats, which have a high flow rate, with pore bodies. Figure 8.6 shows that crystal aggregates located in pore throats grow more in the upstream direction than crystal aggregates located in pore bodies.

A second observation is that in both experiment and simulation the centroids mainly grow towards the center of the channel, as seen exemplary for crystal aggregate 4 in Figure 8.6. The primary cause for this effect is that once the precipitate reaches a wall, it cannot grow further in this direction. Another cause is that the flow velocity close to the wall is small. Therefore, more calcium carbonate gets transported to the side of the crystal aggregate facing towards the center of the channel than to the most upstream point. Consequently, the centroid moves towards the center of the channel.

In contrast to the simulation, the centroid of crystal aggregate 1 moves towards the wall in the experiment, see Figure 8.6. This is one of the major differences observed between model and experiment. One possible reason for this is a new nucleation point in front of crystal aggregate 1 that formed only during the experiment. This new nucleation point cannot be taken into account in the simulation, as it was not present in the model's initial configuration. Another

possible reason are challenges in image segmentation, due to the reflective surface of the crystal aggregate.

In conclusion, the model matches the observed data well, and thus can capture dominating mechanisms for determining crystal-growth directions in this micro-fluidic EICP setup. Growth of the crystal aggregates leads to a shift of centroids in the upstream direction, and this effect is more pronounced in pore throats, where the flow rate is higher.

8.3.2 Growth of Crystal Aggregates

While the previous section focused on the direction of growth of the precipitates, we compare now the volume change of the crystal aggregates. The mathematical model is two-dimensional and assumes that ϕ is constant across the height of the micro-fluidic cell. Therefore, the volume of the precipitates can be computed by integrating over the calcite fraction $1-\phi$ and subsequently multiplying by the height of the cell. The three-dimensional shape of the crystal aggregates is therefore obtained by extruding the two-dimensional data, which cannot analogously be applied for the experimental data. It has been shown in [Weinhardt et al. 2020b], that the most suitable shape approximation for estimating the (3D) volume of the precipitates in micro-fluidic cells from (2D) optical microscopy data is the spheroidal shape. A representative radius is calculated from the projected area of the aggregates. Based on this radius, the volume can be derived for the assumption of a spheroidal shape. This approach is described in [Weinhardt et al. 2020b] and is based on the idea given in [Kim et al. 2020]. During the here investigated time frame of 60 minutes the radii of the crystal aggregates range from approximately 5 μm to 35 μm. Compared to the height of the channel of 85 μm, the radii of the crystal aggregates are smaller than half of the channel height. Therefore, the crystal aggregates are not expected to reach all the way from the bottom to the top of the micro-fluidic cell.

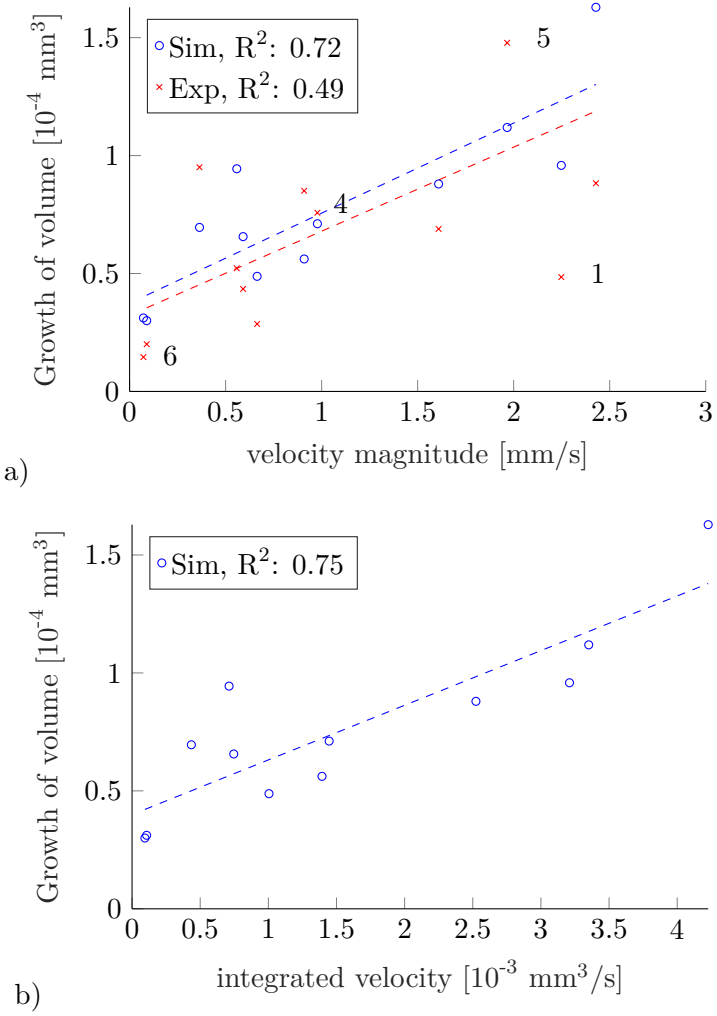

Figure 8.7: Growth of precipitates; a) Total growth of volume over the velocity magnitude at the initial position of the crystal aggregates, obtained from stationary Stokes simulation without precipitates. b) Total growth of the volume over the velocity integrated over the area around the crystal aggregates, as obtained from the numerical model (8.4)–(8.9).

In Figure 8.7 a), the growth of the precipitates is plotted over the velocity magnitude at the initial position of the precipitates. These velocity values are obtained from a stationary flow simulation without any precipitates present. More precisely, this means solving a stationary version of the equations (8.5) and (8.6) with $\phi = 1$ and $J = 0$ everywhere. We call velocities obtained from this simulation initial velocities.

As the growth of the precipitates is mainly driven by the transport of carbonate ions to the crystal aggregates, the initial velocity at the nucleation points gives a good estimate for the carbonate supply at specific locations in the domain. Exemplary, we compare crystal aggregates 4, 5 and 6, as labeled in Figure 8.6 a). Crystal aggregate 6 is located at the outer part of a pore body. This leads to a relatively small initial velocity and a slow growth of volume. In contrast, crystal aggregate 5 lies in the center of the pore body and right after a pore throat. This implies a high initial velocity and, therefore, a large amount of carbonate ions passing by. Crystal aggregate 4 is in a pore-throat, where generally the velocities are high due to the reduced cross-sectional area. However, it sits right at the wall of the throat, where the velocity is reduced due to the shear forces caused by the wall friction.

From this analysis, we conclude that there is a tendency of the crystal aggregates to grow faster and bigger where the initial velocities are higher. This is directly linked to the supply of carbonate ions. The linear regressions, illustrated as dashed lines in Figure 8.6 a) show a good agreement between simulation and the experiments. As already mentioned in Section 8.3.1, crystal aggregate 1 is again an obvious outlier and is therefore excluded for determining the linear regression of the experimental data. The coefficient of determination (R^2) for the simulation data clearly indicates a linear trend, while the one for the experimental Dataset indicates a weaker, but still significant trend.

However, the initial velocity does not take into account that the fluid flow is influenced by the precipitates. Especially in pore-throats

precipitates reduce the cross-sectional area and lead therefore to higher velocities. As our introduced mathematical model includes the influence of precipitates on the fluid flow, we expect a better correlation when evaluating the velocity for the full model. The result can be seen in Figure 8.7 b), where we use the velocity field obtained from the full numerical model for the initial calcite distribution. We cannot evaluate the velocity at the center of the crystal aggregates, as there is no fluid flow in the precipitates. Instead, we now integrate the magnitude of the velocity over a disk shaped area around the crystal aggregates. The center of the disk coincides with the center of the crystal aggregate, and the radius is 1.8 times the diameter of the crystal aggregate.

Compared to Figure 8.7 a), the results in Figure 8.7 b) show a more evident linear correlation between the velocity magnitude close to the precipitates and the volume growth of the precipitates. The coefficient of determination for the simulation increased from 0.72 to 0.75. We conclude that the velocity field plays a significant role for the growth of the precipitates and the influence of precipitates on the flow field should not be neglected.

8.4 Conclusions

We have developed a phase-field approach for modeling crystal growth in enzymatically induced calcite precipitation and compared it to micro-fluidic experiments. Without any additional calibration there is a good qualitative agreement between model and experiment. Quantitatively, there is a very good agreement for the movement of centroids, and a good agreement for the growth of crystal aggregates. Only the predicted time until near-clogging differs significantly.

This joint experimental and numerical study allows for new insights into the dominant processes and mechanisms involved in the growth of crystal aggregates. We have seen that growth is strongly dependent on the flow conditions, i.e., the flow field and corresponding concentrations of the inorganic carbon. The concentrations are subject to

local changes due to reaction but also due to the complexity of the flow field which is influenced by the geometry of the flow cell and the pattern of precipitates. In particular for a single crystal aggregate, the growth is determined by the interplay between transport around the aggregate and diffusion towards the surface.

It has been observed consistently in experiment and simulation that nuclei show a clear tendency towards growing upstream and towards the center of the channel. Additionally, the growth rate is correlated with the magnitude of flow velocity, leading to a faster growth in the center of the channel.

A better understanding of the pore-scale mechanisms involved in EICP-related growth of crystals will contribute to developing optimization strategies for an effective use of the EICP technology. Perspectively, the phase-field approach presented here can be further developed to describe also microbially induced precipitation (MICP), where the mechanisms of growth are even more complex due to the involvement of biofilm in the pore space.

Conclusion

Conclusion and Outlook

We have derived an Allen–Cahn–Navier–Stokes model for reactive transport including mineral precipitation and dissolution in Chapter 2. In Chapter 3 we extended the Cahn–Hilliard–Navier–Stokes model from [Abels, Garcke, et al. 2012] to include a solid phase with reactive fluid–solid interfaces. Using matched asymptotic expansions, we have shown that the phase field models reduce to the expected sharp interface models, when the width of the diffuse interface approaches zero. For multi-phase flow we impose a fixed contact angle at the contact point. In particular, the Navier-slip condition realized in the Cahn–Hilliard–Navier–Stokes model is novel for diffuse fluid–solid interfaces, even in the case without precipitation.

Further research could extend the phase field models to include more physical phenomena. For example, experiments show that the influence of electrostatic fields should not be neglected, and that small mineral particles are transported by the fluid flow. Moreover, precipitation and dissolution process is sensitive to the temperature, and it is a major challenge to formulate thermodynamically consistent non-isothermal extensions of the models presented in this dissertation. In this case, the evaporation of one fluid phase is also of interest.

While the numerical discretization of the Cahn–Hilliard model is well-suited for rapid development of new phase field models, more intricate numerical schemes might provide better performance. In particular, energy decreasing schemes can ensure thermodynamical consistency on a discrete level. By developing preconditioners for the

Cahn–Hilliard model, larger experimental setups can be simulated, and three-dimensional simulations could be feasible.

In this work we have assumed the existence of classical solutions to the phase field models. Further research is needed to prove existence of solutions in a suitable weak form. This would also allow for a-priori bounds, which are necessary for more rigorous upscaling techniques, such as two-scale convergence.

We have derived a diffuse domain model for two fluid phases in Chapter 4. The direct application of this model is to predict the transmissibility of multi-phase pore network models (see Section 4.3). We plan to use the diffuse domain model to find stationary fluid distributions and switch to the Cahn–Hilliard model of Chapter 3 to model precipitation on a slower timescale. Also, data-driven approaches might be needed to speed up the prediction of the transmissibility, as pore network models contain numerous pore throats, which have to be simulated.

When considering a porous medium, the proposed phase field models can be seen as pore-scale models. By assuming the medium to be periodically perforated, we derive an upscaled counterpart of the Allen–Cahn–Navier–Stokes model in Chapter 5. In Chapters 6, and 7 we consider the simplified geometry of a thin strip and derive upscaled models for the Allen–Cahn–Navier–Stokes model and the Cahn–Hilliard–Navier–Stokes model, respectively. The resulting effective equations for flux and ion concentration are valid at the Darcy-scale. We obtain the cell problems providing the effective ion diffusion, permeability and porosity. In particular, the cell problems still contain a phase field model encoding information about the pore-scale geometry. While the cell problems in Chapters 5 and 6 are decoupled, this is not the case for the two-phase flow model in Chapter 7. Only by discretizing the upscaled equations with a finite volume scheme in space and an explicit Euler scheme in time, we obtain microscopic cell problems that are fully decoupled in each time step and can therefore be solved in parallel.

In [Bastidas Olivares et al. 2021], a two-scale iterative scheme is developed for the model proposed in Chapter 5. A cell problem is assigned to each macroscopic grid cell, and cell problems are updated adaptively, based on ideas in [Redeker et al. 2016]. Also, the convergence of the scheme is shown in a simplified setting.

We have investigated the sharp interface limit of the upscaled Cahn–Hilliard model in Chapter 7, and found under additional assumptions on the geometry a fully upscaled model. This model only consists of macroscopic equations for total flux, pressure, ion concentration, and the width of each fluid phase. Additional analysis shows that the upscaling and the sharp interface limit commute.

Further research is needed to generalize the upscaling of two-phase flow in a thin strip in a multitude of directions. The most obvious next step is to consider three-dimensional geometries, such as a thin tube. In such a case, the curvature of the fluid–fluid interface will be bigger by a factor of β^{-2} compared to the two-dimensional case. Therefore, surface tension effects will enter the leading order equations of the momentum equation. As a result, one has to introduce a faster time-scale to resolve relaxation in the cross-section towards an equilibrium state. Another possible direction for future research is the consideration of a finite number of points where the assumption of slow variation along the thin strip is not fulfilled. This includes three phase contact points, as well as the N-waves shown in Section 7.5. Such cases can not be upscaled with the current assumptions, and the numerical investigation shows no agreement between the fully resolved and the upscaled model. In future models, it might be possible to describe regions with fast variation along the thin strip as fully resolved, and couple these regions on each side with the upscaled phase field model.

In Chapter 8 we have compared the Cahn–Hilliard model from Chapter 3 to micro-fluidic EICP experiments. Without additional calibration, we find an excellent agreement for growth and growth direction of crystal aggregates. This comparison allows for new insights into mechanism involved in the growth of crystal aggregates.

Recent micro-fluidic EICP experiments in more complex geometries show the development of a preferential flow path. Further research is needed to predict under which flow conditions this path forms, and the models developed here might give some insight.

In summary, we have developed several phase field models for pore-scale flow with reactive fluid–solid interfaces. We show that these models can accurately predict micro-fluidic EICP experiments. Using homogenization, we have upscaled these phase field models in a periodic porous medium and in a thin strip. The resulting two-scale models are able to encode a large variety of pore-scale geometries via the corresponding cell problems.

Bibliography

Abels, H., H. Garcke, and G. Grün. *Thermodynamically consistent, frame indifferent diffuse interface models for incompressible two-phase flows with different densities*. Mathematical Models & Methods in Applied Sciences 22.03 (2012). DOI: 10.1142/S0218202511500138.

Abels, H. and Y. Liu. *Sharp interface limit for a Stokes/Allen–Cahn system*. Archive for Rational Mechanics and Analysis 229.1 (2018). DOI: 10.1007/s00205-018-1220-x.

Adamson, A. W. and A. P. Gast. *Physical chemistry of surfaces*. Vol. 15. Interscience publishers New York, 1967.

Agosti, A., B. Giovanardi, L. Formaggia, and A. Scotti. *A numerical procedure for geochemical compaction in the presence of discontinuous reactions*. Advances in Water Resources 94 (2016). DOI: 10.1016/j.advwatres.2016.06.001.

Aland, S., J. Lowengrub, and A. Voigt. *Two-phase flow in complex geometries: a diffuse domain approach*. Computer modeling in engineering & sciences: CMES 57.1 (2010). DOI: 10.3970/cmes.2010.057.077.

Alikakos, N. D., P. W. Bates, and X. Chen. *Convergence of the Cahn-Hilliard equation to the Hele-Shaw model*. Archive for Rational Mechanics and Analysis 128.2 (1994). DOI: 10.1007/BF00375025.

Alkämper, M., A. Dedner, R. Klöfkorn, and M. Nolte. *The DUNE-ALUGrid module*. Archive of Numerical Software 4.1 (2016). DOI: 10.11588/ans.2016.1.23252.

Allaire, G. and H. Hutridurga. *Homogenization of reactive flows in porous media and competition between bulk and surface diffusion.* IMA Journal of Applied Mathematics 77.6, SI (2012). DOI: {10.1093/imamat/hxs049}.

Allaire, G. *Homogenization and two-scale convergence.* SIAM Journal on Mathematical Analysis 23.6 (1992). DOI: 10.1137/0523084.

Allen, S. M. and J. W. Cahn. *A microscopic theory for antiphase boundary motion and its application to antiphase domain coarsening.* Acta Metallurgica 27.6 (1979). DOI: 10.1016/0001-6160(79)90196-2.

Anderson, D. M., G. B. McFadden, and A. A. Wheeler. *A phase-field model of solidification with convection.* Physica D 135.1 (2000). DOI: 10.1016/S0167-2789(99)00109-8.

Bahar, T., F. Golfier, C. Oltean, and M. Benioug. *An upscaled model for bio-enhanced NAPL dissolution in porous media.* Transport in Porous Media 113 (2016). DOI: 10.1007/s11242-016-0718-7.

Baňas, L. and H. S. Mahato. *Homogenization of evolutionary Stokes-Cahn-Hilliard equations for two-phase porous media flow.* Asymptotic Analysis 105 (2017). DOI: 10.3233/asy-171436.

Bastian, P., F. Heimann, and S. Marnach. *Generic implementation of finite element methods in the distributed and unified numerics environment (DUNE).* Kybernetika 2 (2010). URL: https://www.kybernetika.cz/content/2010/2/294.

Bastidas Olivares, M., C. Bringedal, and I. S. Pop. *A two-scale iterative scheme for a phase-field model for precipitation and dissolution in porous media.* Applied Mathematics and Computation 396 (2021). DOI: 10.1016/j.amc.2020.125933.

Battiato, I. and D. M. Tartakovsky. *Applicability regimes for macroscopic models of reactive transport in porous media.* Journal of Contaminant Hydrology 120-121 (2011). DOI: 10.1016/j.jconhyd.2010.05.005.

Battiato, I., D. M. Tartakovsky, A. M. Tartakovsky, and T. Scheibe. *On breakdown of macroscopic models of mixing-controlled heterogeneous reactions in porous media.* Advances in Water Resources 32.11 (2009). DOI: 10.1016/j.advwatres.2009.08.008.

Beckermann, C., H.-J. Diepers, I. Steinbach, A. Karma, and X. Tong. *Modeling melt convection in phase-field simulations of solidification.* Journal of Computational Physics 154.2 (1999). DOI: 10.1006/jcph.1999.6323.

Berg, S., H. Ott, S. A. Klapp, A. Schwing, R. Neiteler, N. Brussee, A. Makurat, L. Leu, F. Enzmann, J.-O. Schwarz, M. Kersten, S. Irvine, and M. Stampanoni. *Real-time 3d imaging of haines jumps in porous media flow.* Proceedings of the National Academy of Sciences 110.10 (2013). DOI: 10.1073/pnas.1221373110.

Blowey, J. F. and C. M. Elliott. *The Cahn–Hilliard gradient theory for phase separation with non-smooth free energy part I: mathematical analysis.* European Journal of Applied Mathematics 2.3 (1991). DOI: 10.1017/S095679250000053X.

Blunt, M. J., B. Bijeljic, H. Dong, O. Gharbi, S. Iglauer, P. Mostaghimi, A. Paluszny, and C. Pentland. *Pore-scale imaging and modelling.* Advances in Water Resources 51.Supplement C (2013). DOI: 10.1016/j.advwatres.2012.03.003.

Bosch, J., C. Kahle, and M. Stoll. *Preconditioning of a coupled Cahn-Hilliard Navier-Stokes system.* Communications in Computational Physics 23.2 (2018). DOI: https://doi.org/10.4208/cicp.OA-2017-0037.

Boyer, F., C. Lapuerta, S. Minjeaud, B. Piar, and M. Quintard. *Cahn–Hilliard/ Navier–Stokes model for the simulation of three-phase flows.* Transport in Porous Media 82.3 (2010). DOI: 10.1007/s11242-009-9408-z.

Boyer, F. and C. Lapuerta. *Study of a three component Cahn–Hilliard flow model.* Mathematical Modelling and Analysis 40 (2006). DOI: 10.1051/m2an:2006028.

Boyer, F. and S. Minjeaud. *Hierarchy of consistent n-component Cahn–Hilliard systems.* Mathematical Models & Methods in Applied Sciences 24.14 (2014). DOI: 10.1142/S0218202514500407.

Bringedal, C., I. Berre, I. S. Pop, and F. A. Radu. *A model for non-isothermal flow and mineral precipitation and dissolution in a thin strip.* Journal of Computational and Applied Mathematics 289 (2015). DOI: 10.1016/j.cam.2014.12.009.

Bringedal, C., I. Berre, I. S. Pop, and F. A. Radu. *Upscaling of non-isothermal reactive porous media flow with changing porosity.* Transport in Porous Media 114.2 (2016). DOI: 10.1007/s11242-015-0530-9.

Bringedal, C., I. Berre, I. S. Pop, and F. A. Radu. *Upscaling of nonisothermal reactive porous media flow under dominant Péclet number: the effect of changing porosity.* Multiscale Modeling & Simulation 14.1 (2016). DOI: 10.1137/15M1022781.

Bringedal, C. and K. Kumar. *Effective behavior near clogging in upscaled equations for non-isothermal reactive porous media flow.* Transport in Porous Media 120.3 (2017). DOI: 10.1007/s11242-017-0940-y.

Bronsard, L. and F. Reitich. *On three-phase boundary motion and the singular limit of a vector-valued Ginzburg–Landau equation.* Archive for Rational Mechanics and Analysis 124.4 (1993). DOI: 10.1007/BF00375607.

Bunoiu, R., G. Cardone, R. Kengne, and J. L. Woukeng. *Homogenization of 2d Cahn-Hilliard-Navier-Stokes system.* Journal of Elliptic and Parabolic Equations 6 (2020). DOI: 10.1007/s41808-020-00074-w.

Caffarelli, L. A. and N. E. Muler. *An l-infinity bound for solutions of the Cahn-Hilliard equation.* Archive for Rational Mechanics and Analysis 133.2 (1995). DOI: 10.1007/BF00376814.

Caginalp, G. and P. C. Fife. *Dynamics of layered interfaces arising from phase boundaries.* SIAM Journal on Applied Mathematics 48.3 (1988). DOI: 10.1137/0148029.

Caginalp, G. and X. Chen. *Convergence of the phase field model to its sharp interface limits.* European Journal of Applied Mathematics 9.4 (1998). DOI: 10.1017/S0956792598003520.

Cahn, J. W. and J. E. Hilliard. *Free energy of a nonuniform system. i. interfacial free energy.* The Journal of Chemical Physics 28.2 (1958). DOI: 10.1063/1.1744102.

Chen, Z., S. L. Lyons, and G. Qin. *Derivation of the forchheimer law via homogenization.* Transport in Porous Media 44.2 (2001). DOI: 10.1023/A:1010749114251.

Choquet, C. and A. Mikelić. *Rigorous upscaling of the reactive flow with finite kinetics and under dominant péclet number*. Continuum Mechanics and Thermodynamics 21.2 (2009). DOI: 10.1007/s00161-009-0099-z.

Cunningham, A. B., H. Class, A. Ebigbo, R. Gerlach, A. J. Phillips, and J. Hommel. *Field-scale modeling of microbially induced calcite precipitation*. Computational Geosciences 23 (2019). DOI: 10.1007/s10596-018-9797-6.

Cuthbert, M. O., L. A. McMillan, S. Handley-Sidhu, M. S. Riley, D. J. Tobler, and V. R. Phoenix. *A field and modeling study of fractured rock permeability reduction using microbially induced calcite precipitation*. Environmental Science & Technology 47.23 (2013). DOI: 10.1021/es402601g.

Daly, K. R. and T. Roose. *Homogenization of two fluid flow in porous media*. Proceedings of the Royal Society A 471.2176 (2015). DOI: 10.1098/rspa.2014.0564.

Davit, Y., C. G. Bell, H. M. Byrne, L. A. C. Chapman, L. S. Kimpton, G. E. Lang, K. H. L. Leonard, J. M. Oliver, N. C. Pearson, R. J. Shipley, S. L. Waters, J. P. Whiteley, B. D. Wood, and M. Quintard. *Homogenization via formal multiscale asymptotics and volume averaging: how do the two techniques compare?* Advances in Water Resources 62 (2013). DOI: 10.1016/j.advwatres.2013.09.006.

Dentz, M., T. Le Borgne, A. Englert, and B. Bijeljic. *Mixing, spreading and reaction in heterogeneous media: a brief review*. Journal of Contaminant Hydrology 120-121 (2011). DOI: 10.1016/j.jconhyd.2010.05.002.

Dunbar, O., K. F. Lam, and B. Stinner. *Phase field modelling of surfactants in multi-phase flow*. Interfaces and Free Boundaries. Mathematical Analysis, Computation and Applications 21 (4 2019). DOI: 10.4171/IFB/429.

Egger, A., U. Pillai, K. Agathos, E. Kakouris, E. Chatzi, I. A. Aschroft, and S. P. Triantafyllou. *Discrete and phase field methods for linear elastic fracture mechanics: a comparative study and state-of-the-art review*. Applied Sciences 9.12 (2019). DOI: 10.3390/app9122436.

Elder, K. R., M. Grant, N. Provatas, and J. M. Kosterlitz. *Sharp interface limits of phase-field models*. Physical Review E 64 (2 2001). DOI: 10.1103/PhysRevE.64.021604.

Fatima, T., N. Arab, E. P. Zemskov, and A. Muntean. *Homogenization of a reaction–diffusion system modeling sulfate corrosion of concrete in locally periodic perforated domains*. Journal of Engineering Mathematics 69.2 (2011). DOI: 10.1007/s10665-010-9396-6.

Feder, M. J., V. J. Morasko, A. Akyel, R. Gerlach, and A. J. Phillips. *Temperature-dependent inactivation and catalysis rates of plant-based ureases for engineered biomineralization*. Engineering Reports (2020). DOI: InRevision,ManuscriptID\#ENG-2019-12-0913.

Garcke, H., C. Hecht, M. Hinze, and C. Kahle. *Numerical approximation of phase field based shape and topology optimization for fluids*. SIAM Journal on Scientific Computing 37.4 (2015). DOI: 10.1137/140969269.

Garcke, H., M. Hinze, and C. Kahle. *A stable and linear time discretization for a thermodynamically consistent model for two-phase incompressible flow*. Applied Numerical Mathematics 99 (2016). DOI: https://doi.org/10.1016/j.apnum.2015.09.002.

Garcke, H., M. Hinze, C. Kahle, and K. Fong Lam. *A phase field approach to shape optimization in Navier–Stokes flow with integral state constraint*. Advances in Computational Mathematics (2017). DOI: 10.1007/s10444-018-9586-8.

Garcke, H., B. Nestler, and B. Stoth. *On anisotropic order parameter models for multi-phase systems and their sharp interface limits*. Physica D 115.1 (1998). DOI: 10.1016/S0167-2789(97)00227-3.

Gilbarg, D. and N. Trudinger. *Elliptic partial differential equations of second order*. Classics in Mathematics. Springer Berlin, 2001. DOI: 10.1007/978-3-642-61798-0.

Gray, W. G. and C. T. Miller. *Thermodynamically constrained averaging theory approach for modeling flow and transport phenomena in porous medium systems: 1. motivation and overview*. Advances in Water Resources 28 (2005). DOI: 10.1016/j.advwatres.2004.09.005.

Grün, G. and F. Klingbeil. *Two-phase flow with mass density contrast: stable schemes for a thermodynamic consistent and frame-indifferent diffuse-interface model*. Journal of Computational Physics 257 (2014). DOI: https://doi.org/10.1016/j.jcp.2013.10.028.

Guo, Z., F. Yu, P. Lin, S. Wise, and J. Lowengrub. *A diffuse domain method for two-phase flows with large density ratio in complex geometries*. Journal of Fluid Mechanics 907 (2021). DOI: 10.1017/jfm.2020.790.

Hamdan, N. and E. Kavazanjian. *Enzyme-induced carbonate mineral precipitation for fugitive dust control*. Géotechnique 66.7 (2016). DOI: 10.1680/jgeot.15.P.168.

Harkins, W. D. and A. Feldman. *Films. the spreading of liquids and the spreading coefficient*. Journal of the American Chemical Society 44.12 (1922). DOI: 10.1021/ja01433a001.

Hohenberg, P. C. and B. I. Halperin. *Theory of dynamic critical phenomena*. Reviews of Modern Physics 49 (3 1977). DOI: 10.1103/RevModPhys.49.435.

Hommel, J., A. Akyel, Z. Frieling, A. J. Phillips, R. Gerlach, A. B. Cunningham, and H. Class. *A numerical model for enzymatically induced calcium carbonate precipitation*. Applied Science 10 (2020). DOI: 10.3390/app10134538.

Hommel, J., E. Coltman, and H. Class. *Porosity-permeability relations for evolving pore space: a review with a focus on (bio-)geochemically altered porous media*. Transport in Porous Media 124.2 (2018). DOI: 10.1007/s11242-018-1086-2.

Hornung, U. *Homogenization and porous media*. Vol. 6. Springer Science & Business Media, 1996.

Jackson, A. S., I. Rybak, R. Helmig, W. G. Gray, and C. T. Miller. *Thermodynamically constrained averaging theory approach for modeling flow and transport phenomena in porous medium systems: 9. transition region models*. Advances in Water Resources 42 (2012). DOI: 10.1016/j.advwatres.2012.01.006.

Jeong, D. and J. Kim. *Conservative Allen–Cahn–Navier–Stokes system for incompressible two-phase fluid flows*. Computers & Fluids 156 (2017). DOI: 10.1016/j.compfluid.2017.07.009.

Jeong, J.-H., N. Goldenfeld, and J. A. Dantzig. *Phase field model for three-dimensional dendritic growth with fluid flow*. Physical Review E 64 (4 2001). DOI: 10.1103/PhysRevE.64.041602.

Karadimitriou, N. K., V. Joekar-Niasar, S. M. Hassanizadeh, P. J. Kleingeld, and L. J. Pyrak-Nolte. *A novel deep reactive ion etched (DRIE) glass micro-model for two-phase flow experiments*. Lab on a Chip 12 (18 2012). DOI: 10.1039/C2LC40530J.

Karadimitriou, N. K., M. Musterd, P. J. Kleingeld, M. T. Kreutzer, S. M. Hassanizadeh, and V. Joekar-Niasar. *On the fabrication of PDMS micromodels by rapid prototyping, and their use in two-phase flow studies*. Water Resources Research 49.4 (2013). DOI: 10.1002/wrcr.20196.

Kim, D. H., N. Mahabadi, J. Jang, and L. A. van Paassen. *Assessing the kinetics and pore-scale characteristics of biological calcium carbonate precipitation in porous media using a microfluidic chip experiment*. Water Resources Research 56.2 (2020). DOI: 10.1029/2019WR025420.

Kim, J. *A continuous surface tension force formulation for diffuse-interface models*. Journal of Computational Physics 204.2 (2005). DOI: 10.1016/j.jcp.2004.10.032.

Knabner, P., C. Duijn, and S. Hengst. *An analysis of crystal dissolution fronts in flows through porous media. part 1: compatible boundary conditions*. Advances in Water Resources 18.3 (1995). DOI: 10.1016/0309-1708(95)00005-4.

Kumar, K., M. Neuss-Radu, and I. S. Pop. *Homogenization of a pore scale model for precipitation and dissolution in porous media*. IMA Journal of Applied Mathematics 81.5 (2016). DOI: 10.1093/imamat/hxw039.

Kumar, K., I. S. Pop, and F. A. Radu. *Convergence analysis of mixed numerical schemes for reactive flow in a porous medium*. SIAM Journal on Numerical Analysis 51.4 (2013). DOI: 10.1137/120880938.

Kumar, K., T. L. van Noorden, and I. S. Pop. *Effective dispersion equations for reactive flows involving free boundaries at the microscale*. Multiscale Modeling & Simulation 9.1 (2011). DOI: 10.1137/100804553.

Kumar, K., M. F. Wheeler, and T. Wick. *Reactive flow and reaction-induced boundary movement in a thin channel*. SIAM Journal on Scientific Computing 35 (2013). DOI: 10.1137/130913134.

Lamb, H. *Hydrodynamics*. 6th ed. Cambridge University Press, 1932.

Lauchnor, E. G., L. N. Schultz, S. Bugni, A. C. Mitchell, A. B. Cunningham, and R. Gerlach. *Bacterially induced calcium carbonate precipitation and strontium co-precipitation in a porous media flow system*. Environmental Science & Technology 47.3 (2013). DOI: 10.1021/es304240y.

Lervåg, K. Y. and J. Lowengrub. *Analysis of the diffuse-domain method for solving pdes in complex geometries*. Communications in Mathematical Sciences 13.6 (2015). DOI: 10.4310/CMS.2015.v13.n6.a6.

Li, X., J. Lowengrub, A. Rätz, and A. Voigt. *Solving PDEs in complex geometries: a diffuse domain approach.* Communications in Mathematical Sciences 7.1 (2009). DOI: 10.4310/CMS.2009.v7.n1.a4.

Lowengrub, J. and L. Truskinovsky. *Quasi-incompressible Cahn–Hilliard fluids and topological transitions*. Proceedings of the Royal Society A 454.1978 (1998). DOI: 10.1098/rspa.1998.0273.

Lunowa, S. B., C. Bringedal, and I. S. Pop. *On an averaged model for immiscible two-phase flow with surface tension and dynamic contact angle in a thin strip*. Studies in Applied Mathematics 147 (2021). DOI: 10.1111/sapm.12376.

Metzger, S. and P. Knabner. *Homogenization of two-phase flow in porous media from pore to Darcy scale: a phase-field approach*. Multiscale Modeling & Simulation 19.1 (2021). DOI: 10.1137/19m1287705.

Mikelić, A. *On an averaged model for the 2-fluid immiscible flow with surface tension in a thin cylindrical tube*. Computational Geosciences 7 (2009). DOI: 10.1023/A:1025527716078.

Mikelić, A. and L. Paoli. *On the derivation of the Buckley-Leverett model from the two fluid Navier-Stokes equations in a thin domain*. Computational Geosciences. 4.1 (2000). DOI: 10.1023/A:1011503731330.

Mikelić, A., V. Devigne, and C. J. van Duijn. *Rigorous upscaling of the reactive flow through a pore, under dominant Peclet and Damkohler numbers*. SIAM Journal on Mathematical Analysis 38.4 (2006). DOI: 10.1137/050633573.

Minjeaud, S. *An unconditionally stable uncoupled scheme for a triphasic Cahn–Hilliard/Navier–Stokes model*. Numerical Methods for Partial Differential Equations 29.2 (2013). DOI: https://doi.org/10.1002/num.21721.

Minto, J. M., R. J. Lunn, and G. E. Mountassir. *Development of a reactive transport model for field-scale simulation of microbially induced carbonate precipitation*. Water Resources Research (2019). DOI: 10.1029/2019WR025153.

Minto, J. M., Q. Tan, R. J. Lunn, G. E. Mountassir, H. Guo, and X. Cheng. *'Microbial mortar'-restoration of degraded marble structures with microbially induced carbonate precipitation*. Construction and Building Materials 180 (2018). DOI: 10.1016/j.conbuildmat.2018.05.200.

Mitchell, A. C. and F. G. Ferris. *The coprecipitation of Sr into calcite precipitates induced by bacterial ureolysis in artificial groundwater: Temperature and kinetic dependence*. Geochimica et Cosmochimica Acta 69.17 (2005). DOI: 10.1016/j.gca.2005.03.014.

Molins, S., C. Soulaine, N. I. Prasianakis, A. Abbasi, P. Poncet, A. J. C. Ladd, V. Starchenko, S. Roman, D. Trebotich, H. A. Tchelepi, and C. I. Steefel. *Simulation of mineral dissolution at the pore scale with evolving fluid-solid interfaces: review of approaches and benchmark problem set*. Computational Geosciences (2020). DOI: 10.1007/s10596-019-09903-x.

Molins, S., D. Trebotich, G. H. Miller, and C. I. Steefel. *Mineralogical and transport controls on the evolution of porous media texture using direct numerical simulation*. Water Resources Research 53.5 (2017). DOI: 10.1002/2016WR020323.

Moser, M. J. J. *Sharp interface limits for diffuse interface models with contact angle*. 2021. URL: https://epub.uni-regensburg.de/44389/.

Mottoni, P. D. and M. Schatzman. *Geometrical evolution of developed interfaces*. Transactions of the American Mathematical Society 347.5 (1995). DOI: 10.2307/2154960.

Mu, X., F. Frank, B. Riviere, F. O. Alpak, and W. G. Chapman. *Mass-conserved density gradient theory model for nucleation process*. Industrial & Engineering Chemistry Research 57.48 (2018). DOI: 10.1021/acs.iecr.8b03389.

Mujah, D., M. A. Shahin, and L. Cheng. *State-of-the-art review of biocementation by microbially induced calcite precipitation (MICP) for soil stabilization*. Geomicrobiology Journal 34.6 (2017). DOI: 10.1080/01490451.2016.1225866.

Nassar, M. K., D. Gurung, M. Bastani, T. R. Ginn, B. Shafei, M. G. Gomez, C. M. R. Graddy, D. C. Nelson, and J. T. DeJong. *Large-scale experiments in microbially induced calcite precipitation (MICP): reactive transport model development and prediction*. Water Resources Research 54 (2018). DOI: 10.1002/2017WR021488.

Nemati, M. and G. Voordouw. *Modification of porous media permeability, using calcium carbonate produced enzymatically in situ*. Enzyme and Microbial Technology 33.5 (2003). DOI: 10.1016/S0141-0229(03)00191-1.

Neupane, D., H. Yasuhara, N. Kinoshita, and T. Unno. *Applicability of enzymatic calcium carbonate precipitation as a soil-strengthening technique*. ASCE Journal of Geotechnical and Geoenvironmental Engineering 139.December (2013). DOI: 10.1061/(ASCE)GT.1943-5606.0000959.

Oden, J. T., A. Hawkins, and S. Prudhomme. *General diffuse-interface theories and an approach to predictive tumor growth modeling*. Mathematical Models and Methods in Applied Sciences 20.03 (2010). DOI: 10.1142/S0218202510004313.

Pego, R. L. and O. Penrose. *Front migration in the nonlinear Cahn–Hilliard equation*. Proceedings of the Royal Society A 422.1863 (1989). DOI: 10.1098/rspa.1989.0027.

Phillips, A. J., R. Gerlach, E. Lauchnor, A. C. Mitchell, A. B. Cunningham, and L. H. Spangler. *Engineered applications of ureolytic biomineralization: a review*. Biofouling 29.6 (2013). DOI: 10.1080/08927014.2013.796550.

Phillips, A. J., E. Lauchnor, J. Eldring, R. Esposito, A. C. Mitchell, R. Gerlach, A. B. Cunningham, and L. H. Spangler. *Potential CO_2 leakage reduction through biofilm-induced calcium carbonate precipitation*. Environmental Science & Technology 47.1 (2013). DOI: 10.1021/es301294q.

Phillips, A. J., A. B. Cunningham, R. Gerlach, R. Hiebert, C. Hwang, B. P. Lomans, J. Westrich, C. Mantilla, J. Kirksey, R. Esposito, and L. H. Spangler. *Fracture sealing with microbially-induced calcium carbonate precipitation: a field study*. Environmental Science & Technology 50 (2016). DOI: 10.1021/acs.est.5b05559.

Picchi, D. and I. Battiato. *The impact of pore-scale flow regimes on upscaling of im-miscible two-phase flow in porous media*. Water Resources Research 54 (2018). DOI: 10.1029/2018WR023172.

Pukhnachev, V. V. and V. A. Solonnikov. *On the problem of dynamic contact angle*. Journal of Applied Mathematics and Mechanics 46.6 (1982). DOI: 10.1016/0021-8928(82)90059-4.

Qian, T., X.-P. Wang, and P. Sheng. *Molecular scale contact line hydrodynamics of immiscible flows*. Physical Review E 68 (1 2003). DOI: 10.1103/PhysRevE.68.016306.

Qian, T., X.-P. Wang, and P. Sheng. *A variational approach to moving contact line hydrodynamics*. Journal of Fluid Mechanics 564 (2006). DOI: 10.1017/S0022112006001935.

Quintard, M. and S. Whitaker. *Two-phase flow in heterogeneous porous media: the method of large-scale averaging*. Transport in Porous Media 3 (1988). DOI: 10.1007/BF00233177.

Quintard, M. and S. Whitaker. *Convection, dispersion, and interfacial transport of contaminants: homogeneous porous media*. Advances in Water Resources 17.4 (1994). DOI: 10.1016/0309-1708(94)90002-7.

Quintard, M. and S. Whitaker. *Dissolution of an immobile phase during flow in porous media*. Industrial & Engineering Chemistry Research 38.3 (1999). DOI: 10.1021/ie980212t.

Ray, N., J. Oberlander, and P. Frolkovic. *Numerical investigation of a fully coupled micro-macro model for mineral dissolution and precipitation*. Computational Geosciences 23 (2019). DOI: 10.1007/s10596-019-09876-x.

Redeker, M., C. Rohde, and I. Sorin Pop. *Upscaling of a tri-phase phase-field model for precipitation in porous media*. IMA Journal of Applied Mathematics 81.5 (2016). DOI: 10.1093/imamat/hxw023.

Rybak, I. V., W. G. Gray, and C. T. Miller. *Modeling two-fluid-phase flow and species transport in porous media*. Journal of Hydrology 521 (2015). DOI: 10.1016/j.jhydrol.2014.11.051.

Schlögl, F. *Chemical reaction models for non-equilibrium phase transitions*. Zeitschrift für Physik 253.2 (1972). DOI: 10.1007/BF01379769.

Schmuck, M., M. Pradas, G. A. Pavliotis, and S. Kalliadasis. *Derivation of effective macroscopic Stokes–Cahn–Hilliard equations for periodic immiscible flows in porous media*. Nonlinearity 26.12 (2013). DOI: 10.1088/0951-7715/26/12/3259.

Schmuck, M., M. Pradas, G. A. Pavliotis, and S. Kalliadasis. *Upscaled phase-field models for interfacial dynamics in strongly heterogeneous domains*. Proceedings of the Royal Society A 468.2147 (2012). DOI: 10.1098/rspa.2012.0020.

Schulz, R. *Crystal precipitation and dissolution in a porous medium: evolving microstructure and perforated solid matrix*. Special Topics & Reviews in Porous Media 10 (2019). DOI: 10.1615/SpecialTopicsRevPorousMedia.2019029274.

Schulz, R., N. Ray, F. Frank, H. S. Mahato, and P. Knabner. *Strong solvability up to clogging of an effective diffusion-precipitation model in an evolving porous medium*. European Journal of Applied Mathematics 28.2 (2017). DOI: 10.1017/S0956792516000164.

Sharmin, S., M. Bastidas, C. Bringedal, and I. S. Pop. *Upscaling a Navier-Stokes-Cahn-Hilliard model for two-phase porous-media flow with solute-dependent surface tension effects*. Applicable Analysis (2022). DOI: 10.1080/00036811.2022.2052858.

Sharmin, S., C. Bringedal, and I. S. Pop. *On upscaling pore-scale models for two-phase flow with evolving interfaces*. Advances in Water Resources 142 (2020). DOI: 10.1016/j.advwatres.2020.103646.

Sun, Y. and C. Beckermann. *Diffuse interface modeling of two-phase flows based on averaging: mass and momentum equations*. Physica D 198.3 (2004). DOI: 10.1016/j.physd.2004.09.003.

Takaki, T. *Phase-field modeling and simulations of dendrite growth*. ISIJ International 54.2 (2014). DOI: 10.2355/isijinternational.54.437.

Tartakovsky, A. M., P. Meakin, T. D. Scheibe, and B. D. Wood. *A smoothed particle hydrodynamics model for reactive transport and mineral precipitation in porous and fractured porous media*. Water Resources Research 43.5 (2007). DOI: 10.1029/2005WR004770.

Tartar, L. *H-measures, a new approach for studying homogenisation, oscillations and concentration effects in partial differential equations*. Proceedings of the Royal Society of Edinburgh. Section A. Mathematics 115.3-4 (1990). DOI: 10.1017/S0308210500020606.

Taylor, C. and P. Hood. *A numerical solution of the Navier-Stokes equations using the finite element technique*. An International Journal. Computers & Fluids 1.1 (1973). DOI: 10.1016/0045-7930(73)90027-3.

van Duijn, C. J. and P. Knabner. *Travelling wave behaviour of crystal dissolution in porous media flow*. European Journal of Applied Mathematics 8 (1997).

van Duijn, C. J., A. Mikelić, I. S. Pop, and C. Rosier. *Effective dispersion equations for reactive flows with dominant Péclet and Damkohler numbers. Advances in chemical engineering*. Ed. by G. B. Marin, D. West, and G. S. Yablonsky. Vol. 34. Advances in Chemical Engineering. Academic Press, 2008. DOI: 10.1016/S0065-2377(08)00001-X.

van Duijn, C. J. and I. S. Pop. *Crystal dissolution and precipitation in porous media: pore scale analysis*. Journal für die reine und angewandte Mathematik 577 (2004). DOI: 10.1515/crll.2004.2004.577.171.

van Noorden, T. L. *Crystal precipitation and dissolution in a porous medium: effective equations and numerical experiments*. Multiscale Modeling & Simulation 7.3 (2009). DOI: 10.1137/080722096.

van Noorden, T. L. *Crystal precipitation and dissolution in a thin strip*. European Journal of Applied Mathematics 20.1 (2009). DOI: 10.1017/S0956792508007651.

van Noorden, T. L. and C. Eck. *Phase field approximation of a kinetic moving-boundary problem modelling dissolution and precipitation*. Interfaces and Free Boundaries. Mathematical Analysis, Computation and Applications 13.1 (2011). DOI: 10.4171/IFB/247.

van Noorden, T. L. and I. S. Pop. *A Stefan problem modelling crystal dissolution and precipitation*. IMA Journal of Applied Mathematics 73.2 (2007). DOI: 10.1093/imamat/hxm060.

van Noorden, T. L., I. S. Pop, A. Ebigbo, and R. Helmig. *An upscaled model for biofilm growth in a thin strip*. Water Resources Research 46 (2010). DOI: 10.1029/2009WR008217.

van Noorden, T. L., I. S. Pop, and M. Röger. *Crystal dissolution and precipitation in porous media: L^1-contraction and uniqueness*. Conference Publications 2007.Special (2007).

van Paassen, L. A., R. Ghose, T. J. M. van der Linden, W. R. L. van der Star, and M. C. M. van Loosdrecht. *Quantifying biomediated ground improvement by ureolysis: large-scale biogrout experiment*. Journal of Geotechnical and Geoenvironmental Engineering 136.12 (2010). DOI: 10.1061/(ASCE)GT.1943-5606.0000382.

van Wijngaarden, W. K., L. A. van Paassen, F. J. Vermolen, G. A. M. van Meurs, and C. Vuik. *A reactive transport model for biogrout compared to experimental data*. Transport in Porous Media 111.3 (2016). DOI: 10.1007/s11242-015-0615-5.

Weinhardt, F., H. Class, S. Vahid Dastjerdi, N. Karadimitriou, D. Lee, and H. Steeb. *Optical microscopy and pressure measurements of enzymatically induced calcite precipitation (EICP) in a microfluidic cell*. DaRUS (2020). DOI: 10.18419/darus-818.

Weinhardt, F., H. Class, S. Vahid Dastjerdi, N. K. Karadimitriou, D. Lee, and H. Steeb. *Experimental methods and imaging for enzymatically induced calcite precipitation in a micro-fluidic cell*. Earth and Space Science Open Archive (2020). DOI: 10.1002/essoar.10504060.1.

Weishaupt, K. *Model concepts for coupling free flow with porous medium flow at the pore-network scale: from single-phase flow to compositional non-isothermal two-phase flow*. Universität Stuttgart, 2020. DOI: 10.18419/opus-10932.

Whitaker, J. M., S. Vanapalli, and D. Fortin. *Improving the strength of sandy soils via ureolytic $CaCO_3$ solidification by sporosarcina ureae*. Biogeosciences Discussions 2018 (2018). DOI: 10.5194/bg-2017-517.

Whitaker, S. *The method of volume averaging*. Vol. 13. Springer Science & Business Media, 1999.

Whitaker, S. *Flow in porous media ii: the governing equations for immiscible, two-phase flow*. Transport in Porous Media 1 (1986). DOI: 10.1007/BF00714688.

Wildenschild, D. and A. P. Sheppard. *X-ray imaging and analysis techniques for quantifying pore-scale structure and processes in subsurface porous medium systems*. Advances in Water Resources 51.Supplement C (2013). DOI: 10.1016/j.advwatres.2012.07.018.

Witterstein, G. *Sharp interface limit of phase change flows*. Advances in Mathematical Sciences and Applications 20 (2 2010).

Witterstein, G. *Phase change flows with mass exchange*. Advances in Mathematical Sciences and Applications 21 (2 2011).

Wood, B. D., F. Golfier, and M. Quintard. *Dispersive transport in porous media with biofilms: local mass equilibrium in simple unit cells*. International Journal of Environment and Waste Management 7.1-2 (2011). DOI: 10.1504/IJEWM.2011.037364.

Wood, B. D. *Inertial effects in dispersion in porous media*. Water Resources Research 43.12 (2007). DOI: 10.1029/2006WR005790.

Woolley, M. A., L. van Paassen, and E. Kavazanjian. *Impact on surface hydraulic conductivity of EICP treatment for fugitive dust mitigation. Geo-congress 2020.* DOI: 10.1061/9780784482834.015.

Xia, Y. and G. M. Whitesides. *Soft lithography.* Angewandte Chemie International Edition 37.5 (1998). DOI: 10.1002/(SICI)1521-3773(19980316)37:5<550::AID-ANIE550>3.0.CO;2-G.

Xu, X., Y. Di, and H. Yu. *Sharp-interface limits of a phase-field model with a generalized Navier slip boundary condition for moving contact lines.* Journal of Fluid Mechanics 849 (2018). DOI: 10.1017/jfm.2018.428.

Xu, Z. and P. Meakin. *Phase-field modeling of solute precipitation and dissolution.* Journal of Chemical Physics 129.1 (2008). DOI: 10.1063/1.2948949.

Yu, F., Z. Guo, and J. Lowengrub. *Higher-order accurate diffuse-domain methods for partial differential equations with dirichlet boundary conditions in complex, evolving geometries.* Journal of Computational Physics 406 (2020). DOI: 10.1016/j.jcp.2019.109174.

Zhang, Q. and X.-P. Wang. *Phase field modeling and simulation of three-phase flow on solid surfaces.* Journal of Computational Physics 319 (2016). DOI: 10.1016/j.jcp.2016.05.016.

Zhang, T. and I. Klapper. *Mathematical model of biofilm induced calcite precipitation.* Water Science and Technology 61.11 (2010). DOI: 10.2166/wst.2010.064.

Zhang, T. and I. Klapper. *Mathematical model of the effect of electrodiffusion on biomineralization.* International Journal of Non-Linear Mechanics 46.4 (2011). DOI: 10.1016/j.ijnonlinmec.2010.12.008.

Abstract

The overarching topic of this dissertation is multi-phase flow in porous media. In the presence of salts and their ions, precipitation and dissolution can alter the pore-space and have a great impact on flow through porous media. Therefore, we need reliable models that can describe these effects accurately both on the pore-scale and on larger scales.

In this dissertation, we first propose several pore-scale models for multi-phase flow including reactive fluid–solid interfaces. In these models, both fluid–fluid and fluid–solid interfaces are resolved as diffuse interfaces using the phase field method. We investigate the thermodynamical consistency of the models and find their sharp interface limit using asymptotic analysis. We proceed to upscale the pore-scale models either using homogenization in a periodic porous medium or transversal averaging in the simplified geometry of a thin strip. The results are multi-scale models consisting of averaged equations for flux and ion concentration, with parameters that have to be determined through cell problems. These cell problems encode information about the geometry of the microscale at each macroscopic point.

Lastly, we apply the developed models to investigate enzymatically induced calcite precipitation. We compare simulation results to micro-fluidic experiments and find excellent agreement, in particular for the growth direction of crystal aggregates.